HAL
open science

Reservoir-induced dynamics and information processing in quantum optical systems

Zejian Li

To cite this version:

Zejian Li. Reservoir-induced dynamics and information processing in quantum optical systems. Quantum Physics [quant-ph]. Université Paris Cité, 2022. English. NNT : 2022UNIP7228 . tel-03937848v2

HAL Id: tel-03937848

https://hal.science/tel-03937848v2

Submitted on 18 Jan 2024

HAL is a multi-disciplinary open access archive for the deposit and dissemination of scientific research documents, whether they are published or not. The documents may come from teaching and research institutions in France or abroad, or from public or private research centers.

L'archive ouverte pluridisciplinaire **HAL**, est destinée au dépôt et à la diffusion de documents scientifiques de niveau recherche, publiés ou non, émanant des établissements d'enseignement et de recherche français ou étrangers, des laboratoires publics ou privés.

Université Paris Cité

École doctorale 564 : Physique en Île-de-France

Laboratoire Matériaux et Phénomènes Quantiques (UMR 7162)

Thèse de doctorat en physique

Reservoir-induced dynamics and information processing in quantum optical systems

Dynamique et traitement de l'information induits par réservoir dans des systèmes d'optique quantique

présentée par

Zejian LI

sous la direction de

Cristiano Ciuti

Jury

PR	Giuseppe Carleo	École polytechnique fédérale de Lausanne	Rapporteur
PR	Cristiano Ciuti	Université Paris Cité	Directeur de thèse
PR	Claudio Conti	Sapienza University of Rome	Rapporteur
PR	Sara Ducci	CNRS (MPQ)	Présidente
PR	Giovanna Morigi	Saarland University	Examinatrice

Présentée et soutenue publiquement à Paris le 8 decembre 2022

细推**物理**须行乐，何用浮名绊此身。

— 杜甫 (Du Fu), 《曲江二首》

Acknowledgements

Looking back from the completion of this dissertation, I could not feel more grateful to everyone who rendered this work possible and who made me survive and enjoy the three unconventional years that elapsed since the beginning of my doctoral studies.

I would like to first express my sincere gratitude to my thesis supervisor, Cristiano Ciuti, an exceptional researcher that I look up to, for his warm welcome and firm support since our very first contacts, and most importantly, for the rich mentorship he provided. Cristiano has truly been a coach with experience, understanding and patience. I have always been motivated by his endless enthusiasm and optimism in science and in life, and his characteristic sense of humor that never fails to resonate with us. I will not forget the relativistic moves that we pulled off together thanks to his responsiveness at ultrafast time scales.

Also, many thanks to Giuseppe Carleo and Claudio Conti, for accepting to be my thesis referees, and equally to all the members of my jury, Sara Ducci and Giovanna Morigi, for the inspiring discussions we had during the defense and their corrections that improved the present manuscript.

I am greatly obliged to all my collaborators in the various projects involved in the course of this thesis (whether or not finally giving rise to publications). A significant portion of the credit goes undoubtedly to my group-mates in *l'équipe theorie*: to Zakari Denis, who has been more of a mentor to me that is always prepared to answer my questions in all subjects while claiming to be "not an expert", who also shared his handcrafted LaTeX template that this manuscript is based upon; to Valentin Heyraud, the mathematician and *rugbyman*, who accompanied me in taking relativity courses and proofread an early draft of Chapter 1 of this manuscript; to Kaelan Donatella, dear deskmate in this Ph.D. adventure, who is never short of interesting research ideas; to Filippo Vicentini, who generously taught me numerics; to Alexandre Le Boité, one of the few colleagues I could talk to in my native language; to Ariane Soret, who co-authored my very first research publication; and also to Hugo Tschirhart for the great parties he organized. I also appreciate the working experience with Vincent Vinel from the DON team, my talented experimentalist friend that cheered me up with his enthusiasm and physical intuitions when I was drowning in the pandemic lockdown. I would like to acknowledge the group of Alberto Bramati at LKB for the experiments they performed and the group of Jacqueline Bloch at C2N for the inspiring exchanges.

Of course, a principal component of this journey consists in the interactions with all the people in the group as well as the rest of the lab, which now becomes the good old days that I shall keep in my memory. I therefore thank: Geva Arwas, who gave me kind advice on academia as a senior; Federico Borletto, who mobilized his Italian

connections to help me; Danh-Phuong Nguyen, with his cute gift allowing me to take naps with comfort; Luca Giacomelli, for the interesting discussions about semiclassical general relativity; Dalin Borici, who always shared his biscuits in time (when I would start to get hungry in the office); Mao Yuncheng, a brave parent, with whom I also wish to play duet one day; and the former members of the group as well, including Alberto Biella and Cassia Naudet-Baulieu. I would like to give a special thanks to Batiste Janvier, our lab technician by day and an experienced stargazer at night, who initiated me into deep-sky astrophotography by sharing his instruments and his Bortle-class-5 garden; and certainly also to his lovely family, who tolerated our crazy overnight star parties at their house. In fact, a small part of this manuscript was written during the signal acquisition sessions, where photons emitted from galaxies a few million light-years away were being collected on my CMOS sensor. I thank as well our IT admin Loïc Noël for our fun adventures in the server room, where I had the chance to play with bare-metal machines and to experience the quotidian life of a cluster administrator. I encountered also at the lab the best administration team so far in my career: Nathalie Merlet, Sandrine Di Concetto and Jocelyne Moreau, who have always been extremely thoughtful and efficient.

Just like Dirac-delta switching functions can lead to unphysical predictions when modeling interactions, real-life human interactions are also smeared in spacetime. Therefore, I thank my former colleagues Supanut Thanasilp and Marc-Antoine Lemonde, and my former supervisors, Dimitris Angelakis at CQT and Jacques Laskar at IMCCE, for their long-time support.

I take the chance to thank as well the people who intersected my world line outside of the lab, making up another principal component of this journey, among them, *camarades* at Ecole polytechnique: Li Yunzhe, Liu Mingkun, Abel Thayil; and my neighbor Lu Yunjiao at CIUP. I thank Zhu Mengcheng for taking the time and interest to come to my defense and assisting in my *pot*, but also Wang Haina and Xu Yi, who joined me remotely despite the nonnegligible time-zone barrier.

I am grateful to my piano teacher Patrice Holiner for his strict yet enlightening coaching, and also to my former duet partners Daniya, Brian Lee, Li Haohan and Abderrahmane for playing good music together after school.

I am deeply indebted to Mme Evelyne Altes, my French equivalent of grandmother, for her everlasting kindness and encouragement, as well as her marvelous cuisine that I had the chance to feast on countless times.

I would like to heartfully acknowledge Zhu Yafan, who helped solve my existential problems, to whom a substantial part of my current state shall be credited.

Finally, I must thank my parents for their unconditional backing in every imaginable way, as well as the other family members, without which I could not have possibly gone thus far.

21 December 2022, on flight FR9135

Summary

This thesis is devoted to the study of reservoir-induced dynamics and reservoir computing in the context of quantum optics, structured along three major axes: (1) the dissipative dynamics of a quantum system in the presence of the environment (modeled as a reservoir); (2) harnessing dissipation as a resource by appropriate design of the reservoir to achieve desired control over a quantum system (reservoir engineering) and (3) exploiting the dynamics of a reservoir itself for information-processing applications (reservoir computing). In the first part, we study a dissipative phase transition in a photonic system subjected to a coherent optical drive. We propose an all-optical technique of tuning the spatial geometry of the system *in situ* and demonstrate that a first-order dissipative phase transition emerges in a two-dimensional (2D) configuration but not in 1D. We show the experiments validating our theoretical predictions, representing the first experimental demonstration of the role of dimensionality in determining criticality in photonic systems. In the second part, we address the theory of reservoir engineering. We derive the effective dynamics induced by a strongly dissipative single-mode reservoir, and propose a photonic quantum simulator for antiferromagnetic spins by applying the theory. We show that the reservoir is capable of mediating both coherent and dissipative antiferromagneticlike couplings between the simulated spins, and that the dissipative coupling alone can induce frustration in the system. The final part explores the paradigm of reservoir computing in relativistic quantum information. Here, the *reservoir* refers to a generic physical system with nontrivial response dynamics when subjected to some input, that one can exploit to construct useful representations of the input information. The system studied consists of a quantum detector undergoing relativistic motion inside a cavity, that can be implemented on analog platforms such as circuit QED. We illustrate the proposed reservoir-computing scheme with a supervised classification task via numerical simulation of the system, and show that the relativistic quantum effects bring a considerable enhancement to the performance of the classifier. This shows that one can harness information-processing power from the fundamental laws of physics, providing a first instance of relativity-inspired quantum reservoir computing.

Keywords: quantum optics, open quantum systems, phase transitions, polaritons, nonequilibrium systems, many-body physics, reservoir engineering, quantum simulation, frustrated magnetism, reservoir computing, machine learning, relativistic quantum information, quantum engineering

Résumé

Cette thèse est consacrée à l'étude de la dynamique et l'apprentissage automatique induits par réservoir dans le contexte de l'optique quantique. Elle est structurée autours de trois axes majeurs : (1) la dynamique dissipative d'un système quantique en présence de son environnement (modélisé par un réservoir) ; (2) le contrôle d'un système quantique par une conception appropriée du réservoir (ingénierie de réservoir) et (3) l'exploitation de la dynamique d'un réservoir lui-même pour traiter de l'information (calcul par réservoir). Dans la première partie, nous étudions une transition de phase dissipative dans un système photonique soumis à un pompage optique cohérent. Nous proposons une technique permettant d'ajuster *in situ* la géométrie spatiale du système de manière purement optique. Nous montrons l'émergence d'une transition de phase du premier ordre en deux dimensions et son absence en une dimension. Nous présentons les expériences confirmant nos prédictions théoriques, ce qui représente la première démonstration expérimentale du rôle de la dimensionnalité dans l'existence de la criticalité dans des systèmes photoniques. Dans la deuxième partie, Nous traitons la théorie de l'ingénierie de réservoir. Nous dérivons la dynamique effective induite par un réservoir fortement dissipatif à un seul mode, et proposons un simulateur photonique pour des spins antiferromagnétiques en appliquant cette théorie. Nous démontrons que le réservoir est capable d'induire des couplages antiferromagnétiques cohérents et dissipatifs entre les spins simulés, et que le couplage dissipatif seul donne lieu à la frustration dans le système. Enfin, nous explorons dans la dernière partie l'apprentissage automatique au moyen de réservoirs dans l'information quantique relativiste. Ici, le *réservoir* est un système physique générique qui réagit par une dynamique non triviale en réponse à une excitation en entrée. Cette dynamique peut être exploitée pour construire des représentations utiles de l'entrée. Le système étudié comprend un détecteur quantique en mouvement relativiste dans une cavité, que l'on peut implémenter sur des plateformes analogiques comme des circuits supraconducteurs. Nous illustrons le protocole proposé sur un problème de classification par simulation numérique du système, et constatons une augmentation considérable de la performance dans le régime relativiste. Nos résultats constituent un premier exemple du calcul par réservoir quantique inspiré de la relativité, montrant que l'on peut tirer parti des lois fondamentales de la physique pour traiter de l'information.

Mots-clés : optique quantique, systèmes quantiques ouverts, transitions de phase, polaritons, systèmes hors équilibre, physique à N corps, ingénierie de réservoir, simulation quantique, magnétisme frustré, calcul par réservoir, apprentissage automatique, information quantique relativiste, ingénierie quantique

Publications

The scientific publications produced in the course of this thesis are listed below and are indexed with Greek letters. The present manuscript is based mainly upon the results reported in [α], [γ], and [ϵ].

[α] Z. Li, A. Soret and C. Ciuti,
"Dissipation-induced antiferromagneticlike frustration in coupled photonic resonators",
Physical Review A **103**, 022616 (2021).

[β] V. Vinel*, Z. Li*, A. Borne, A. Bensemhoun, I. Favero, C. Ciuti and G. Leo,
"Non-Hermitian bath model for arrays of coupled nanoresonators",
Optics Express **29**, 34015 (2021).

[γ] Z. Li*, F. Claude*, T. Boulier, E. Giacobino, Q. Glorieux, A. Bramati and C. Ciuti,
"Dissipative Phase Transition with Driving-Controlled Spatial Dimension and Diffusive Boundary Conditions",
Physical Review Letters **128**, 093601 (2022).

[δ] V. Heyraud, Z. Li, Z. Denis, A. Le Boité and C. Ciuti,
"Noisy quantum kernel machines",
Physical Review A **106**, 052421 (2022).

[ϵ] Z. Li, V. Heyraud, K. Donatella, Z. Denis and C. Ciuti,
"Machine learning via relativity-inspired quantum dynamics",
Physical Review A **106**, 032413 (2022).

* Both authors contributed equally to this work.

Contents

General introduction **1**

1 Theory of quantum optics **5**

I Quantum description of a cavity resonator . . . 6
I.1 From Maxwell's equations to photons . . . 6
II Coupling to a reservoir . . . 10
II.1 Master equation . . . 10
III Light-matter interaction . . . 15
III.1 The Unruh-DeWitt model (without moving parts) . . . 15
III.2 Exciton-polaritons in a single-mode cavity . . . 16
III.3 Exciton-polaritons in a planar cavity . . . 20
IV Light-matter interaction under relativistic settings . . . 23
IV.1 Hamiltonian as the generator of time translation . . . 24
IV.2 The Unruh-DeWitt model for a relativistic detector . . . 25
IV.3 Unruh effect . . . 26
IV.4 Hawking radiation . . . 29
V Conclusion . . . 31

2 Dissipative phase transition of light **32**

I Introduction . . . 32
I.1 Phase transitions in different regimes . . . 33
I.2 Phase transitions in driven-dissipative open quantum systems . . . 34
II Dissipative phase transitions in photonic systems . . . 35
II.1 Single-mode Kerr cavity . . . 36
II.2 Bose-Hubbard lattice . . . 36
III Technique for probing a dimension-dependent phase transition in a continuous photonic system . . . 38
III.1 Theoretical model . . . 39
III.2 Experimental setup . . . 40
III.3 Numerical methods . . . 42
IV Results and discussion . . . 45
IV.1 Steady-state behavior . . . 45
IV.2 Critical slowing down of the dynamics in the 2D configuration . . . 47
IV.3 Effect of the cavity wedge . . . 48

V Conclusion and outlook . . . 48

3 Effective dynamics induced by a dissipative reservoir **51**
I Single-mode reservoir . . . 51
II The generic master equation . . . 54
II.1 The single-mode reservoir revisited . . . 55
III Example: realization of two-photon drive and dissipation . . . 56
III.1 The quadratically driven Kerr cavity . . . 57

4 Dissipation-induced antiferromagneticlike frustration in coupled photonic resonators **60**
I Introduction . . . 60
II Theoretical model . . . 61
II.1 Theoretical intuition for the dimer case . . . 62
II.2 Adiabatic elimination of the reservoir mode . . . 64
II.3 Effective driven-dissipative dynamics . . . 65
III Results and discussion . . . 67
III.1 The dimer system . . . 67
III.2 The trimer system . . . 68
III.3 Benchmarking the effective model against exact results . . . 71
IV Conclusion and outlook . . . 73

5 Relativistic quantum reservoir computing **74**
I Introduction . . . 75
II Supervised learning and reservoir computing . . . 76
II.1 Reservoir computing . . . 77
II.2 Optimization . . . 78
II.3 The kernel point of view . . . 79
III Relativistic quantum reservoir-computing model . . . 80
III.1 Reservoir-computing protocol . . . 82
IV Results and discussion . . . 83
IV.1 Implementation with circuit QED . . . 85
IV.2 Results with a qubit instead of a harmonic oscillator . . . 87
V Conclusions . . . 89

General conclusion **90**

Appendix A Change of frame and interaction picture **92**
I Interaction picture . . . 93

Appendix B Scalar quantum field theory **94**
I Quantization in a cavity . . . 94
II Quantization in free space . . . 95

Appendix C World line of an accelerated observer 97

Appendix D Gaussian formalism 98

Annexe E Résumé substantiel 99

General introduction

Ever since Max Planck's *quantum* hypothesis in his explanation of blackbody radiation in the year 1900 [1], the development of modern quantum mechanics in the early decades of the XXth has revolutionized our understanding of the universe around us. While quantum physics proves to be one of the most successful theories ever invented in the history of science surviving precise experimental tests[1] [3], and serves as the fundamental framework for the standard model of modern particle physics [4], it has hardly been an easy pill to swallow due to its counterintuitiveness, even for the founders of this theory. Niels Bohr, who proposed the first successful quantum model for the Hydrogen atom [5], once said to Werner Heisenberg, "those who are not shocked when they first come across quantum theory cannot possibly have understood it." [6] Indeed, unlike in classical mechanics, where the state of a particle can be completely specified by its position and momentum, the state of a quantum mechanical particle lives in a (possibly infinite-dimensional) complex vector space known as the *Hilbert space* and can be a *coherent* superposition of classically different states, i.e. it can be both *here and there* at the same time. Moreover, the coherence signifies that the different states involved in a superposition have well-defined phase relations, such that they can interfere with each other just like waves do[2], which manifests the famous *wave-particle duality*. While it might still be acceptable to imagine a single electron in a double-slit experiment [7] to go through both slits and interfere with itself, or to interpret the angular momentum of a silver atom to be both up and down in the Stern–Gerlach experiment [8], it would be a daunting idea to consider a macroscopic cat as being in a coherent superposition of being both dead and alive. The celebrated *Schrödinger's cat* thought experiment was original conceived by Erwin Schrödinger [9] in a discussion with Albert Einstein as a "ridiculous case" to question the interpretation of quantum mechanics.

Although it still remains a philosophical debate to explain how quantum theory might correspond to some "reality", general consensus has been reached among physicists regarding why we never observe macroscopic objects (such as cats) in coherent superposition states. This is because every realistic system is in contact with its surrounding environment, which can be regarded as a *reservoir* consisting of virtually infinitely many degrees of freedom. This interaction causes the system to be entangled with the environment, such that the coherence irreversibly leaks into the environment and can no longer be recovered

[1] Let us not forget that there is another elegant theory in physics that deserves this claim, namely *general relativity*, which, unfortunately has not yet been successfully reconciled with quantum physics, despite being conceived by Albert Einstein [2], a pioneer in quantum mechanics.

[2] Note that this is different from a probabilistic mixture of classical states, in which case no interference would occur.

on the system alone. This process is known as *decoherence*, and has been well supported by experimental evidences [10]. The larger a system is, the more it couples to the environment, which means that it will suffer more decoherence and retain less quantumness, therefore aligning better with our daily intuitions.

Today, merely a century after the birth of quantum mechanics, we are in the midst of the *second quantum revolution* [11], where the rapid development in experimental techniques has started to allow us to conceive and construct complex devices exploiting the fundamental laws of quantum mechanics. One of the most exciting avenues of research in quantum technologies is *quantum computing* [12], a field at the interface of information theory, computer science and quantum physics, which can date back to the idea of simulating quantum physics using quantum systems as presented by Richard Feynman in 1982 [13]. Due to the immensity of the Hilbert space and the inherent parallelism provided by quantum superpositions, quantum computers are expected to overwhelmingly beat their classical counterparts in solving *certain* classes of problems [14]. While classical computers can be easily built in large scales with more than a hundred billion transistors on a single chip that runs under room conditions, quantum computers are much more fragile since their advantage relies on the quantumness, which can be easily destroyed by the environment via decoherence, the same process that kills the Schrödinger's cat [15]. Among several explored implementations for quantum computing, such as trapped ions [16–18], nuclear magnetic resonance [19, 20] and quantum dots [21, 22], quantum optical platforms [23–25] and superconducting circuits [26, 27] (which are analogs of quantum optics) are often considered as the most promising candidates. The first demonstrations of *quantum advantage* have been realized on these platforms (for specific and limited tasks) in very recent years [28, 29]. Yet, there is still a long way ahead before large-scale universal and fault-tolerant quantum computers can be realized. Despite remarkable advances in experimental techniques of isolating and protecting a quantum system, a finite coupling to the environment cannot yet be avoided [30–32] due to the macroscopic nature of the experimental devices.

We are currently in the so-called Noisy Intermediate-Scale Quantum (NISQ) [33] era, where quantum devices have to live with noise and decoherence, but can still be useful in other applications, such as exploring many-body quantum physics and quantum neuromorphic computing [34]. It is therefore a crucial *problématique* to understand the dynamics of quantum system in the inevitable presence of the environment, that is commonly modeled as a *reservoir*. Several paths of research can be identified following our discussion, which will be the main subjects treated in this manuscript.

Dissipative quantum dynamics

When coupled to a reservoir, a quantum system exhibits dissipative dynamics and can be treated in the framework of *open quantum systems* [35]. In contrast to equilibrium physics, where the state of a system relaxes to thermal equilibrium with the environment, a dissipative system with an external drive evolves towards a nonequilibrium steady state, which can exhibit rich and exotic properties that are absent in their equilibrium counterparts [36–38]. In the first part of the manuscript, the driven-dissipative dynamics of light will be studied in a quantum optical system, namely the semiconductor microcav-

ity [39]. Due to the light-matter interaction, the photons can strongly interact with each other in such cavities, making them ideal platforms for studying many-body physics and hydrodynamics of photons [40, 41]. In particular, we will study a *dissipative phase transition* [42] of light, an out-of-equilibrium phenomenon resulting from the rich interplay between the driving, the quantum fluctuations and dissipation. We will also show the first experimental demonstration of the role of spatial dimensionality in determining phase transitions of photons based on our theoretical study [γ].

Reservoir engineering

Since coupling to a reservoir is inevitable for a quantum system, we can rather try to harness the effect of dissipation to achieve desirable control on the system via appropriate design of the reservoir and the coupling, a process called *reservoir engineering*. Indeed, it has been demonstrated that engineered dissipation does not necessarily lead to decoherence, but can instead help stabilize certain quantum states (even analogs of Schrödinger cats) [43–46]. In the second part of the manuscript, we show how a strongly dissipative cavity can serve as an engineered reservoir when coupled to another quantum system. The dissipative nature of the reservoir implies that it has a much faster time scale as compared to the system it couples to, such that the fast and slow dynamics effectively decouple, which allows us to derive an effective description in terms of the system alone by adiabatically eliminating the fast dynamics of the reservoir [47, 48]. The effective dynamics induced by the reservoir can be regarded as both coherent and dissipative couplings between the system's degrees of freedom mediated via the reservoir, which can be harvested as computational resources, such as for analog simulation of antiferromagnetism and frustration [α].

Reservoir computing

In recent years, the field of *machine learning* has blossomed with a wide variety of applications [49, 50], and is now going hand-in-hand with quantum physics. On one hand, artificial neural networks have been proven to be powerful tools for solving quantum many-body problems [51–59], designing quantum circuits [59–61] and beyond [62–65]. On the other hand, the field of *quantum machine learning* [66, 67] has also emerged in the last decade, where potential advantages of quantum systems in machine-learning applications are explored. We will be focusing on the latter aspect in this manuscript, and more specifically the paradigm of *quantum reservoir computing* [68].

In this context, the term *reservoir* refers to a generic quantum system that exhibits nontrivial response dynamics when subjected to some input (just like an actual reservoir of water), such that it effectively transforms the input into a (high-dimensional) *feature space*, that we can exploit to perform machine-learning tasks, such as learning to approximate a function. Such paradigm requires virtually no degree of control over the physical system acting as the reservoir, which is therefore well suited for NISQ applications. The last part of the manuscript will explore the framework of reservoir computing for a relativistic quantum system, where the feature-space embedding is provided by the quantum dynamics of a detector undergoing relativistic motion inside a cavity. This is a

typical model studied in the field of relativistic quantum information [69, 70], where one seeks to understand and harness relativistic effects in quantum information-processing protocols. By exploiting the framework of reservoir computing, we demonstrate that one can harness information-processing power from relativistic effects stemming from the fundamental laws of physics [ϵ].

Structure of the manuscript

Chapter 1 will give an overview of a few general concepts in quantum optics and provide the theoretical building blocks for the rest of the manuscript. The notion of photons will first be introduced by quantizing the classical electromagnetic field in a cavity. The master-equation formalism will then be derived, which allows modeling the driven-dissipative dynamics of a quantum system coupled to a reservoir (the environment). This will be followed by discussions on light-matter interactions in various systems, in both static and relativistic regimes.

Chapter 2 is dedicated to the study of critical phenomena of light in a nonlinear photonic system based on our work [γ]. The background and theoretical framework for studying dissipative phase transitions will be discussed in the beginning. We then introduce the experimental technique proposed for probing the role of spatial dimension in determining phase transitions in such photonic systems, followed by our theoretical predictions and the experimental results obtained by our collaborators at *Laboratoire Kastler Brossel*.

In Chapter 3, the general theory for deriving the effective dynamics induced by a reservoir will be presented, with a focus on the special case of a single-mode dissipative cavity serving as the reservoir. The theoretical framework therein prepares for the discussion in the following chapter.

Chapter 4 will present the results in our work [α], which builds on the general theory introduced in the previous chapter. A photonic simulator of antiferromagnetism will be proposed, where the desired effective dynamics is realized via reservoir engineering. This will be supported by numerical simulations presented thereafter. We further demonstrate that the dissipative effective coupling mediated by the engineered reservoir is capable of inducing frustration in the simulated antiferromagnetic system.

Chapter 5 will explore the paradigm of relativistic quantum reservoir computing [ϵ]. We will first introduce the general background of relativistic quantum information and reservoir computing, and provide the necessary theoretical tools for treating reservoir-computing problems. The proposed information-processing protocol will then be presented and demonstrated on an illustrative supervised-learning task, showing the enhanced performance provided by relativistic quantum dynamics. A possible analog implementation scheme in circuit QED platforms will also be discussed.

Finally, the manuscript will be closed in the general conclusion, where we summarize the main results and the perspectives.

1 Theory of quantum optics

This chapter will give a short introduction to the theory of quantum optics, with the aim of laying the theoretical building blocks for the topics covered in the present manuscript. In quantum optics, light is studied as a quantized field, where the elementary excitations take the form of individual quanta of light, known as *photons*. Historically, the idea of a particle theory of light was first founded by Isaac Newton in his work on optics [71]. Roughly two hundred years later, Max Planck hypothesized that light be emitted in discrete quanta of energy in his theory of blackbody radiation [1] introduced in the year 1900 (that is often regarded as the birth of quantum physics), which was further evidenced by the photoelectric effect as explained by Albert Einstein in 1905 [72]. This lead to the modern formulations of quantum mechanics in the mid-1920s. Later in the 1960s, the demonstration of the first working lasers [73] marked the beginning of modern quantum optics, which focuses on the study of interaction between light and matter at a quantum level. Quantum optics today plays an important role in modern physics, with applications ranging from quantum metrology [74] (which lead to the first observation of gravitational waves [75]) to quantum information and computation [76].

Our discussion will start with the quantum description of a cavity resonator, the paradigmatic system of central importance in quantum optics. In Sec. I, we will start from the classical Maxwell equations and perform the quantization procedure, from which the notion of photons naturally appear. In Sec. II, the effect of the surrounding environment on the cavity will be discussed by modeling the cavity field coupled to a reservoir. Under certain approximations, an effective description known as the master equation can be derived, which allows us to model the driven-dissipative dynamics of photons in the cavity. Starting from Sec. III, we will introduce light-matter interactions based on a simple phenomenological model describing a quantum detector inside an optical cavity. Sec. III focuses on the regime where both the cavity and detector are at rest, which is the conventional setting considered in quantum optics. In particular, exciton-polariton systems will be discussed in detail, as a typical platform for strong light-matter interactions. In Sec. IV, we will focus on the regime where the quantum detector undergoes (relativistic) motion in a static cavity (or free field), where the same theoretical framework established in the previous sections allows us to derive some elegant results such as the Unruh effect and Hawking radiation. Finally, we conclude this chapter in Sec. V.

I Quantum description of a cavity resonator

One of the most important systems studied in quantum optics is the cavity resonator, which in the simplest case can be schematically visualized as a device consisting of two parallel mirrors capable of confining light. When the mirrors are highly reflective, light will go through many round trips between them before escaping. Therefore, if one places atoms inside the cavity, this will allow the study of interactions between light and matter in a well-controlled setting, a subject known as cavity quantum electrodynamics (QED) [77–79]. To prepare for this discussion, we first provide a brief introduction to the quantum model of light, obtained by quantizing the classical theory of electromagnetism.

I.1 From Maxwell's equations to photons

The classical theory of electromagnetism is summarized by the famous Maxwell's equations [80], which well established the wave-like aspect of light before the dawn of quantum physics. In the absence of sources (charge or currents), these equations can be written as

$$\begin{aligned} \nabla \times \boldsymbol{B} &= \frac{1}{c^2}\frac{\partial}{\partial t}\boldsymbol{E}\,, \qquad & \nabla \cdot \boldsymbol{E} &= 0\,, \\ \nabla \times \boldsymbol{E} &= -\frac{\partial}{\partial t}\boldsymbol{B}\,, \qquad & \nabla \cdot \boldsymbol{B} &= 0\,, \end{aligned} \tag{1.1}$$

where $\boldsymbol{E}$ and $\boldsymbol{B}$ are the electric and magnetic fields, and $c = 1/\sqrt{\varepsilon_0\mu_0}$ is the speed of light in vacuum, with ε_0 the vacuum permittivity and μ_0 the vacuum permeability. In the covariant formalism of electromagnetism, it is convenient to define the four-potential $A^\mu = (\phi/c, \boldsymbol{A})$, with ϕ the electric potential and $\boldsymbol{A}$ the magnetic vector potential, such that

$$\boldsymbol{E} = -\nabla\phi - \frac{\partial}{\partial t}\boldsymbol{A}\,, \quad \boldsymbol{B} = \nabla \times \boldsymbol{A}\,. \tag{1.2}$$

Defining the electromagnetic field strength tensor [81] $F_{\mu\nu} \equiv \partial_\mu A_\nu - \partial_\nu A_\mu$, the Maxwell's equations can be elegantly derived from the Lagrangian density[1]

$$\mathcal{L} = -\frac{1}{4\mu_0}F_{\mu\nu}F^{\mu\nu} = \frac{1}{2}\left(\varepsilon_0\|\boldsymbol{E}\|^2 - \frac{1}{\mu_0}\|\boldsymbol{B}\|^2\right), \tag{1.3}$$

which is a Lorentz scalar. The equations of motion are obtained by the variational principle[2]:

$$\delta S \equiv \delta\left(\int \mathrm{d}^4x\ \mathcal{L}\right) = 0 \quad \Longrightarrow \quad \partial_\mu F^{\mu\nu} = 0\,, \tag{1.4}$$

giving the first line of Eq. (1.1). The other two equations can be written as the Bianchi identity

$$\partial_\mu F_{\nu\lambda} + \partial_\nu F_{\lambda\mu} + \partial_\lambda F_{\mu\nu} = 0\,, \tag{1.5}$$

[1] The raising and lowering of indices are done with the Minkowski metric tensor, i.e. $\eta_{\mu\nu} = \mathrm{diag}(+1,-1,-1,-1)$ when expressed in Cartesian coordinates $x^\mu \equiv (x^0, x^1, x^2, x^3) = (ct, x, y, z)$. Throughout this manuscript, we always adopt the sign convention with "+" for the timelike component and "−" for the spacelike ones in the metric. In addition, we adopt Einstein's summation convention where repeated indices are summed over.

[2] Note that the dynamical field is A^μ, with respect to which the action S is varied.

which is automatically satisfied by electromagnetic fields derived from a four-potential A^μ, as one can explicitly check using the definition of $F_{\mu\nu}$. The Lagrangian density (1.3) also gives us the conjugate momentum Π^μ and the Hamiltonian density $\mathcal{H}$[3]:

$$\begin{aligned} \Pi^\mu &= \frac{\partial \mathcal{L}}{\partial(\partial_0 A^\mu)}\,, \\ \mathcal{H} &= \Pi^\mu \partial_0 A_\mu - \mathcal{L} = \frac{1}{2}\left(\varepsilon_0 \|\boldsymbol{E}\|^2 + \frac{1}{\mu_0}\|\boldsymbol{B}\|^2\right), \end{aligned} \tag{1.6}$$

which will be useful when we perform the canonical quantization of the electromagnetic field later. Note that the field strength tensor $F^{\mu\nu}$ is invariant under the gauge transformation $A_\mu \to A_\mu - \partial_\mu \chi$ for any scalar function $\chi(x^\mu)$. In the so-called *Lorenz gauge* where one chooses $\chi(x^\mu)$ such that $\partial_\mu A^\mu = 0$, the equation of motion becomes

$$\Box A^\nu \equiv \partial^\mu \partial_\mu A^\nu = 0\,. \tag{1.7}$$

In free space, this equation admits plane wave solutions of the form $A^\mu \propto \epsilon^\mu(\boldsymbol{k}) \mathrm{e}^{\pm \mathrm{i}(\omega_{\boldsymbol{k}} t - \boldsymbol{k}\cdot\boldsymbol{x})}$ with the dispersion relation $\omega_{\boldsymbol{k}} = c\|\boldsymbol{k}\|$ and ϵ^μ is a polarization vector. One can further impose the *Coulomb gauge* condition by setting $A^0 = 0$, which implies $\nabla \cdot \boldsymbol{A} = 0$ and uniquely determines A^μ with no more gauge freedom left. Note that this choice leads to $\boldsymbol{k} \cdot \boldsymbol{\epsilon} = 0$, which means that only two physical independent degrees of freedoms (the two transverse polarizations) are allowed in the four-component vector A^μ. In fact, this redundancy in the degree of freedom of A^μ resulting from the gauge invariance of electromagnetism makes the canonical quantization of the electromagnetic an awkward subject [82]. One typically needs to explicitly choose a gauge that breaks the Lorentz symmetry (which is not elegant), such as the Coulomb gauge, or use modern methods to perform a gauge-invariant quantization, as detailed in [83, 84].

For simplicity, let us continue our discussion in the Coulomb gauge, and quantize the electromagnetic field propagating along a single direction (the z direction) in a cavity consisting of two infinite planar mirrors (parallel to the Oxy plane) separated by a distance of L_C along the z axis, as sketched in Fig. 1.1. Assuming the cavity mirrors to be ideal conductors, the electric field (and hence the vector potential, since we are in the Coulomb gauge) must have zero tangential component at the cavity walls $z = z_* \in \{0, L_c\}$. We will consider the quantization of the field within some volume $V = L_c \mathcal{A}$ delimited by a surface area of $\mathcal{A}$ along the cavity plane[4]. The general solution of the field can therefore be expanded in the orthonormal basis of sine functions:

$$\boldsymbol{A}(t,z) = \sum_{n=1}^{\infty}\sum_{\sigma=1}^{2} \boldsymbol{\epsilon}_\sigma q_{n,\sigma}(t) \sqrt{\frac{2}{\varepsilon_0 V}} \sin(k_n z)\,, \tag{1.8}$$

where $k_n = n\pi/L_c$ and $\boldsymbol{\epsilon}_\sigma$ is a unit vector that satisfies $\boldsymbol{\epsilon}_\sigma^\dagger \boldsymbol{\epsilon}_{\sigma'} = \delta_{\sigma,\sigma'}$ and $\boldsymbol{\epsilon}_\sigma^\dagger \boldsymbol{e}_z = 0$, representing the two possible transverse polarizations of the electric field propagating

[3] We dropped a total derivative term in $\mathcal{H}$ that will vanish when integrated over all space, by assuming that the fields must vanish at infinity.

[4] This helps to obtain correct dimensions for the quantized field.

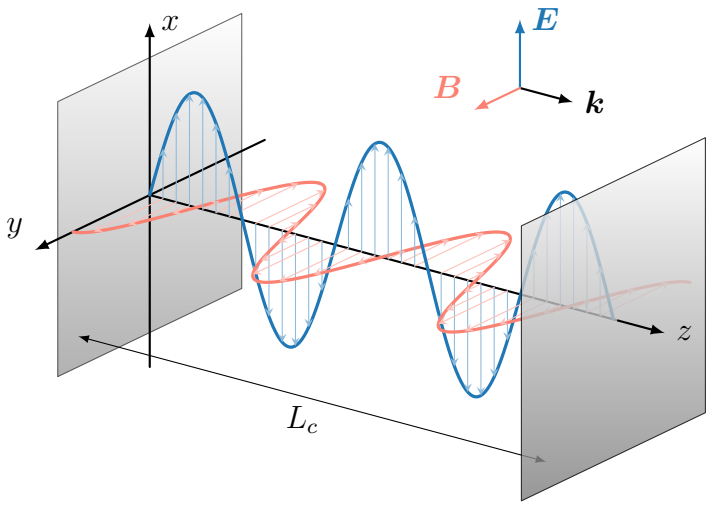

Figure 1.1: Schematic representation of an optical cavity consisting of two parallel mirrors separated by a distance of L_c, with electromagnetic fields propagating orthogonal to the mirrors, along the z direction. The mode function for an x-polarized electric field in the $n = 5$ mode is sketched.

along $\boldsymbol{e}_z$. The total Lagrangian and Hamiltonian are the integrals of the corresponding densities:

$$\begin{aligned} L &= \int_{\mathcal{A}} \mathrm{d}x\mathrm{d}y \int_0^{L_c} \mathrm{d}z \frac{1}{2}\left(\varepsilon_0 \|\boldsymbol{E}\|^2 - \frac{1}{\mu_0}\|\boldsymbol{B}\|^2\right) = \sum_{n,\sigma} \frac{1}{2}\left(\dot{q}_{n,\sigma}^2 - c^2 k_n^2 q_{n,\sigma}^2\right), \\ H &= \int_{\mathcal{A}} \mathrm{d}x\mathrm{d}y \int_0^{L_c} \mathrm{d}z \frac{1}{2}\left(\varepsilon_0 \|\boldsymbol{E}\|^2 + \frac{1}{\mu_0}\|\boldsymbol{B}\|^2\right) = \sum_{n,\sigma} \frac{1}{2}\left(p_{n,\sigma}^2 + c^2 k_n^2 q_{n,\sigma}^2\right), \end{aligned} \tag{1.9}$$

with $p_{n,\sigma} = \dot{q}_{n,\sigma}$ the conjugate momentum. The equations above describe nothing but a set of decoupled unit-mass simple harmonic oscillators with frequencies $\omega_n = ck_n$. The canonical quantization then follows directly by promoting the conjugate variable to operators $(p_{n,\sigma}, q_{n,\sigma}) \mapsto (\hat{p}_{n,\sigma}, \hat{q}_{n,\sigma})$ satisfying the canonical commutation relation $[\hat{q}_{n,\sigma}, \hat{p}_{n',\sigma'}] = \mathrm{i}\hbar\delta_{n,n'}\delta_{\sigma,\sigma'}$. Defining the usual creation and annihilation operators $\hat{a}_{n,\sigma}^{(\dagger)}$ via

$$\begin{aligned} \hat{q}_{n,\sigma} &= \sqrt{\frac{\hbar}{2\omega_n}}\left(\hat{a}_{n,\sigma}^\dagger + \hat{a}_{n,\sigma}\right), \\ \hat{p}_{n,\sigma} &= \mathrm{i}\sqrt{\frac{\hbar\omega_n}{2}}\left(\hat{a}_{n,\sigma}^\dagger - \hat{a}_{n,\sigma}\right), \end{aligned} \tag{1.10}$$

with the standard bosonic commutation relations $[\hat{a}_{n,\sigma}, \hat{a}_{n',\sigma'}^\dagger] = \delta_{n,n'}\delta_{\sigma,\sigma'}$, the Hamiltonian operator finally takes the familiar shape

$$\hat{H} = \sum_{n,\sigma} \hbar\omega_n \left(\hat{a}_{n,\sigma}^\dagger \hat{a}_{n,\sigma} + \frac{1}{2}\right), \tag{1.11}$$

which completely determines the dynamics of the cavity field via the Schrödinger equation

$$\mathrm{i}\hbar \frac{\mathrm{d}}{\mathrm{d}t}|\psi\rangle = \hat{H}|\psi\rangle. \tag{1.12}$$

The state vector $|\psi\rangle$ lives in the Hilbert space spanned by the Fock basis

$$|N_{l_1}, N_{l_2}, \ldots, N_{l_i}, \ldots\rangle \equiv \frac{1}{\sqrt{N_{l_1}!\, N_{l_2}! \cdots N_{l_i}! \cdots}} (\hat{a}_{l_1}^\dagger)^{N_{l_1}} (\hat{a}_{l_2}^\dagger)^{N_{l_2}} \cdots (\hat{a}_{l_i}^\dagger)^{N_{l_i}} \cdots |0\rangle\,, \tag{1.13}$$

where $l \equiv (n, \sigma)$ labels the mode number and polarization and $|0\rangle$ is the vacuum state defined by $\hat{a}_l|0\rangle = 0\,, \forall l$. $N_l \geq 0$ represents the number of elementary excitations, known as *photons*, in the l-th mode of the cavity. Finally, we can write the operators for the field observables in the interaction picture[5]:

$$\begin{aligned}
\hat{\boldsymbol{A}}(t,z) &= \sum_l \boldsymbol{\epsilon}_l \sqrt{\frac{\hbar}{\varepsilon_0 V \omega_l}} \left(\hat{a}_l \mathrm{e}^{-\mathrm{i}\omega_l t} + \hat{a}_l^\dagger \mathrm{e}^{\mathrm{i}\omega_l t}\right) \sin(k_l z)\,, \\
\hat{\boldsymbol{E}}(t,z) &= \mathrm{i} \sum_l \boldsymbol{\epsilon}_l \sqrt{\frac{\hbar\omega_l}{\varepsilon_0 V}} \left(\hat{a}_l \mathrm{e}^{-\mathrm{i}\omega_l t} - \hat{a}_l^\dagger \mathrm{e}^{\mathrm{i}\omega_l t}\right) \sin(k_l z)\,, \\
\hat{\boldsymbol{B}}(t,z) &= \frac{1}{c} \sum_l (\boldsymbol{e}_z \times \boldsymbol{\epsilon}_l) \sqrt{\frac{\hbar\omega_l}{\varepsilon_0 V}} \left(\hat{a}_l \mathrm{e}^{-\mathrm{i}\omega_l t} + \hat{a}_l^\dagger \mathrm{e}^{\mathrm{i}\omega_l t}\right) \cos(k_l z)\,,
\end{aligned} \tag{1.14}$$

where the quantity $\sqrt{\hbar\omega_l/\varepsilon_0 V}$ has the dimension of electric field.

So far, we have only considered modes with zero wavevector component parallel to the cavity planes, which is a valid assumption in many quantum-optical settings, as the cavity modes can be laterally confined with various experimental techniques [85, 86], making the cavity effectively a "photonic box"[6]. We will also ignore the polarization (spin) degree of freedom of the photons from now on, which is a safe assumption for all the phenomenology considered in this manuscript as one often works with a single polarization in many experimental circumstances in quantum optics [39]. In addition, as the energy spacing between different modes is inversely proportional to the cavity length ($\omega_n = cn\pi/L$), in situations where all relevant physical processes happen quasiresonantly around the energy of a certain mode, it is customary to assume that the cavity hosts only a single photonic mode.

In the complementary scenario where the cavity photons are not confined laterally and are free to propagate in the plane parallel to the cavity mirrors, the Hamiltonian for the quantized field reads[7]

$$\hat{H} = \sum_{k_z} \int \mathrm{d}^2\boldsymbol{k}_\parallel \hbar\omega(\boldsymbol{k}) \hat{a}^\dagger(\boldsymbol{k}) \hat{a}(\boldsymbol{k}), \tag{1.15}$$

where $k_z = n\pi/L$ is quantized as before (hence the discrete sum), while the in-plane component $\boldsymbol{k}_\parallel$ forms a continuum and serves as a good quantum number due to the translational symmetry of the system in the Oxy plane. The commutation relations become $[\hat{a}(\boldsymbol{k}), \hat{a}^\dagger(\boldsymbol{k}')] = \delta_{k_z,k_z'} \delta^2(\boldsymbol{k}_\parallel - \boldsymbol{k}_\parallel')$. For a fixed k_z, the dispersion relation with

[5] For free fields this is same as the Heisenberg picture. See Appendix A for more details.

[6] Strictly speaking, the mode functions will differ since the confinement modifies the boundary conditions, but one can perform a similar quantization procedure for the specific geometry and arrive at the same Hamiltonian [87].

[7] We ignore the zero-point energy from now on.

respect to $k \equiv \left\|\boldsymbol{k}_{\parallel}\right\|$ is

$$\omega(k) = c\sqrt{k_z^2 + k^2} \simeq \omega^{k=0} + \frac{\hbar k^2}{2m_{\text{cav}}}\,, \tag{1.16}$$

where $\omega^{k=0} = ck_z$ and $m_{\text{cav}} = \hbar\omega^{k=0}/c^2$ is the effective mass of the cavity photon, which arises due to the confinement along the z direction. This dispersion relation resembles that of a relativistic particle with rest mass m_{cav}, and is approximately parabolic for small in-plane wavevector k. For cavities embedding a medium with constant refractive index n_0, it suffices to rescale the speed of light $c \mapsto c/n_0$ in the above expressions to obtain the correct dispersion relation.

II Coupling to a reservoir

The Schrödinger equation (1.12) we wrote down previously for the cavity field is valid if the cavity is free from interaction with any other system. However, this is never the case in reality, as the perfect isolation of a quantum system still presents a major experimental challenge (which is one of our biggest obstacles to realizing universal quantum computers[8] [30, 31]). In other words, a realistic quantum system is constantly interacting with its *environment* [32], and is therefore part of a (much) larger (and messy) quantum system with virtually infinitely many degrees of freedom, making the exact modeling of its dynamics intractable in practice. Luckily, under certain approximations, an effective description involving only the system's degrees of freedom can be derived, which allows us to study the dissipative dynamics of the system under the influence of the environment. This can be achieved by modeling the environment as a Markovian *reservoir* that is weakly coupled to the system, and we will follow [48] to derive the so-called *master equation* formalism.

II.1 Master equation

Let us model the environment with a reservoir consisting of a large set of harmonic oscillators (bosonic modes), which can well describe, for example, the electromagnetic field in the environment when the system of interest is an optical cavity, a typical scenario considered in this manuscript. In this section, we will focus of a single bosonic mode of the system weakly coupled to the reservoir, i.e. a *local* reservoir for the system. The more general case involving possibly nonlocal reservoirs will be discussed in Chapter 3.

The bare Hamiltonians of the system ($\hat{H}_S$) and the reservoir ($\hat{H}_R$) are given by

$$\hat{H}_S = \hbar\omega_S \hat{a}^\dagger \hat{a}\,,\ \hat{H}_R = \sum_\lambda \hbar\omega_\lambda \hat{c}_\lambda^\dagger \hat{c}_\lambda\,, \tag{1.17}$$

where $\hat{a}$ ($\hat{c}_\lambda$) is the annihilation operator of the system (reservoir) mode with bare angular frequency ω_S (ω_λ). Assuming that the system and the reservoir, originally decoupled,

[8] And since quantum computing (or any other quantum technology) always necessitates certain measurement steps, a quantum system of practical interest shall not be isolated at least when we need to measure it.

are put into contact at time t_0, the system-reservoir coupling can be captured by the interaction Hamiltonian

$$\begin{aligned}\hat{H}_I &= \hbar\hat{S}\otimes\hat{R}\,,\\ &\equiv \hbar(\hat{a}+\hat{a}^\dagger)\otimes\sum_\lambda\Big(g_\lambda^*\hat{c}_\lambda + g_\lambda\hat{c}_\lambda^\dagger\Big)\,,\end{aligned} \tag{1.18}$$

which takes a minimally coupled form, where we absorbed the coupling constants g_λ (with dimension of frequency) into the bath operator $\hat{R}$. The full state of the system-reservoir ensemble can be represented by a density matrix $\hat{\rho}_{SR}$, that undergoes unitary time evolution generated by Hamiltonian:

$$\frac{\mathrm{d}}{\mathrm{d}t}\hat{\rho}_{SR} = -\frac{\mathrm{i}}{\hbar}\Big[\hat{H}_S+\hat{H}_R+\hat{H}_I,\hat{\rho}_{SR}\Big]\,. \tag{1.19}$$

We now transform into the interaction picture (see Appendix A) using the free Hamiltonian $\hat{H}_0\equiv\hat{H}_S+\hat{H}_R$, and denote the transformed operators by $\tilde{O}(t)=\mathrm{e}^{\mathrm{i}\hat{H}_0(t-t_0)/\hbar}\hat{O}\mathrm{e}^{-\mathrm{i}\hat{H}_0(t-t_0)/\hbar}$. The dynamical equation can then be rewritten as

$$\frac{\mathrm{d}}{\mathrm{d}t}\tilde{\rho}_{SR}(t) = -\frac{\mathrm{i}}{\hbar}\Big[\tilde{H}_I(t),\tilde{\rho}_{SR}(t)\Big]\,, \tag{1.20}$$

which can be integrated to give

$$\tilde{\rho}_{SR}(t) = \tilde{\rho}_{SR}(t_0) - \frac{\mathrm{i}}{\hbar}\int_{t_0}^{t}\mathrm{d}t'\Big[\tilde{H}_I(t'),\tilde{\rho}_{SR}(t')\Big]\,. \tag{1.21}$$

Plugging this back to Eq. (1.20) and taking the partial trace over the reservoir degrees of freedom, we obtain the effective dynamics for the reduced density matrix of the system $\tilde{\rho}_S\equiv\mathrm{Tr}_R[\tilde{\rho}_{SR}]$:

$$\frac{\mathrm{d}}{\mathrm{d}t}\tilde{\rho}_S(t) = -\frac{1}{\hbar^2}\int_{t_0}^{t}\mathrm{d}t'\mathrm{Tr}_R\Big\{\Big[\tilde{H}_I(t),[\tilde{H}_I(t'),\tilde{\rho}_{SR}(t')]\Big]\Big\}\,, \tag{1.22}$$

where we assumed $\mathrm{Tr}_R\{[\tilde{H}_I(t),\tilde{\rho}_{SR}(t_0)]\}=0$ (which is satisfied for example when the reservoir is initially in a thermal state). This equation is still exact yet intractable, and we need further assumptions to simplify it. We now assume that the system-reservoir coupling is sufficiently weak to have negligible influence on the state of the reservoir, such that the reservoir is constantly in its steady state $\hat{\rho}_R(t_0)$ with respect to its bare Hamiltonian [i.e. we have $[\hat{H}_R,\hat{\rho}_R]=0$ and $\tilde{\rho}_R(t)=\hat{\rho}_R(t)=\hat{\rho}_R(t_0),\forall t$]. This is known as the *Born approximation*, where we replace $\tilde{\rho}_{SR}$ in the integrand by the factorized tensor product

$$\tilde{\rho}_{SR}(t)\simeq\tilde{\rho}_S(t)\otimes\hat{\rho}_R(t_0), \tag{1.23}$$

which is valid for coarse-grained time scales with respect to the lifetime of the reservoir excitations τ_R due to the interaction with the system. This leads to a closed equation for the system density matrix when inserted into Eq. (1.22):

$$\frac{\mathrm{d}}{\mathrm{d}t}\tilde{\rho}_S(t) = -\frac{1}{\hbar^2}\int_{t_0}^{t}\mathrm{d}t'\mathrm{Tr}_R\Big\{\Big[\tilde{H}_I(t),[\tilde{H}_I(t'),\tilde{\rho}_S(t')\otimes\hat{\rho}_R(t_0)]\Big]\Big\}\,. \tag{1.24}$$

We now transform back into the Schrödinger picture and invoke the form of the interaction Hamiltonian $\hat{H}_I = \hbar\hat{S}\otimes\hat{R}$. Defining the reservoir correlation function

$$\mathcal{G}(\tau) \equiv \left\langle \hat{R}(t_0+\tau)\hat{R}(t_0)\right\rangle = \mathrm{Tr}\left[\hat{R}\mathrm{e}^{-\mathrm{i}\hat{H}_R\tau}\hat{R}\hat{\rho}_R(t_0)\mathrm{e}^{\mathrm{i}\hat{H}_R\tau}\right], \tag{1.25}$$

the equation of motion becomes

$$\frac{\mathrm{d}}{\mathrm{d}t}\hat{\rho}_S(t) = -\frac{\mathrm{i}}{\hbar}\left[\hat{H}_S,\hat{\rho}_S(t)\right] - \int_0^{t-t_0}\mathrm{d}\tau\left\{\mathcal{G}(\tau)\left[\hat{S},\mathrm{e}^{-\mathrm{i}\hat{H}_S\tau}\hat{S}\hat{\rho}_S(t-\tau)\mathrm{e}^{\mathrm{i}\hat{H}_S\tau}\right] + \mathrm{H.c.}\right\} \tag{1.26}$$

which involves the state of the reservoir at times prior to t. We now perform the *Markov approximation* by ignoring the effect of the reservoir on the dynamics of the system state at time scales $\tau \lesssim \tau_R$ [i.e. assuming $\mathrm{e}^{-\mathrm{i}\hat{H}_S\tau}\hat{\rho}_S(t-\tau)\mathrm{e}^{\mathrm{i}\hat{H}_S\tau} = \hat{\rho}_S(t)$, which is equivalent to setting $\tilde{\rho}_S(t') = \tilde{\rho}_S(t)$ in Eq. (1.24)] and by pushing the reference time to the past infinity $t_0 \to -\infty$, resulting in a Markovian equation of motion known as the Bloch-Redfield master equation [35]:

$$\begin{aligned}\frac{\mathrm{d}}{\mathrm{d}t}\hat{\rho}_S(t) &= -\frac{\mathrm{i}}{\hbar}\left[\hat{H}_S,\hat{\rho}_S(t)\right] - \int_0^{\infty}\mathrm{d}\tau\left\{\mathcal{G}(\tau)\left[\hat{S},\tilde{S}(-\tau)\hat{\rho}_S(t)\right] + \mathrm{H.c.}\right\}\\ &= -\frac{\mathrm{i}}{\hbar}\left[\hat{H}_S,\hat{\rho}_S(t)\right] + \left[\hat{V}\hat{\rho}_S(t),\hat{S}\right] + \left[\hat{S},\hat{\rho}_S(t)\hat{V}^\dagger\right],\end{aligned} \tag{1.27}$$

where we defined

$$\hat{V} = \int_0^{\infty}\mathrm{d}\tau\mathcal{G}(\tau)\tilde{S}(-\tau) = \Gamma(\omega_S)\hat{a} + \Gamma(-\omega_S)\hat{a}^\dagger, \tag{1.28}$$

with $\Gamma(\omega) = \int_0^\infty \mathrm{d}\tau\mathcal{G}(t)\mathrm{e}^{\mathrm{i}\omega\tau}$ the reservoir correlation spectrum. To make the equation preserve the semipositivity of the system density matrix, we further perform the *rotating-wave approximation* by keeping only the resonant terms in the commutators involving $\hat{V}^{(\dagger)}$ and $\hat{S}$. After splitting the real and imaginary parts of the spectral function $\Gamma(\omega) \equiv \frac{1}{2}\gamma(\omega) + \mathrm{i}\Lambda(\omega)$, this approximation leads to the Lindblad master equation

$$\frac{\mathrm{d}}{\mathrm{d}t}\hat{\rho}_S = -\frac{\mathrm{i}}{\hbar}\left[\hat{H}_S + \hbar\omega_{LS}\hat{a}^\dagger\hat{a},\hat{\rho}_S\right] + \gamma(\omega_S)\mathcal{D}[\hat{a}]\hat{\rho}_S + \gamma(-\omega_S)\mathcal{D}[\hat{a}^\dagger]\hat{\rho}_S, \tag{1.29}$$

where $\omega_{LS} = \Lambda(\omega_S) + \Lambda(-\omega_S)$ is the *Lamb-shift* frequency and the *dissipator* is defined as

$$\mathcal{D}[\hat{L}]\hat{\rho} = \hat{L}\hat{\rho}\hat{L}^\dagger - \frac{1}{2}\left(\hat{L}^\dagger\hat{L}\hat{\rho} + \hat{\rho}\hat{L}^\dagger\hat{L}\right) \tag{1.30}$$

for a Lindblad *jump operator* $\hat{L}$ and density matrix $\hat{\rho}$. The Lindblad master equation (1.29) generates a dynamical map that is completely positive and trace preserving (CPTP). Indeed, one can show [35] that for a quantum system undergoing generic CPTP dynamics, the evolution of its density matrix $\hat{\rho}$ can always be cast into the Lindblad form as

$$\frac{\mathrm{d}}{\mathrm{d}t}\hat{\rho} = \mathcal{L}(\hat{\rho}) \equiv -\frac{\mathrm{i}}{\hbar}\left[\hat{H},\hat{\rho}\right] + \sum_j \gamma_j\mathcal{D}[\hat{L}_j]\hat{\rho}, \tag{1.31}$$

where we denoted the generator of this dynamical map by the superoperator $\mathcal{L}$ known as the *Liouvillian*.

Surprisingly, the formalism presented above can be directly exploited to derived the Unruh effect [88–90], which is closely related to the celebrated Hawking radiation [91] of black holes, without invoking the machinery of quantum field theory in curved spacetimes. We will postpone this derivation to Sec. IV.3 when we introduce the relativistic quantum model for light-matter interactions. To prepare for this discussion, let us now study the dynamics of the system when coupled to a heat bath.

Case of a heat bath

Consider now the case where the reservoir is a heat bath in a thermal state with inverse temperature $\beta = 1/k_B T$, its density matrix can then be written as

$$\hat{\rho}_R = \frac{\mathrm{e}^{-\beta \hat{H}_R}}{\mathrm{Tr}\left[\mathrm{e}^{-\beta \hat{H}_R}\right]}, \tag{1.32}$$

which represents the canonical thermal equilibrium distribution. The reservoir correlation function can then be explicitly evaluated:

$$\begin{aligned}
\mathcal{G}(\tau) &= \mathrm{Tr}\left[\hat{R}\mathrm{e}^{-\mathrm{i}\hat{H}_R\tau}\hat{R}\hat{\rho}_R(t_0)\mathrm{e}^{\mathrm{i}\hat{H}_R\tau}\right] \\
&= \left\langle \mathrm{e}^{\mathrm{i}\hat{H}_R\tau}\hat{R}\mathrm{e}^{-\mathrm{i}\hat{H}_R\tau}\hat{R}\right\rangle_R \\
&= \sum_{\lambda,\lambda'}\left\langle \left(g^*_\lambda \hat{c}_\lambda \mathrm{e}^{-\mathrm{i}\omega_\lambda\tau} + g_\lambda \hat{c}^\dagger_\lambda \mathrm{e}^{\mathrm{i}\omega_\lambda\tau}\right)\left(g^*_{\lambda'}\hat{c}_{\lambda'} + g_{\lambda'}\hat{c}^\dagger_{\lambda'}\right)\right\rangle_R \\
&= \sum_\lambda |g_\lambda|^2\left[(\bar{n}_\lambda + 1)\mathrm{e}^{-\mathrm{i}\omega_\lambda\tau} + \bar{n}_\lambda \mathrm{e}^{\mathrm{i}\omega_\lambda\tau}\right] \\
&= \int_0^\infty \mathrm{d}\omega' D(\omega)|g(\omega')|^2\left[(\bar{n}_\beta(\omega') + 1)\mathrm{e}^{-\mathrm{i}\omega'\tau} + \bar{n}_\beta(\omega')\mathrm{e}^{\mathrm{i}\omega'\tau}\right],
\end{aligned} \tag{1.33}$$

where $\langle \bullet \rangle_R \equiv \mathrm{Tr}[\bullet \hat{\rho}_R]$, $\bar{n}_\lambda \equiv \langle \hat{c}^\dagger_\lambda \hat{c}_\lambda \rangle_R = 1/(\mathrm{e}^{\beta\hbar\omega_\lambda} - 1) \equiv \bar{n}_\beta(\omega_\lambda)$ is the mean population of mode λ, and in the last step we introduced the density of states $D(\omega)$ to pass from the sum to the integral $\sum_\lambda \to \int \mathrm{d}\omega' D(\omega')$. The spectrum can then be computed via the Fourier transform

$$\begin{aligned}
\Gamma(\omega) &= \int_0^\infty \mathrm{d}\tau \mathcal{G}(\tau)\mathrm{e}^{\mathrm{i}\omega\tau} = \frac{1}{2}\gamma(\omega) + \mathrm{i}\Lambda(\omega), \\
\gamma(\omega) &= \int_0^\infty \mathrm{d}\omega' 2\pi D(\omega')|g(\omega')|^2[(\bar{n}_\beta(\omega') + 1)\delta(\omega - \omega') + \bar{n}_\beta(\omega')\delta(\omega + \omega')] \\
&= \begin{cases} 2\pi D(\omega)|g(\omega)|^2[\bar{n}_\beta(\omega) + 1], & \omega \geq 0; \\ 2\pi D(-\omega)|g(-\omega)|^2\bar{n}_\beta(-\omega), & \omega < 0, \end{cases} \\
\Lambda(\omega) &= \mathcal{P}\left\{\int_0^\infty \mathrm{d}\omega' D(\omega')|g(\omega')|^2\left(\frac{\bar{n}_\beta(\omega') + 1}{\omega - \omega'} + \frac{\bar{n}_\beta(\omega')}{\omega + \omega'}\right)\right\},
\end{aligned} \tag{1.34}$$

where $\mathcal{P}$ denotes the Cauchy principal value, which arises from the identity $\int_0^\infty \mathrm{d}\tau \mathrm{e}^{\mathrm{i}\omega\tau} = \pi\delta(\omega) + \mathrm{i}\mathcal{P}\{1/\omega\}$. We finally arrive at the standard form of the quantum optical master equation:

$$\frac{\mathrm{d}}{\mathrm{d}t}\hat{\rho}_S = -\frac{\mathrm{i}}{\hbar}\left[\hat{H}_S + \hbar\omega_{LS}\hat{a}^\dagger\hat{a}, \hat{\rho}_S\right] + (\bar{N} + 1)\gamma\mathcal{D}[\hat{a}]\hat{\rho}_S + \bar{N}\gamma\mathcal{D}[\hat{a}^\dagger]\hat{\rho}_S, \tag{1.35}$$

with $\gamma \equiv 2\pi D(|\omega_S|)|g(|\omega_S|)|^2$ and $\bar{N} \equiv \bar{n}_\beta(\omega_S)$. As one can verify, the steady state of the system is given by

$$\hat{\rho}_S(t \to \infty) = \frac{\mathrm{e}^{-\beta \hat{H}_S}}{\mathrm{Tr}\left[\mathrm{e}^{-\beta \hat{H}_S}\right]}\,, \tag{1.36}$$

which is a thermal state associated to the bare Hamiltonian of the system at the same temperature as the reservoir. Later in Sec. IV.3 we will see that the same steady state can be achieved when the reservoir is in the (Minkowski) vacuum while the system undergoes an eternally accelerated motion, where the latter perceives an effective temperature proportional to its acceleration.

Drive and dissipation

Consider now a single-mode optical cavity of frequency ω_S as the system. At low-enough temperatures, we typically have $\bar{N} \simeq 0$ for optical frequencies, which means that the steady state given by Eq. (1.36) is effectively the vacuum state with zero photons in the cavity. To inject photons, one can drive the cavity with a laser, which can be modeled by a time-dependent Hamiltonian term describing an external monochromatic coherent field coupled to the cavity mode:

$$\hat{H}_{\mathrm{drive}}(t) = \hbar(\hat{a} + \hat{a}^\dagger)(F\mathrm{e}^{-\mathrm{i}\omega_d t} + F^*\mathrm{e}^{\mathrm{i}\omega_d t})\,, \tag{1.37}$$

where F is the amplitude of drive, with angular frequency ω_d. Assuming the drive amplitude is weak compared to the cavity bare frequency, i.e. $|F|/\omega_S \ll 1$, the drive can be regarded as a perturbation such that it does not affect our derivation of the master equation above. Therefore, we simply add $\hat{H}_{\mathrm{drive}}$ to the master equation (1.35) to model the driven-dissipative dynamics of the cavity. By transforming into the rotating frame[9] defined by $\hat{U}^\dagger = \mathrm{e}^{\mathrm{i}\omega_d \hat{a}^\dagger \hat{a} t}$ and neglecting fast-rotating terms $\sim \mathrm{e}^{\pm\mathrm{i}(\omega_S+\omega_d)t}$, the master equation takes a time-independent form[10]

$$\frac{\mathrm{d}}{\mathrm{d}t}\hat{\rho} = -\mathrm{i}\Big[-\Delta\hat{a}^\dagger\hat{a} + (F^*\hat{a} + F\hat{a}^\dagger), \hat{\rho}\Big] + \gamma\mathcal{D}[\hat{a}]\hat{\rho}\,, \tag{1.38}$$

where $\Delta \equiv \omega_d - \omega_S$ is the drive-cavity detuning. As one can explicitly verify, the steady state is a coherent state[11] $\hat{\rho}_{\mathrm{SS}} = |\alpha\rangle\langle\alpha|$ with amplitude

$$\alpha = \frac{\mathrm{i}F}{\mathrm{i}\Delta - \frac{\gamma}{2}}\,, \tag{1.39}$$

and the mean photon population is given by $|\alpha|^2 = |F|^2/(\Delta^2+\gamma^2/4)$, which is a Lorentzian form as a function of the pump frequency. Therefore, the dissipation rate γ is also known as the cavity line width, that can be determined experimentally via spectroscopy.

[9] Note that throughout this manuscript, we adopt the convention $\hat{\rho} \mapsto \hat{U}^\dagger\hat{\rho}\hat{U}$ and $\hat{H} \mapsto \hat{U}^\dagger\hat{H}\hat{U} - \mathrm{i}\hbar\hat{U}^\dagger\partial_t\hat{U}$ for changing the internal frame. See Appendix A for more details.

[10] We absorb the Lamb shift into the cavity frequency ω_S.

[11] A coherent state can be defined as $\hat{a}|\alpha\rangle \equiv \alpha|\alpha\rangle$, i.e. the eigenstate of the annihilation operator with eigenvalue α.

III Light-matter interaction

As electromagnetism is a linear theory in terms of its fields, free photons cannot interact with each other directly [though in quantum electrodynamics, they can interact indirectly via the Euler–Heisenberg process by exchanging electron and positron pairs [92, 93], whose cross section is ridiculously small for photons in the visible spectrum and negligible for quantum optics]. However, effective photon-photon interactions can be easily achieved via light-matter coupling, such as by inserting a nonlinear medium in an optical cavity resonator, which effectively replaces the electron-positron pairs in the photon-photon scattering process by electron-hole pairs provided by the medium, and require much lower energies to produce. Such hybrid light-matter systems provide a versatile platform for studying quantum many-body phenomena [39, 94], quantum computing [95] and quantum simulation [96, 97].

The simplest quantum model for light-matter interaction is the Jaynes-Cummings model [98], which describes the coupling between a two-level atom (at a fixed position) and a single mode of the electromagnetic field inside a cavity. In this manuscript, instead of repeating the standard microscopic derivation that one can find in any quantum optics textbook (for example [99]), we will start from a simple phenomenological model (the Unruh-DeWitt model [90, 100]), and show how it reduces to the light-matter interaction model used in quantum optics under quite general assumptions.

III.1 The Unruh-DeWitt model (without moving parts)

The Unruh-DeWitt model was originally proposed to explain certain phenomena predicted by quantum field theory in general relativistic settings, such as Hawking radiation [91]. It consists of a massless scalar quantum field minimally coupled to a point-like detector via monopole interaction [101], where the scalar field can well approximate the electromagnetic field when there is no exchange of angular momentum between the detector and the field [102]. In this section, we will first consider the simple case where the detector is at rest (at position $\boldsymbol{x}_0$[12]) inside a cavity with discrete field modes (the more general case will be discussed in Sec. IV.2). The full Hamiltonian reads

$$\begin{aligned}\hat{H} &= \hat{H}_{\text{field}} + \hat{H}_{\text{det}} + \hat{H}_I \,, \\ &= \sum_n \hbar\omega_n \hat{a}_n^\dagger \hat{a}_n + \hbar\Omega \hat{b}^\dagger \hat{b} + \hbar\lambda \hat{m}\hat{\phi}(\boldsymbol{x}_0) \,,\end{aligned} \tag{1.40}$$

where $\hat{\phi}$ is the quantum field operator in the Schrödinger picture, with mode expansion

$$\hat{\phi}(\boldsymbol{x}) = \sum_n \left[u_n(\boldsymbol{x})\hat{a}_n + u_n^*(\boldsymbol{x})\hat{a}_n^\dagger \right] ; \tag{1.41}$$

$\hat{b}$ is the lowering operator for the detector, whose monopole[13] is $\hat{m} \equiv \hat{b} + \hat{b}^\dagger$. In the originally proposed model, the detector is considered to be a two-level system with $\hat{b} =$

[12] Not to be confused with the zeroth spacetime coordinate x^0. In fact, as the coordinate tuple x^μ is not a four-vector in general, its index should never be lowered.

[13] Not to be confused with the concept of "electric monopole". In fact, this quantity can be physically interpreted as the electric dipole moment in the case of a two-level detector.

$\hat{\sigma}^- \equiv (\hat{\sigma}^x - \mathrm{i}\hat{\sigma}^y)/2$. We will also consider the case where the detector is a harmonic oscillator [103] with annihilation operator $\hat{b}$. Note that we have the commutation relation $[\hat{b}, \hat{b}^\dagger\hat{b}] = \hat{b}$ in both scenarios, which means that the Hamiltonian will continue to share the same form in the interaction picture. Indeed, transforming into the interaction picture[14] with the free Hamiltonian $\hat{H}_0 = \hat{H}_{\text{field}} + \hat{H}_{\text{det}}$, we have

$$\begin{aligned}\hat{H}_I(t)/\hbar &= \lambda\hat{m}(t)\hat{\phi}(t, \boldsymbol{x}_0) \\ &= \lambda(\hat{b}\mathrm{e}^{-\mathrm{i}\Omega t} + \hat{b}^\dagger\mathrm{e}^{\mathrm{i}\Omega t})\sum_n\Big[u(\boldsymbol{x}_0)\hat{a}_n\mathrm{e}^{-\mathrm{i}\omega_n t} + u^*(\boldsymbol{x}_0)\hat{a}^\dagger\mathrm{e}^{\mathrm{i}\omega_n t}\Big] \\ &= \lambda\sum_n\Big[u(\boldsymbol{x}_0)\Big(\hat{a}_n\hat{b}\mathrm{e}^{-\mathrm{i}(\omega_n+\Omega)t} + \hat{a}_n\hat{b}^\dagger\mathrm{e}^{-\mathrm{i}(\omega_n-\Omega)t}\Big) + \text{H.c.}\Big]\,.\end{aligned} \tag{1.42}$$

Now suppose that $\lambda \ll \Omega, \omega_n$ and that the detector's frequency is quasiresonant with one of the cavity modes $\Omega \simeq \omega_\star$, such that their detuning is much smaller than the level spacing of the cavity spectrum. Then, the only relevant (slowly-oscillating) terms in the interaction Hamiltonian will be

$$\hat{H}_I/\hbar = \lambda u_\star(\boldsymbol{x}_0)\hat{a}_\star\hat{b}^\dagger\mathrm{e}^{-\mathrm{i}(\omega_\star-\Omega)t} + \text{H.c.}\,, \tag{1.43}$$

and the contribution from all the other terms will average to zero due to their fast oscillating nature, which is the usual rotating-wave approximation. Defining the *Rabi frequency* $\Omega_R \equiv \lambda u_\star(\boldsymbol{x}_0)$[15] and dropping the index for the resonant cavity mode, the total Hamiltonian can be written back in the Schrödinger picture as

$$\hat{H} = \hbar\omega\hat{a}^\dagger\hat{a} + \hbar\Omega\hat{b}^\dagger\hat{b} + \hbar\Omega_R(\hat{a}\hat{b}^\dagger + \hat{a}^\dagger\hat{b})\,. \tag{1.44}$$

Note that in the case where $\hat{b} = \hat{\sigma}^-$, this is nothing but the well-known Jaynes-Cummings model. In what follows, we will focus on the case where $\hat{b}$ is a bosonic annihilation operator. The Hamiltonian then describes two linearly coupled harmonic oscillators, which provides a good model for exciton-photon coupling in a single-mode cavity.

III.2 Exciton-polaritons in a single-mode cavity

An exciton is a hydrogen-atom-like quasiparticle composed of an electron-hole pair bound by Coulomb attraction [104], that can be found as elementary excitations in semiconductor quantum wells (QWs, properly engineered two-dimensional heterostructures that confine both the electrons and holes within a thin layer of semiconductor). At low exciton densities, i.e. the interparticle distance being much larger than their Bohr radius, such QW excitations are quasi-bosonic particles as one can neglect Pauli exclusion effects for the electrons and holes [39]. When a QW is embedded in a laterally confined photonic box with the exciton frequency quasiresonant to one of the cavity modes, the coupling between the QW and the cavity can be well approximated by the Hamiltonian (1.44), with $\hat{b}$ the annihilation operator for the exciton mode.

[14] We use the same symbol for an operator in different frames when there is no ambiguity from the context.

[15] Note that $u_n(\boldsymbol{x})$ is a real function for a Cavity with Dirichlet boundary conditions. Otherwise, the complex phase could be absorbed into the mode operator if it were complex.

As this Hamiltonian is symmetric and bilinear in the mode operators, it can be readily diagonalized by a Bogoliubov transformation:

$$\hat{H}/\hbar = \begin{pmatrix}\hat{a}^\dagger & \hat{b}^\dagger\end{pmatrix}\begin{pmatrix}\omega & \Omega_R \\ \Omega_R & \Omega\end{pmatrix}\begin{pmatrix}\hat{a} \\ \hat{b}\end{pmatrix} = \begin{pmatrix}\hat{a}^\dagger & \hat{b}^\dagger\end{pmatrix} P^T D P \begin{pmatrix}\hat{a} \\ \hat{b}\end{pmatrix}, \tag{1.45}$$

where

$$D = \begin{pmatrix}\omega_{\mathrm{LP}} & 0 \\ 0 & \omega_{\mathrm{UP}}\end{pmatrix}, \quad P = \begin{pmatrix}C & -X \\ X & C\end{pmatrix}, \tag{1.46}$$

that can be expressed as the original Hamiltonian parameters as

$$\omega_{\mathrm{UP,LP}} = \frac{\omega+\Omega}{2} \pm \sqrt{\left(\frac{\omega-\Omega}{2}\right)^2 + \Omega_R^2}\,; \quad X, C = \left[1 + \left(\frac{\Omega_R}{\omega_{\mathrm{LP}} - \omega}\right)^{\pm 2}\right]^{-1/2}. \tag{1.47}$$

The Hamiltonian therefore becomes decoupled in terms of the two normal modes:

$$\begin{pmatrix}\hat{a}_{\mathrm{LP}} \\ \hat{a}_{\mathrm{UP}}\end{pmatrix} \equiv \begin{pmatrix}C & -X \\ X & C\end{pmatrix}\begin{pmatrix}\hat{a} \\ \hat{b}\end{pmatrix}, \quad \hat{H} = \hbar\omega_{\mathrm{LP}}\hat{a}^\dagger_{\mathrm{LP}}\hat{a}_{\mathrm{LP}} + \hbar\omega_{\mathrm{UP}}\hat{a}^\dagger_{\mathrm{UP}}\hat{a}_{\mathrm{UP}}\,, \tag{1.48}$$

which are known as the lower (LP) and upper (UP) *polaritons*. They are hybrid excitations of light and matter (QW excitons in the present case), and are also called *dressed photons*. As the Bogoliubov coefficients satisfy $|C|^2 + |X|^2 = 1$, we define the exciton (photon) fraction of the lower (upper) polariton mode to be $|X|^2$, as represented in Fig. 1.2. At resonance ($\omega = \Omega$), the two branches reach their minimum separation $2\Omega_R$ with equal exciton-photon fraction for both UP and LP modes. For large detunings, the normal modes reduce to purely photonic or excitonic ones, that are effectively decoupled.

Effective photon-photon interactions

Unlike photons, the excitons can interact with each other via the Coulomb force, an additional term $\hat{H}_{\mathrm{nl}}$ is therefore due in the Hamiltonian to correct for this nonlinear effect. This can be modeled by a *Kerr nonlinearity* that represents a two-body contact potential [39]:

$$\begin{aligned}\hat{H}_{\mathrm{nl}}/\hbar &= \frac{V}{2}\hat{b}^{\dagger 2}\hat{b}^2 \\ &= \frac{V}{2}\left(-X\hat{a}^\dagger_{\mathrm{LP}} + C\hat{a}^\dagger_{\mathrm{UP}}\right)^2\left(-X\hat{a}_{\mathrm{LP}} + C\hat{a}_{\mathrm{UP}}\right)^2 \\ &\simeq \frac{V}{2}\left(X^4\hat{a}^{\dagger 2}_{\mathrm{LP}}\hat{a}^2_{\mathrm{LP}} + C^4\hat{a}^{\dagger 2}_{\mathrm{UP}}\hat{a}^2_{\mathrm{UP}} + 4X^2C^2\hat{a}^\dagger_{\mathrm{LP}}\hat{a}_{\mathrm{LP}}\hat{a}^\dagger_{\mathrm{UP}}\hat{a}_{\mathrm{UP}}\right),\end{aligned} \tag{1.49}$$

where V represents the nonlinearity strength. In the second line, we used the reverse Bogoliubov transformation $\hat{b} = -X\hat{a}_{\mathrm{LP}} + C\hat{a}_{\mathrm{UP}}$ to rewrite the nonlinear Hamiltonian in terms of the polariton modes, and in the last step we performed again the rotating-wave approximation to keep only the resonant terms, which is valid when the Rabi splitting $2\Omega_R$ between UP and LP modes is much larger than any other relevant energy scale in the system, the regime that we will work with in the following sections. Consequently,

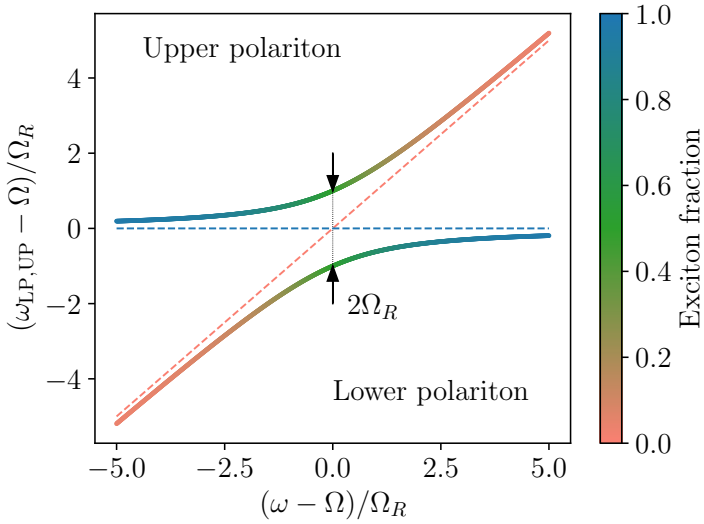

Figure 1.2: Frequencies of the upper and lower polariton modes as a function of the photon-exciton detuning, with the exciton fraction represented in the colorbar. The minimum splitting between the two branches is $2\Omega_R$ with equal exciton-photon fractions in both modes, attained at zero detuning.

both the lower and upper polariton modes inherent the Kerr nonlinearity with strengths $U_{\mathrm{LP}} = VX^4$ and $U_{\mathrm{UP}} = VC^4$ respectively, and the two modes are nonlinearly coupled via a cross-Kerr interaction of strength $4VX^2C^2$. This can be interpreted as an effective interaction between the dressed photons, that is mediated via the coupling to the matter degrees of freedom. Note that this nonlinearity is also present in the Jaynes-Cummings model (i.e. when $\hat{b} = \hat{\sigma}^-$), since the two-level system can be understood as the hardcore limit $V \to \infty$ for the Bosonic mode.

Driven-dissipative Kerr model

As discussed in Sec. II, real life cavities are subject to dissipation due to their interaction with the environment, the polariton modes therefore have finite line widths. Under typical experimental circumstances, one drives quasiresonantly the lower-polariton mode. In the regime of large Rabi splitting between LP and UP, we can safely ignore the UP mode and describe the dynamics of the system uniquely with the LP mode. This implies that we are working in the so-called *strong-coupling* regime [39], where the Rabi splitting exceeds the linewidths of the bare cavity and the exciton. The free (i.e. undriven) Hamiltonian then reads (dropping the LP subscript):

$$\hat{H}_{\mathrm{Kerr}}/\hbar = \omega \hat{a}^\dagger \hat{a} + \frac{U}{2} \hat{a}^{\dagger 2} \hat{a}^2 \,, \tag{1.50}$$

which effectively describes a single-mode photonic cavity with Kerr nonlinearity. This so-called Kerr model is extremely useful and serves as the building block for many problems in quantum optics and condensed matter physics, such as the Bose-Hubbard model [105], which describes a lattice of such nonlinear Bosonic modes that are linearly

coupled between neighbors. Another typical implementation of the Kerr model can be found in superconducting circuits (circuit QED [106]), where an LC oscillator with a Josephson junction (a nonlinear element) gives rise to the same Hamiltonian (1.50) when quantized[16].

The full driven-dissipative master equation for the LP mode is then[17]

$$\frac{\mathrm{d}}{\mathrm{d}t}\hat{\rho} = -\frac{\mathrm{i}}{\hbar}\Big[\hat{H}_{\mathrm{Kerr}} + \hat{H}_{\mathrm{drive}}, \hat{\rho}\Big] + \gamma\mathcal{D}[\hat{a}]\hat{\rho}\,, \tag{1.51}$$

where $\hat{H}_{\mathrm{drive}}$ is the same as the previously considered driving term (1.37). Transforming again into the frame rotating at ω_d as done in Sec. II.1, the equation becomes

$$\frac{\mathrm{d}}{\mathrm{d}t}\hat{\rho} = \mathrm{i}\Big[-\Delta\hat{a}^\dagger\hat{a} + \frac{U}{2}\hat{a}^{\dagger 2}\hat{a}^2 + (F^*\hat{a} + F\hat{a}^\dagger), \hat{\rho}\Big] + \gamma\mathcal{D}[\hat{a}]\hat{\rho}\,, \tag{1.52}$$

with $\Delta = \omega_d - \omega$, which has an additional nonlinear term compared to Eq. (1.38). When $U \neq 0$, the steady state will no longer be a coherent state, but one can make the *mean-field* approximation for weak nonlinearities by assuming the state to be coherent, and solve for the dynamics of the amplitude $\alpha \equiv \langle\hat{a}\rangle = \mathrm{Tr}[\hat{\rho}\hat{a}]$:

$$\frac{\mathrm{d}}{\mathrm{d}t}\alpha = -\mathrm{i}\Big[-\Delta\alpha + U|\alpha|^2\alpha + F\Big] - \frac{\gamma}{2}\alpha\,, \tag{1.53}$$

where the cubic terms comes from the factorization $\langle\hat{a}^{\dagger m}\hat{a}^n\rangle \simeq \alpha^{*m}\alpha^n$ by the mean-field approximation. The steady-state solution α_{SS} satisfies the nonlinear relation

$$|\alpha_{\mathrm{SS}}|^2\left[(\Delta - U|\alpha_{\mathrm{SS}}|^2)^2 + \frac{\gamma^2}{4}\right] = |F|^2\,, \tag{1.54}$$

which admits bistable solutions if $\Delta > \sqrt{3}\gamma/2$ (assuming $U > 0$), as illustrated by the S-shaped curve in Fig. 1.3.

Note that if one solves the master equation (1.52) directly, the exact solution for the steady state is always unique [107] even in the mean-field bistable regime, as the quantum fluctuations induce switchings between the two classical solutions and the unique steady-state density matrix corresponds to their average. However, a bistable behavior similar to the mean-field prediction can be observed experimentally [108, 109], due to the fact that the switching time can be astronomical if the system approaches criticality, which causes the observed state to depend on the initial conditions and exhibit hysteresis in an experiment with finite duration. Such critical phenomena will be discussed in more detail in Chapter 2.

[16] In semiconductor platforms one typically has $U > 0$, where as for in circuit QED we have $U < 0$ and the nonlinearity can be made much higher (with respect to the line width) compared to semiconductor platforms.

[17] By a similar argument to our discussion in Sec. II.1, we assume that the presence of Kerr nonlinearity does not affect the form of the master equation. In other words, we are assuming here that the reservoir spectrum is flat on the scale of $\omega \pm U$.

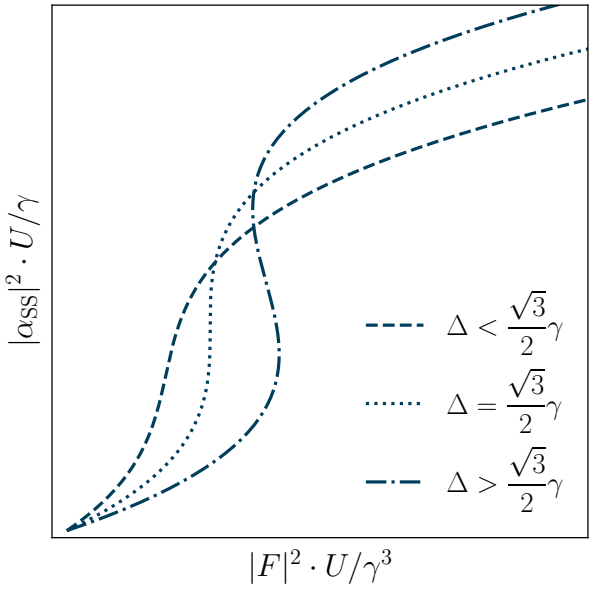

Figure 1.3: Steady-state population α_{SS} of a single-mode Kerr cavity as a function of the drive intensity $|F|^2$ in the mean-field approximation, for different regimes of the pump-cavity detuning $\Delta = \omega_d - \omega$. The mean-field solution is bistable for detunings larger than $\sqrt{3}\gamma/2$.

III.3 Exciton-polaritons in a planar cavity

Consider now a planar cavity with no lateral confinement, i.e. both photons and excitons can move freely in the cavity plane. The in-plane wavevector $\boldsymbol{k}_\parallel$ is therefore a good quantum number due to the in-plane translational symmetry, and k_z takes discrete values due to the cavity confinement. For a fixed k_z, the quadratic part $\hat{H}_0$ (without Kerr nonlinearity) of the total Hamiltonian is the integral over all $\boldsymbol{k}_\parallel$ modes[18]:

$$\hat{H}_0 = \int \mathrm{d}^2\boldsymbol{k}\hat{H}(\boldsymbol{k})\,, \tag{1.55}$$

where the contribution from each $\boldsymbol{k}$ takes the same form as Eq. (1.44)[19] in the rotating-wave approximation:

$$\begin{aligned}\hat{H}(\boldsymbol{k})/\hbar = \omega(\boldsymbol{k})\hat{a}^\dagger(\boldsymbol{k})\hat{a}(\boldsymbol{k}) + \Omega(\boldsymbol{k})\hat{b}^\dagger(\boldsymbol{k})\hat{b}(\boldsymbol{k}) \\ + \Omega_R\Big[\hat{a}(\boldsymbol{k})\hat{b}^\dagger(\boldsymbol{k}) + \hat{a}^\dagger(\boldsymbol{k})\hat{b}(\boldsymbol{k})\Big]\,,\end{aligned} \tag{1.56}$$

where $\omega(\boldsymbol{k})$ is the dispersion relation of the cavity photon given by Eq. (1.16) and is sketched in Fig. 1.4, and $\Omega(\boldsymbol{k})$ is that of the exciton, which takes a similar form (denoting $k \equiv \|\boldsymbol{k}\|$):

$$\Omega(\boldsymbol{k}) = \Omega^{k=0} + \frac{\hbar k^2}{2m_X}\,, \tag{1.57}$$

[18] We drop the subscript in $\boldsymbol{k}_\parallel$ for the rest of this section, i.e. denoting $\boldsymbol{k} \equiv (k_x, k_y)$ since the in-plane wavevector uniquely determines the total wavevector for a fix k_z.

[19] The photons couple to the excitons with the same $\boldsymbol{k}$ due to conservation of the in-plane momentum.

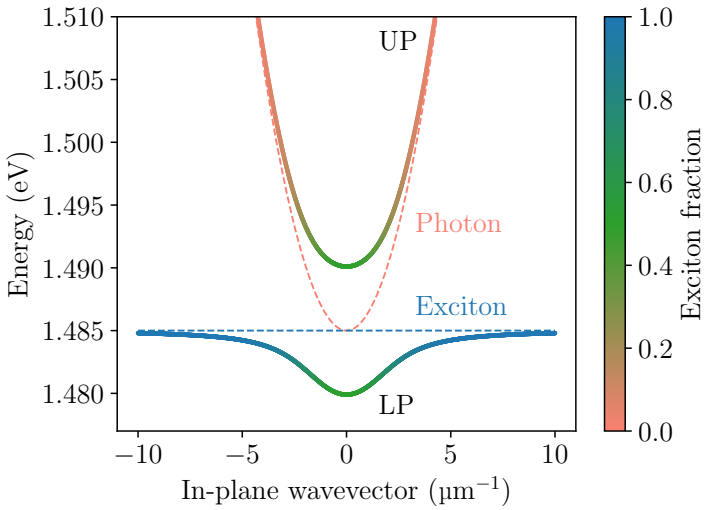

Figure 1.4: Energies of the exciton-polariton modes in a planar cavity as a function of the in-plane wavevector $\|\boldsymbol{k}\|$, with the exciton fraction represented in the colorbar. The parameters are taken from [γ]: $m_{\text{cav}} = 2.8 \times 10^{-5} m_e$, $\hbar\Omega_R = 5.1$ meV, $\hbar\Omega = 1.458$ meV, where m_e is the bare electron mass.

with m_X the exciton mass. As typically $m_X \gg m_{\text{cav}}$ [39], we can ignore the exciton dispersion in practice and consider $\Omega(\boldsymbol{k}) = \Omega$ as a constant. $\hat{H}(\boldsymbol{k})$ can be diagonalized in the same way as done in Sec. III.2, giving

$$\hat{H}(\boldsymbol{k}) = \hbar\omega_{\text{LP}}(\boldsymbol{k})\hat{a}^\dagger_{\text{LP}}(\boldsymbol{k})\hat{a}_{\text{LP}}(\boldsymbol{k}) + \hbar\omega_{\text{UP}}(\boldsymbol{k})\hat{a}^\dagger_{\text{UP}}(\boldsymbol{k})\hat{a}_{\text{UP}}(\boldsymbol{k}) \,, \tag{1.58}$$

where $\omega_{\text{UP,LP}}(\boldsymbol{k})$ is given by Eq. (1.47) with the appropriate dispersion relations $\omega(\boldsymbol{k})$ and $\Omega(\boldsymbol{k})$ inserted into the expression. The resulting spectrum is plotted in Fig. 1.4 for typical parameters in semiconductor planar microcavities (the values considered in [γ]), which is essentially the same plot as Fig. 1.2 but with the horizontal axis reparametrized by the in-plane wavevector $\boldsymbol{k}$.

Driven-dissipative dynamics

When the system is driven quasi-resonantly close to the bottom of the LP branch, we can again ignore the UP modes provided that Ω_R is much larger than other energy scales [39]. The coherent drive [with spatial-temporal profile $\mathcal{F}(\boldsymbol{r}, t)$] in terms of the LP field can be written as

$$\hat{H}_{\text{drive}} = \int \mathrm{d}^2\boldsymbol{r}\ \hbar\Big[\mathcal{F}(\boldsymbol{r}, t)\hat{\psi}^\dagger(\boldsymbol{r}) + \mathcal{F}^*(\boldsymbol{r}, t)\hat{\psi}(\boldsymbol{r})\Big] \,, \tag{1.59}$$

where $\hat{\psi}(\boldsymbol{r})$ is the position-space representation of the annihilation operator $\hat{a}_{\text{LP}}(\boldsymbol{k})$ related via the Fourier transform,

$$\hat{\psi}(\boldsymbol{r}) \equiv \frac{1}{2\pi}\int \mathrm{d}^2\boldsymbol{k}\ \hat{a}_{\text{LP}}(\boldsymbol{k})\mathrm{e}^{\mathrm{i}\boldsymbol{k}\cdot\boldsymbol{r}} \,, \quad \hat{a}_{\text{LP}}(\boldsymbol{k}) = \frac{1}{2\pi}\int \mathrm{d}^2\boldsymbol{r}\ \hat{\psi}(\boldsymbol{r})\mathrm{e}^{-\mathrm{i}\boldsymbol{k}\cdot\boldsymbol{r}} \,, \tag{1.60}$$

for the in-plane position vector $\boldsymbol{r} \equiv (x, y)$. The nonlinear part of the Hamiltonian can be approximated by the effective LP-LP contact potential [39] with strength g:

$$\hat{H}_{\mathrm{nl}} = \int \mathrm{d}^2\boldsymbol{r} \frac{\hbar g}{2} \hat{\psi}^\dagger(\boldsymbol{r})^2 \hat{\psi}(\boldsymbol{r})^2 \,, \tag{1.61}$$

which is the continuous analogue of the Kerr nonlinearity. The quadratic part $\hat{H}_0$ can also be written in the position representation (keeping only the LP terms):

$$\begin{aligned} \hat{H}_0 &= \int \mathrm{d}^2\boldsymbol{k}\ \hbar\omega_{\mathrm{LP}}(\boldsymbol{k}) \hat{a}^\dagger_{\mathrm{LP}}(\boldsymbol{k}) \hat{a}_{\mathrm{LP}}(\boldsymbol{k}) \\ &\simeq \int \mathrm{d}^2 \hat{\psi}^\dagger(\boldsymbol{r}) \left(\hbar\omega_{\mathrm{LP}}^{k=0} - \frac{\hbar^2\nabla^2}{2m} \right) \hat{\psi}(\boldsymbol{r}) \,, \end{aligned} \tag{1.62}$$

where we approximated the bottom of the LP branch by a parabolic dispersion relation $\omega_{\mathrm{LP}}(\boldsymbol{k}) \simeq \omega_{\mathrm{LP}}^{k=0} + \hbar k^2/2m$, with m the effective LP mass. Finally, the driven-dissipative dynamics of the LP field under the Born-Markov approximation can be cast in the Lindblad master equation in terms of its density matrix $\hat{\rho}$:

$$\frac{\mathrm{d}}{\mathrm{d}t}\hat{\rho} = -\frac{\mathrm{i}}{\hbar}\left[\hat{H}_0 + \hat{H}_{\mathrm{nl}} + \hat{H}_{\mathrm{drive}}, \hat{\rho}\right] + \mathcal{D}\hat{\rho} \,, \tag{1.63}$$

with the dissipator

$$\mathcal{D}\hat{\rho} = \int \mathrm{d}^2\boldsymbol{r} \frac{\gamma}{2} \left[2\hat{\psi}(\boldsymbol{r})\hat{\rho}\hat{\psi}^\dagger(\boldsymbol{r}) - \left\{ \hat{\psi}^\dagger(\boldsymbol{r})\hat{\psi}(\boldsymbol{r}), \hat{\rho} \right\} \right] , \tag{1.64}$$

where γ is the LP dissipation rate.

Under the mean-field approximation $\langle \hat{\psi}^{\dagger m}(\boldsymbol{r}) \hat{\psi}^n(\boldsymbol{r}) \rangle \simeq \langle \hat{\psi}^\dagger(\boldsymbol{r}) \rangle^m \langle \hat{\psi}(\boldsymbol{r}) \rangle^n$, the dynamical equation for the mean field $\psi \equiv \langle \hat{\psi} \rangle$ can be derived from the master equation:

$$\mathrm{i}\frac{\partial}{\partial t}\psi(\boldsymbol{r}, t) = \left(\omega_{\mathrm{LP}}^{k=0} - \frac{\hbar\nabla^2}{2m} \right) \psi(\boldsymbol{r}, t) + g|\psi(\boldsymbol{r}, t)|^2 \psi(\boldsymbol{r}, t) - \mathrm{i}\frac{\gamma}{2}\psi(\boldsymbol{r}, t) + \mathcal{F}(\boldsymbol{r}, t) \,, \tag{1.65}$$

which is known as the driven-dissipative Gross-Pitaevskii equation [39].

Planar cavity as a "continuous lattice"

As the planar cavity is a continuous system (in terms of the spatial coordinates), one typically needs to perform certain kind of discretization in order to study it numerically. In fact, upon discretizing using a square grid with step size $\Delta x \times \Delta x$, the master equation (1.63) for the LP field in the planar cavity can be exactly mapped to that of a driven-dissipative Bose-Hubbard lattice consisting of coupled Kerr resonators. The discretization consists of the approximation

$$\int \mathrm{d}^2\boldsymbol{r} f(\boldsymbol{r}) \longrightarrow \sum_j \Delta x^2 f(\boldsymbol{r}_j) \,, \tag{1.66}$$

where $\boldsymbol{r}_j$ denotes the j-th lattice site, for a (possibly operator-valued) function $f(\boldsymbol{r})$. The discretized commutation relation hence becomes $[\hat{\psi}(\boldsymbol{r}_j), \hat{\psi}^\dagger(\boldsymbol{r}_{j'})] = \delta_{j,j'}/\Delta x^2$. We can

define the dimensionless annihilation operator $\hat{a}_j \equiv \hat{\psi}(\boldsymbol{r}_j)\Delta x$, whose action is to annihilate an excitation at the grid site j, with the standard Bosonic commutation relations $[\hat{a}_j, \hat{a}_{j'}^\dagger] = \delta_{j,j'}$. The Laplacian in the Hamiltonian (1.62) can be discretized via the finite-difference formula

$$\begin{aligned}\nabla^2\hat{\psi}(\boldsymbol{r}_j) &= (\partial_x^2 + \partial_y^2)\hat{\psi}(\boldsymbol{r}) \\ &\simeq \sum_{\sigma\in\{x,y\}} \frac{\hat{\psi}(\boldsymbol{r}_j + \Delta x \boldsymbol{e}_\sigma) + \hat{\psi}(\boldsymbol{r}_j - \Delta x \boldsymbol{e}_\sigma) - 2\hat{\psi}(\boldsymbol{r}_j)}{\Delta x^2} \\ &= \frac{\sum_{j'\in N(j)} \hat{a}_{j'} - z\hat{a}_j}{\Delta x^4}\,,\end{aligned} \tag{1.67}$$

where $N(j)$ denotes the set of neighboring sites of j, and $z = 4$ is the coordination number (number of nearest neighbors per site) in 2D. The discretized full Hamiltonian reads

$$\hat{H}/\hbar = \sum_j \left[\omega_0 \hat{a}_j^\dagger \hat{a}_j + \frac{U}{2}\hat{a}_j^{\dagger 2}\hat{a}_j^2 + F_j(t)\hat{a}_j^\dagger + F_j^*(t)\hat{a}_j\right] - J\sum_{\langle j,j'\rangle} \hat{a}_j^\dagger \hat{a}_{j'}\,, \tag{1.68}$$

where $\langle j, j'\rangle$ denotes (ordered) pairs of nearest neighbor, with the identification for the parameters

$$J = \frac{\hbar}{2m\Delta x^2}\,, \quad \omega_0 = \omega_{\mathrm{LP}}^{k=0} + zJ\,, \quad U = \frac{g}{\Delta x^2}\,, \quad F_j(t) = \mathcal{F}(\boldsymbol{r}_j, t)\Delta x\,. \tag{1.69}$$

The dissipator becomes

$$\mathcal{D}\hat{\rho} = \frac{\gamma}{2}\sum_j \left(2\hat{a}_j\hat{\rho}\hat{a}_j^\dagger - \left\{\hat{a}_j^\dagger\hat{a}_j, \hat{\rho}\right\}\right)\,, \tag{1.70}$$

which, together with the Hamiltonian (1.68), completely defines the dynamics of the lattice. This discretized model describes a lattice of driven-dissipative single-mode Kerr resonators with bare frequency ω_0 and Kerr nonlinearity U on each site. The kinetic energy of the polaritons becomes a coupling term with amplitude J, which allows excitations to hop between the neighboring lattice sites. The planar cavity can therefore be regarded as the continuous limit $\Delta x \to 0$ of the driven-dissipative Bose-Hubbard lattice.

IV Light-matter interaction under relativistic settings

Our discussion of light-matter interaction based on the cavity-detector (Unruh-DeWitt) model so far does not involve any mechanically moving parts yet, i.e. both the matter and the cavity are assumed to be at fixed positions. In this section, we will partially lift this constraint and allow the matter (the detector) to move within a static setup (cavity or free space). (Note that we will not consider the complementary scenario, where the cavity is in motion, throughout this manuscript, although it is equally interesting. A well-known phenomenon in this regime the *dynamical Casimir effect* [110, 111], where an accelerated mirror can produce photons out of the vacuum.)

When the motion of the detector inside the cavity is relativistic, this brings a subtle complication to our consideration. While the time evolution of a quantum system is

generated by the Hamiltonian operator, *time* is an observer-dependent notion in relativity, i.e. if different parts in a system are undergoing relative motion, they will experience different times in general. One therefore needs to be careful with the question: "with respect to which time is the Hamiltonian generating time-translation ?" The answer to this question will lead to the general Unruh-DeWitt model that we will introduce in Sec. IV.2, which is capable of describing the quantum dynamics of a detector undergoing relativistic motion coupled to a quantum field. Before arriving at this model, we will first introduce how the Hamiltonian transforms under a reparametrization of the time (following the discussion in [103, 112]), which is inevitable when changing between reference frames with relative motion.

IV.1 Hamiltonian as the generator of time translation

Let us consider a general time-dependent Hamiltonian $\hat{H}^t(t)$, which generates translation in time with respect to some time parameter t via the Schrödinger equation

$$\frac{\mathrm{d}}{\mathrm{d}t}|\psi(t)\rangle = -\frac{\mathrm{i}}{\hbar}\hat{H}^t(t)|\psi(t)\rangle\,, \tag{1.71}$$

for the quantum state of some system $|\psi(t)\rangle$, and the superscript in the Hamiltonian serves to specify the parameter with respect to which the Hamiltonian generates time translation. Suppose we want to reparametrize the time with a new parameter τ via a given function $t(\tau)$. The time-translation generator for the reparametrized state $|\psi(\tau)\rangle \equiv |\psi(t(\tau))\rangle$ can be found by differentiating with respect to the new parameter τ:

$$\begin{aligned}\frac{\mathrm{d}}{\mathrm{d}\tau}|\psi(t(\tau))\rangle &= \frac{\mathrm{d}t(\tau)}{\mathrm{d}\tau}\frac{\mathrm{d}}{\mathrm{d}t}|\psi(t)\rangle\Big|_{t=t(\tau)} \\ &= \frac{\mathrm{d}t(\tau)}{\mathrm{d}\tau}\Big[-\frac{\mathrm{i}}{\hbar}\hat{H}^t(t)|\psi(t)\rangle\Big]_{t=t(\tau)} \\ &\equiv -\frac{\mathrm{i}}{\hbar}\hat{H}^\tau(\tau)|\psi(\tau)\rangle\,,\end{aligned} \tag{1.72}$$

from which we identify the Hamiltonian for the parameter τ:

$$\hat{H}^\tau(\tau) = \frac{\mathrm{d}t(\tau)}{\mathrm{d}\tau}\hat{H}^t(t(\tau))\,. \tag{1.73}$$

Note that the appearance of the *redshift factor* $\mathrm{d}t/\mathrm{d}\tau$ guarantees the invariance of the time-evolution operator under reparametrization:

$$\begin{aligned}\hat{U} &= \mathcal{T}\exp\Big[-\frac{\mathrm{i}}{\hbar}\int \mathrm{d}\tau\hat{H}^\tau(\tau)\Big] \\ &= \mathcal{T}\exp\Big[-\frac{\mathrm{i}}{\hbar}\int \mathrm{d}\tau\frac{\mathrm{d}t}{\mathrm{d}\tau}\hat{H}^t(t)\Big] \\ &= \mathcal{T}\exp\Big[-\frac{\mathrm{i}}{\hbar}\int \mathrm{d}t\hat{H}^t(t)\Big]\,.\end{aligned} \tag{1.74}$$

IV.2 The Unruh-DeWitt model for a relativistic detector

We are now ready to introduce the relativistic model for light-matter interaction. Consider an idealized point-like detector moving along a classical world line $x^\mu(\tau) = (ct(\tau), \boldsymbol{x}(\tau))$, that is coupled to a quantum field (for example, the field in a static cavity) in Minkowski spacetime. Similar to Eq. (1.40), the Hamiltonian is still of the form

$$\hat{H} = \hat{H}_{\text{field}} + \hat{H}_{\text{det}} + \hat{H}_I \,, \tag{1.75}$$

but the terms in Eq. (1.40) cannot be directly added as they are not generating time translation with respect to the same time. The free field Hamiltonian with respect to the Minkowski coordinate time t is (using the notation in Sec. III.1)

$$\hat{H}^t_{\text{field}} = \sum_n \hbar\omega_n \hat{a}^\dagger_n \hat{a}_n \,, \tag{1.76}$$

and the free detector Hamiltonian for its *proper time* τ (time measured by a clock carried by the detector) is

$$\hat{H}^\tau_{\text{det}} = \hbar\Omega \hat{b}^\dagger \hat{b} \,. \tag{1.77}$$

The interaction Hamiltonian is still[20]

$$\begin{aligned} \hat{H}^\tau_I(\tau) &= \hbar\lambda \hat{m}\hat{\phi}(\boldsymbol{x}(\tau)) \\ &= \hbar\lambda(\hat{b}^\dagger + \hat{b}) \sum_n \Big[u_n(\boldsymbol{x}(\tau))\hat{a}_n + u^*_n(\boldsymbol{x}(\tau))\hat{a}^\dagger_n \Big] \,, \end{aligned} \tag{1.78}$$

which is local on the world line of the detector and generates time translation in the detector's proper frame with respect to τ. We will be studying the dynamics of the detector in its proper frame in this manuscript, and we therefore choose to parameterize the total Hamiltonian using the proper time τ. Using Eq. (1.73), the Hamiltonian can be written as

$$\begin{aligned} \hat{H}^\tau(\tau) &= \frac{\mathrm{d}t(\tau)}{\mathrm{d}\tau} \hat{H}^t_{\text{field}} + \hat{H}^\tau_{\text{det}} + \hat{H}^\tau_I(\tau) \\ &= \hat{H}^\tau_{\text{field}}(\tau) + \hat{H}^\tau_{\text{det}} + \hat{H}^\tau_I(\tau) \,, \end{aligned} \tag{1.79}$$

where $t(\tau)$ is given by the time component of the detector's world line. Let us now transform into the interaction picture using the (proper-time dependent) free Hamiltonian $\hat{H}^\tau_{\text{field}}(\tau) + \hat{H}^\tau_{\text{det}}$. Since the τ-dependence in $\hat{H}^\tau_{\text{field}}$ appears as a global factor, the free Hamiltonian commutes with itself between different times. The unitary transformation operator is therefore simply (See Appendix A)

$$\begin{aligned} \hat{U}_0(\tau) &= \exp\left[-\frac{\mathrm{i}}{\hbar} \int_0^\tau \mathrm{d}\tau' \left(\frac{\mathrm{d}t}{\mathrm{d}\tau'} \hat{H}^t_{\text{field}} + \hat{H}^\tau_{\text{det}} \right) \right] \\ &= \exp\left[-\frac{\mathrm{i}}{\hbar} \left(\hat{H}^t_{\text{field}} t(\tau) + \hat{H}^\tau_{\text{det}} \tau \right) \right] \\ &= \exp\left[-\mathrm{i} \left(\sum_n \omega_n \hat{a}^\dagger_n \hat{a}_n \right) t(\tau) - \mathrm{i}\Omega \hat{b}^\dagger \hat{b} \tau \right] \,, \end{aligned} \tag{1.80}$$

[20] The following discussion also applies when the quantum field $\hat{\phi}$ admits a continuum mode expansion.

which gives the interaction-picture Hamiltonian

$$\begin{aligned}\tilde{H}_I^\tau(\tau) &= \hat{U}_0^\dagger(\tau)\hat{H}_I^\tau\hat{U}_0(\tau)\\ &= \hbar\lambda\Big(\hat{b}^\dagger \mathrm{e}^{\mathrm{i}\Omega\tau} + \hat{b}\mathrm{e}^{-\mathrm{i}\Omega\tau}\Big)\sum_n\Big[u_n(\boldsymbol{x}(\tau))\hat{a}_n\mathrm{e}^{-\mathrm{i}\omega_n t(\tau)} + u_n^*(\boldsymbol{x}(\tau))\hat{a}_n^\dagger\mathrm{e}^{\mathrm{i}\omega_n t(\tau)}\Big]\\ &= \hbar\lambda\hat{m}(\tau)\hat{\phi}[x^\mu(\tau)]\,,\end{aligned} \tag{1.81}$$

where $\hat{m}(\tau)$ is the detector's monopole operator in the interaction picture, and $\hat{\phi}[x^\mu(\tau)]$ is the interaction-picture quantum field operator evaluated at the world line of the detector. Eq. (1.81) is the Unruh-DeWitt Hamiltonian, which accounts for relativistic effects in light-matter interaction for a detector undergoing general motion. Note that we are no longer performing the rotating-wave nor single-mode approximation here, as the resonance condition in the phases $-\mathrm{i}[\Omega\tau \pm \omega_n t(\tau)]$ depends on the parametrization $t(\tau)$, which is a manifestation of the time-dilation effect in relativity.

It is worth clarifying at this point that the Unruh-DeWitt model is a semiclassical model for light-matter (field-detector) interaction in the sense that

1. the detector is a first-quantized quantum-mechanical particle (unlike in quantum field theory where particles can be created or annihilated) undergoing classical motion on a specified trajectory $x^\mu(\tau)$;

2. the background spacetime is treated in a completely classical manner, which is fixed and thus not accounting for any possible coupling to the quantum field (which may carry energy and momentum)[21].

Very recently, there has been theoretical studies to generalize the Unruh-DeWitt model by considering a second-quantized detector [114] or quantum superpositions of the detector's motion [115–117], which address the first remark above. Regarding the second, a fully quantum model requires a quantized theory of gravity, which is still an open challenge to date. Decades of effort has given rise to candidates such as string theory [118] and loop quantum gravity [119], which are beyond the scope of the present manuscript.

Despite its semiclassical nature, the Unruh-DeWitt model serves as a good approximation in the context of quantum optics. This model combined with the master-equation formalism in Sec. II.1 can be used to demonstrate an interesting phenomenon originally predicted by quantum field theory in curved spacetime, which is the Unruh effect.

IV.3 Unruh effect

We now set $c = \hbar = 1$ to simplify the notations. Consider now the detector, whose internal degree of freedom is modeled by a harmonic oscillator, that is moving along the world line $x^\mu(\tau) = (t(\tau), \boldsymbol{x}(\tau))$ with constant proper acceleration through the (3+1)D[22]

[21] In classical general relativity, the spacetime metric $g_{\mu\nu}$ satisfies the Einstein field equation [113] $R_{\mu\nu} - \frac{1}{2}g_{\mu\nu}R = 8\pi G T_{\mu\nu}$, where the right-hand side describes the distribution of energy and momentum of matter, and the left-hand side describes the shape of spacetime, which is a (very complicated) function of the metric.

[22] This notations means we consider 3 spatial dimensions and 1 time dimension.

Minkowski vacuum of a massless scalar field $\hat{\phi}$ in free space to which it is weakly coupled. In the interaction picture, the quantum field operator $\hat{\phi}$ admits the mode expansion (see Appendix B)

$$\hat{\phi}(t,\boldsymbol{x}) = \int \frac{\mathrm{d}^3\boldsymbol{k}}{(2\pi)^{\frac{3}{2}}}\sqrt{\frac{1}{2\omega_{\boldsymbol{k}}}}\Big(\hat{a}_{\boldsymbol{k}}\mathrm{e}^{-\mathrm{i}(\omega_{\boldsymbol{k}}t-\boldsymbol{k}\cdot\boldsymbol{x})} + \hat{a}^{\dagger}_{\boldsymbol{k}}\mathrm{e}^{\mathrm{i}(\omega_{\boldsymbol{k}}t-\boldsymbol{k}\cdot\boldsymbol{x})}\Big), \tag{1.82}$$

with the dispersion relation $\omega_{\boldsymbol{k}} = \|\boldsymbol{k}\|$. The interaction Hamiltonian is given by Eq. (1.78), which takes the form of Eq. (1.18) (by identifying $\hat{S} = \hat{m}$ and $\hat{R} = \lambda\hat{\phi}$). This allows us to derive the master equation for the density matrix $\hat{\rho}$ of the detector using the formalism presented in Sec. II.1. As we consider an eternally accelerated detector, we can assume the reservoir correlation function $\mathcal{G}(\tau)$ to be translational invariant with respect to τ, which is given by[23]

$$\mathcal{G}(\tau) = \lambda^2\langle 0|\hat{\phi}[x(\tau)]\hat{\phi}[x(0)]|0\rangle = \lambda^2 D^+[x(\tau),x(0)], \tag{1.83}$$

where we identify the so-called *positive frequency Wightman function* [120] for the massless scalar field, defined as $D^+(x,x') = \langle 0|\hat{\phi}(x)\hat{\phi}(x')|0\rangle$. Using the mode expansion (1.82), this Wightman function can be explicitly evaluated to be

$$D^+(x,x') = -\frac{1}{4\pi^2}\frac{1}{(x^0-x'^0-\mathrm{i}\epsilon)^2 - \|\boldsymbol{x}-\boldsymbol{x}'\|^2}, \tag{1.84}$$

where $\epsilon > 0$ is an infinitesimal positive real quantity added to the imaginary part of the time coordinate[24] when computing the Wightman function to make the integral over $\boldsymbol{k}$ converge. Let us assume that the detector moves along the x^1 axis with constant proper acceleration a. Its world line can be expressed as (see Appendix C)

$$x^0(\tau) = \frac{1}{a}\sinh(a\tau)\,,\ x^1(\tau) = \frac{1}{a}\cosh(a\tau)\,,\ x^2(\tau) = x^3(\tau) = 0\,, \tag{1.85}$$

as illustrated by the hyperbola in Fig. 1.5(a). The correlation function is then

$$\begin{aligned}\mathcal{G}(\tau) &= -\frac{\lambda^2}{4\pi^2}\frac{1}{[x^0(\tau)-x^0(0)-\mathrm{i}\epsilon]^2 - [x^1(\tau)-x^1(0)]^2}\\ &= -\frac{\lambda^2 a^2}{16\pi^2}\sinh^{-2}\left[\frac{a\tau}{2}-\mathrm{i}\epsilon\right]\\ &= -\frac{\lambda^2}{4\pi^2}\sum_{n=-\infty}^{\infty}\frac{1}{(\tau-\mathrm{i}\epsilon-\mathrm{i}2\pi n/a)^2}\,,\end{aligned} \tag{1.86}$$

[23] We drop the index μ for the spacetime coordinates inside function arguments when there is no ambiguity.

[24] This technique is known as an analytic continuation where we extended the domain of the function from the real line to the complex plane. It is customary to keep the $\mathrm{i}\epsilon$ in intermediate calculations (and absorb finite positive quantities into ϵ), and take the limit $\epsilon \to 0^+$ only at the end. Therefore, we are effectively considering the principal value of the integral (as a distribution).

where we used the identity $\sinh^{-2}(z) = \sum_{n\in\mathbb{Z}}(z + in\pi)^{-2}$. The real part of the reservoir correlation spectrum can be obtained via the Fourier transform[25]:

$$\begin{aligned}\gamma(\omega) &= \int_{-\infty}^{\infty} \mathrm{d}\tau \mathrm{e}^{\mathrm{i}\omega\tau}\mathcal{G}(\tau) \\ &= -\frac{\lambda^2}{4\pi^2}\sum_{n=-\infty}^{\infty}\int_{-\infty}^{\infty}\mathrm{d}\tau\frac{\mathrm{e}^{\mathrm{i}\omega\tau}}{(\tau - \mathrm{i}\epsilon - \mathrm{i}2\pi n/a)^2} \\ &= \begin{cases}\lambda^2\dfrac{\omega}{2\pi}\left(\dfrac{1}{\mathrm{e}^{2\pi\omega/a}-1}+1\right), & \omega \geq 0\,; \\ -\lambda^2\dfrac{\omega}{2\pi}\dfrac{1}{\mathrm{e}^{-2\pi\omega/a}-1}, & \omega < 0\,,\end{cases}\end{aligned} \tag{1.87}$$

where the integral is first performed for each k using the residual theorem (and the contour to chose depends on the sign of ω), and then summed over k as a geometric series. Note that we have picked up the Planck factor

$$\bar{n}_\beta(\omega) = \frac{1}{\mathrm{e}^{\beta\hbar\omega}-1}\,,\ \beta = \frac{2\pi c}{\hbar a} \equiv \frac{1}{k_B T_{\mathrm{Unruh}}}\,, \tag{1.88}$$

with the SI units restored. This corresponds to a temperature of

$$T_{\mathrm{Unruh}} = \frac{\hbar a}{2\pi c k_B}\,, \tag{1.89}$$

which is the *Unruh temperature*. Denoting $\gamma \equiv \lambda^2\frac{\Omega}{2\pi}$, $\bar{N} \equiv \bar{n}_\beta(\Omega)$ and using Eq. (1.29), we immediately recover the same master equation (1.35) for the detector, whose steady state is consequently the thermal state at the Unruh temperature. This means that the Minkowski vacuum perceived by the accelerated detector is no longer void of particles, but instead appears to be a thermal bath with temperature proportional to the acceleration. This seems to contradict the conservation of energy at first sight, as one might argue that the reservoir state in any instantaneous inertial frame comoving with the detector should always be vacuum and cannot supply energy to the detector. There is of course no paradox [101]. As the acceleration of the detector must be maintained by an external agent (such as a rocket booster), we are constantly feeding energy into the detector-reservoir system. From the point of view of an inertial observer, the work done by the external agent causes the detector to *emit* particles, which are then absorbed by itself, the net effect being the detection of a thermal spectrum.

Alternatively, the Unruh effect can also be derived in the frame of the accelerated observer, where the positive and negative frequency modes of the quantum field are defined with respect to the observer's proper time instead of the Minkowski coordinate time. The mode operators in different frames are related by a Bogoliubov transformation, where, in particular, the annihilation operator defined in the accelerated frame is a combination of both annihilation and creation operators of the static frame. Therefore, the accelerated observer will in general disagree with an inertial observer on the particle content of a given quantum state, and perceive the Minkowski vacuum to be a thermal state in his/her frame.

[25] Note that $\mathcal{G}(\tau)^* = \mathcal{G}(-\tau)$.

A detailed derivation using quantum field theory in curved spacetimes[26] can be found in textbooks such as [121].

Let us conclude our discussion on the Unruh effect by remarking that the direct observation of the Unruh temperature would require extremely high accelerations. Indeed, one can see from Eq. (1.89) that to achieve a temperature of 1 kelvin via the Unruh effect, the required acceleration would be on the order of 10^{20} m/s^2, which is well beyond experimental reach. Recently, there have been several theoretical proposals to measure the Unruh effect via indirect signatures, such as using Berry's phase [122] or classical electrodynamics [123], which are in principle within reach of current technologies.

IV.4 Hawking radiation

Finally, let us end this chapter with a very brief introduction to Hawking radiation, which is an elegant result that follows naturally from the Unruh effect and the equivalence principle. The spacetime diagram for an eternally accelerated observer with constant proper acceleration a in the Minkowski spacetime is shown in Fig. 1.5, where the world line of the observer is a hyperbola given by Eq. (1.85), with asymptotes $x = \pm t$. As the light cones are at $\pm 45°$ everywhere in this diagram, the observer perceives a *future horizon* as he/she cannot receive any light signal from the region $t \geq x$, and a *past horizon* as no signal sent from the observer can reach the region $t \leq -x$. This situation bears striking similarity with the scenario where an observer hovers at a static position outside a black hole, as depicted in Fig. 1.5(b) for the maximally extended Schwarzschild spacetime in Kruskal-Szekeres coordinates (T, X) where the world line is also a hyperbola with asymptotes $X = \pm T$, and the future horizon $X = T$ is the celebrated event horizon of the black hole. The similarity between the two pictures is in fact *physical*, as formalized by Rindler [124], and can be used to derive the temperature of Hawking radiation from a black hole.

The spacetime outside a chargeless and spinless black hole can be described in the Schwarzschild coordinates (t, r, θ, ϕ), and the metric is given by[27] [113, 125]

$$\mathrm{d}s^2 \equiv g_{\mu\nu}\mathrm{d}x^\mu \mathrm{d}x^\nu = \left(1 - \frac{2GM}{r}\right)\mathrm{d}t^2 - \left(1 - \frac{2GM}{r}\right)^{-1}\mathrm{d}r^2 - r^2(\mathrm{d}\theta^2 + \sin^2\theta \mathrm{d}\phi^2)\,, \quad (1.90)$$

where M is the mass and G is the gravitational constant, and the event horizon is located at the Schwarzschild radius $r_S \equiv 2GM$. For an observer with constant spatial coordinates at (r, θ, ϕ), one can show via elementary calculations in general relativity that he/she experiences a constant proper acceleration with magnitude[28]

$$a(r) = \frac{GM}{r^2\sqrt{1 - \dfrac{2GM}{r}}}\,. \quad (1.91)$$

[26] Note that the spacetime in the frame of the accelerated observer is still flat with zero curvature, as it is just the flat Minkowski spacetime written in different coordinates.

[27] Note that we are using the $(+, -, -, -)$ signature.

[28] If we plug in the mass and the radius of the earth for M and r respectively we find the gravitational acceleration $a \simeq 9.8\mathrm{m/s}^2$ that we experience every day. This is because the coordinates are chosen to reduce to the usual spherical coordinates where/when the spacetime is approximately flat.

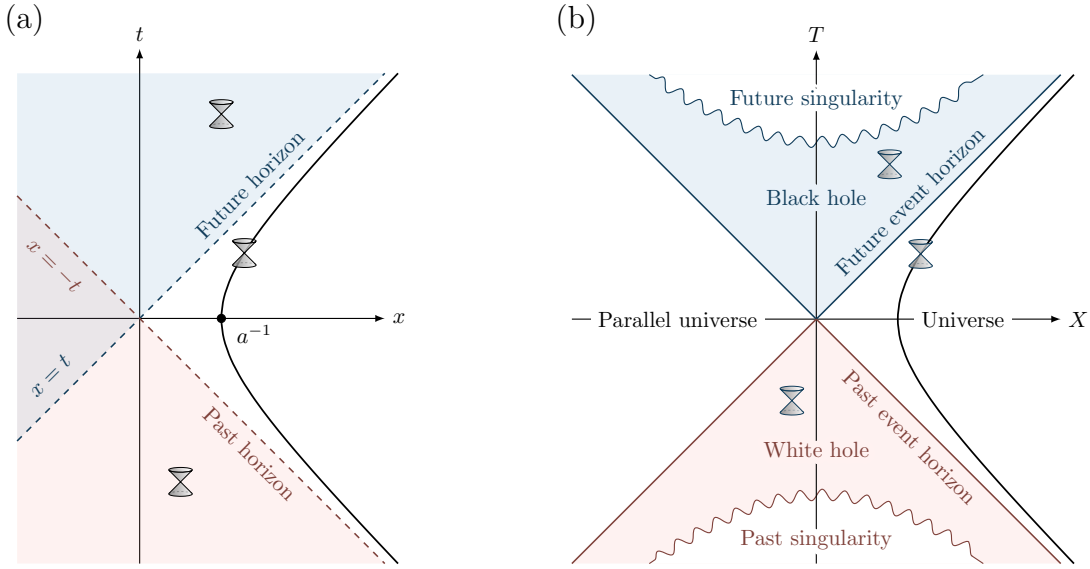

Figure 1.5: Spacetime diagram for (a) an observer with constant proper acceleration in Minkowski spacetime, and (b) a static observer outside a Schwarzschild black hole (in Kruskal–Szekeres coordinates), which also has constant proper acceleration. In both diagrams, light cones are at ±45 degrees everywhere, and the world line of the observer is a hyperbola. The observer perceives a horizon (unidirectional membrane beyond which no signal can be sent to / received from the observer) in both scenarios.

Indeed, one needs to constantly accelerate (such as by firing a rocket booster or hanging on a rope) to resist the gravitational pull of the black hole and hover at a static position. This quantity diverges to infinity[29] as $r \to r_S^+$, such that at scales set by $a^{-1} \ll r_S$, the spacetime looks locally flat close to the horizon [121, 124]. Assuming that the state of a scalar quantum field looks like the Minkowski vacuum (free of excitations) in any free-falling (i.e., inertial) frame close to the horizon, we can then deduce using the equivalence principle that the observer at $r \to r_S^+$ experiences an Unruh temperature of

$$T_{\text{Unruh}}(r) = \frac{a(r)}{2\pi} \,. \tag{1.92}$$

This thermal radiation propagates to infinity with a redshift factor [121]

$$V(r) \equiv \frac{\sqrt{g_{tt}(r)}}{\sqrt{g_{tt}(\infty)}} = \sqrt{1 - \frac{2GM}{r}} \,, \tag{1.93}$$

where g_{tt} is the coefficient of $\mathrm{d}t^2$ in the metric (1.90). The temperature of the radiation perceived by a static observer at infinity is therefore (restoring the SI units)

$$T_{\text{Hawking}} = \lim_{r \to r_S^+} V(r) T_{\text{Unruh}}(r) = \frac{1}{2\pi} \times \frac{GM}{r_S^2} = \frac{\hbar c^3}{8\pi k_B GM} \,, \tag{1.94}$$

[29] This implies that it is impossible to hover anything massive on (or beyond) the black hole horizon.

which is known as the *Hawking temperature*. This predicts that the black hole's horizon emits a blackbody radiation at temperature T_{Hawking}, which is therefore expected to consume the black hole's mass and cause *black hole evaporation*. Again, these theorized phenomena are extremely hard, if not impossible, to detect directly. For a black hole with the same initial mass as the sun, the Hawking temperature would be around merely 60 nanokelvins, which is much fainter than the cosmic microwave background radiation which is at 2.7 K. The inverse proportionality to the mass in Eq (1.94) suggests that one could have better chances of detecting Hawking radiation with micro black holes [126, 127], yet there has not been direct experimental evidence to date. Interestingly, analog (acoustic) black holes have been successfully implemented with Bose-Einstein condensates in exciton-polariton platforms [128] (that we have introduced in Sec. III) as well as other systems [129–131], where the equivalent of Hawking radiation can be experimentally observed.

V Conclusion

In this chapter, we have reviewed the general concepts in quantum optics that the remainder of this manuscript is based upon. Starting from the Maxwell equations, we performed the quantization of the electromagnetic field, which allows for a quantum description of cavity resonators. We then introduced the model for light-matter interactions in the static regime, and derived the driven-dissipative dynamics for nonlinear photonic cavities, which are the systems studied in Chapters 2 to 4. Finally, we discussed the light-matter interaction model in the noninertial (relativistic) regime with the pedagogic example of the Unruh effect (and Hawking radiation), setting the ground for our study of relativistic reservoir computing in Chapter 5.

2 Dissipative phase transition of light

In this chapter, we will investigate critical phenomena in optical systems, as a result of the collective behavior of interacting photons in a many-body context. In particular, we will be interested in the role of spatial dimensionality in determining the presence of phase transitions in photonic systems. The considered physical system is a planar semiconductor microcavity in the strong light-matter coupling regime, where polariton excitations are injected by a quasi-resonant optical driving field. As shown in the previous chapter, this system can be regarded as the continuous limit of a driven-dissipative Bose-Hubbard lattice considered in many previous theoretical works. We propose a technique for tuning the spatial dimension of the system, where the geometry is controlled by designing the intensity profile of the driving field. We investigate the emergence of criticality by increasing the spatial size of the driven region, which approaches the thermodynamic limit in the present context. We show that no phase transition occurs using a 1D driving geometry, while for a 2D configuration we do observe the emergence of a first-order phase transition. The demonstrated technique allows all-optical and *in-situ* control of the system geometry, providing a versatile platform for exploring the many-body physics of photons.

This chapter is structured as follows. We will introduce the context and general theory of dissipative phase transitions in Sec. I. Then, in Sec. II we will set the ground for discussing the first-order dissipative phase transitions in photonic system with the pedagogic example of a single-mode Kerr resonator. Sec. III introduces the technique we propose for probing the role of dimensionality in dissipative phase transitions of continuous photonic system, where we describe in detail our theoretical model and the experiments performed by the group of A. Bramati at *Laboratoire Kastler Brossel* confirming our theoretical predictions. The original results of our study are presented in Sec. IV. Finally, we conclude this chapter in Sec. V.

I Introduction

The study of phase transitions and critical phenomena is at the heart of condensed matter physics and material science [132]. A *phase* refers to a state of matter with essentially uniform physical properties throughout the material, and *phase transitions* are abrupt changes of the state of matter under the modification of certain external parameters. One of the most well known examples might be the transition of water (under atmospheric

pressure) from solid ice[1] to liquid and to vapor, when the temperatures is increased. Such abrupt changes can be modeled as nonanalytical behavior of the system state as a function of the external parameters. For a physical system with finite number N of degrees of freedom, the dependence of the state is usually smooth on parameters such as the temperature, such that no phase transition can occur. However, in the *thermodynamic limit* where $N \to \infty$, one can expect nonanalytical dependence (such as a cusp) to emerge. Indeed, phases transitions are collective phenomena in the organization of complex physical systems, that bear striking similarity to collective behavior found in biological swarms [134] and even in our social dynamics [135, 136], all of which being vivid manifestations of *more is different* [137].

I.1 Phase transitions in different regimes

Phase transitions are present in different regimes of physics, while the mechanism behind can be dramatically different, as summarized in Table 2.1. For systems in thermal equilibrium at finite temperature T, the state $\hat{\rho}$ of a system with Hamiltonian $\hat{H}$ minimizes the free energy

$$F(\hat{\rho}) \equiv \langle \hat{H} \rangle_{\hat{\rho}} - TS(\hat{\rho}) \,, \tag{2.1}$$

where S denotes the entropy. *Thermal phase transitions* in such systems are then driven by thermal fluctuations due to the competition between the energy and the entropy. Such systems are commonly referred to as "classical" since one assumes that the thermal fluctuations completely dominate over the quantum ones, i.e. $k_B T \gg \hbar\omega$, with ω the characteristic frequency scale of the system. In the opposite limit where $T \to 0$, the entropy plays no more role and the state minimizing the energy is consequently the ground state of the Hamiltonian, which can be a function of some other parameter than the temperature, such as an external field applied to the system. When the ground state depends non-analytically on the external parameter, this is referred as a *quantum phase transition*, which is driven by quantum fluctuations due to the Heisenberg uncertainty principle (i.e. the competition of noncommuting terms in the Hamiltonian) [138]. One spectacular example of quantum phase transition is the superconductor-insulator transition [139] that occurs to certain materials close to the absolute zero temperature.

On the other hand, open quantum systems subject to driving and dissipation can exhibit dissipative phase transitions for the non-equilibrium steady state, where the physics is decided by the rich interplay between the Hamiltonian evolution, dissipation-induced fluctuations and driving. Driven-dissipative phase transitions have been theoretically studied for various systems, such as photonic resonators [107, 140–152], exciton-polariton condensates [153–156], and spin systems [42, 157–163]. Experimental investigations have studied dissipative phase transitions in single-mode semiconductor microcavity pillars [108] and superconducting resonators [164, 165]. In this chapter, we will be focusing on dissipative phase transitions in the non-equilibrium steady state of photonic systems.

[1] A less well-known example might be the fact that there are more than 10 different phases of water ice, and new ones are still being discovered [133].

	Thermal phase transition (finite temperature T)	Quantum phase transition ($T = 0$)	Dissipative phase transition (non-equilibrium)
System operator	Hamiltonian $\hat{H}$	Hamiltonian $\hat{H}$	Liouvillian $\mathcal{L}$
Relevant quantity	Free energy $F(\hat{\rho}) = \langle \hat{H} \rangle_{\hat{\rho}} - TS(\hat{\rho})$	Eigenvalues of $\hat{H}$ $E: \ \hat{H}\|\psi\rangle = E\|\psi\rangle$	Eigenvalues of $\mathcal{L}$ $\lambda: \ \mathcal{L}(\hat{\rho}) = \lambda\rho$
Relevant state	Thermal state, minimising F	Ground state, minimising E	Steady state, $\mathcal{L}(\hat{\rho}) = 0$
Phase transition	Nonanalyticity in the Thermal state	Nonanalyticity in the ground state	Nonanalyticity in the steady state

Table 2.1: Comparison between the thermal phase transition, the quantum phase transition and the dissipative phase transition. Adapted from [42].

I.2 Phase transitions in driven-dissipative open quantum systems

The dynamics of an open quantum system can be modeled by the Lindblad master equation (1.31)

$$\frac{\mathrm{d}}{\mathrm{d}t}\hat{\rho} = \mathcal{L}\hat{\rho}\,, \tag{2.2}$$

where $\mathcal{L}$ is the Liouvillian superoperator that generates the time evolution, which we assume to be independent of time[2]. The full information on the system dynamics is contained in the spectrum of the Liouvillian $\{\lambda_j, \hat{\rho}_j\}_j$, where $\hat{\rho}_j$ is the right eigenmatrix of the superoperator $\mathcal{L}$ with eigenvalue λ_j, i.e.

$$\mathcal{L}\hat{\rho}_j = \lambda_j \hat{\rho}_j\,, \tag{2.3}$$

with $\mathrm{Re}[\lambda_j] \leq 0$, $\forall j$ [168] and it is customary to order the eigenvalues by increasing absolute value of the real part $|\mathrm{Re}[\lambda_0]| < |\mathrm{Re}[\lambda_1]| < \cdots$. Under quite general conditions, the Liouvillian admits a unique steady state

$$\mathcal{L}\hat{\rho}_{\mathrm{SS}} = 0\,, \mathrm{Tr}[\hat{\rho}_{\mathrm{SS}}] = 1\,, \tag{2.4}$$

which is a right eigenmatrix associated to $\lambda_0 = 0$, and the eigenmatrices with $\mathrm{Re}[\lambda_j] \neq 0$ are all traceless [168]. Similarly, one can also define the left eigenmatrices of the Liouvillian via the relation $\mathcal{L}^\dagger \hat{\sigma}_j = \lambda_j^* \hat{\sigma}_j$ with the normalization $\mathrm{Tr}[\hat{\sigma}_j^\dagger \hat{\rho}_k] = \delta_{jk}$. Assuming that the eigenmatrices $\{\hat{\rho}_j\}_j$ form a complete basis for the operator space, the time evolution of

[2] This can be achieved in typical quantum optical models with periodic drive when we adopt the rotating wave approximation and transform into an appropriate frame. Even if the rotating wave approximation does not apply, one could still make the generator time-independent via the Floquet approach [166, 167] and consider the dynamics in an extended Hilbert space.

any initial density matrix $\hat{\rho}(0)$ can be accessed via the unique decomposition

$$\begin{aligned}\hat{\rho}(0) &= \hat{\rho}_{\mathrm{SS}} + \sum_{j\geq 1} c_j \hat{\rho}_j \,, \\ \hat{\rho}(t) &= \mathrm{e}^{\mathcal{L}t}\hat{\rho}(0) \\ &= \hat{\rho}_{\mathrm{SS}} + \sum_{j\geq 1} c_j \mathrm{e}^{\lambda_j t}\hat{\rho}_j \,,\end{aligned} \tag{2.5}$$

with $c_j = \mathrm{Tr}[\hat{\sigma}_j^\dagger \hat{\rho}(0)]$. It is then clear that the long-time behavior is governed by the *Liouvillian gap* defined as $\lambda \equiv |\mathrm{Re}[\lambda_1]|$, also known as the asymptotic decay rate [42], since it gives the slowest relaxation rate towards the steady state[3]:

$$\hat{\rho}(t \to \infty) \simeq \hat{\rho}_{\mathrm{SS}} + c_1 \mathrm{e}^{-\lambda t}\hat{\rho}_1 \,. \tag{2.6}$$

As a dissipative phase transition in the steady state is characterized by the nonanalytical behavior of $\hat{\rho}_{\mathrm{SS}}$, which is associated to the eigenvalue λ_0, it is therefore necessary to have a level crossing in the Liouvillian spectrum for the phase transition to occur [169], which corresponds to the closure of the Liouvillian gap $\lambda \to 0$. This implies via Eq. (2.6) that the time required to relax towards the steady state would diverge to infinity when the gap closes, which is known as the *critical slowing down* and can result in metastable states.

Formally, for a system admitting a thermodynamic limit $N \to \infty$, a dissipative phase transition of order M can be characterized by the nonanalytical behavior of some observable $\hat{O}$ when an external parameter ξ approaches the critical value ξ_c, and the order is the smallest integer M such that [168]

$$\lim_{\xi\to\xi_c} \left| \frac{\partial^M}{\partial \xi^M} \lim_{N\to\infty} \mathrm{Tr}[\hat{\rho}_{\mathrm{SS}}(\xi, N)\hat{O}] \right| = \infty \,. \tag{2.7}$$

II Dissipative phase transitions in photonic systems

Let us focus on first-order dissipative phase transitions in photonic systems from now on. In terms of the definition (2.7), the observable $\hat{O}$ can be chosen as the photon population, the parameter ξ is the drive applied to the system, and the thermodynamic limit $N \to \infty$ will be explained later. A first-order ($M = 1$) transition then means a discontinuity in the population as a function of the drive, since its first derivative diverges according to the definition. We will first illustrate this phenomenon in the pedagogic example of a single-mode Kerr cavity and then show its natural relation with the driven-dissipative Bose-Hubbard lattice.

[3]This expression assumes no degeneracy in the real part of the first nonzero eigenvalue. In the degenerate case, λ_1 may have an imaginary part resulting in oscillations of $\hat{\rho}(t)$ [168], which will be eventually washed out due to the damping by the negative real part. Therefore, the long-term relaxation rate is still λ in the presence of degeneracy.

II.1 Single-mode Kerr cavity

Let us consider again the driven-dissipative Kerr model introduced in Sec. III.2 of the previous chapter, with the master equation (1.52) that we copy below for convenience:

$$\begin{aligned} \hat{H}/\hbar &= -\Delta \hat{a}^\dagger \hat{a} + \frac{U}{2}\hat{a}^{\dagger 2}\hat{a}^2 + F^* \hat{a} + F\hat{a}^\dagger \,, \\ \frac{\mathrm{d}}{\mathrm{d}t}\hat{\rho} &= \mathcal{L}\hat{\rho} = -\frac{\mathrm{i}}{\hbar}[\hat{H}, \hat{\rho}] + \gamma \mathcal{D}[\hat{a}]\hat{\rho} \,, \end{aligned} \tag{2.8}$$

where we assume $U > 0$. For reasons that will become clear in the next section (II.2), we introduce a dimensionless parameter N such that

$$U = \frac{U_0}{N} \,, \quad F = \sqrt{N} F_0 \,, \tag{2.9}$$

and the thermodynamic limit for this system will be defined as $N \to \infty$. Note that this scaling increases the drive and weakens the nonlinearity while keeping UF^2 constant, and therefore this thermodynamic limit can be understood as the limit of infinite number of photons in the cavity. This also implies that the mean-field solution of the rescaled steady-state population $\langle \hat{a}^\dagger \hat{a} \rangle_{\mathrm{SS}}/N$ as a function of F_0 will be independent of N. In particular, the mean-field theory always predicts bistable solutions in the regime of $\Delta > \sqrt{3}\gamma/2$, as shown by the dashed line in Fig. 2.1(a). The exact solution to the master equation is also shown for different values of the scaling parameter N in the same plot. Note that the exact steady-state is unique for each value of F even in the bistable regime predicted by mean-field theory. The population $\langle \hat{a}^\dagger \hat{a} \rangle_{\mathrm{SS}}/N$ exhibits a crossover from the lower branch to the higher one, with the slope increasing with N, which implies the emergence of a first-order phase transition in the limit $N \to \infty$. This observation is consistent with the behavior of the Liouvillian gap λ presented in Fig. 2.1(b), obtained by exact diagonalization of the Liouvillian $\mathcal{L}$. The gap shows a dip for driving values close to the crossover $|F|^2 \simeq 9\gamma^2$, which lowers as N increases. This implies the closure of the gap in the thermodynamic limit $N \to \infty$ at the critical driving value, and that the relaxation time from some initial state towards the steady state diverges. In practice, this means that if the system is prepared in a low- (high-) population state with the driving just above (below) the critical value, the state is metastable and will remain stuck for a time on the order of $1/\lambda$ before relaxing to the steady state, which explains the optical bistability or hysteresis observed in actual experiments with finite duration [108].

II.2 Bose-Hubbard lattice

The thermodynamic limit defined via the scaling (2.9) may seem artificial at first sight, but it is in fact closely related to the usual thermodynamic limit of a Bose-Hubbard lattice with N sites [145]. Consider a D-dimensional hypercubic lattice of driven-dissipative Kerr resonators with nearest-neighbor coupling and periodic boundary conditions, whose Hamiltonian is given by Eq. (1.68):

$$\hat{H}/\hbar = \sum_j \left[-\Delta \hat{a}_j^\dagger \hat{a}_j + \frac{U}{2}\hat{a}_j^{\dagger 2}\hat{a}_j^2 + F^* \hat{a}_j + F\hat{a}_j^\dagger \right] - J \sum_{\langle j,j' \rangle} \hat{a}_j^\dagger \hat{a}_{j'} \,, \tag{2.10}$$

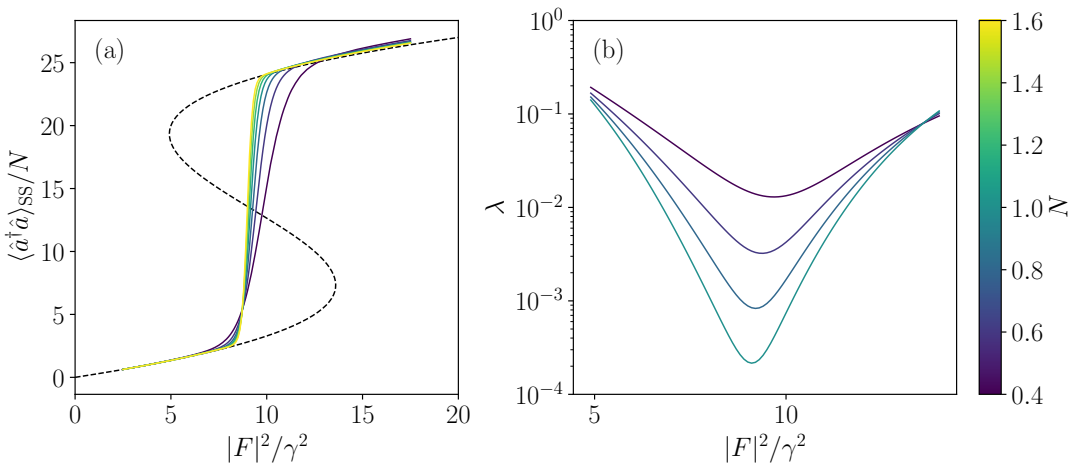

Figure 2.1: (a) Rescaled steady-state population $\langle \hat{a}^\dagger \hat{a} \rangle_{\rm SS}/N$ from the exact solution of the master equation (solid lines) and the mean-field solution (dashed line) and (b) the Liouvillian gap λ of the driven-dissipative Kerr cavity as a function of the drive intensity $|F|^2$, for different values of the scaling parameter N (see colorbar). The exact solution is unique as opposed to the bistability predicted by mean-field theory. As N increases, a first-order phase transition emerges, accompanied by the closure of the Liouvillian gap at the critical driving intensity. Parameters: $\Delta = 2\gamma (> \sqrt{3}\gamma/2)$ and $U = 0.1\gamma$.

which we have rewritten in the rotating frame assuming a single-tone constant drive that uniformly addresses all sites, with the dissipator (1.70):

$$\mathcal{D}\hat{\rho} = \frac{\gamma}{2} \sum_j \Big(2\hat{a}_j \hat{\rho} \hat{a}_j^\dagger - \big\{ \hat{a}_j^\dagger \hat{a}_j, \hat{\rho} \big\} \Big) = \gamma \sum_j \mathcal{D}[\hat{a}_j]\hat{\rho} \,. \tag{2.11}$$

To reveal the connection with the single-cavity model, let us consider the lattice in the momentum space via the discrete Fourier transform on the operators:

$$\hat{a}_{\boldsymbol{k}} = \frac{1}{\sqrt{N}} \sum_j \mathrm{e}^{-\mathrm{i}\boldsymbol{k}\cdot\boldsymbol{r}_j} \hat{a}_j \,, \quad \hat{a}_j = \frac{1}{\sqrt{N}} \sum_{\boldsymbol{k}} \mathrm{e}^{\mathrm{i}\boldsymbol{k}\cdot\boldsymbol{r}_j} \hat{a}_{\boldsymbol{k}} \,, \tag{2.12}$$

where the quasimomentum $\boldsymbol{k} \equiv (k_1, k_2, \cdots, k_d, \cdots, k_D)$ takes values on the D-dimensional reciprocal lattice and $\boldsymbol{r}_j$ is the position of the j-th site. The Hamiltonian becomes

$$\begin{aligned} \hat{H}/\hbar = &- \sum_{\boldsymbol{k}} \left(\Delta + 2J \sum_{d=1}^{D} \cos(k_d a) \right) \hat{a}_{\boldsymbol{k}}^\dagger \hat{a}_{\boldsymbol{k}} \\ &+ \frac{U}{2N} \sum_{\boldsymbol{k},\boldsymbol{p},\boldsymbol{q}} \hat{a}_{\boldsymbol{k}}^\dagger \hat{a}_{\boldsymbol{p}}^\dagger \hat{a}_{\boldsymbol{q}} \hat{a}_{\boldsymbol{k}+\boldsymbol{p}-\boldsymbol{q}} \\ &+ \sqrt{N}(F^* \hat{a}_{\boldsymbol{0}} + F \hat{a}_{\boldsymbol{0}}^\dagger) \,, \end{aligned} \tag{2.13}$$

where a is the lattice constant. The dissipator remains local in the momentum space:

$$\mathcal{D}\hat{\rho} = \gamma \sum_{\boldsymbol{k}} \mathcal{D}[\hat{a}_{\boldsymbol{k}}]\hat{\rho} \,. \tag{2.14}$$

We notice that since the drive is uniform in the position representation, only the $\boldsymbol{k} = \mathbf{0}$ mode is driven, while all $\boldsymbol{k}$ modes are equally dissipated. As a rough approximation, we can assume that the excitations in all the $\boldsymbol{k} \neq \mathbf{0}$ modes (due to coupling to the $\boldsymbol{k} = \mathbf{0}$ via the four-wave scattering term) are negligible and keep only the $\boldsymbol{k} = \mathbf{0}$ terms in the model. This results in the single-mode Hamiltonian

$$\hat{H}/\hbar = -\Delta_{\mathbf{0}}\hat{a}^\dagger_{\mathbf{0}}\hat{a}_{\mathbf{0}} + \frac{U}{2N}\hat{a}^{\dagger 2}_{\mathbf{0}}\hat{a}^2_{\mathbf{0}} + \sqrt{N}(F^*\hat{a}_{\mathbf{0}} + F\hat{a}^\dagger_{\mathbf{0}})\,, \tag{2.15}$$

where $\Delta_{\mathbf{0}} \equiv \Delta + zJ$ is the detuning with respect to the $\boldsymbol{k} = \mathbf{0}$ mode, with $z = 2D$ the coordination number. We have therefore recovered the scaling (2.9) defined previously, and the quantity $\langle \hat{a}^\dagger_{\mathbf{0}}\hat{a}_{\mathbf{0}}\rangle/N$ can be interpreted as an approximation for the population density on the lattice. The thermodynamic limit $N \to \infty$ then naturally signifies the limit of infinitely large lattice.

Role of dimensionality

The naïve single-mode approximation above suggests that a first-order dissipative phase transition (as discussed in Sec. II.1) may take place in the Bose-Hubbard lattice as well. While this argument seems valid for high dimensions where one expects the fluctuations in $\boldsymbol{k} \neq \mathbf{0}$ modes to be suppressed, there is no guarantee that these fluctuations will not deplete the criticality in systems of low dimensionality. Indeed, the emergence of a phase transition can be drastically affected by the spatial dimensionality of the system in general [138]. Recent theoretical works on the driven-dissipative Bose-Hubbard lattice [147, 152] predicted that a first-order dissipative phase transition emerges in two-dimensional (2D) lattices (with periodic boundary conditions), while in 1D chains there is no critical phenomenon. Their results show that while the $\boldsymbol{k} = \mathbf{0}$ mode is dominant in population, local fluctuations in low dimension (1D) are significant enough to destroy the criticality.

In what follows, we propose a technique for probing the emergence of this first-order phase transition as a function of the spatial dimension in a continuous photonic system, and show the experiments performed by our collaborators which confirm our predictions.

III Technique for probing a dimension-dependent phase transition in a continuous photonic system

Let us explore the role of spatial dimension for a dissipative phase transition using a planar semiconductor microcavity, where polariton excitations are injected via quasi-resonant driving. As illustrated in Sec. III.3 of the previous chapter, this system can be regarded as the continuous limit of the Bose-Hubbard lattice considered in the recent theoretical works [147, 152]. We propose theoretically an all-optical way to enforce the dimensionality via the spatial shape of the driving beam. In particular, we consider a top-hat spot with constant driving intensity. The shape of the spot can be tailored *in-situ* to create a 2D or 1D geometry[4]. This scheme also features "diffusive" boundary conditions, since the

[4]In principle, one could also use etching techniques, that may lead to better defined structures, to study the effect of spatial dimension on dissipative phase transitions. However, the present all-optical

polaritons can diffuse away from the driven region. While increasing the spatial size of the spot, which is the thermodynamic limit in the present context, we show in the next section (IV) that a first-order phase transition occurs using a 2D geometry, while it disappears in the 1D configuration. This technique has been experimentally implemented by the group of A. Bramati [*Laboratoire Kastler Brossel (LKB), Sorbonne Université*], providing the first experimental demonstration of the role of dimensionality in driven-dissipative phase transitions of photonic systems.

III.1 Theoretical model

Consider a planar semiconductor microcavity in the strong light-matter coupling regime, where polariton excitations are coherently injected by a quasi-resonant optical drive. As introduced in Sec. III.3 of the previous chapter, the system dynamics can be described in terms of the lower polariton field $\hat{\psi}(\boldsymbol{r})$, where $\boldsymbol{r} = (x, y)$ are in-plane coordinates parallel to the cavity mirrors. Within the mean-field approximation, the time evolution of $\psi(\boldsymbol{r}) \equiv \langle\hat{\psi}(\boldsymbol{r})\rangle$ in the frame rotating at the driving frequency ω_d can be described by the driven-dissipative Gross-Pitaevskii equation (1.65) [39]:

$$\mathrm{i}\frac{\partial}{\partial t}\psi(\boldsymbol{r},t) = \left(-\Delta - \frac{\hbar}{2m}\nabla^2\right)\psi(\boldsymbol{r},t) + g|\psi(\boldsymbol{r},t)|^2\psi(\boldsymbol{r},t) - \mathrm{i}\frac{\gamma}{2}\psi(\boldsymbol{r},t) + \mathcal{F}(\boldsymbol{r})\,, \tag{2.16}$$

where $\Delta = \omega_d - \omega_{\mathrm{LP}}^{k=0}$ is the detuning of the drive with respect to the $k = 0$ mode of the lower polariton branch, m is the lower-polariton effective mass, g is the polariton-polariton interaction constant, γ is the lower-polariton decay rate and $\mathcal{F}(\boldsymbol{r})$ encodes the amplitude and spatial shape of the coherent drive.

In the following, We adopt a top-hat driving scheme [see Fig. 2.2(c)], where the amplitude $\mathcal{F}(\boldsymbol{r})$ is defined by

$$\mathcal{F}(\boldsymbol{r}) = F\mathbb{1}_A(\boldsymbol{r}), \tag{2.17}$$

where $\mathbb{1}_A$ is the indicator function of a compact region A of the plane, such that the drive is constant within the region A and zero elsewhere. To force a 1D geometry, the driving region will be chosen as an elliptical spot with fixed minor axis b and variable major axis $l \gg b$. To induce a 2D geometry, instead, the driving region will be chosen as a circular disk of variable diameter l. The only difference between the 1D and 2D configurations is the spatial shape of the top-hat drive, while the planar microcavity sample is the same. Note that the way we distinguish 1D and 2D is not via the absolute size of the top-hat spot, but the different ways they approach the thermodynamic limit: in 1D only the major axis l increases with b fixed, such that in the thermodynamic limit $\lim_{l\to\infty} b/l = 0$, whereas in 2D both axes increase at the same rate, keeping the spot always circular and its aspect ratio constant. The boundary conditions in terms of the driven region are therefore of diffusive nature, which means that the polaritons can freely diffuse and decay out of the driving spot.

In order to probe a dissipative phase transition with respect to the driving intensity $I = |F|^2$, we will be interested in the steady-state polariton density averaged over a disk

approach provides flexibility and can be used to explore the effect of a gradual change of dimensionality *in situ* using the same sample.

D of diameter l_D at the center of the driven region:

$$n_D^{\mathrm{SS}} = \frac{1}{\mu(D)} \int_D \mathrm{d}^2\boldsymbol{r} |\psi_{\mathrm{SS}}(\boldsymbol{r})|^2, \tag{2.18}$$

where $\mu(D)$ denotes the area of the disk D and ψ_{SS} is the steady-state field such that $\partial_t \psi_{\mathrm{SS}} = 0$. In the thermodynamic limit of $l \to \infty$, a transition between two phases is characterized by the non-analytical behavior of n_D^{SS} when I tends to some critical value I_c. As defined in Eq. (2.7), a transition of order M in our specific case can be described as [168]

$$\lim_{I \to I_c} \left| \frac{\partial^M}{\partial I^M} \lim_{l \to \infty} n_D^{\mathrm{SS}} \right| = +\infty. \tag{2.19}$$

In this study, we will present a first order ($M = 1$) phase transition, that is a discontinuity of steady-state polariton density n_D^{SS} with respect to the drive intensity I, which are the two quantities that we measure in our experiments.

III.2 Experimental setup

The sample used in the experiments performed by our collaborators at LKB is a 2λ GaAs high-finesse semiconductor microcavity cooled to the temperature of 4K in an open-flow helium cryostat. The cavity embeds three $\mathrm{In_{0.04}Ga_{0.96}As}$ quantum wells (QWs) between a pair of distributed Bragg mirrors made of 21 (top) and 24 (bottom) alternated layers of GaAs/AlAs. Each QW is located on an antinode of the cavity electromagnetic field to have a strong coupling of QW excitons to the cavity photons, giving rise to the exciton-polariton modes. The cavity spacer has a small wedge ($\hbar w \simeq 0.7$ µeV/µm) whereby the photon-exciton detuning can be finely adjusted to around 0 meV by changing the excitation position. At this detuning the lower polariton branch has an effective mass $m = 5.7 \times 10^{-5} m_{\mathrm{e}}$, where m_{e} is the bare electron mass. The Rabi frequency, the lower-polariton decay rate and the polariton-polariton interaction constant are respectively measured to be $\hbar\Omega_R = 5.1$ meV, $\hbar\gamma = 0.08$ meV, and $\hbar g = 0.01$ meV·µm^2. The drive detuning is fixed at $\Delta = \gamma$ with respect to the bottom of the lower polariton branch. This implies that the Rabi frequency $\hbar\Omega_R$, which determines the minimum splitting between the lower and upper polariton branches, is much larger than all the other energy scales in the problem. We can therefore consider effectively only the lower polariton in our theoretical treatment [39].

The polaritons are excited by a circularly polarized continuous-wave Ti:Sapphire laser whose output Gaussian mode is reshaped with a spatial light modulator (SLM) (Fig. 2.2). The SLM liquid crystal matrix plane is imaged on that of the cavity and contains a blazed grating of tunable contrast, which diffracts in the first order a fraction of the driving field intensity. The first order component is sent at normal incidence through the cavity, while the non-diffracted part (zero order) is blocked in the Fourier plane with a slit [Fig. 2.2(a)]. The intensity distribution between the zero and the first order components is modified by locally adjusting the grating contrast. In this way, with a well-calibrated anti-Gaussian contrast gradient — minimum at the center and maximum at the edge of the spot — a flat top-hat intensity profile is produced in the first order component. Then, by adding

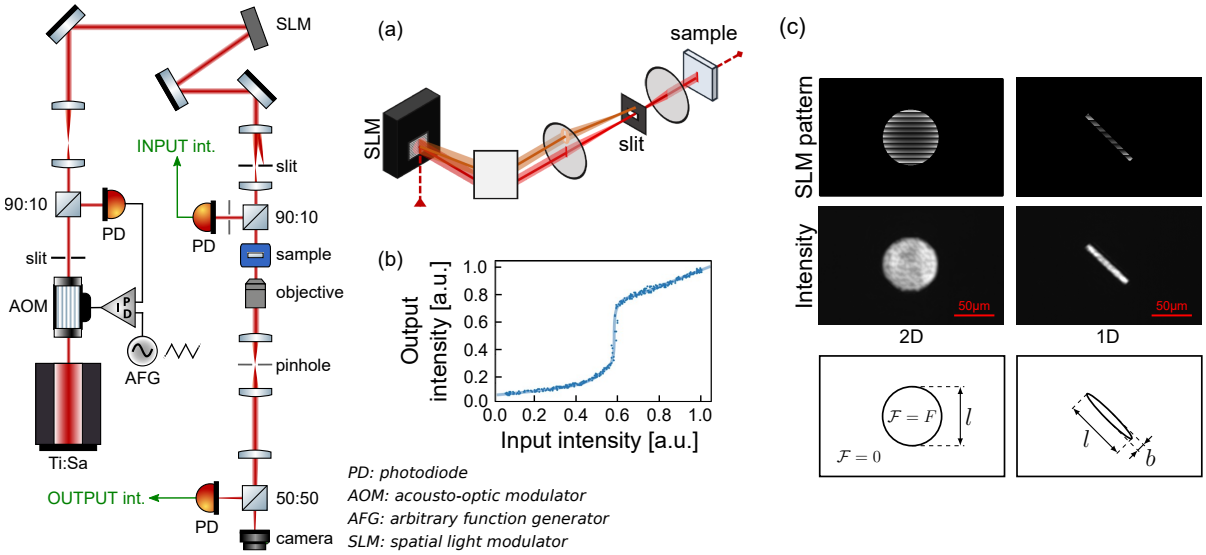

Figure 2.2: Sketch of the experimental setup by the group of A. Bramati at LKB [γ]. The laser is slaved using a proportional–integral–derivative (PID) controller, an arbitrary function generator (AFG) and an acousto-optic modulator (AOM) loop to produce a power ramp; its intensity profile is reshaped using a spatial light modulator (SLM). Two photodiodes (PD) measure the power inside disks of diameter $l_D = 5\mu m$ at the center of the beams at the sample input and output. (a) Pump intensity profile shaping method: the light (dark) beam represents the zero (first) order of the diffracted beam from the SLM. (b) Output intensity from the sample as a function of the input intensity, plotted for a pump detuning of $\Delta = \gamma$ and a 2D top-hat drive of diameter $l = 30\mu m$. (c) SLM phase pattern (upper) for obtaining 2D (left) and 1D (right) flat-top beam profiles (middle) of different sizes and intensities (bottom).

a non-diffracting mask over the grating, one can select which area of the beam profile is reflected into the first order component. Thus, the shape of the driving spot in the cavity reproduces the one defined by the contours of the mask [Fig. 2.2(c)]. With this reshaping method, a 2D circular driving spot or a 1D elliptical one can be achieved by configuring the SLM with a blazed grating masked by a circular aperture or by a narrow slit respectively (see Fig. 2.2). In the following, the spot sizes in the cavity plane are tuned by changing the mask dimension. For the 1D geometry, the minor axis of intensity profile is set at $b = 6.4\mu\text{m}$. This value is chosen such that it is large compared to the optical wavelength of the laser to avoid undesirable diffraction effects so as to produce a well-defined top-hat. At the same time, it is small enough to ensure that the crossover slope of the steady-state polariton density as a function of the drive for the smallest top-hat is mild enough to be measured experimentally, which allows us to study the asymptotic behavior (convergence or divergence) of the growing slope.

In order to probe the phase transition, an acousto-optic modulator (AOM) modulates the driving field power with a low-frequency ramp (200 Hz) of sufficient amplitude to be able to scan a wide range of polariton density. The input and output intensities of the cavity are measured using two photodiodes which detect through pinholes (of diameter $l_D = 5\mu\text{m}$) at the center of the driving spot. Note that as the probing disk D is placed concentrically with the top-hat profile, the chosen value ensures that it is always contained within the driven region. However, we expect that asymptotically (in the limit of large l), the observed effects should not depend on its specific position as long as the probing disk is far enough from the boundary (or the edges of the major axis in the 1D case) of the top-hat. The polariton density is then directly observed as a function of the driving intensity by plotting, one with respect to the other, the powers detected by the two photodiodes [see Fig. 2.2(b)].

III.3 Numerical methods

The mean-field equation (2.16) is a partial differential equation, which typically requires certain kind of discretization to be solved numerically. We performed a finite-difference discretization and verified the convergence in terms of both the discretization step size and the size of the simulated system. In the case of the 2D configuration, a further simplification can be made exploiting the symmetry of the system.

Driven-dissipative dynamics in polar coordinates

In the configuration where a 2D round top-hat is applied, we can efficiently simulate the mean-field equation by adopting the polar coordinates and taking advantage of the cylindrical symmetry of the problem. The Laplacian of a scalar field ϕ in polar coordinates (r, θ) can be written as

$$\nabla^2\phi = \partial_r^2\phi + \frac{1}{r^2}\Big(\partial_\theta^2\phi + r\partial_r\phi\Big). \tag{2.20}$$

In the presence of cylindrical symmetry (where we ignore the effect of the wedge), we can look for solutions of the form $\psi = \psi(r, t)$ that have no angular dependence, which means

$\partial_\theta \psi = 0$. Therefore, Eq. (2.16) becomes the radial equation

$$\mathrm{i}\frac{\partial}{\partial t}\psi(r,t) = \left[-\Delta - \frac{\hbar}{2m}\left(\partial_r^2 + \frac{1}{r}\partial_r\right)\right]\psi + g|\psi|^2\psi - \mathrm{i}\frac{\gamma}{2}\psi + \mathcal{F}(r), \tag{2.21}$$

which significantly reduces the computational cost.

The truncated Wigner approximation method

To justify the use of the mean-field (MF) approximation for our numerical simulations, we benchmark the solutions against the truncated Wigner (TW) approximation method [39, 170], which requires discretizing the quantum lower-polariton field $\hat{\psi}$ in the cavity into a 2D lattice. We denote $\varphi_j = \varphi(\boldsymbol{r}_j)$ the complex field amplitude (not to be confused with the mean-field classical parameter ψ in the Gross-Pitaevskii equation) at the lattice position $\boldsymbol{r}_j$, and $\Delta V = \Delta x^2$ the size of the elementary cell of the discrete lattice (where we adopt a step length of Δx when discretizing both dimensions). Note that the discretized field operators satisfy the commutation relation $[\hat{\psi}_j, \hat{\psi}_{j'}^\dagger] = \delta j, j'/\Delta V$. The time evolution of the discretized field can be exactly described by a third-order partial differential equation in terms of its Wigner distribution (which is a representation of the density matrix [35]). In the limit of $g/(\gamma\Delta V) \ll 1$, the third-order derivative terms can be neglected, resulting in a Fokker-Planck equation [171], that can be solved using stochastic trajectories defined via the set of Langevin equations in terms of the amplitude φ_j:

$$\mathrm{d}\varphi_j(t) = F_j\{\varphi\}\mathrm{d}t + \sqrt{\frac{\gamma}{4\Delta V}}\mathrm{d}W_j, \tag{2.22}$$

where $F_j\{\varphi\} = F\{\varphi\}(\boldsymbol{r} = \boldsymbol{r}_j)$ is the drift force on the lattice site j, with

$$F\{\varphi\}(\boldsymbol{r}) = -\mathrm{i}\left[-\Delta - \frac{\hbar}{2m}\nabla^2 - \mathrm{i}\frac{\gamma}{2} + g\left(|\varphi(\boldsymbol{r},t)|^2 - \frac{1}{\Delta V}\right)\right]\varphi(\boldsymbol{r},t) + \mathcal{F}(\boldsymbol{r}) \tag{2.23}$$

and $\mathrm{d}W_j$ is a zero-mean complex Gaussian noise satisfying

$$\begin{aligned} \mathrm{d}W_j\mathrm{d}W_{j'} &= 0, \\ \mathrm{d}W_j^*\mathrm{d}W_{j'} &= 2\mathrm{d}t\delta_{j,j'}. \end{aligned} \tag{2.24}$$

Within this formalism, the expectation values for symmetrized products of field operators [170] are given by the statistical expectation over different stochastic trajectories:

$$\begin{aligned} \left\langle \{(\hat{\psi}_j^\dagger)^n, \hat{\psi}_k^m)\}_s \right\rangle &= \mathbb{E}\left[(\varphi_{j,r}^*)^n \varphi_{k,r}^m\right] \\ &\simeq \frac{1}{N_{\mathrm{traj}}}\sum_r (\varphi_{j,r}^*)^n \varphi_{k,r}^m, \end{aligned} \tag{2.25}$$

where the index r labels the N_{traj} random trajectories. For example, the polariton density at each site, that we are interested in, can be calculated as

$$\begin{aligned} n_j = \left\langle \hat{\psi}_j^\dagger \hat{\psi}_j \right\rangle &= \left\langle \frac{1}{2}(\hat{\psi}_j^\dagger\hat{\psi}_j + \hat{\psi}_j\hat{\psi}_j^\dagger) - \frac{1}{2}[\hat{\psi}_j, \hat{\psi}_j^\dagger] \right\rangle \\ &= \left\langle \{\hat{\psi}_j^\dagger, \hat{\psi}_j\}_s \right\rangle - \frac{1}{2\Delta V} \\ &\simeq \frac{1}{N_{\mathrm{traj}}}\sum_r \varphi_{j,r}^*\varphi_{j,r} - \frac{1}{2\Delta V}. \end{aligned} \tag{2.26}$$

We performed the truncated Wigner simulations for the 2D configuration with a top-hat spot $l = 45\mu\text{m}$ driving the centre of a $105\mu\text{m} \times 105\mu\text{m}$ square lattice (this corresponds to a non-driven region with minimum width 30µm surrounding the driving spot, which, as we verified, is sufficient for the result to converge), where the discretization is set to $\Delta x = 2\mu\text{m}$ (thus $g/(\gamma\Delta V) = 0.03125$). This will be the largest driving spot considered in our results, and it therefore suffices to verify the validity of the mean-field approximation for this case, which is expected to be the closest case to possible criticality. Note that the lattice has $53 \times 53 = 2809$ sites, which is the number of coupled stochastic differential equations to solve in each single trajectory. For comparison, we simulate the same configuration ($l = 45\mu\text{m}$ at the centre of a disk with diameter 105µm) with the mean-field equation in polar coordinates as introduced previously, with a discretization step length of $\Delta r = 0.5\mu\text{m}$ in the radial dimension, where we have only 105 deterministic equations to solve. In Fig. 2.3 we compare the time evolution of the polariton density averaged over the probing disk with driving $F = 1.35\gamma/\mu\text{m}$, ($I = |F|^2 = 1.8225\gamma^2/\mu\text{m}^2$), simulated with the two aforementioned methods, where we averaged over $N_{\text{traj}} = 1000$ trajectories in the truncated Wigner simulation. The relative error in the polariton density stays well below 5% of the steady-state density throughout the time evolution, and decreases to less than 1% as the steady state is reached, showing a good agreement between the two. In Fig. 2.4 we compare the steady-state polariton density averaged over the probing disk for different driving intensities across the crossover, and we took $N_{\text{traj}} = 100$ for each driving value due to the high computational cost. The relative error in the driving intensity stayed well below 1% throughout the crossover. We therefore choose to use the mean-field equation for the numerical study, which gives accurate results at much lower computational cost as compared to the truncated Wigner method.

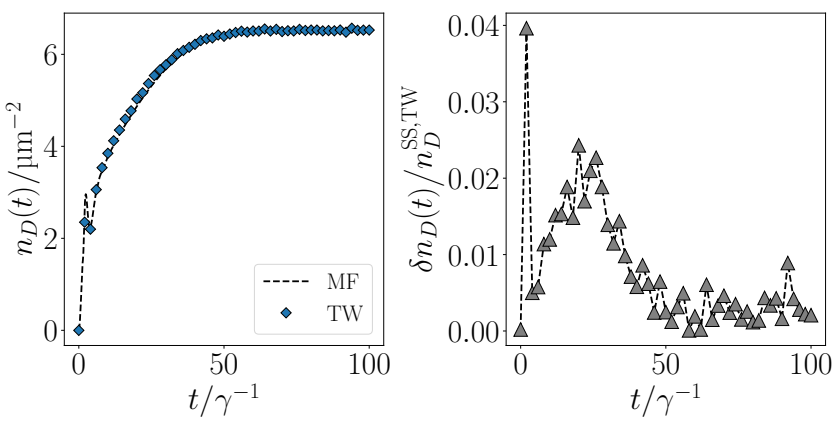

Figure 2.3: Left: time evolution of the polariton density averaged over the probing disk, computed with both mean-field (dashed line) and truncated Wigner (diamonds) methods. Right: relative error in the mean-field results with respect to the steady-state density, as a function of time, where $\delta n_D(t) = |n_D^{\text{TW}}(t) - n_D^{\text{MF}}(t)|$. The driving is $F = 1.35\gamma/\mu\text{m}$, ($I = |F|^2 = 1.8225\gamma^2/\mu\text{m}^2$) with a top-hat size of $l = 45\mu\text{m}$. Error bars are within the symbol size.

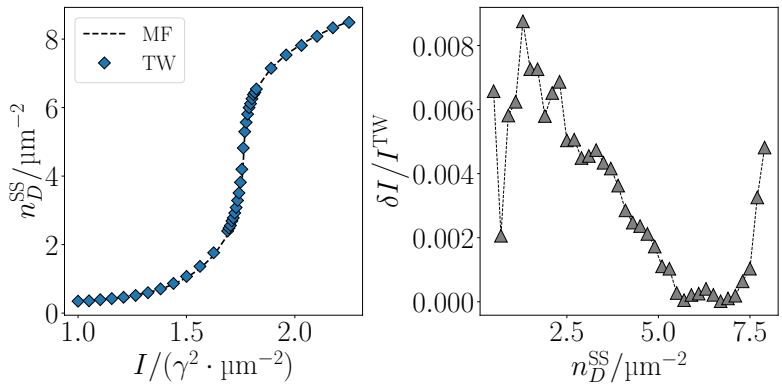

Figure 2.4: Left: steady-state polariton density averaged over the probing disk as a function of the drive, computed with both mean-field (dashed line) and truncated Wigner (diamonds) methods. Right: relative error of the driving in the mean-field results as a function of the density, where $\delta I = \left|I^{\mathrm{TW}} - I^{\mathrm{MF}}\right|$. The top-hat size is $l = 45\mu\mathrm{m}$. Error bars are within the symbol size.

IV Results and discussion

To investigate the steady-state behavior of the system and probe the phase transition, we solved Eq. (2.16) numerically with the experimental parameters introduced in the previous section. Throughout the simulation results presented in this section, the cavity wedge is not taken into account for more efficient simulations. The effect of the cavity wedge will be discussed later in Sec. IV.3. The detuning is set to $\Delta = \gamma$ in the simulation (same value as in the experiments), which is in the regime where a driven-dissipative Kerr cavity exhibits mean-field bistability [108, 109]. This can be equivalently viewed as the approximation of considering only the $k = 0$ mode under uniform drive F [145], since the steady-state mean-field equation can be written as

$$|\psi_{\mathrm{SS}}|^2 \left[\left(\Delta - g|\psi_{\mathrm{SS}}|^2 \right)^2 + \frac{\gamma^2}{4} \right] = |F|^2 \,, \tag{2.27}$$

which is essentially the same as Eq. (1.54) for a single-mode Kerr resonator. Note that the non-linear relation between $|\psi_{\mathrm{SS}}|^2$ and $I = |F|^2$ predicts a bistable regime if $\Delta/\gamma > \sqrt{3}/2$, as shown by the dashed line in Fig. 2.5(d), that we will compare with our numerical results. In all the simulations, the diameter of the probing disk D is set to $l_D = 5\mu\mathrm{m}$.

IV.1 Steady-state behavior

In Fig. 2.5(a)-(c) [(d)-(f)] we present the results obtained from our theoretical model and the LKB experiments for the 1D (2D) driving geometry. In both configurations, the steady-state polariton density n_D^{SS} averaged over the probing disk increases as a function of the driving intensity I and the maximum slope $\mathcal{S}(l) = \max_I \{ \frac{\partial n_D^{\mathrm{SS}}(I,l)}{\partial I} \}$ of the crossover from low density to high density (obtained with a noise-robust numerical differentiation method [172]) is monitored as a function of the top-hat size l, which allows us to probe

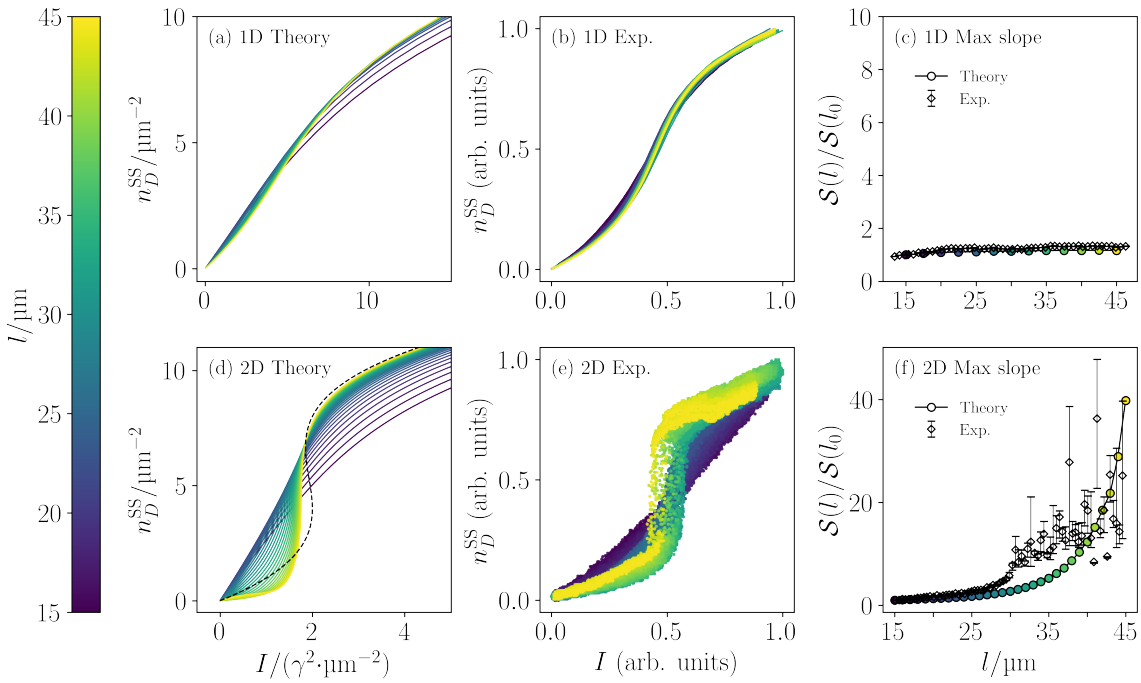

Figure 2.5: (a) [(b)] Results from our theory and LKB experiments for the steady-state polariton density n_D^{SS} averaged over the probing disk as a function of the drive intensity I for different top-hat spot sizes l (see colorbar) in the 1D configuration with detuning $\Delta = \gamma$. (c) The maximum derivative $\mathcal{S}(l)$ for each top-hat size l normalized by the maximum derivative at $l_0 = 15\mu m$, for both theoretical and experimental results (see legend). (d)-(f) The same quantities as in (a)-(c) for the 2D configuration. The dashed line in (d) is the prediction of the mean-field theory in Eq. (2.27). Note that as the top-hat increases in size, the slope in the 1D configuration quickly saturates for increasing size l, while in the 2D configuration the slope sharply increases in both theory and experiment, as expected for a first order phase transition.

the emergence of phase transitions defined by Eq. (2.19). In the 1D configuration, where the top-hat drive takes the shape of an elliptical spot with fixed minor axis, the slope $\mathcal{S}(l)$ saturates to a finite value with low enhancement [$\mathcal{S}(l)/\mathcal{S}(l_0) < 2$ with $l_0 = 15\mu m$ for all values of l measured] as the major axis l increases, signifying a smooth crossover with no phase transition in the thermodynamic limit.

In sharp contrast to the 1D configuration, with a 2D driving geometry, the slope presents a significant enhancement (by a factor of around 40 in theory, and a comparable value in the experimental results) as the top-hat diameter l increases, suggesting the emergence of a first-order phase transition in the thermodynamic limit of $l \to \infty$. We would like to also point out that, while in the 1D configuration we observed no bistability, in the experiments with 2D geometry we observed slight bistability for top-hat diameters $l \gtrsim 35\mu m$ [in this case we consistently took the lower branch when computing the slope (the higher one would give similar results)], which is consistent with the critical slowing down (see Sec. IV.2) of the dynamics as the system approaches criticality in 2D. Note that for $\mathcal{S}(l)/\mathcal{S}(l_0) \gtrsim 10$ [corresponding to a top-hat size of $l \gtrsim 30$ in the experimental

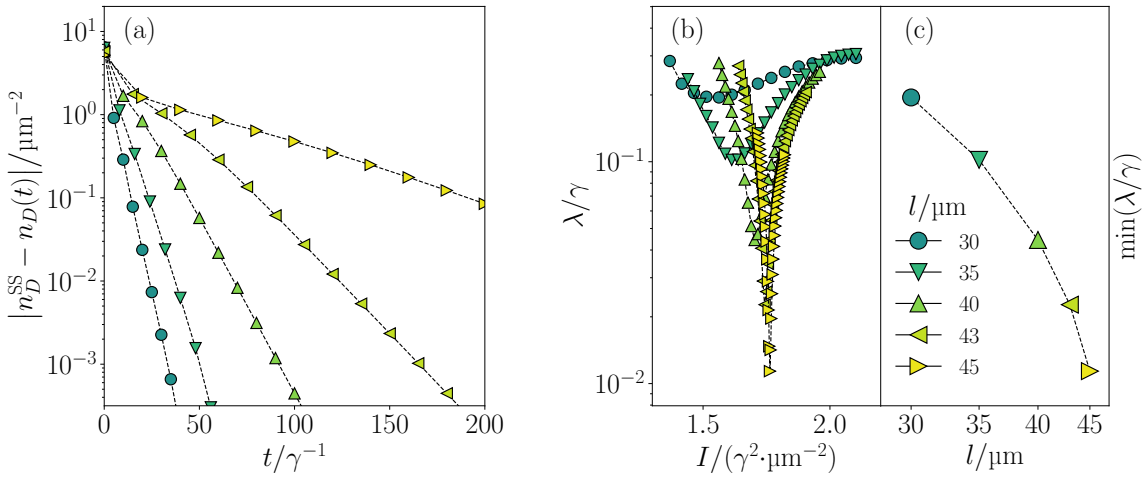

Figure 2.6: Critical slowing down and the closing of the Liouvillian gap for a 2D top-hat drive observed in numerical simulations. (a) The relaxation of $n_D(t)$ towards the steady state n_D^{SS} for difference driving spot sizes l (see legend) at $I = 1.7689\gamma^2/\mu m^2$. (b) The Liouvillian gap λ evaluated from the asymptotic decay rate as a function of the driving intensity I for different values of l. The error bars are within the symbol size. (c) The minimum of λ as a function of l.

results in Fig. 2.5(e)], the curve becomes almost vertical, which makes the numerically computed derivatives more sensitive to small errors in the measurements, resulting in the relatively larger errorbars on the experimental curve in Fig. 2.5(f) in this regime. The deviation between the theoretical and the experimental curves could originate from a slightly higher detuning in the experiment than the nominal value $\Delta = \gamma$. Nevertheless, the main objective of this plot is to show the divergence in the 2D configuration for both theory and experiment, which is in clear contrast to the 1D case.

IV.2 Critical slowing down of the dynamics in the 2D configuration

In a master-equation formalism of the problem

$$\frac{\mathrm{d}}{\mathrm{d}t}\hat{\rho} = \mathcal{L}\hat{\rho}\,, \tag{2.28}$$

The slowest relaxation dynamics of the density matrix towards the steady state is governed by the spectral gap λ of the Liouvillian superoperator $\mathcal{L}$, which is also known as the asymptotic decay rate [168]. As introduced in Sec. I.2, a dissipative phase transition can be characterised by the closing of the Liouvillian gap $\lambda \to 0$ in the thermodynamic limit, and is associated with a critical slowing down in the transient dynamics [152, 168].

To further investigate the dynamical properties of the emerging criticality in 2D, we simulate the time evolution of the polariton density $n_D(t)$ averaged over the probing disk towards the steady state n_D^{SS} in the 2D configuration, with a vacuum initial state. For driving intensities close to the critical point, the difference $n_D(t) - n_D^{SS}$ decays exponentially to zero for large time scales $t \gg 1/\gamma$, as reported in Fig. 2.6(a) showing the particular case of $I = 1.7689\gamma^2/\mu m^2$ for different driving spot sizes l. The decay exhibits a critical slowing

down as l increases, and we can estimate the Liouvillian gap λ by fitting the decay to an exponential form $n_D(t) = n_D^{\mathrm{SS}} + A\exp(-\lambda t)$, as the asymptotic decay is dominated by the Liouvillian gap in this regime [152, 168]. The dependence of λ as a function of the driving intensity I and spot size l is quantified in Fig. 2.6(b) and (c): $\lambda(I)$ presents a dip for each size l, and the minimum keeps decreasing as the driven area is increased. This evidence suggests the closing of the Liouvillian gap λ in the thermodynamic limit, confirming the emergence of the first-order dissipative phase transition from the dynamical point of view. We can also estimate the critical driving intensity to be $I_c \simeq 1.76\gamma^2/\mu\mathrm{m}^2$ from this figure.

Note that in our theoretical results, unlike the prediction of the single-mode mean-field theory given by Eq. (2.27), where the steady-state should always exhibit bistability across the transition, no bistability has been observed throughout the presented simulations (for larger sizes in 2D we would expect its appearance as we approach the limit of driving only the $k = 0$ mode), despite the absence of quantum fluctuations in the mean-field equation. This can be explained by the fact that our top-hat drive (that is non-uniform across the planar microcavity) excites both the $k = 0$ mode and other $k \neq 0$ modes. While only the $k = 0$ mode is responsible for the phase transition [145, 152], the other $k \neq 0$ modes serve as a reservoir in the Fourier k space, whose fluctuations, despite being at the mean-field level, suffice to suppress the bistability.

IV.3 Effect of the cavity wedge

In order to study the effect of the cavity wedge that we excluded for a more efficient solution of the mean-field equation, we present in this section the simulation results of the 2D configuration with the wedge taken into account. The detuning Δ becomes position dependent and can be modelled as

$$\Delta(x, y) = \Delta(x_0) + w(x - x_0), \tag{2.29}$$

where we have orientated the x axis along the gradient of the wedge. The steady-state polariton density distribution of the lower phase in the planar microcavity typically exhibits a distorted ring-shaped pattern, shown in Fig. 2.7(a) and (b), as the result of the wedge breaking the cylindrical symmetry of the system, whereas the distorsion is less visible in the higher density phase, as shown in Fig. 2.7(c) and (d). Despite the distortion, we obtain qualitatively similar behavior of the steady state as a function of the drive (Fig. 2.8) compared to the case without wedge. Note that for top-hat sizes $l \lesssim 40\mu\mathrm{m}$ (which is the main range of our experimental results), the difference in the maximum slope between the two cases remains minor, which justifies our choice of neglecting the wedge in 2D simulations when comparing the results to the experiments, in return for more efficient simulations. On the other hand, for larger driving spots in 2D experiments where the wedge is present, we should expect a less significant growth or even the saturation of the slope compared to the ideal wedgeless scenario.

V Conclusion and outlook

In this chapter, we have investigated the emergence of a first-order dissipative phase transition of polaritons in a planar microcavity subjected to a top-hat driving scheme with

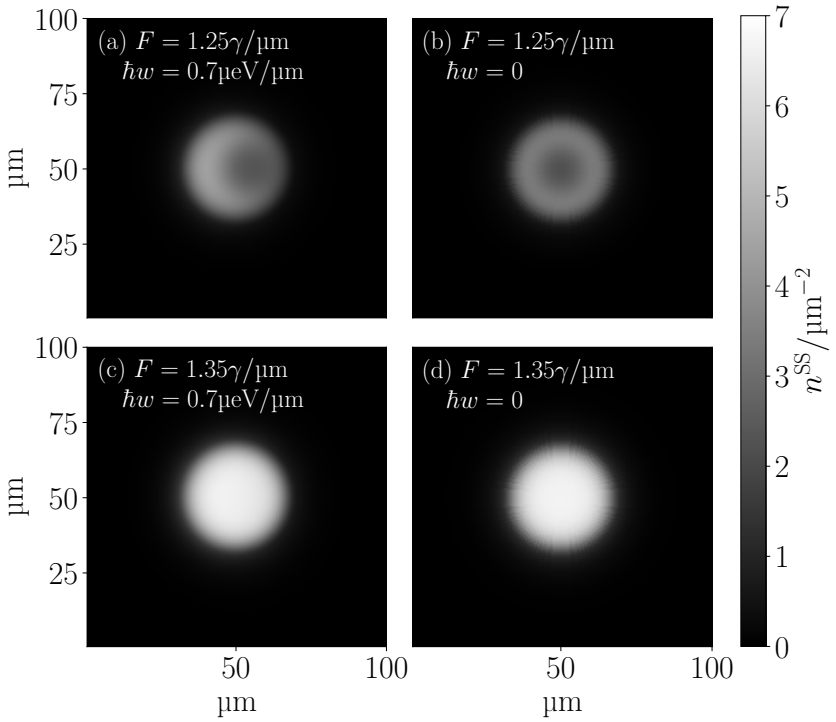

Figure 2.7: Steady-state polariton density (see colorbar) distribution in the planar microcavity simulated with experimental parameters with a 2D top-hat ($l = 40\mu m$) for different driving and wedge values (see annotation); the detuning with respect to the center of the driving spot is $\Delta = \gamma$. The left (resp. right) column corresponds to the wedge value $\hbar w = 0.7\mu eV$ (resp. $w = 0$). The driving in the top (resp. bottom) row corresponds to the lower (resp. higher) density phase close to the crossover.

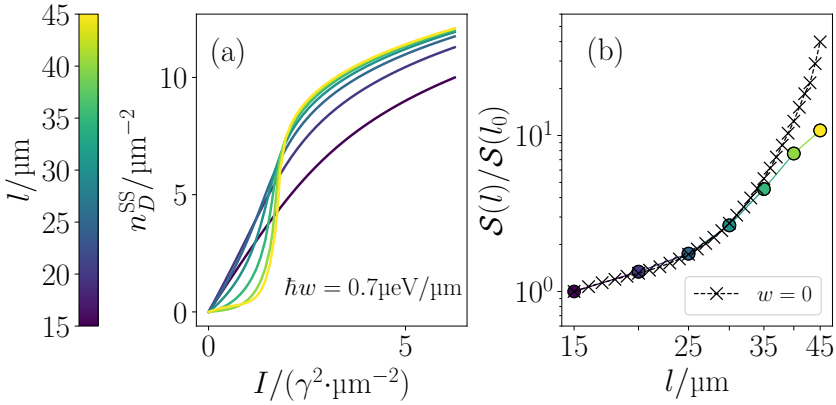

Figure 2.8: (a) Steady-state polariton density n_D^{SS} averaged over the probing disk as a function of driving intensity I simulated with the experimental parameters for different 2D top-hat spot sizes l (see colorbar) with the wedge $\hbar w = 0.7$ µeV/µm taken into account, and the detuning at the center of the top-hat is $\Delta = \gamma$. (b) The maximum crossover slope of each top-hat size $\mathcal{S}(l)$ normalized by the maximum slope at $l_0 = 15$µm in log-log scale, and the dashed line with "×" markers represents the results with $w = 0$ in the simulation as presented in Fig. 2.5.

naturally diffusive boundary conditions. We have shown that the emergence of criticality in such photonic system with Kerr nonlinearity is determined by the spatial dimension via the geometry imposed by the top-hat driving spot: a 1D geometry leads to a crossover behavior with no phase transition, while a 2D geometry shows a behavior consistent with a first-order transition between two phases with different densities. Our theoretical predictions have been validated by the experiments performed by our collaborators at LKB, which, to the best of our knowledge, is the first experimental demonstration of the role of dimensionality in determining criticality in driven-dissipative photonic systems.

The technique presented in this work allows the study of both 1D and 2D problems using the same planar cavity. The ability to control the criticality of the system via the spatial profile of the drive can also bring new insights to the design of polaritonic devices such as all-optical polariton transistors [173]. This scheme can be potentially generalized to more complicated geometries imprinted by the shape of the driving field, such as fractal patterns or quasi-periodic lattices, which could open the possibilities for studying effects of gradual changes of the dimensionality on phase transitions, paving the way to a novel approach to exploring the many-body physics of photons and critical phenomena.

The original results presented in this chapter are published in [γ].

3 Effective dynamics induced by a dissipative reservoir

In the previous chapter, we have seen how dissipative dynamics of a photonic system can give rise to intriguing phenomena such as dissipative phase transitions. On the other hand, one can also actively harness dissipation as a resource for engineering quantum systems, the possibility that we will now explore. In this chapter, we will focus on the scenario where a quantum system is coupled to a strongly dissipative reservoir, such that the reservoir degrees of freedom can be eliminated adiabatically due to their fast time scales. The main difference with respect to the master equation derived in Chapter 1 is that we no longer assume the reservoir to be local. In other words, different (and possibly distant) modes in the system can share a common reservoir that is spatially extended, resulting in nonlocal effects within the system, which can be harnessed to achieve engineered couplings between the system's degrees of freedom.

This chapter is structured as follows. In Sec. I, we will derive the general theory for the effective dynamics induced by a single-mode dissipative reservoir, where the coupling is assumed to be linear with an arbitrary system operator. This scenario is then recast in a more general picture in Sec. II using the theory presented in [47]. Finally, to prepare for the discussion in the next Chapter, we present in Sec. III a simple example of the application of the general theory, where one can realize two-photon drive and dissipation by adiabatically eliminating a single-mode dissipative cavity as the reservoir.

I Single-mode reservoir

Let us consider a simple case, where a (possibly open) quantum system is coupled to a strongly dissipative single-mode oscillator (such as a bad cavity) that we will refer to as the "reservoir", with bosonic annihilation operator $\hat{b}$. The assumption of strong dissipation implies that the typical time scale of the reservoir dynamics is much shorter than that of the system, such that the reservoir can be traced out adiabatically, resulting in an effective description in terms of the system alone, which is similar to our derivation of the master equation by eliminating the environmental degrees of freedom.

Formally, consider the system-reservoir entity subjected to the master equation[1]

$$\frac{\mathrm{d}}{\mathrm{d}t}\hat{\rho}_{SR} = \mathcal{L}_S\hat{\rho}_{SR} + \mathcal{L}_R\hat{\rho}_{SR} - \mathrm{i}[\hat{H}_I, \hat{\rho}_{SR}]\,, \tag{3.1}$$

[1] Let us adopt natural units with $\hbar = c = 1$ from now on to simplify the notations.

where $\mathcal{L}_S$ is the bare Liouvillian of the system which involves only operators acting on the system's Hilbert space. $\mathcal{L}_R$ is the bare Liouvillian of the reservoir, of which we assume the form

$$\mathcal{L}_R(\bullet) = -\mathrm{i}[-\tilde{\Delta}\hat{b}^\dagger\hat{b}, \bullet] + \gamma_b \mathcal{D}[\hat{b}](\bullet)\,, \tag{3.2}$$

where $\tilde{\Delta}$ is some constant of the dimension of frequency, and γ_b is the dissipation rate of the reservoir. Note that this form guarantees that the steady-state of $\mathcal{L}_R$ is the vacuum, such that any reservoir correlation function decays to 0 at a time scale of $\sim \gamma_b^{-1}$, which allows us to proceed with the adiabatic elimination of the reservoir mode. The interaction Hamiltonian $\hat{H}_I$ represents the system-reservoir coupling, which we assume to be linear:

$$\hat{H}_I = \lambda\gamma_b(\hat{A}^\dagger\hat{b} + \hat{A}\hat{b}^\dagger)\,, \tag{3.3}$$

where $\hat{A}$ acts only on the system's Hilbert space, and λ is a dimensionless small quantity which serves as a reminder that the system-reservoir coupling rate is small compared to the reservoir relaxation rate. We also make the *adiabatic assumption*:

$$\|\mathcal{L}_S\hat{\rho}_{SR}\|/\gamma_b \lesssim \lambda^2\,, \tag{3.4}$$

i.e. that the system bare dynamics is much slower compared to that of the reservoir. This typically requires us to work in some rotating frame where the possibly fast frequencies in $\mathcal{L}_S$ are eliminated, and consequently $\tilde{\Delta}$ can be interpreted as a detuning. As the reservoir is strongly dissipated, we can perturbatively develop $\hat{\rho}_{SR}$ around the reservoir vacuum:

$$\begin{aligned}\hat{\rho}_{SR} =& \hat{\rho}_{00}|0\rangle\langle 0| + \lambda(\hat{\rho}_{01}|0\rangle\langle 1| + \hat{\rho}_{10}|1\rangle\langle 0|)\\ &+ \lambda^2(\hat{\rho}_{11}|1\rangle\langle 1| + \hat{\rho}_{02}|0\rangle\langle 2| + \hat{\rho}_{20}|2\rangle\langle 0|)\\ &+ O(\lambda^3)\,,\end{aligned} \tag{3.5}$$

where $|m\rangle\langle n|$ acts on the reservoir's Hilbert space, and $\hat{\rho}_{mn}$ acts on that of the system. We aim to find the effective dynamics of the system in terms of the reduced density matrix

$$\hat{\rho}_S = \mathrm{Tr}_R[\hat{\rho}_{SR}] \simeq \hat{\rho}_{00} + \lambda^2\hat{\rho}_{11}\,, \tag{3.6}$$

where the reservoir mode is traced out and we keep terms up to second order in λ. By plugging the ansatz (3.5) into the master equation (3.1), we obtain

$$\begin{aligned}\frac{1}{\gamma_b}\frac{\mathrm{d}}{\mathrm{d}t}\hat{\rho}_{00} &= \frac{1}{\gamma_b}\mathcal{L}_s(\hat{\rho}_{00}) - \mathrm{i}\lambda^2(\hat{A}^\dagger\hat{\rho}_{10} - \hat{\rho}_{01}\hat{A}) + \lambda^2\hat{\rho}_{11} + O(\lambda^3)\,,\\ \frac{1}{\gamma_b}\frac{\mathrm{d}}{\mathrm{d}t}\hat{\rho}_{10} &= -\mathrm{i}\hat{A}\hat{\rho}_{00} + \Big(\mathrm{i}\frac{\tilde{\Delta}}{\gamma_b} - \frac{1}{2}\Big)\hat{\rho}_{10} + O(\lambda)\,,\\ \frac{1}{\gamma_b}\frac{\mathrm{d}}{\mathrm{d}t}\hat{\rho}_{11} &= -\mathrm{i}(\hat{A}\hat{\rho}_{01} - \hat{\rho}_{10}\hat{A}^\dagger) - \hat{\rho}_{11} + O(\lambda)\,,\\ \hat{\rho}_{01} &= \hat{\rho}_{10}^\dagger\,,\end{aligned} \tag{3.7}$$

where the dynamics for $\hat{\rho}_{10}$ and $\hat{\rho}_{11}$ are calculated to the zeroth order in λ since they are already second order terms in the equation for $\hat{\rho}_{00}$, which is the relevant quantity for $\hat{\rho}_S$. Let us now focus on the right-hand side of the equation for $\hat{\rho}_{10}$, where the time dependence

of $\hat{\rho}_{00}$ makes the equation hard to solve exactly. However, our adiabatic assumption implies that $\|\partial_t \hat{\rho}_{00}\| \sim \lambda^2 \gamma_b$, while $\hat{\rho}_{10}$ is damped at rate γ_b, which is much faster than the temporal variation of $\hat{\rho}_{00}$. We can therefore make the *adiabatic approximation* that $\hat{\rho}_{10}$ is constantly in its steady state on time scales much larger than γ_b^{-1}. This gives

$$\hat{\rho}_{10} = S\hat{A}\hat{\rho}_{00} + O(\lambda)\,, \tag{3.8}$$

where the dimensionless factor S is defined as

$$S \equiv \frac{\mathrm{i}\gamma_b}{\mathrm{i}\tilde{\Delta} - \frac{\gamma_b}{2}} \equiv \frac{1}{\gamma_b}\Big(\Lambda - \frac{\mathrm{i}}{2}\Gamma\Big)\,, \quad \Lambda = \frac{\gamma_b^2 \tilde{\Delta}}{\tilde{\Delta}^2 + \frac{\gamma_b^2}{4}}\,, \quad \Gamma = \frac{\gamma_b^3}{\tilde{\Delta}^2 + \frac{\gamma_b^2}{4}}\,, \tag{3.9}$$

that we decompose into real and imaginary parts for future convenience. With a similar argument applied to the equation for $\hat{\rho}_{11}$, we find

$$\hat{\rho}_{11} = \gamma_b^{-1}\Gamma\hat{A}\hat{\rho}_{00}\hat{A}^\dagger + O(\lambda)\,. \tag{3.10}$$

Inserting these back into Eq. (3.7), we obtain the effective master equation for the reduced density matrix of the system

$$\frac{\mathrm{d}}{\mathrm{d}t}\hat{\rho}_S = \mathcal{L}_S\hat{\rho}_S - \mathrm{i}[\lambda^2\Lambda\hat{A}^\dagger\hat{A}, \hat{\rho}_S] + \lambda^2\Gamma\mathcal{D}[\hat{A}]\hat{\rho}_S\,, \tag{3.11}$$

with the appearance of an effective Hamiltonian term

$$\hat{H}_S^{(1)} \equiv \lambda^2\Lambda\hat{A}^\dagger\hat{A}\,, \tag{3.12}$$

which resembles the Lamb shift that appeared in our derivation of the Lindblad master equation. Indeed, in the case where the system consists of a single mode $\hat{A} = \hat{a}$, we recover exactly the same form of the master equation (1.35) with the reservoir in the thermal vacuum, and this derivation can be regarded as an explicit special case of the discussion in Sec. II.1 of Chapter 1 where the reservoir has only one mode.

Eq. (3.11) above is the main analytical result of this chapter (developed from [α] and inspired by [43]) that we will further elaborate in Sec. III with a concrete example. Despite its simplicity, this model bears remarkable differences compared to the master equation (1.35) describing the effect of a *local* reservoir coupled to a system mode. In general, the system operator $\hat{A}$ can involve several modes which are possibly distant, making the reservoir effectively *extended* in space. The effective coherent contribution $\hat{H}_S^{(1)}$ from the reservoir then results in an effective coupling between different system modes on top of the Lamb shift, which can be visualized as system excitations traveling between different modes via (virtual) excitations of the reservoir [47]. Furthermore, the effective dissipator $\mathcal{D}[\hat{A}]$ can also induce a *dissipative coupling* between system modes, that is mediated via the coupling to the reservoir as well. These reservoir-induced effects potentially allow the design of lattices with engineered couplings, which we will further explore later in the next chapter.

II The generic master equation

The result above can be alternatively cast in a more general framework. In this section, we will derive (following [47, 48]) the effective master equation for a generic open quantum system (with time-independent bare Liouvillian $\mathcal{L}_S$) coupled to an extended reservoir (with time-independent bare Liouvillian[2] $\mathcal{L}_R$). The full master equation still takes the form of Eq. (3.1), where we now assume the generic form for the interaction Hamiltonian

$$\hat{H}_I = \lambda \sum_j \hat{S}_j \otimes \hat{R}_j \,, \tag{3.13}$$

where $\hat{S}_i$ and $\hat{R}_i$ act on the Hilbert spaces of the system and the reservoir respectively, and $\lambda \ll 1$ is still a small dimensionless constant. Following the same procedure as Sec. II.1 of Chapter 1, the Born-Markov approximation leads to an equation similar to Eq. (1.25) [47]:

$$\begin{aligned}
\frac{\mathrm{d}}{\mathrm{d}t}\hat{\rho}_S(t) &= \mathcal{L}_S\hat{\rho}_S(t) + \mathcal{L}_S^{(1)}\hat{\rho}_S(t)\,, \\
\mathcal{L}_S^{(1)}\hat{\rho}_S(t) &= -\lambda^2 \sum_{ij} \int_0^\infty \mathrm{d}\tau \Big\{ \mathcal{G}_{ij}(\tau)[\hat{S}_i, \mathrm{e}^{\mathcal{L}_S\tau}(\hat{S}_j\hat{\rho}_S(t-\tau))] + \mathrm{H.c.} \Big\} \\
&\simeq -\lambda^2 \sum_{ij} \int_0^\infty \mathrm{d}\tau \Big\{ \mathcal{G}_{ij}(\tau)[\hat{S}_i, \mathrm{e}^{-\mathrm{i}\hat{H}_S\tau}\hat{S}_j\mathrm{e}^{\mathrm{i}\hat{H}_S\tau}\hat{\rho}_S(t)] + \mathrm{H.c.} \Big\}\,,
\end{aligned} \tag{3.14}$$

where $\hat{H}_S$ is the system bare Hamiltonian, introduced to approximate the effect of $\mathcal{L}_S$ on time scales $\tau \lesssim \tau_R$ (lifetime of reservoir excitations). $\mathcal{G}_{ij}(\tau)$ is the reservoir correlation function defined as

$$\mathcal{G}_{ij}(\tau) = \mathrm{Tr}\Big[\hat{R}_i \mathrm{e}^{\mathcal{L}_R\tau}(\hat{R}_j\hat{\rho}_R(0))\Big] \equiv \langle \hat{R}_i(\tau)\hat{R}_j(0)\rangle\,, \tag{3.15}$$

which is taken on the reservoir steady state (therefore invariant by translations in time) using the bare Liouvillian of the reservoir. Indeed, effects due to the system's back action will be at most of order $O(\lambda)$ and negligible, as $\mathcal{L}_S^{(1)}$ is already of second order in λ, which is the highest order we keep[3]. To proceed with the rotating wave approximation as done in Sec. II.1 of Chapter 1, we can decompose the system operators into eigenmodes of the system Hamiltonian [35]:

$$\hat{S}_i = \sum_\alpha \hat{s}_{i,\alpha}\,, \quad [\hat{H}_S, \hat{s}_{i,\alpha}] = -\omega_\alpha \hat{s}_{i,\alpha}\,, \tag{3.16}$$

where the set $\{\omega_\alpha\}_\alpha$ contains all possible energy differences between eigenstates of $\hat{H}_S$.[4] This allows us to simplify Eq. (3.14) via the relation

$$\mathrm{e}^{-\mathrm{i}\hat{H}_S\tau}\hat{s}_{i,\alpha}\mathrm{e}^{\mathrm{i}\hat{H}_S\tau} = \mathrm{e}^{\mathrm{i}\omega_\alpha\tau}\hat{s}_{i,\alpha}\,, \tag{3.17}$$

[2] Again, we work in a frame where the steady state of $\mathcal{L}_R$ is of thermal nature (such as the vacuum state), such that all correlations decay to 0 fast enough, allowing us to perform the adiabatic elimination.

[3] Note that this is also the lowest order where we can have nontrivial effective dynamics stemming from the system-reservoir coupling, as is the case in our derivation of the master equation in Sec. II.1 of Chapter 1, which is also explicit from our discussion in Sec. I.

[4] Note that this definition implies $[\hat{H}_s, \hat{s}_{i,\alpha}^\dagger] = +\omega_\alpha \hat{s}_{i,\alpha}$.

which is reminiscent of the transformation of ladder operators between the Schrödinger picture and the interaction picture. The eigenoperator $\hat{s}_{i,\alpha}$ can therefore be regarded as a generalized ladder operator which induces transitions between energy levels of difference ω_α. Assuming that the energy spectrum of $\hat{H}_S$ is discrete and that the energy differences $|\omega_\alpha - \omega_{\alpha'}|$ are much larger than the system's own relaxation rate for $\omega_\alpha \neq \omega_{\alpha'}$ (which is the typically the case in quantum optics [35]), we can keep only the resonant terms in Eq. (3.14), finding

$$\mathcal{L}_S^{(1)}\hat{\rho}_S(t) = \lambda^2 \sum_{i,j,\alpha} \left\{ G_{ij}^\alpha [\hat{s}_{j,\alpha}\hat{\rho}_S(t), \hat{s}_{i,\alpha}^\dagger] + \text{H.c.} \right\}, \tag{3.18}$$

with the reservoir correlation spectrum G_{ij}^α defined via the Fourier transform

$$G_{ij}^\alpha \equiv \int_0^\infty \mathrm{d}\tau\ \mathcal{G}_{ij}^\alpha(\tau) \mathrm{e}^{\mathrm{i}\omega_\alpha \tau}. \tag{3.19}$$

To reveal the Lindblad form of Eq. (3.18), let us decompose G_{ij}^α (viewed as a matrix labeled by α) into Hermitian and anti-Hermitian parts:

$$\mathbf{G}^\alpha \equiv \frac{1}{2}\mathbf{\Gamma}^\alpha + \mathrm{i}\mathbf{\Lambda}^\alpha, \tag{3.20}$$

where $\mathbf{\Gamma}^\alpha$ and $\mathbf{\Lambda}^\alpha$ are Hermitian matrices. We can therefore diagonalize $\mathbf{\Gamma}$ with a unitary matrix $\mathbf{U}^\alpha$:

$$\mathbf{U}^\alpha \mathbf{\Gamma}^\alpha \mathbf{U}^{\alpha\dagger} = \mathrm{diag}(\gamma_1^\alpha, \gamma_2^\alpha, \cdots), \tag{3.21}$$

which brings Eq. (3.18) into the Lindblad form:

$$\mathcal{L}_S^{(1)}\hat{\rho}_S(t) = -\mathrm{i}\left[\lambda^2 \sum_{i,j,\alpha} \Lambda_{ij}^\alpha \hat{s}_{i,\alpha}^\dagger \hat{s}_{j,\alpha}, \hat{\rho}_S(t)\right] + \lambda^2 \sum_{i,\alpha} \gamma_i^\alpha \mathcal{D}\left[\sum_j U_{ij}^\alpha \hat{s}_{j,\alpha}\right]\hat{\rho}_S(t), \tag{3.22}$$

giving rise to a Lamb-shift-like Hamiltonian term and a dissipative term, both of which can be nonlocal, resulting in reservoir-mediated couplings between different system modes, as we have discussed in Sec. I. Note that this is also the most generic master equation one can obtain for the system coupled to a possibly extended reservoir [47], while assuming no more that the usual Born, Markov and rotating-wave approximations.

II.1 The single-mode reservoir revisited

To recover our results in Sec. I on a single-mode dissipative reservoir using the generic formalism presented above, let us identify the operators in the interaction Hamiltonian (3.3) using the notations in the current section:

$$\hat{S}_1 \equiv \hat{A}, \quad \hat{S}_2 \equiv \hat{A}^\dagger, \quad \hat{R}_1 \equiv \gamma_b \hat{b}^\dagger, \quad \hat{R}_2 \equiv \gamma_b \hat{b}, \tag{3.23}$$

and invoke the reservoir's bare Liouvillian (3.2), whose steady state is the vacuum. The correlation functions $\mathcal{G}_{ij}(\tau)$ can then be calculated using the quantum regression theorem [35], and the only nonvanishing one reads

$$\mathcal{G}_{21}(\tau) = \gamma_b^2 \langle \hat{b}(\tau)\hat{b}^\dagger(0)\rangle_R = \gamma_b^2 \mathrm{e}^{(\mathrm{i}\tilde{\Delta} - \frac{\gamma_b}{2})\tau}. \tag{3.24}$$

To find the effective dynamics up to second order in λ as we did in Sec. I, it suffices to approximate the integrand of Eq. (3.14) up to zeroth order in λ. This can be achieved by approximating $\mathcal{G}_{21}$ in Eq. (3.14) with the Dirac delta

$$\mathcal{G}_{21}(\tau) \simeq \frac{\gamma_b^2}{\frac{\gamma_b}{2} - \mathrm{i}\tilde{\Delta}}\delta(\tau) = \left(\frac{1}{2}\Gamma + \mathrm{i}\Lambda\right)\delta(\tau)\,, \tag{3.25}$$

where Γ and Λ are defined in Eq. (3.10). This delta-correlation approximation in fact follows from our adiabatic assumption (3.4), such that $\omega_\alpha/\gamma_b \sim O(\lambda^2)$ for the frequencies involved in the eigendecomposition of $\hat{A}$. One can validate this approximation for $\mathcal{G}_{21}$ via explicit calculation of the correlation spectrum:

$$G_{21}(\omega_\alpha) \equiv \gamma_b^2 \int_0^\infty \mathrm{d}\tau\; \mathcal{G}_{21}\mathrm{e}^{\mathrm{i}\omega_\alpha\tau} = \frac{\gamma_b^2}{\frac{\gamma_b}{2} - \mathrm{i}(\tilde{\Delta} + \omega_\alpha)} = G_{21}(0) + \gamma_b O(\lambda^2)\,, \tag{3.26}$$

where the approximately flat spectrum implies the Dirac-delta correlation. Inserting the correlation function (3.25) back into Eq. (3.14), we obtain

$$\begin{aligned}\mathcal{L}_S^{(1)}\hat{\rho}_S &= \lambda^2\left\{\left(\frac{1}{2}\Gamma + \mathrm{i}\Lambda\right)[\hat{A}\hat{\rho}_S, \hat{A}^\dagger] + \text{H.c.}\right\} \\ &= -\mathrm{i}[\lambda^2\Lambda\hat{A}^\dagger\hat{A}, \hat{\rho}_S] + \lambda^2\Gamma\mathcal{D}[\hat{A}]\hat{\rho}_S\,,\end{aligned} \tag{3.27}$$

which is exactly Eq. (3.11).

III Example: realization of two-photon drive and dissipation

To appreciate the general result derived above and prepare for our discussion on quantum simulation of antiferromagnetism in the next Chapter, let us apply the theory to a simple example where we derive an effective two-photon drive and dissipation via adiabatic elimination of a single-mode reservoir. Our starting point will be the following Hamiltonian (written in a rotating frame) for a degenerate parametric oscillator [174]:

$$\hat{H} = F\hat{b}^\dagger + F^*\hat{b} + g\hat{a}^{\dagger 2}\hat{b} + g^*\hat{a}^2\hat{b}^\dagger\,, \tag{3.28}$$

where the modes $\hat{a}$ and $\hat{b}$ are subjected to single-body losses $\gamma_a\mathcal{D}[\hat{a}]$ and $\gamma_b\mathcal{D}[\hat{b}]$ respectively, with $\gamma_b \gg \gamma_a$. This model can be readily realized in circuit QED platforms [43, 106, 175, 176], where two cavities are coupled nonlinearly via a Josephson junction, and the lossy cavity (with mode $\hat{b}$) is subjected two a two-tone single-body driving scheme (see [43] for details)[5]. Denoting $\lambda \equiv |g|/\gamma_b$, we assume $F/\gamma_b \sim O(\lambda)$ and $\gamma_a/\gamma_b \sim O(\lambda^2)$ as considered in [43]. To make the bare dynamics of mode $\hat{b}$ match the form (3.2), we can displace

[5]For simplicity, we did not include Kerr terms in the Hamiltonian (3.28), which are present in [43], as these terms have negligible effect on the adiabatic elimination in the regime they considered

the reservoir mode by redefining $\hat{b} \to \hat{b} + \beta$ to eliminate the driving term, where β is a constant that we now determine. In the displaced frame, the Hamiltonian reads

$$\begin{aligned}\hat{H} = &(F - \frac{\mathrm{i}}{2}\gamma_b\beta)\hat{b}^\dagger + (F^* + \frac{\mathrm{i}}{2}\gamma_b\beta^*)\hat{b} \\ &+ g\hat{a}^{\dagger 2}\hat{b} + g^*\hat{a}^2\hat{b}^\dagger \\ &+ g\beta\hat{a}^{\dagger 2} + g^*\beta^*\hat{a}^2\,,\end{aligned} \tag{3.29}$$

where the first line can be made to vanish by setting $\beta = 2F/\mathrm{i}\gamma_b$, which is precisely the mean field solution of $\langle\hat{b}\rangle$ given by the bare dynamics of the reservoir, whose steady state is consequently the vacuum in the displaced frame. The redefined operator $\hat{b}$ therefore represents the quantum fluctuations on top of the coherent state (in the nondisplaced frame) to which the reservoir is driven. The bare Liouvillian of the reservoir now becomes $\mathcal{L}_R = \gamma_b\mathcal{D}[\hat{b}]$, which is of the form (3.2) with $\tilde{\Delta} = 0$. We can then identify the interaction Hamiltonian $\hat{H}_I$ from the second line, which is of the form (3.3), where we have $\hat{A} = g^*\hat{a}^2/|g|$. The last line corresponds to a bare system Hamiltonian

$$\hat{H}_S = \hat{H}_2 \equiv \frac{G}{2}\hat{a}^{\dagger 2} + \frac{G^*}{2}\hat{a}^2\,, \tag{3.30}$$

with the identification $G \equiv -4\mathrm{i}gF/\gamma_b$. With all the assumptions of Sec. I satisfied, we can now read off the effective dynamics of the mode $\hat{a}$ from Eq. (3.11):

$$\frac{\mathrm{d}}{\mathrm{d}t}\hat{\rho}_S = -\mathrm{i}[\hat{H}_2, \hat{\rho}_S] + \gamma_a\mathcal{D}[\hat{a}]\hat{\rho}_S + \eta\mathcal{D}[\hat{a}^2]\hat{\rho}_S\,, \tag{3.31}$$

with $\eta \equiv 4|g|^2/\gamma_b$. The effective dissipator $\mathcal{D}[\hat{a}^2]$ is known as the *two-photon loss*, since it has the effect of annihilating two photons at a time upon acting on a state, and η corresponds to the two-photon loss rate. Similarly, the effective Hamiltonian $\hat{H}_2$ is known as the *two-photon drive* (or *quadratic drive*, since it is quadratic in the mode operator as opposed to a single-body drive) with G the two-photon drive amplitude. Finally, the rotating-frame Hamiltonian (3.30) can be written in the lab frame

$$\hat{H}_2(t) = \frac{G}{2}\hat{a}^{\dagger 2}\mathrm{e}^{-\mathrm{i}\omega_d t} + \frac{G^*}{2}\hat{a}^2\mathrm{e}^{\mathrm{i}\omega_d t} \tag{3.32}$$

with the time-dependence restored, where ω_d is the driving frequency.

III.1 The quadratically driven Kerr cavity

A Kerr cavity (of bare frequency ω_0) subjected to two-photon drive can be described by the Hamiltonian (in the frame rotating at the frequency $\omega_d/2$)

$$\hat{H} = -\Delta\hat{a}^\dagger\hat{a} + \frac{U}{2}\hat{a}^{\dagger 2}\hat{a}^2 + \frac{G}{2}\hat{a}^{\dagger 2} + \frac{G^*}{2}\hat{a}^2\,, \tag{3.33}$$

where $\Delta = \omega_d/2 - \omega_0$ is the drive-cavity detuning, together with the master equation

$$\frac{\mathrm{d}}{\mathrm{d}t}\hat{\rho} = -\mathrm{i}[\hat{H}, \hat{\rho}] + \gamma\mathcal{D}[\hat{a}]\hat{\rho} + \eta\mathcal{D}[\hat{a}]\hat{\rho}\,, \tag{3.34}$$

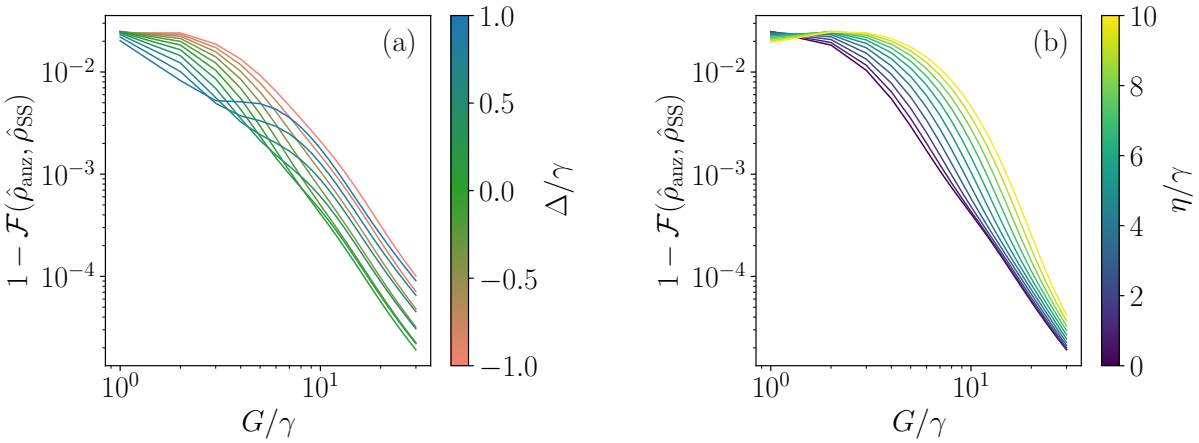

Figure 3.1: Infidelity $1-\mathcal{F}(\hat{\rho}_{\rm ans},\hat{\rho}_{\rm SS})$ of the ansatz $\hat{\rho}_{\rm ans}$ with respect to the exact steady state $\hat{\rho}_{\rm SS}$ of the quadratically driven Kerr cavity for (a) $\eta=0$ and different detunings Δ (see colorbar) and (b) fixed $\Delta=0$ and different two-photon loss rates η (see colorbar). The nonlinearity is $U=5\gamma$ for both plots. In the limit of large driving, the infidelity tends to zero, implying the accuracy of the ansatz $\hat{\rho}_{\rm ans}$.

with one- and two-photon loss rates γ and η respectively. This model has been explored extensively both theoretically [44, 107, 177–179] and experimentally [43], and has sparkled rapidly growing interest in communities of quantum information [179] and quantum simulation. Indeed, due to the presence of the quadratic drive instead of a single-body drive, the Liouvillian represented by Eq. (3.34) preserves the $\mathbb{Z}_2$ parity symmetry ($\hat{a}\to-\hat{a}$) of the photonic field, leading to bimodal states, which are ideal candidates for qubits or spin simulators. In particular, the steady state of the quadratically-driven Kerr cavity can be approximated by a statistical mixture of coherent states with opposite phases and equal probability:

$$\hat{\rho}_{\rm ans}(\alpha)=\frac{1}{2}(|\alpha\rangle\langle\alpha|+|-\alpha\rangle\langle-\alpha|)\,. \tag{3.35}$$

As shown in Fig. 3.1, we have simulated the exact steady states $\hat{\rho}_{\rm SS}$ of the master equation (3.34) and compared it to the ansatz $\hat{\rho}_{\rm SS}(\alpha_{\rm SS})$ with $\alpha_{\rm SS}=\sqrt{{\rm Tr}(\hat{\rho}_{\rm SS}\hat{a}^2)}$ via the *fidelity* measure defined as

$$\mathcal{F}(\hat{\rho}_1,\hat{\rho}_2)\equiv\left|{\rm Tr}\left(\sqrt{\sqrt{\hat{\rho}_2}\hat{\rho}_1\sqrt{\hat{\rho}_2}}\right)\right|^2, \tag{3.36}$$

for various values of Δ, η and G. The ansatz proves to be an accurate description of the exact steady state in the regime of strong two-photon drive, as indicated by the decreasing infidelity $1-\mathcal{F}(\hat{\rho}_{\rm ans},\hat{\rho}_{\rm SS})$. The state $\hat{\rho}_{\rm ans}$ can be equivalently written in an orthonormal basis[6] $|C_\pm(\alpha)\rangle\equiv\mathcal{N}_\pm(|\alpha\rangle\pm|-\alpha\rangle)$, which are known as *Schrödinger cat states* with opposite parities, and $\mathcal{N}_\pm=1/\sqrt{2(1\pm{\rm e}^{-2|\alpha|^2})}$ is the normalization factor such that

[6]Note that $|\pm\alpha\rangle$ are not orthogonal states as $\langle\alpha|-\alpha\rangle={\rm e}^{-2|\alpha|^2}$.

$\langle C_\sigma | C_{\sigma'} \rangle = \delta_{\sigma\sigma'}$. The state $\hat{\rho}_{\text{ans}}$ in the cat basis then reads

$$\begin{aligned} \hat{\rho}_{\text{ans}} &= \frac{1}{2}(|\alpha\rangle\langle\alpha| + |-\alpha\rangle\langle-\alpha|) \\ &= \frac{1}{4\mathcal{N}_+^2}|C_+(\alpha)\rangle\langle C_+(\alpha)| + \frac{1}{4\mathcal{N}_-^2}|C_-(\alpha)\rangle\langle C_-(\alpha)| \,. \end{aligned} \tag{3.37}$$

Note that in the limit of large driving $G \to \infty$, we have $|\alpha| \to \infty$ [177], $\langle\alpha|-\alpha\rangle \to 0$ and $\mathcal{N}_\pm \to 1/\sqrt{2}$, making the two bases $\{|C_\pm\rangle\}$ and $\{|\pm\alpha\rangle\}$ essentially the same up to a rotation. Moreover, in the absence of single-body loss γ and the Kerr nonlinearity U, the steady state will be confined in the quantum manifold spanned by $|C_\pm\rangle$, which includes all the coherent superpositions of these states instead of a classical mixture, making the system effectively a qubit commonly referred to as the *cat qubit*. This has been experimentally demonstrated on circuit QED platforms in regimes with the two-photon loss η significant enough compared to single-photon loss γ, such that coherent dynamics can be observed in the transient [43, 180, 181]. Such two-photon-driven cavities can also be engineered to couple to each other [182], allowing one to build artificial photonic lattices [96, 183, 184]. In the next chapter, we will propose a simple simulator of antiferromagnetism and frustration using quadratically driven Kerr cavity with engineered coupling and dissipation.

4 Dissipation-induced antiferromagneticlike frustration in coupled photonic resonators

In this chapter, we propose a photonic quantum simulator for antiferromagnetic spin systems based on the general theory derived in the previous chapter. We consider a scheme where quadratically driven dissipative Kerr cavities are indirectly coupled via lossy ancillary cavities, which can be adiabatically eliminated as a dissipative reservoir. We show that the resulting effective dynamics consists of dissipative and Hamiltonian antiferromagneticlike couplings between the system cavities. By solving the master equation for a triangular configuration, we demonstrate that the non-equilibrium steady state of the system bears full analogy with the ground state of an antiferromagnetic Ising model, exhibiting key signatures of frustration. We show that when the effective photon hopping amplitude is zero, the engineered nonlocal dissipation alone is capable of inducing antiferromagnetic interaction and frustration. This scheme applies to more general lattice geometries, providing a simple recipe for simulating antiferromagnetism and frustration on a controlled quantum optical platform.

This chapter is structured as follows. We first introduce the background and context in Sec. I. In Sec. II we present the considered scheme consisting of target and ancillary cavities and then derive the effective dynamics for the system using results from the previous chapter. In Sec. III we present and discuss numerical results for the dimer and triangular geometries. Finally, we draw our conclusions and perspectives in Sec. IV.

I Introduction

For decades, the physics of frustrated systems has gathered a great deal of interest as a fundamental problem in condensed matter physics. In a system with multiple constraints that cannot be satisfied simultaneously, the emerging frustration leads to interesting properties such as highly degenerate ground states [185, 186], extensive entropy at zero temperature [187] and exotic phases of matter, with connections to high-T_c superconductivity [188, 189] or quantum critical phases [190]. Although first studied in water ice [191], the phenomenon of frustration has later been particularly explored in spin systems [192–198], usually as a result of an antiferromagnetic interaction combined with incompatible geometric constraints. A simple and paradigmatic model consists of antiferromagnetically interacting spins arranged on a triangular lattice, a system admitting a spin-liquid phase as its ground state [199].

Recent impressive developments in experimental techniques have triggered an increasing interest in the field of quantum simulation of spin systems using Rydberg atoms [200, 201], quantum gas microscopes [202], optical [203–205] and photonic simulators [206–208] with semiconductors [39, 209–212] or circuit quantum electrodynamics (QED) [183, 213, 214]. However, their application on simulating frustrated spin systems is in its infancy. A recent theoretical study [215] revealed that coupled quadratically driven photonic cavities can simulate the antiferromagnetic Ising model [192], yet the model relies on a negative photon hopping amplitude between cavities, the implementation of which remains a major challenge despite possible realizations with sophisticated techniques [216, 217].

In this chapter, we propose a simple realization of antiferromagneticlike frustration in lattices of quadratically driven dissipative photonic cavities achieved via reservoir engineering. By indirectly coupling the target cavities (system) via lossy ancillary cavities (engineered reservoir), we obtain an effective description for the system with both an antiferromagneticlike Hamiltonian interaction (an effective photon hopping amplitude that can be tuned to be negative) and nonlocal dissipation coupling that is capable of inducing antiferromagnetic behavior in the system. By simulating the effective model via a consistently derived master equation for the reduced density matrix, we determine the first-order coherence correlation function and the von Neumann entropy. We demonstrate that when applied to a triangular geometry, our scheme yields a simulator for antiferromagnetically coupled Ising spins exhibiting key signatures of frustration.

II Theoretical model

Let us consider a one-dimensional (1D) chain of N pairs of single-mode cavities with annihilation operators $\{\hat{a}_1, \hat{b}_1, \hat{a}_2, \hat{b}_2, \cdots, \hat{a}_N, \hat{b}_N\}$ and periodic boundary conditions. The *system* cavities are described by the bosonic mode annihilation operators $\hat{a}_j$ while the lossy *reservoir* cavities by the operators $\hat{b}_j$. Each system site is coupled to the neighboring reservoir sites via the photon hopping coupling with amplitude J (> 0). Each system cavity is also assumed to have a mode frequency ω_0 and Kerr nonlinearity U and is subjected to a coherent two-photon drive with amplitude G, driving frequency ω_d, and two-photon dissipation rate η. The reservoir cavity modes have frequency $\omega_0 - \tilde{\Delta}$ and are assumed to be undriven and linear. We further assume the presence of single-photon loss for both the system sites (with rate γ) and the reservoir ones (with rate γ_b). The considered ensemble is schematically depicted in Fig. 4.1 (left panel) for the case $N = 3$. The Hamiltonian of the ensemble reads

$$\begin{aligned}
\hat{H}(t) &= \sum_j \hat{H}_j(t)\,, \\
\hat{H}_j(t) &= \omega_0 \hat{a}_j^\dagger \hat{a}_j + (\omega_0 - \tilde{\Delta})\hat{b}_j^\dagger \hat{b}_j \\
&\quad - J\Big[(\hat{a}_j + \hat{a}_{j+1})\hat{b}_j^\dagger + (\hat{a}_j^\dagger + \hat{a}_{j+1}^\dagger)\hat{b}_j\Big] \\
&\quad + \frac{U}{2}\hat{a}_j^{\dagger 2}\hat{a}_j^2 + \frac{G}{2}\hat{a}_j^{\dagger 2}\mathrm{e}^{-\mathrm{i}\omega_d t} + \frac{G^*}{2}\hat{a}_j^2 \mathrm{e}^{\mathrm{i}\omega_d t}\,.
\end{aligned} \tag{4.1}$$

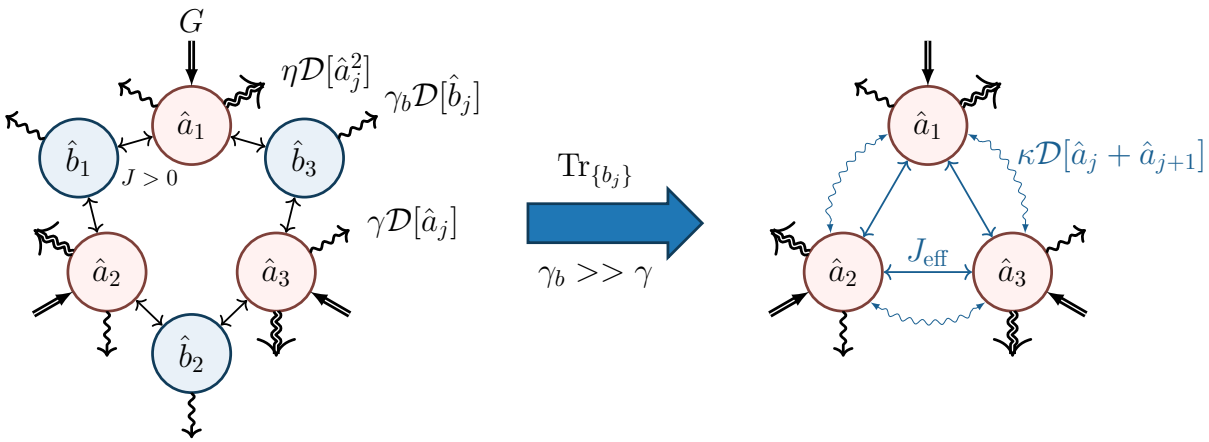

Figure 4.1: Schematic of the considered system-reservoir ensemble for the case with $N = 3$ system cavities, where $\hat{a}_j$ is the photon annihilation operator on the j-th cavity, G is the two-photon driving amplitude, γ is the single-photon loss rate, and η is the two-photon loss rate. The system cavities are coupled indirectly via the undriven lossy reservoir cavities: $\hat{b}_j$ is the corresponding ancillary mode annihilation operator and $\gamma_b \gg \gamma$ is its single-photon loss. The hopping coupling constant J between reservoir and system cavities is assumed to be positive. The effective model for the system is obtained by tracing out the ancillary degrees of freedom. This produces an effective coupling between system cavities that has both a coherent contribution (via the photon hopping J_{eff}) and a dissipative part (via the dissipator $\kappa\mathcal{D}[\hat{a}_j+\hat{a}_{j+1}]$). The effective hopping amplitude J_{eff} can be tuned to be negative, positive, or zero depending on the choice of parameters. The nonlocal dissipator has a symmetric jump operator that favors antiferromagnetic-like correlations.

Under the Born-Markov approximation, the state of the ensemble can be described by the density matrix $\hat{\rho}$ whose dynamics is governed by the Lindblad master equation:

$$\frac{\mathrm{d}\hat{\rho}}{\mathrm{d}t} = -\,\mathrm{i}[\hat{H}, \hat{\rho}] + \sum_j \left(\gamma\mathcal{D}[\hat{a}_j] + \gamma_b\mathcal{D}[\hat{b}_j] + \eta\mathcal{D}[\hat{a}_j^2]\right)\hat{\rho}\,. \tag{4.2}$$

We are interested in the regime where $\gamma_b \gg \gamma$, such that the modes $\hat{b}_j$ can be traced out with the adiabatic elimination techniques derived in Chapter 3. As we will show in the following, the resulting effective dynamics introduces antiferromagneticlike interactions between the system sites.

II.1 Theoretical intuition for the dimer case

To understand why this configuration can give rise to antiferromagneticlike interaction, let us first focus on the basic building block of our proposed scheme — a dimer consisting of $N = 2$ system cavities as illustrated in Fig. 4.2. In the absence of the ancillary reservoir cavity, the tight-binding (linear) part of the Hamiltonian is simply (assuming rotating-wave approximation for the coupling)

$$\hat{H}_0 = \omega_0(\hat{a}_1^\dagger\hat{a}_1 + \hat{a}_2^\dagger\hat{a}_2) - J(\hat{a}_1^\dagger\hat{a}_2 + \hat{a}_2^\dagger\hat{a}_2) = \begin{pmatrix}\hat{a}_1^\dagger & \hat{a}_2^\dagger\end{pmatrix}\begin{pmatrix}\omega_0 & -J\\ -J & \omega_0\end{pmatrix}\begin{pmatrix}\hat{a}_1\\ \hat{a}_2\end{pmatrix}, \tag{4.3}$$

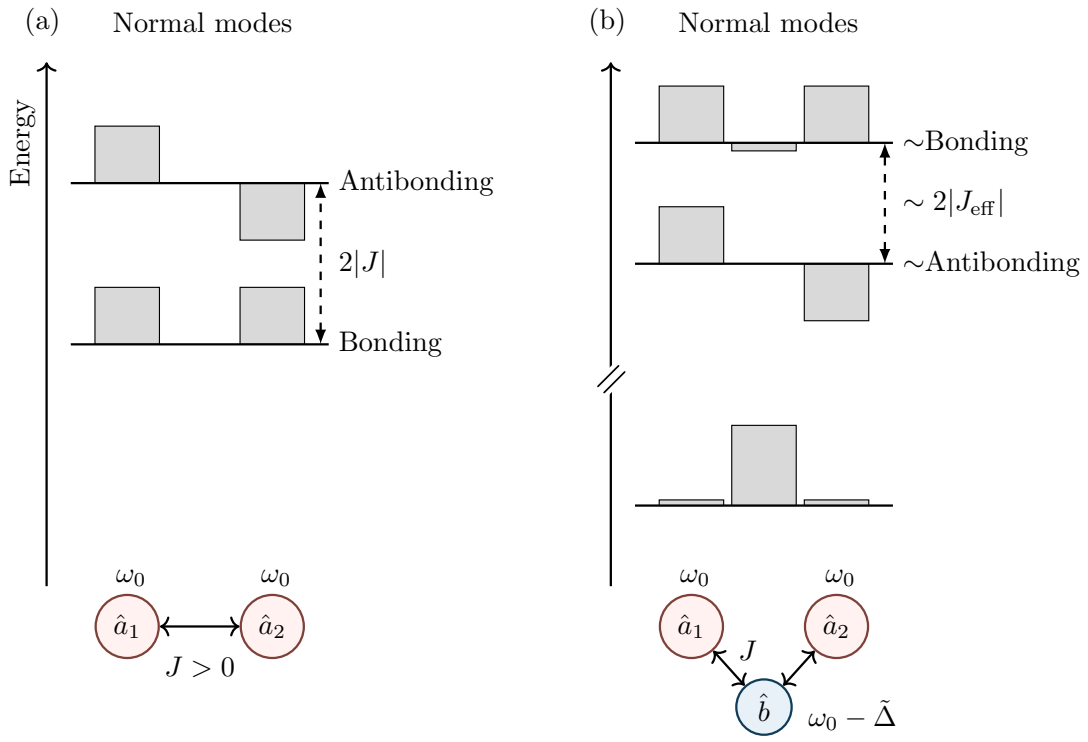

Figure 4.2: (a) Normal mode amplitudes and corresponding eigenfrequencies of two directly coupled cavities of bare frequency ω_0 with coupling amplitude $J > 0$. The normal mode splitting is $2|J|$ with the antibonding mode having a higher energy. (b) Same quantities for two cavities indirectly coupled via an ancillary cavity of bare frequency $\omega_0 - \tilde{\Delta}$, with $J > 0$ and $\tilde{\Delta} \gg J$. The two normal modes with higher energies resemble the bonding and antibonding modes, while the bonding mode has a higher energy. This implies an effective coupling $J_{\text{eff}} < 0$ between the two indirectly coupled cavities.

which can be diagonalized just as we did in Sec. III.2 of Chapter 1 to give an antisymmetric "antibonding" mode and a symmetric "bonding" mode with eigenfrequency $\omega \pm J$ respectively. Note that when $J > 0$, which is the usual case in quantum optics, the bonding mode will have lower energy, as illustrated in Fig. 4.2(a). In other words, if we seek to achieve a negative coupling J, the bonding mode should be made to have a high energy compared to the antibonding one. This can be achieved by adding an ancillary cavity at bare frequency $\omega_0 - \tilde{\Delta}$ and let the two system cavities both couple to the ancilla (with amplitude $J > 0$) instead of a direct coupling between them, as illustrated in Fig. 4.2(b). The tight-binding Hamiltonian of the ensemble then takes the form

$$\begin{aligned}\hat{H}_0 &= \omega_0(\hat{a}_1^\dagger \hat{a}_1 + \hat{a}_2^\dagger \hat{a}_2) + (\omega_0 - \tilde{\Delta})\hat{b}^\dagger \hat{b} - J(\hat{a}_1^\dagger + \hat{a}_2^\dagger)\hat{b} - J(\hat{a}_1 + \hat{a}_2)\hat{b}^\dagger \\ &= \begin{pmatrix} \hat{a}_1^\dagger & \hat{a}_2^\dagger & \hat{b}^\dagger \end{pmatrix} \begin{pmatrix} \omega_0 & 0 & -J \\ 0 & \omega_0 & -J \\ -J & -J & \omega_0 - \tilde{\Delta} \end{pmatrix} \begin{pmatrix} \hat{a}_1 \\ \hat{a}_2 \\ \hat{b} \end{pmatrix},\end{aligned} \tag{4.4}$$

which can again be diagonalized to give the normal modes. The eigenfrequencies are found to be

$$\begin{aligned}\omega_1 &= \omega_0 + \frac{1}{2}\left(\sqrt{8J^2+\tilde{\Delta}^2} - \tilde{\Delta}\right),\\ \omega_2 &= \omega_0\,,\\ \omega_3 &= \omega_0 - \frac{1}{2}\left(\sqrt{8J^2+\tilde{\Delta}^2} + \tilde{\Delta}\right),\end{aligned} \tag{4.5}$$

which are order by decreasing energy assuming $\tilde{\Delta} > 0$. The amplitudes of the eigenmodes are represented in Fig. 4.2(b) in the regime of $\tilde{\Delta} \gg J$, where ω_2 corresponds to the antisymmetric antibonding mode, ω_1 corresponds to a bonding-like mode which is symmetric in $\hat{a}_1$ and $\hat{a}_2$ but with a small residual amplitude for the $\hat{b}$ mode, and ω_3 is at a much lower energy, with the amplitudes mostly localized on the reservoir mode. With this configuration, we have successfully achieved a symmetric mode being on a higher energy than the antisymmetric mode, as if the effective coupling J_{eff} between the bare system modes were negative. As a rough estimate, the splitting between these two eigenmodes can be identified to be $\sim 2J_{\text{eff}}$ via analogy with the scenario in Fig. 4.2. In the limit of large $\tilde{\Delta}/J$, this effective coupling is estimated to be

$$J_{\text{eff}} \simeq \frac{1}{2}(\omega_2 - \omega_1) \simeq \frac{J^2}{\tilde{\Delta}}\,. \tag{4.6}$$

This estimation, however, fails to capture the full effective dynamics arising from the reservoir. For example, the finite linewidths of the bare modes due to dissipation are not taken into account, and the limit $\tilde{\Delta}/J \to \infty$ is not physically valid either, since it implies the breakdown of the rotating-wave approximation which is assumed when writing down the tight-binding Hamiltonian. To better describe the effective dynamics in terms of the two indirectly coupled cavities, we shall resort to the general theory presented in Chapter 3, which allows us to adiabatically trace out the ancilla mode.

II.2 Adiabatic elimination of the reservoir mode

Let us consider the system and reservoir described by the Hamiltonian (4.4), with the single-body dissipations $\gamma\mathcal{D}[\hat{a}]$ and $\gamma_b\mathcal{D}[\hat{b}]$. In the regime where $\gamma_b \gg \gamma$, the reservoir mode $\hat{b}$ can be traced out adiabatically. Defining $\lambda \equiv J/\gamma_b$, which we assume to be a small quantity, we will consider the regime where $\gamma/\gamma_b \sim O(\lambda^2)$. As argued in Chapter 1 when we wrote down the driven-dissipative master equations (1.38) and (1.52), assuming the drive G and nonlinearity U to be only perturbative, these terms can be added afterwards when we have derived the effective master equation for the undriven linear system. To apply our result in Sec. I of Chapter 3, we first rewrite the Hamiltonian (4.4) in the frame rotating at ω_0 define by the unitary transformation $\hat{U}^\dagger(t) \equiv \exp\left[\mathrm{i}\omega_0(\hat{a}_1^\dagger\hat{a}_1 + \hat{a}_2^\dagger\hat{a}_2 + \hat{b}^\dagger\hat{b})t\right]$, which reads

$$\hat{H}_0 = -\tilde{\Delta}\hat{b}^\dagger\hat{b} + \lambda\gamma_b(\hat{A}^\dagger\hat{b} + \hat{A}\hat{b}^\dagger)\,, \tag{4.7}$$

with $\hat{A} = -(\hat{a}_1 + \hat{a}_2)$, and the dissipators take the same form as in the nonrotating frame. We have recovered the same form as Eqs. (3.2) and (3.3), and can therefore read off the

effective master equation for the system modes from Eq. (3.11):

$$\begin{aligned}\frac{\mathrm{d}}{\mathrm{d}t}\hat{\rho} &= -\mathrm{i}[-\hat{H}_{\mathrm{eff}}, \hat{\rho}] + \gamma\mathcal{D}[\hat{a}] + \kappa\mathcal{D}[\hat{a}_1 + \hat{a}_2]\,,\\ \hat{H}_{\mathrm{eff}} &= -J_{\mathrm{eff}}(\hat{a}_1^\dagger + \hat{a}_2^\dagger)(\hat{a}_1 + \hat{a}_2)\\ &= -J_{\mathrm{eff}}(\hat{a}_1^\dagger\hat{a}_1 + \hat{a}_2^\dagger\hat{a}_2) - J_{\mathrm{eff}}(\hat{a}_1^\dagger\hat{a}_2 + \hat{a}_1\hat{a}_2^\dagger)\,,\end{aligned} \tag{4.8}$$

with the effective parameters defined as

$$J_{\mathrm{eff}} = \frac{-J^2\tilde{\Delta}}{\frac{\gamma_b^2}{4} + \tilde{\Delta}^2}\,, \quad \kappa = \frac{\gamma_b J^2}{\frac{\gamma_b^2}{4} + \tilde{\Delta}^2}\,, \tag{4.9}$$

where J_{eff} gives the strength of the Lamb shift and the effective photon hopping between the system sites, which are the coherent contributions of the reservoir to the effective dynamics. Note that J_{eff} agrees with our naive estimate (4.6) in the previous section in the limit of large $\tilde{\Delta}$. In addition, we also obtain a dissipative coupling of rate κ, since the dissipator $\mathcal{D}[\hat{a}_1 + \hat{a}_2]$ is nonlocal.

II.3 Effective driven-dissipative dynamics

The effective model derived above can be easily generalized to the case with N cavities, since the reservoir sites are independent of each other and can hence be eliminated separately. Each reservoir site with $\hat{b}_j$ sandwiched between the cavities of modes $\hat{a}_j$ and $\hat{a}_{j'}$ contributes to a Lamb shift $-J_{\mathrm{eff}}(\hat{a}_j^\dagger\hat{a}_j + \hat{a}_{j'}^\dagger\hat{a}_{j'})$, an effective coherent coupling $-J_{\mathrm{eff}}(\hat{a}_j^\dagger\hat{a}_{j'} + \hat{a}_{j'}^\dagger\hat{a}_j)$ and a dissipative coupling $\kappa\mathcal{D}[\hat{a}_j + \hat{a}_{j'}]$, when adiabatically traced out, as illustrated in Fig. 4.1 (right panel). Restoring the Kerr and drive terms, the effective model for the full system-reservoir ensemble defined by Eqs. (4.1) and (4.2) reads (in the frame rotating at the frequency $\omega_d/2$):

$$\hat{H}_{\mathrm{eff}} = \sum_j\Big(-\Delta_{\mathrm{eff}}\hat{a}_j^\dagger\hat{a}_j + \frac{U}{2}\hat{a}_j^{\dagger 2}\hat{a}_j^2 + \frac{G}{2}\hat{a}_j^{\dagger 2} + \frac{G^*}{2}\hat{a}_j^2\Big) - J_{\mathrm{eff}}\sum_{\langle j,j'\rangle}\hat{a}_j^\dagger\hat{a}_{j'}\,, \tag{4.10}$$

where the summation of $\langle j, j'\rangle$ runs over nearest neighbors, and $\Delta_{\mathrm{eff}} \equiv \omega_d/2 - \omega_0 + zJ_{\mathrm{eff}}$ is the effective detuning, with $z = 2$ (the coordination number) in the case of a 1D chain. The effective master equation for the reduced density matrix of the target system is a Lindlad equation described by the effective Liouvillian $\mathcal{L}_{\mathrm{eff}}$ defined as

$$\mathcal{L}_{\mathrm{eff}}(\bullet) = -\,\mathrm{i}[\hat{H}_{\mathrm{eff}}, \bullet] + \sum_j(\gamma\mathcal{D}[\hat{a}_j] + \eta\mathcal{D}[\hat{a}_j^2] + \kappa\mathcal{D}[\hat{a}_j + \hat{a}_{j+1}])(\bullet). \tag{4.11}$$

From now on, it will be convenient to work with the effective parameters Δ_{eff}, J_{eff}, and κ, as the original Hamiltonian parameters can be obtained as functions of them:

$$\Delta = \Delta_{\mathrm{eff}} - zJ_{\mathrm{eff}}\,, \tag{4.12}$$

$$\tilde{\Delta} = -\frac{\gamma_b J_{\mathrm{eff}}}{\kappa}\,, \tag{4.13}$$

$$J = \sqrt{\frac{\kappa\gamma_b}{4} + \frac{\gamma_b J_{\mathrm{eff}}^2}{\kappa}}\,, \tag{4.14}$$

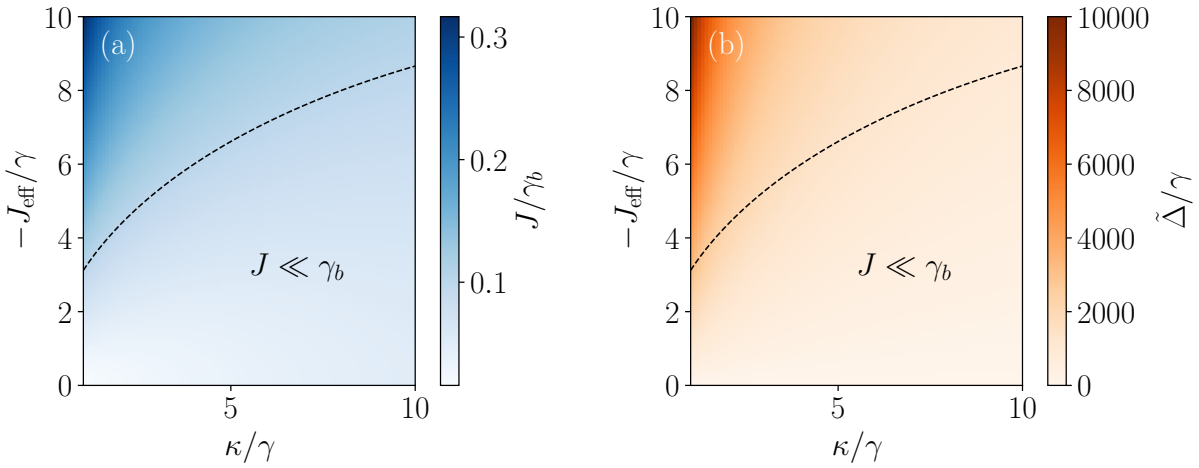

Figure 4.3: The original Hamiltonian parameters J and $\tilde{\Delta}$ of the system-reservoir ensemble (see colorbar) as a function of the effective parameters κ and J_{eff} plotted for $\gamma_b = 1000\gamma$. The dashed line indicates the boundary of the region satisfying $J < 0.1\gamma_b$. These plots indicates that in the regime of small J_{eff}, relatively small values of the system-reservoir coupling and detuning are required to achieve the effective model, which are consistent with our assumptions for the adiabatic elimination.

and the transformation is well defined as long as $\kappa > 0$. The dependence of the original parameters J and $\tilde{\Delta}$ on the effective parameters J_{eff} and κ are shown in Fig. 4.3 for the case of $\gamma_b = 1000\gamma$, with the boundary of the region satisfying $J < 0.1\gamma_b$ marked by dashed lines[1]. This roughly indicates the "safe zone" for the effective parameters, as our adiabatic elimination assumes J/γ_b to be a small quantity. On the other hand, the detuning between the system and reservoir cavities should not be too large, as the form of our coupling Hamiltonian assumes the rotating-wave approximation. Fig. 4.3(b) shows that for the regime of small J_{eff} (which will be the case considered in the main results of the current chapter, where we will study the effective of a purely dissipative coupling $\kappa > 0$ with $J_{\text{eff}} = 0$), a relatively small detuning $\tilde{\Delta}$ is required[2], which is consistent with our rotating-wave approximation.

At this stage, it is already important to summarize the main features of the proposed scheme:

1. The nearest neighbors in the effective model are dissipatively coupled via the dissipators $\kappa\mathcal{D}[\hat{a}_j + \hat{a}_{j+1}]$, that preserve the $\mathbb{Z}_2$ symmetry of the system (invariance under a global sign change $\hat{a}_j \to -\hat{a}_j$, $\forall j$) and are capable of inducing frustration, as we will show in the next section.

2. The effective photon hopping amplitude J_{eff} can be tuned and can be also negative when $\tilde{\Delta} > 0$.

[1]This boundary depends on the value of γ_b/γ. For a larger γ_b, the boundary will be pushed further to include larger values of J_{eff} and κ

[2]For example, the value of ω_0/γ is on the order of 10^5 for the semiconductor polariton microcavity considered in [γ], which is a typical case in quantum optics.

3. This scheme is not limited to 1D arrays and can be easily adapted for more general lattices by placing an ancilla between neighboring sites $\langle j, j'\rangle$, so that the two system sites sharing a reservoir will experience an effective photon hopping J_{eff} of tunable sign together with a dissipative coupling $\kappa\mathcal{D}[\hat{a}_j + \hat{a}_{j'}]$.

As studied in [215] and discussed in Sec. III.1 of Chapter 3, in the limit of $G/\gamma \to \infty$, each cavity will be driven into a statistical mixture of two coherent states with opposite phase $|\pm\alpha\rangle$ and we have $\alpha \to \infty$ in this limit[3]. Thus, the steady state can be mapped to Ising spins with the identification $|\alpha\rangle \to |\uparrow\rangle$, $|-\alpha\rangle \to |\downarrow\rangle$, since we have

$$\lim_{|\alpha|\to\infty} \langle -\alpha|\alpha\rangle = \lim_{|\alpha|\to\infty} \exp\Big\{(-2|\alpha|^2)\Big\} = 0. \tag{4.15}$$

The operator $\hat{a}_j$ can be mapped to $\alpha\hat{\sigma}_j^z$ when projected onto the spin basis in the limit of large driving. Therefore, from the spin point of view, the Hamiltonian (4.10) gives an effective Ising interaction $\hat{\sigma}_j^z\hat{\sigma}_{j'}^z$ with coupling constant proportional to J_{eff}. The nonlocal dissipator $\mathcal{D}[\hat{a}_j + \hat{a}_{j+1}]$ is expected to induce anti-alignment of nearest neighbors, i.e. $|\pm\alpha, \mp\alpha, \pm\alpha, \mp\alpha, \cdots\rangle$. In fact, the jump operator destroys excitations where there is alignment.

III Results and discussion

To investigate the behavior of the steady state of the system, we numerically solve the master equation using the effective model to obtain the steady state density matrix $\hat{\rho}_{\text{SS}}$ that satisfies $\mathcal{L}_{\text{eff}}\hat{\rho}_{\text{SS}} = 0$, where the detuning is set to $\Delta_{\text{eff}} = J_{\text{eff}}$ in order to favor the $k = \pi$ modulation of the photonic field $|\pm\alpha, \mp\alpha, \pm\alpha, \mp\alpha, \cdots\rangle$ (the phase of the driven cavity field changes by π moving from one cavity to the nearest one), corresponding to the $k = \pi$ mode in the single-particle spectrum of the Bose-Hubbard Hamiltonian [215]. We will be interested in the first-order coherence correlation function, defined as

$$g_{1,2}^{(1)} = \frac{\text{Tr}[\hat{\rho}_{\text{SS}}\hat{a}_1^\dagger\hat{a}_2]}{\text{Tr}[\hat{\rho}_{\text{SS}}\hat{a}_1^\dagger\hat{a}_1]}, \tag{4.16}$$

and the von Neumann entropy

$$S = -\text{Tr}[\hat{\rho}_{\text{SS}} \ln \hat{\rho}_{\text{SS}}]. \tag{4.17}$$

Note that with the mapping $\hat{a}_j \to \alpha\hat{\sigma}_j^z$, we have $g_{1,2}^{(1)} \simeq \langle\hat{\sigma}_1^z\hat{\sigma}_2^z\rangle$ for $|\alpha| \gg 1$, i.e. for sufficiently strong driving.

III.1 The dimer system

To reveal the antiferromagnetic behavior of the considered system, we first investigate the case with $N = 2$ sites. In this dimer configuration, we expect to see the antiferromagnetic ordering since there is no geometric frustration. In Fig. 4.4(a)-(c) we present the results

[3] This can be concluded with a semiclassical analysis as derived in Ref. [177].

for a finite value of the effective photon hopping amplitude $J_{\text{eff}} = -5\gamma < 0$ and different values of the nonlocal dissipative coupling κ. As the driving G increases, the correlation $g^{(1)}_{1,2}$ converges to -1, directly witnessing the antiferromagnetic alignment of the simulated spins in the two sites. Moreover, the entropy converges to $\ln(2)$ for all values of κ. This suggests that the steady-state density matrix can be approximated by the ansatz

$$\hat{\rho}_2(\alpha) = \frac{1}{2}(|\alpha, -\alpha\rangle\langle\alpha, -\alpha| + |-\alpha, \alpha\rangle\langle-\alpha, \alpha|) \tag{4.18}$$

in the strong driving limit. Indeed, as shown in the figure, the fidelity $\mathcal{F}$ between the steady-state density matrix $\hat{\rho}_{\text{SS}}$ and the ansatz $\hat{\rho}_2(\alpha_{\text{SS}})$ converges to 1 for increasing driving G. Such fidelity is defined as

$$\mathcal{F}(\hat{\rho}_{\text{SS}}, \hat{\rho}_2(\alpha_{\text{SS}})) = \left|\text{Tr}\left(\sqrt{\sqrt{\hat{\rho}_2}\hat{\rho}_{\text{SS}}\sqrt{\hat{\rho}_2}}\right)\right|^2, \tag{4.19}$$

where $\alpha_{\text{SS}} = \sqrt{\text{Tr}(\hat{\rho}_{\text{SS}}\hat{a}_1^2)}$.

Note that when the dissipative coupling strength κ increases, we achieve also a faster convergence, which implies that the dissipator $\kappa\mathcal{D}[\hat{a}_j + \hat{a}_{j+1}]$ enhances the antiferromagnetic interaction. Importantly, the nonlocal dissipative coupling *alone* is sufficient to obtain the key antiferromagnetic signatures [i.e. $g^{(1)}_{1,2} \to 1$, $S \to \ln(2)$ and $\mathcal{F} \to 1$], as shown in Fig. 4.4(d)-(f) where $J_{\text{eff}} = 0$. In fact, this antiferromagnetic character can be preserved even for a positive J_{eff} that is sufficiently small. We present in Fig. 4.4(g)-(i) the result for the $N = 2$ system with a positive $J_{\text{eff}} = 0.4\gamma > 0$, where the key antiferromagnetic signatures are preserved. This shows that the antiferromagnetic effect due to the nonlocal dissipative coupling can even overcome a moderate ferromagnetic coherent coupling. which further stresses the dissipative origin of the antiferromagnetic behavior in our setup.

III.2 The trimer system

We now consider the more interesting case of $N = 3$ where geometric frustration can emerge. Similar to the $N = 2$ case, we expect the steady-state density matrix to be approximated by the ansatz

$$\begin{aligned}\hat{\rho}_3(\alpha) = \frac{1}{6}(&|\alpha, \alpha, -\alpha\rangle\langle\alpha, \alpha, -\alpha| \\ &+ |\alpha, -\alpha, \alpha\rangle\langle\alpha, -\alpha, \alpha| \\ &+ |-\alpha, \alpha, \alpha\rangle\langle-\alpha, \alpha, \alpha| \\ &+ |-\alpha, -\alpha, \alpha\rangle\langle-\alpha, -\alpha, \alpha| \\ &+ |-\alpha, \alpha, -\alpha\rangle\langle-\alpha, \alpha, -\alpha| \\ &+ |\alpha, -\alpha, -\alpha\rangle\langle\alpha, -\alpha, -\alpha|),\end{aligned} \tag{4.20}$$

where we have a clear analogy with the sixfold degenerate ground state of the antiferromagnetic triangular Ising model.

We first demonstrate that with a finite value of $J_{\text{eff}} < 0$, our model is capable of simulating the frustrated Ising spins. Figure 4.5 summarizes the steady-state behavior of

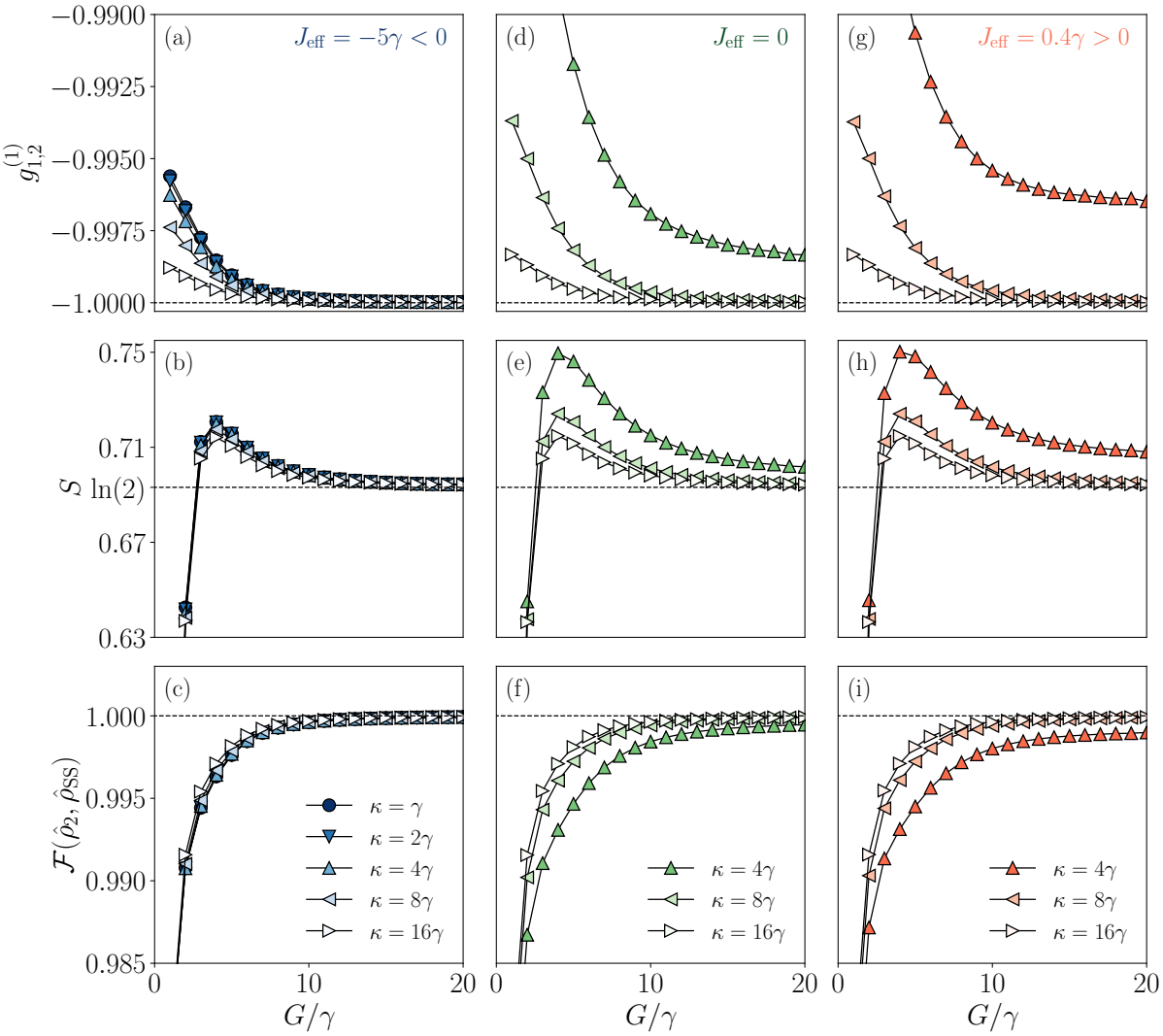

Figure 4.4: Steady-state behavior of the $N = 2$ system with $U = 4\gamma$ and $\eta = \gamma$. (a) The first-order coherence correlation function $g^{(1)}_{1,2}$, (b) the von Neumann entropy S and (c) the fidelity $\mathcal{F}$ between the numerical solution $\hat{\rho}_{\text{SS}}$ and the ansatz $\hat{\rho}_2$ are plotted vs the two-photon driving amplitude G, with a finite antiferromagnetic effective coupling $\Delta_{\text{eff}} = J_{\text{eff}} = -5\gamma$. (d)-(f) Same quantities for zero coherent effective coupling, i.e. $J_{\text{eff}} = 0$ and the dissipative coupling alone. (g)-(i) Same quantities for a small ferromagnetic coupling $J_{\text{eff}} = 0.4\gamma > 0$ in the presence of the dissipative coupling. Different markers (see legend) correspond to different values of the effective nonlocal dissipation rate κ.

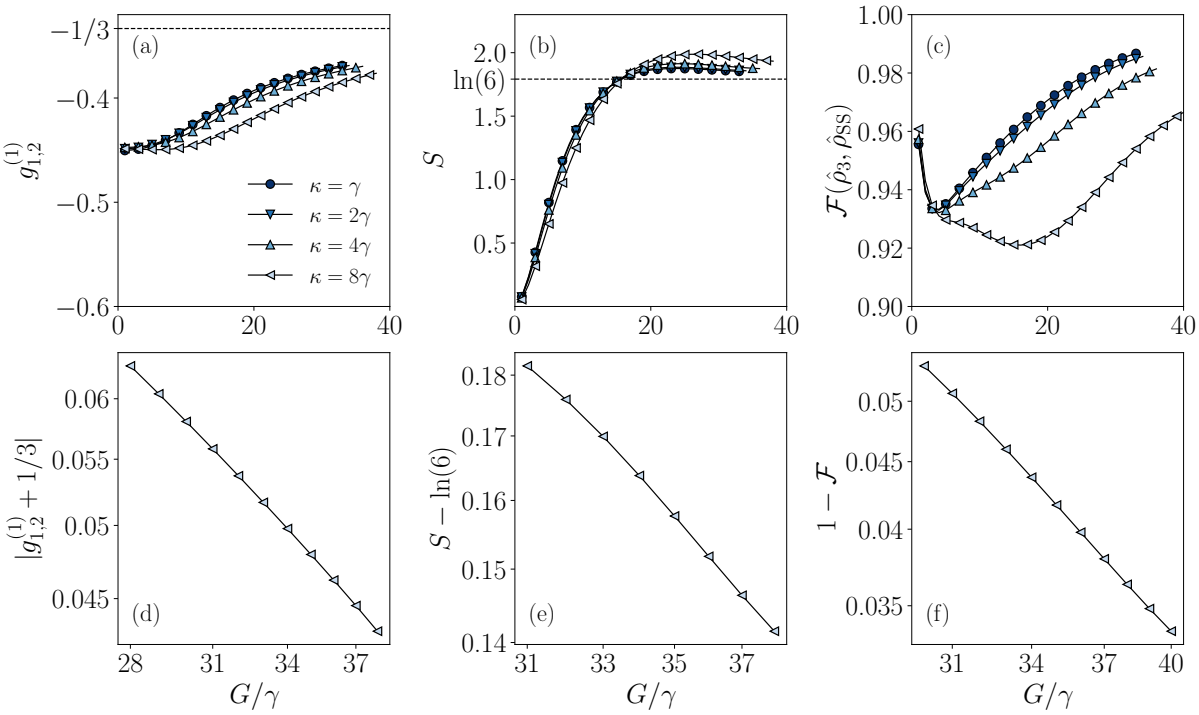

Figure 4.5: Steady-state behavior of the $N = 3$ triangular system for $\Delta_{\text{eff}} = J_{\text{eff}} = -5\gamma$, $U = 10\gamma$ and $\eta = \gamma$. All quantities are plotted vs the two-photon driving G. The panels report the results for (a) the first-order coherence correlation function $g^{(1)}_{1,2}$ [(d) the quantity $|g^{(1)}_{1,2} + 1/3|$], (b) the von Neumann entropy S [(e) the quantity $S - \ln(6)$], and (c) the fidelity $\mathcal{F}$ between the numerical solution $\hat{\rho}_{\text{SS}}$ and the ansatz $\hat{\rho}_3$ [(f) the quantity 1-$\mathcal{F}$]. The lower panels are all plotted in log-log scale, showing the asymptotic convergence of the respective quantities.

our model as a function of driving G for different values of the nonlocal dissipation rate κ. As the driving increases, the value of the first-order coherence correlation function $g^{(1)}_{1,2}$ converges asymptotically to $-1/3$, which is also the spin correlation value in the corresponding antiferromagnetic triangular Ising model [218]. The von Neumann entropy S converges asymptotically to $\ln(6)$, agreeing with the sixfold degenerate ground state of the simulated antiferromagnetic Ising mode. Furthermore, the fidelity $\mathcal{F}$ of the density matrix $\hat{\rho}_{\text{SS}}$ with respect to the ansatz $\hat{\rho}_3$ also converges to 1, validating the analogy with the spin system we made previously.

Our most important result is for the case of $\Delta = J_{\text{eff}} = 0$ and $\kappa > 0$, as summarized in Fig. 4.6. Despite the absence of a coherent antiferromagnetic interaction in the Hamiltonian, we successfully recovered the key signatures of frustration [$g^{(1)}_{1,2} \to -1/3$, $S \to \ln(6)$ and $\mathcal{F}(\hat{\rho}_3, \hat{\rho}_{\text{SS}}) \to 1$]. For comparison, we also simulated the trivial hypothetical scenario of $\kappa = 0$ [4], in which case the correlation $g^{(1)}_{1,2} = 0$ as the modes $\hat{a}_j$ are entirely decoupled, and the entropy tends to $\ln(8)$ instead of $\ln(6)$, corresponding to the $2^3 = 8$-fold degener-

[4]Note that in our effective model we always have $\kappa > 0$. The case where $\kappa = 0$ is simulated only for illustrative purposes to show the direct effect of the dissipative coupling.

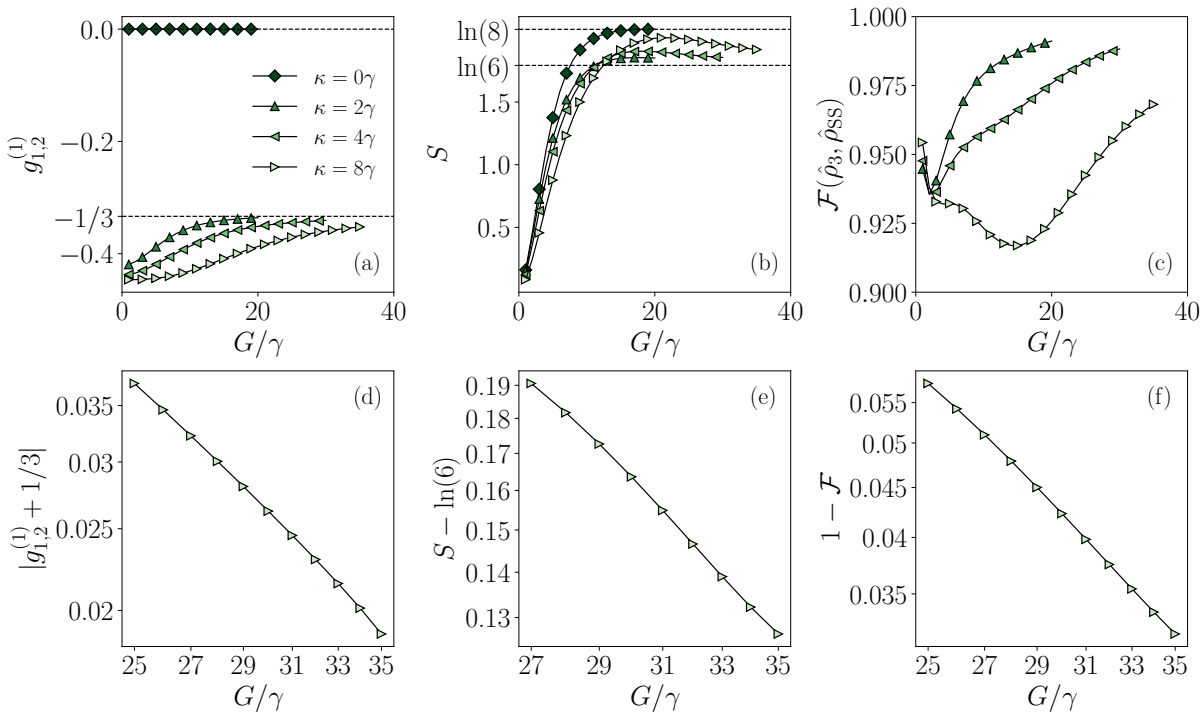

Figure 4.6: Same as Fig. 4.5 but with $\Delta_{\text{eff}} = J_{\text{eff}} = 0$, $U = 10\gamma$ and $\eta = \gamma$. Note that here the antiferromagnetic frustration effects are purely of a dissipative nature via the nonlocal dissipative coupling.

acy of the ground state of the non-interacting triangular model. This highlights the fact that the frustration in the case of $J_{\text{eff}} = 0$ is directly induced by the engineered dissipation $\kappa\mathcal{D}[\hat{a}_j + \hat{a}_{j+1}]$.

III.3 Benchmarking the effective model against exact results

To benchmark the effective model we derived above, we first simulate the $N = 2$ system-reservoir ensemble using the full master equation and compare the results with those obtained using the effective model. Note that as we have only two system sites, it suffices to consider only one ancilla cavity (b_1), sandwiched between the two system cavities (a_1, a_2), in the full simulation. We denote the steady-state density matrix of the full model by $\hat{\rho}^{\text{full}}_{\text{SS}}$, obtained by solving the master equation [Eq. (4.2)]:

$$\mathcal{L}\hat{\rho}^{\text{full}}_{\text{SS}} = 0. \tag{4.21}$$

Tracing out the ancilla mode gives the reduced density matrix $\hat{\rho}^{\text{full,r}}_{\text{SS}}$ for the system:

$$\hat{\rho}^{\text{full,r}}_{\text{SS}} = \text{Tr}_{\hat{b}_1}[\hat{\rho}^{\text{full}}_{\text{SS}}]. \tag{4.22}$$

We denote also the steady-state density matrix of the effective model by $\hat{\rho}_{\text{SS}}$, which is determined by

$$\mathcal{L}_{\text{eff}}\hat{\rho}_{\text{SS}} = 0. \tag{4.23}$$

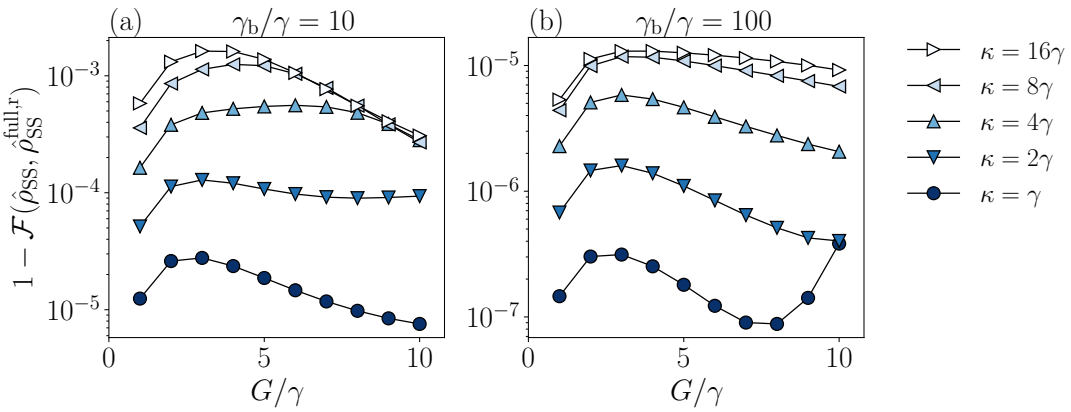

Figure 4.7: The infidelity $1 - \mathcal{F}$ of the effective model steady-state density matrix $\hat{\rho}_{SS}$ with respect to the reduced density matrix $\hat{\rho}_{SS}^{full,r}$ calculated from the full solution as a function of the driving G for different values of the nonlocal dissipative coupling κ. Dissipation parameters: (a) $\gamma_b/\gamma = 10$ and (b) $\gamma_b/\gamma = 100$. The other parameters are $\Delta_{eff} = J_{eff} = -5\gamma$, $U = 4\gamma$, and $\eta = \gamma$. The effective model is extremely accurate in a wide range of parameters as witnessed by the very small infidelities.

To quantify the benchmarking, we have calculated the fidelity $\mathcal{F}$ between the two solutions, defined as $\mathcal{F} = \mathcal{F}(\hat{\rho}_{SS}, \hat{\rho}_{SS}^{full,r})$, of course by using the same parameters. To demonstrate the validity of the effective model, here we report results of simulations for $\Delta_{eff} = J_{eff} = -5\gamma$, $U = 4\gamma$, and $\eta = \gamma$, which are the same parameters used to calculate Fig. 4.4(a)-(c), using different values of γ_b/γ.

As shown in Fig. 4.7, for $\gamma_b/\gamma = 10$, the infidelity $1 - \mathcal{F}$ is tiny, being at least smaller than 10^{-2} for all the considered combinations of κ and G, even when the adiabatic assumption $\gamma \ll \gamma_b$ is not fully respected. When the ratio is set to $\gamma_b = 100\gamma$, we have $1 - \mathcal{F} \ll 10^{-4}$ in all cases tested, indicating that the effective model we derived provides a very accurate description of the full model in the adiabatic limit.

The benchmarking for the $N = 3$ case is extremely difficult, as the full system-reservoir ensemble contains 6 modes in total, and the dimension of the Hilbert space (with a truncation on the occupation number that is sufficient for convergence) required for the numerical simulation is exponentially larger than the $N = 2$ case, which contains only 3 modes. Therefore, we chose to benchmark the effective model in the regime of very low photon numbers for a single set of parameters (see caption of Fig. 4.8), and compare the time evolution between the exact model and the effective one. In Fig. 4.8(a), the photon occupation number of the system ($\langle \hat{a}_j^\dagger \hat{a}_j \rangle^{full}$) and reservoir modes ($\langle \hat{b}_j^\dagger \hat{b}_j \rangle^{full}$), and the unnormalized system correlation function $\langle \hat{a}_j^\dagger \hat{a}_{j+1} \rangle^{full}$ obtained by simulating the full model are plotted as a function of the time. The corresponding quantities given by the effective model are not shown, as they overlap almost exactly with the exact solutions. The infidelity $1 - \mathcal{F}$ between the density matrices of the two solutions are shown in Fig. 4.8(b) along the time evolution, indicating that the effective model remains accurate for the trimer system.

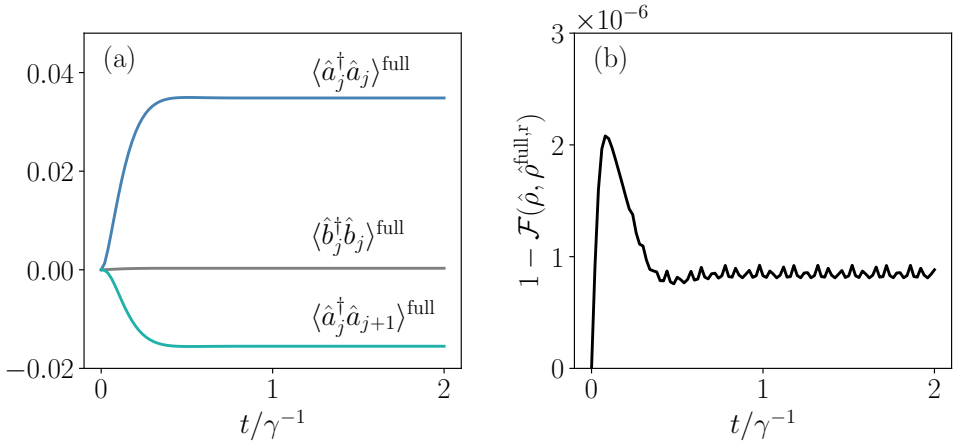

Figure 4.8: Benchmarking of the effective model for the trimer configuration. (a) The time evolution of the occupation number of the system ($\langle \hat{a}_j^\dagger \hat{a}_j \rangle^{\text{full}}$) and reservoir modes ($\langle \hat{b}_j^\dagger \hat{b}_j \rangle^{\text{full}}$), and the unnormalized system correlation function $\langle \hat{a}_j^\dagger \hat{a}_{j+1} \rangle^{\text{full}}$ given by the full model. The corresponding quantities predicted by the effective model (unshown) overlap almost exactly with the exact solutions. (b) The infidelity $1 - \mathcal{F}$ between the system density matrices obtained from the effective model $\hat{\rho}$ and from the full model $\hat{\rho}^{\text{full},r}$ as a function of time. The infidelity remains on the order of 10^{-6} throughout the time evolution. Parameters: $\gamma_b = 1000\gamma$, $\Delta_{\text{eff}} = J_{\text{eff}} = -\gamma$, $U = 10\gamma$, $\eta = \gamma$, $\kappa = 8\gamma$ and $G = 2\gamma$. The initial state is the vacuum state for the ensemble.

IV Conclusion and outlook

In this chapter, we have proposed a reservoir-engineering scheme allowing for the quantum simulation of frustrated Ising antiferromagnets with coupled photonic resonators subjected to coherent two-photon pumping. We have shown theoretically that the proposed configuration displays a dissipative coupling inducing antiferromagneticlike behavior and frustration even when the effective photon hopping amplitude is zero. By numerically solving the master equation for the cases with two and three system sites, respectively, we demonstrated the full analogy between the steady state of our model and the antiferromagnetic Ising model supported by the first-order coherence correlation and the von Neumann entropy.

The scheme proposed here provides a building block for simulating antiferromagnetic spin lattices, where the interaction depends on the easily tunable coherent photon hopping amplitude and the dissipative coupling rate, and which can be implemented in quantum optical platforms.

The original results presented in this chapter are published in [α].

5 Relativistic quantum reservoir computing

So far, we have explored the effective dynamics that a reservoir can induce on quantum systems in different regimes. Namely, we have seen in Chapter 1 and 2 how uncontrolled local thermal reservoirs give rise to dissipative dynamics in the system. We then discussed in Chapter 3 and 4 how one can harness the dissipation of nonlocal reservoirs to achieve both coherent and dissipative effective couplings in the system. This process is known as reservoir engineering, where one designs the reservoir (and its coupling to the system) to obtain desired effective dynamics in the system. There can be, however, an alternative point of view, where it suffices to engineer only the reservoir *experienced* by the system instead of the reservoir itself. Indeed, from our discussion on light-matter interaction under relativistic settings in Chapter 1, in order for a quantum detector weakly coupled to a reservoir to experience a temperature T, one can either directly prepare the reservoir in a thermal state with temperature T and leave the detector static, or let the reservoir be in the vacuum state but give the detector an eternal acceleration $a = 2\pi T$. This might seem ridiculously useless in practice, yet it bears fundamental interest in the field of relativistic quantum information, where one tries to understand and harness the effect of relativity in controlling quantum systems and processing quantum information, at least in theory. (Later we shall see that analog implementation of relativistic quantum models is also possible.) This is exactly the motivation of this chapter, where we will study *relativistic quantum reservoir computing*, a paradigm yet to be explored in relativistic quantum information. It is worth clarifying now that the significance of the term *reservoir* in the context of *reservoir computing* subtly differs from what we have been considering in previous chapters. Here, a reservoir generally refers to some physical system (not necessarily coupled to another *system* in a bipartite setting) that exhibits nontrivial dynamics when subjected to some kind of input, such that it is capable of transforming the input into some useful representation that one can exploit to process the input information.

In this chapter, we present a machine-learning scheme based on the relativistic dynamics of a quantum system. We consider a paradigmatic model describing a quantum detector undergoing relativistic motion inside a cavity resonator. An equivalent analog model can be realized for example in a circuit QED platform subject to properly modulated driving fields. We exploit the reservoir-computing framework where the input data are embedded in the the acceleration of the detector and the output data are obtained by linear combinations of measured observables. As an illustrative example, we simulate such a relativistic quantum reservoir-computing protocol for a supervised classification task, showing a significant enhancement of the learning performance in the relativistic

regime.

This chapter is structured as follows. Sec. I gives a very brief introduction to relativistic quantum information and reservoir computing, the two fields that we would like to blend in this chapter. In Sec. II, we will review the general concepts in supervised learning and reservoir computing, to prepare for the presentation of our relativistic quantum reservoir-computing protocol in Sec. III. In Sec. IV, we discuss the results obtained for an illustrative supervised classification task, together with with a possible implementation scheme with circuit QED. Finally, we conclude this chapter in Sec. V.

I Introduction

The interplay between general relativity and quantum physics has always been a fascinating field of research that is of fundamental importance. For instance, it was predicted from the study of quantum field theory in curved spacetime that a non-inertial observer in a quantum field would observe a different state compared to an inertial observer. As we have introduced in Sec. IV of Chapter 1, a famous example is the Unruh effect, where a uniformly accelerated observer in Minkowski vacuum detects a thermal bath at finite temperature, which bears the same nature as the celebrated black hole Hawking radiation.

On the other hand, the rapid development of quantum-information theory in the past decades has lead to the emergence of the exciting field of relativistic quantum information [69, 70], where one seeks to understand and harness relativistic effects in quantum information-processing protocols. In particular, it has been demonstrated that non-inertial motion, or, via the equivalence principle, gravitational fields, can be used to generate quantum gates. Recent theoretical works have demonstrated that a non-uniformly accelerated cavity can generate cluster states [219], two-mode squeezing [220], mode mixing [221] as well as other entangling gates [222] for continuous-variable quantum computing [223]. In the complementary scenario, where a cavity remains inertial but hosts accelerated detectors, it has also been shown that universal single-qubit rotations can be performed [224]. While all the existing proposals for relativistic quantum computing require a very challenging control of mechanical motion, the corresponding models can be however synthesized in artificial platforms [225–227] such as those based on circuit QED [106] or trapped ions [228].

In recent years, *reservoir computing* has emerged as an appealing paradigm of information processing [229]. This framework consists in approximating a target function by feeding its arguments as an input of a physical system referred to as the *reservoir*, whose dynamics nonlinearly maps the data into a high dimensional space. The resulting output data are then fed into a parametrized linear transformation to yield a trial function. These parameters are finally optimized through supervised learning. The advantage of this framework is that one may harness computing resources from the (usually nonlinear) dynamics of a physical system while requiring virtually no degree of control over it, and the computational cost involved in the training process remains relatively modest. This has led to proposals and realizations in diverse platforms, including free-space optics [230–232], photonics [233, 234], nonlinear polariton lattices [235–237], memristors [238, 239] and beyond [240–243]. Very recently, such an approach has been explored in a quantum

context [34, 244], with applications in quantum metrology [245, 246], quantum-state control [247–249] and image recognition [δ, 250]; although, to the best of our knowledge, never yet in a relativistic scenario. Surprisingly, reservoir computing has been demonstrated to have a high performance in much less well-controlled situations, such as speech recognition using an actual bucket of water [251], as well as other classification tasks performed using cat brains [252] and gene regulatory networks in the bacterium *Escherichia Coli* [253]. Although it was long thought that a strong nonlinearity of the equations of motion was an essential element of reservoir computing, recent works have shown great performances relying on systems with almost no intrinsic nonlinearity, namely by exploiting the nonlinearity of the measurement [232, 254, 255] or drawing links with approximate kernel evaluation [256–258]. In this chapter, we take a step further and study the performance of a reservoir consisting of coupled *linear* oscillators whose nonlinear dynamics stem from their relativistic motion, thus harnessing computing resources from the nonlinearity of fundamental laws of physics. Before introducing our relativistic quantum model, let us first briefly review the general concepts in supervised learning and reservoir computing.

II Supervised learning and reservoir computing

The goal of supervised machine learning is to try to best approximate a (usually nonlinear) target function $y = f(\mathbf{x})$ of some D-dimensional input vector $\mathbf{x} = (\mathrm{x}_1, \mathrm{x}_2, \ldots, \mathrm{x}_D)$ with a parametrized trial function $\hat{y} = \hat{f}(\mathbf{x})$ from a set of known example pairs. The input data are distributed in some *input space* according to a probability measure $\mu(\mathrm{d}\mathbf{x})$, from which a restricted set of samples with their corresponding target values is known, $\{(\mathbf{x}^{(i)}, y^{(i)})\}_i$. These are split into a training set of size N_{train}, that one exploits to optimize the trial function $\hat{f}$ (hence the name "supervised learning"), and a testing set of size N_{test}, used to asses the performance of the trained model. This optimization procedure (commonly referred to as *training*) is typically done by minimizing a task-dependent *cost function* that quantifies the error of the parametrized model over the training dataset. The simplest and perhaps also the best known example of supervised learning is the task of linear regression, where one tries to fit a set of data points to a straight line (or a hyperplane in general for multiple input arguments). In this case, the trial function is simply a linear combination of its input arguments, parametrized by the linear weights whose optimization can be achieved (analytically) by minimizing the sum of squared errors, known as the method of *least squares* [259].

In general, the architecture of the model is determined by the parametrization of the trial function. A popular category of parametrizations in the context of machine learning is known as the *artificial neural network* (ANN) [260], where the trial function consists of layers[1] of parametrized nonlinear transformations, which mimics the architecture of our brains, and has been proven to be universal function approximators. Such ANN models and are typically implemented by software that runs on standard (i.e., von Neumann architecture [261]) computers, and usually contain numerous trainable parameters. A simpler alternative approach is provided by the architecture of "shallow models", such as

[1] In the sense of function compositions.

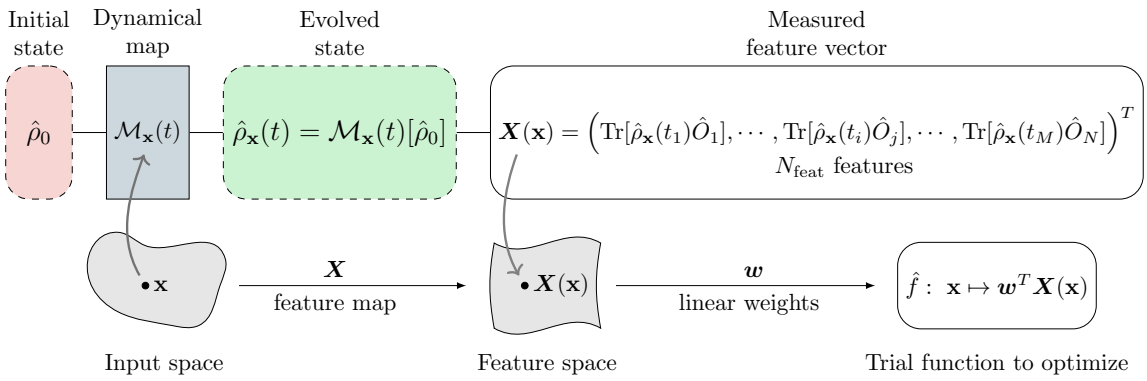

Figure 5.1: General scheme of constructing a reservoir-computing trial function $\hat{f}(\mathbf{x})$ using a physical system. The system, prepared in a fixed initial state $\hat{\rho}_0$, is subjected to a time evolution depending on the input $\mathbf{x}$. This dependence can be realized, for example, via some kind of driving on the system determined by $\mathbf{x}$, such as considered in [δ]. We formally denote this time evolution with the dynamical map $\mathcal{M}_{\mathbf{x}}(t)$, which gives the state of the evolved physical system at a later time: $\hat{\rho}_{\mathbf{x}}(t) = \mathcal{M}_{\mathbf{x}}(t)[\hat{\rho}_0]$. During this time evolution, a set of observables $\{\hat{O}_i\}_i$ are measured at different times $\{t_j\}_j$. [We assume ensemble measurements for quantum systems, such that we can measure the expectation values of multiple (possibly noncommuting) observables.] The input $\mathbf{x}$ is therefore transformed into a feature vector $\boldsymbol{X}(\mathbf{x})$ containing N_{feat} features of the form $\mathrm{Tr}[\hat{\rho}_{\mathbf{x}}(t_j)\hat{O}_i]$ (the order does not matter). Finally, the trial function is obtained by linearly transforming the feature vector: $\hat{f}(\mathbf{x}) = \boldsymbol{w}^T\boldsymbol{X}(\mathbf{x})$, and the components of $\boldsymbol{w}$ are the linear weights to be optimized.

reservoir computing or extreme learning learning machines [262], which will be the main focus of this chapter.

II.1 Reservoir computing

The architecture of reservoir-computing models can be viewed as a simplified version of neural networks, such that the parameters in the network are randomly fixed and not optimized, except for those in the final linear output layer. Therefore, the construction of the trial function $\hat{f}(\mathbf{x})$ can be seen as a two-fold procedure:

1. the input $\mathbf{x}$ is transformed into a *feature vector* $\boldsymbol{X}(\mathbf{x})$ via the fixed neural network, whose action can be formally viewed as a *feature map* $\boldsymbol{X}(\bullet)$ from the input space to the *feature space*;

2. The feature vector is linearly transformed to yield the trial function[2]

$$\hat{f}(\mathbf{x}) = \boldsymbol{w}^T\boldsymbol{X}(\mathbf{x})\,, \tag{5.1}$$

[2]In the case of a *classification* problem, i.e. where the target function $f(\mathbf{x})$ attributes the input $\mathbf{x}$ to a class (out of a finite number of possible classes), the prediction given by the trial function $\hat{f}(\mathbf{x})$ is to be understood up to a discretization of its output value. For example, in a binary classification problem, a popular choice is to associate the sign of the trial function $\mathrm{sgn}[\hat{f}(\mathbf{x})]$ to the predicted classes.

where $\boldsymbol{w}$ represents the linear weights to be optimized.

Note that the feature map $\boldsymbol{X}(\bullet)$ in the step (1) above is a fixed transformation that contains no parameter to be optimized. This makes reservoir computing particularly suitable for implementation in physical systems, since one can exploit the natural dynamics of a system to perform the feature map that transforms the input, while requiring very little control[3] over the system. The general scheme of constructing a reservoir-computing trial function using a physical system is represented in Fig. 5.1. The system is subject to some time dynamics depending on the input $\mathbf{x}$, and then several system observables are measured at different times to yield the feature vector $\boldsymbol{X}(\mathbf{x})$ of length N_{feat}. In order for the trial function $\hat{f}(\mathbf{x}) = \boldsymbol{w}^T \boldsymbol{X}(\mathbf{x})$ to be expressive (i.e., to be able to approximate many classes of functions), one typically expects the physical system to have rich dynamics, such that the feature map $\boldsymbol{X}(\bullet)$ is very nontrivial, which is why such physical systems are referred to as "reservoirs" in the context of reservoir computing.

II.2 Optimization

Given the training set $\mathcal{S} = \{(\mathbf{x}^{(i)}, y^{(i)})\}_i^{N_{\text{train}}}$, the optimal weights can be determined by minimizing a cost function of the form

$$\mathcal{C}(\boldsymbol{w} \mid \mathcal{S}) = \frac{1}{N_{\text{train}}} \sum_{i=1}^{N_{\text{train}}} \mathcal{E}\Big(y^{(i)}, \hat{f}(\mathbf{x}^{(i)})\Big) + l \cdot J(\boldsymbol{w}) \,, \quad \boldsymbol{w}_\star = \underset{\boldsymbol{w}}{\operatorname{argmin}}\{\mathcal{C}(\boldsymbol{w} \mid \mathcal{S})\} \,, \tag{5.2}$$

where $\mathcal{E}(y^{(i)}, \hat{f}(\mathbf{x}^{(i)}))$ is a pointwise error function that measures the prediction error of the trial function for the i-th sample point in the training set, and $J(\boldsymbol{w})$ is a penalty function that is generally chosen to be increasing with the norm of $\boldsymbol{w}$, and l is known as the *regularization* parameter that controls the strength of the penalty. This regularization term can be understood as a soft cutoff on the number of free parameters in the model, which serves to prevent overfitting. In this chapter, we will consider the error function to be the squared error:

$$\mathcal{E}\Big(y^{(i)}, \hat{f}(\mathbf{x}^{(i)})\Big) = \frac{1}{2}\Big(y^{(i)} - \hat{f}(\mathbf{x}^{(i)})\Big)^2 \,, \tag{5.3}$$

which is a popular choice for regression and corresponds to least square problems. It has also been shown to perform well for classification [263], although most classification problems are commonly treated with other cost error functions [259]. We also choose the so-called L_2 regularization, which takes the form

$$J(\boldsymbol{w}) = \frac{1}{2}\|\boldsymbol{w}\|_2^2 = \frac{1}{2}\sum w_i^2 \,. \tag{5.4}$$

This regularization is (on average) equivalent to having a zero-mean Gaussian noise of variance l in the measured features [i.e. components of the feature vector $\boldsymbol{X}(\mathbf{x})$] [50]. These choices completely define the cost function:

$$\mathcal{C}(\boldsymbol{w} \mid \mathcal{S}) = \frac{1}{2N_{\text{train}}} \sum_{i=1}^{N_{\text{train}}} \Big(y^{(i)} - \boldsymbol{w}^T \boldsymbol{X}(\mathbf{x}^{(i)})\Big)^2 + \frac{l}{2}\|\boldsymbol{w}\|_2^2 \,, \tag{5.5}$$

[3] This is opposed to implementing neural networks in physical systems, where extremely accurate control would be required since the network parameters should be updated during the optimization.

whose minimization is a convex problem and can be analytically solved by setting

$$\frac{\partial}{\partial \boldsymbol{w}} (\boldsymbol{w} \mid \mathcal{S}) = 0 \,. \tag{5.6}$$

Denoting $\boldsymbol{\Phi}$ the $N_{\text{feat}} \times N_{\text{train}}$ matrix whose j-th column is $\boldsymbol{X}(\mathbf{x}^{(j)})$, and $\boldsymbol{y}$ the column vector of the training labels $y^{(i)}$, the solution to the equation above can be written as

$$\boldsymbol{w}_\star = (\boldsymbol{\Phi}\boldsymbol{\Phi}^T + lN_{\text{train}}\mathbb{1})^{-1}\boldsymbol{\Phi}\boldsymbol{y} \,. \tag{5.7}$$

II.3 The kernel point of view

The representation of the input data in the feature space via the feature map realized by the reservoir is best understood by introducing the kernel function [259]

$$k(\mathbf{x}, \mathbf{x}') = \boldsymbol{X}(\mathbf{x}')^T \boldsymbol{X}(\mathbf{x}) \,, \tag{5.8}$$

which is a scalar product in the feature space, and can be understood as a measure of similarity between two inputs $\mathbf{x}$ and $\mathbf{x}'$. As this function is symmetric and positive-definite, Mercer's theorem [264, 265] guarantees that the kernel function admits an eigendecomposition of the form:

$$k(\mathbf{x}, \mathbf{x}') = \sum_i \gamma_i \psi_i(\mathbf{x}) \psi_i(\mathbf{x}') \,, \tag{5.9}$$

where $\{\gamma_i\}_i$ are the positive (due to the positivity of the kernel function) eigenvalues and $\{\psi_i\}_i$ are the associated eigenfunctions which are orthonormal with respect to the inner product on L^2_μ [the space of square-integrable functions on the input space with respect to the probability measure $\mu(\mathrm{d}\mathbf{x})$]:

$$\langle \psi_i, \psi_j \rangle \equiv \int \mu(\mathrm{d}\mathbf{x}) \psi_i(\mathbf{x}) \psi_j(\mathbf{x}) = \delta_{ij} \,. \tag{5.10}$$

The eigendecomposition (5.9) can be found by solving the eigenvalue problem:

$$\int \mu(\mathrm{d}\mathbf{x}) k(\mathbf{x}, \mathbf{x}') \psi(\mathbf{x}') = \gamma \psi(\mathbf{x}) \,, \tag{5.11}$$

which can be empirically estimated from a set of samples drawn from the input distribution $\mu(\mathrm{d}\mathbf{x})$, for example the training set[4]. Indeed, one can approximate the distribution $\mu(\mathrm{d}\mathbf{x})$ by the empirical one [266]:

$$\check{\mu}(\mathrm{d}\mathbf{x}) = \frac{1}{N_{\text{train}}} \sum_{i=1}^{N_{\text{train}}} \delta\Big(\mathbf{x} - \mathbf{x}^{(i)}\Big) \mathrm{d}\mathbf{x} \,. \tag{5.12}$$

This translates Eq. (5.11) into a discrete eigenvalue problem:

$$\frac{1}{N_{\text{train}}} \sum_{i=1}^{N_{\text{train}}} k\Big(\mathbf{x}^{(j)}, \mathbf{x}^{(i)}\Big) \check{\psi}\Big(\mathbf{x}^{(i)}\Big) = \check{\gamma} \check{\psi}\Big(\mathbf{x}^{(j)}\Big) \,, \ \forall j. \tag{5.13}$$

[4] Note that target output values associated to the inputs are not required to estimate this eigendecomposition. In other words, the eigendecomposition only depends on the distribution of the input data and is independent on the specific task.

The empirical eigenvalues $\check{\gamma}$ are therefore the nonzero eigenvalues of the matrix $\mathbf{K}/N_{\text{train}}$ where $\mathbf{K}$ is known as the *empirical kernel matrix* defined by

$$\mathrm{K}_{ij} \equiv k\Big(\mathbf{x}^{(i)}, \mathbf{x}^{(j)}\Big)\,. \tag{5.14}$$

Recalling that we previously defined $\Phi_{ij} = X_i(\mathbf{x}^{(j)})$, it follows that

$$\mathbf{K} = \mathbf{\Phi}^T\mathbf{\Phi}\,, \tag{5.15}$$

which is a matrix of size $N_{\text{train}} \times N_{\text{train}}$. As one can easily check[5], $\mathbf{K}$ shares the same nonzero eigenvalues with the $N_{\text{feat}} \times N_{\text{feat}}$ matrix $\mathbf{k} \equiv \mathbf{\Phi}\mathbf{\Phi}^T$. As we will be working in the regime where the dataset contains much more samples than the number of features, i.e. $N_{\text{train}} \gg N_{\text{feat}}$, it is therefore more suitable to diagonalize the smaller matrix $\mathbf{k}/N_{\text{train}}$ to find the empirical spectrum of the kernel.

We now show that the spectrum of the kernel contains crucial information on the expressivity of the reservoir-computing model. The set of kernel eigenfunctions $\{\psi_i\}_i$ can be completed to be an orthonormal basis of L^2_μ by including eigenfunctions associated with $\gamma_i = 0$. The trial function (5.1) can then be expanded in the above kernel eigenbasis as

$$\begin{aligned}\hat{f}(\mathbf{x}) &= \sum_i w_i X_i(\mathbf{x}) \\ &= \sum_{i,j} w_i \langle \psi_j, X_i\rangle \psi_j(\mathbf{x}) \\ &\equiv \beta_j \psi_j(\mathbf{x})\,,\end{aligned} \tag{5.16}$$

where $\{\beta_j\}_j$ are the weights to be optimized, which can be viewed as the independent degrees of freedom (due to the orthogonality of the eigenbasis) of the model. It then follows [259] that the regularization penalty (5.4) in the cost function (5.5) becomes

$$J(\boldsymbol{w}) = \frac{1}{2}\|\boldsymbol{w}\|_2^2 = \frac{1}{2}\sum_j \frac{\beta_j^2}{\gamma_j} \tag{5.17}$$

in the kernel eigenbasis representation. The effect of the regularization becomes clear: the smaller the eigenvalue γ_j, the more the corresponding eigenfunction ψ_j is penalized (i.e. it cannot have a large weight in the trial function). In other words, the regularization acts as a soft cutoff on the eigenfunctions such that those with vanishingly small associated eigenvalues do not contribute to the trial function [258], and vice versa. One can therefore use the kernel spectrum to assess the expressivity of the model *without* training on a specific task.

III Relativistic quantum reservoir-computing model

Let us now exploit the framework of reservoir computing in the context of relativistic quantum information. Consider the paradigmatic model describing a quantum harmonic

[5] Consider the eigenvalue problem $\mathbf{\Phi}^T\mathbf{\Phi}\boldsymbol{u} = \lambda\boldsymbol{u}$ for some $\lambda \neq 0$ and $\boldsymbol{u} \neq \mathbf{0}$ (therefore $\mathbf{\Phi}\boldsymbol{u} \neq \mathbf{0}$). Premultiplication by $\mathbf{\Phi}$ gives $(\mathbf{\Phi}\mathbf{\Phi}^T)(\mathbf{\Phi}\boldsymbol{u}) = \lambda(\mathbf{\Phi}\boldsymbol{u})$, i.e. λ is also an eigenvalue of $\mathbf{\Phi}\mathbf{\Phi}^T$.

detector with proper frequency Ω, minimally coupled to a quantum field $\hat{\phi}$ inside an optical cavity that stationarily lies in (1+1)D Minkowski spacetime. As we have derived in Sec. IV.2 of Chapter 1, the interaction-picture Hamiltonian takes the Unruh-DeWitt form [90, 100, 103]

$$\hat{H}(\tau) = \lambda \hat{m}(\tau)\hat{\phi}[x^{\mu}(\tau)]\,, \tag{5.18}$$

where τ is the proper time of the detector, λ is the coupling constant, and $\hat{m}(\tau) = \hat{b}\mathrm{e}^{-\mathrm{i}\Omega\tau} + \hat{b}^{\dagger}\mathrm{e}^{\mathrm{i}\Omega\tau}$ is the monopole operator of the detector that depends on its annihilation (creation) operator $\hat{b}$ ($\hat{b}^{\dagger}$). Finally, $x^{\mu}(\tau) = (t(\tau), x(\tau))$ is the world line of the detector.

In the scenario involving no exchange of angular momentum, the cavity field $\hat{\phi}$ can be well approximated by a massless scalar field. For a cavity with perfectly reflecting mirrors [224, 267], the quantum field admits the following mode expansion (see Appendix B):

$$\hat{\phi}(t,x) = \sum_{n=1}^{\infty} \frac{1}{\sqrt{\omega_n L}} \left(\mathrm{e}^{-\mathrm{i}\omega_n t}\hat{a}_n + \mathrm{e}^{\mathrm{i}\omega_n t}\hat{a}_n^{\dagger}\right) \sin(k_n x)\,, \tag{5.19}$$

where $\omega_n = k_n = n\pi/L$ and L is the cavity length. The mode operators (denoting $\hat{a}_0 \equiv \hat{b}$ for the detector) satisfy bosonic commutation relations $[\hat{a}_n, \hat{a}_m^{\dagger}] = \delta_{nm}$. The full interaction Hamiltonian is therefore

$$\begin{aligned}\hat{H}(\tau) = \lambda \sum_{n=1}^{\infty} \frac{\sin[k_n x(\tau)]}{\sqrt{L\omega_n}} \times \\ \left(\hat{b}\hat{a}_n \mathrm{e}^{-\mathrm{i}[\Omega\tau + \omega_n t(\tau)]} + \hat{b}\hat{a}_n^{\dagger}\mathrm{e}^{-\mathrm{i}[\Omega\tau - \omega_n t(\tau)]}\right) + \mathrm{H.c.}\,,\end{aligned} \tag{5.20}$$

where both rotating and counter-rotating terms are present and contribute in the non-inertial regime [99, 120, 224, 268].

Let us prepare the cavity in a single-mode coherent state $|\alpha_{\omega_i}\rangle$ whose frequency is resonant with that of the detector [224, 267]. As shown in [224], for a qubit detector undergoing constant acceleration for a finite period of time in a cavity prepared in a single-mode coherent state, the main effect (of first order in λ) in the qubit dynamics is a coherent rotation on the Bloch sphere instead of thermalization (e.g. Unruh effect[6]), which is of second order in λ. This therefore serves to amplify the noninertial effects on the detector dynamics. Let us also consider the detector initially in its ground state $\hat{\rho}_{0,(a)} = |0_a\rangle\langle 0_a|$. The initial density matrix of the detector-cavity ensemble then reads:

$$\hat{\rho}_0 = \hat{\rho}_{0,(a)} \otimes |\alpha_{\omega_i}\rangle\langle\alpha_{\omega_i}| \otimes \bigotimes_{j\neq i} |0_{\omega_j}\rangle\langle 0_{\omega_j}|. \tag{5.21}$$

For a given $x^{\mu}(\tau)$, the time evolution of the density matrix is given by

$$\frac{\mathrm{d}\hat{\rho}(\tau)}{\mathrm{d}\tau} = -\mathrm{i}[\hat{H}(\tau), \hat{\rho}(\tau)]. \tag{5.22}$$

Since all the considered modes are bosonic and the Hamiltonian is quadratic, the Gaussianity of the initial state is preserved during the evolution. The dynamics of $\hat{\rho}(\tau)$ can therefore be solved exactly using the covariance-matrix formalism for Gaussian states [103, 269–271] (see Appendix D).

[6] Unruh effect in a cavity has been studied in [103].

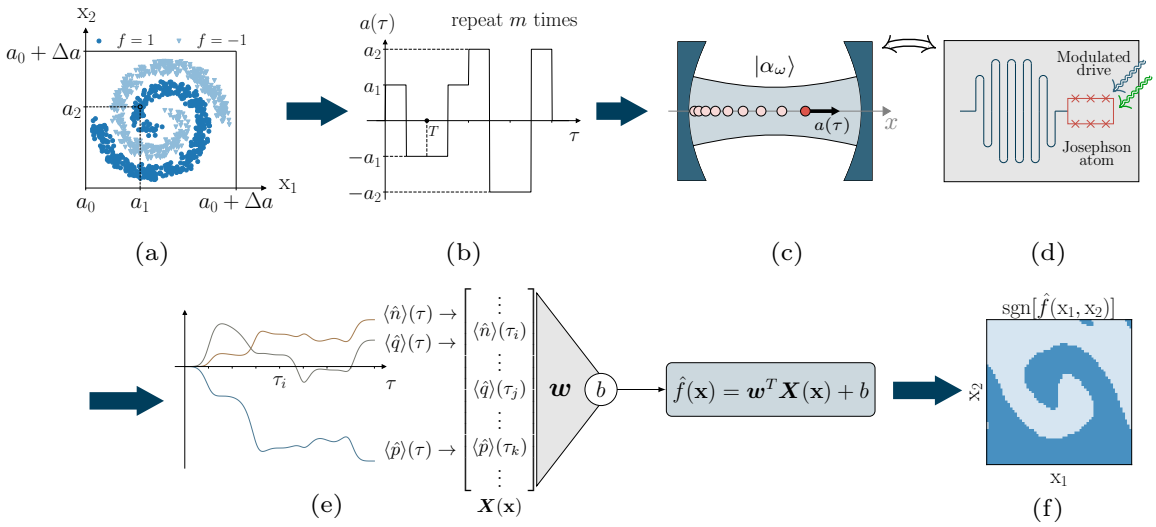

Figure 5.2: Scheme of the relativistic reservoir-computing protocol illustrated with a binary classification task. (a) Each input $\mathbf{x}=(x_1,x_2)$ of the dataset is linearly mapped to acceleration values (a_1,a_2) according to Eq. (5.23). (b) The acceleration values are used to construct a piecewise-constant acceleration profile $a(\tau)$. (c) The quantum detector, initially at rest in the cavity prepared in a single-mode coherent state, undergoes noninertial motion with proper acceleration $a(\tau)$. (d) Analog circuit QED system where the analogous of the proper acceleration is controlled by modulated driving fields. (e) Observables of the detector are measured at different times giving the feature vector $\boldsymbol{X}(\mathbf{x})$ and the affine trial function $\hat{f}(\mathbf{x})=\boldsymbol{w}^T\boldsymbol{X}(\mathbf{x})+b$. (f) The classification result is predicted by $\mathrm{sgn}[\hat{f}(x_1,x_2)]$.

III.1 Reservoir-computing protocol

Now we show how the dynamics of the considered relativistic quantum system can be harnessed to perform reservoir-computing tasks. The goal is to learn a (nonlinear) function $f(\mathbf{x})$ of the D-dimensional input $\mathbf{x}=(x_1,x_2,\ldots,x_D)$. In the framework of reservoir computing, our system is used to perform the feature map $\boldsymbol{X}(\bullet)$ obtained in a two-step procedure:

(i) each input $\mathbf{x}$ determines a specific world line of the detector;

(ii) a set of observables of the detector are measured at different times to yield the feature vector $\boldsymbol{X}(\mathbf{x})$.

This is schematically represented in Fig. 5.2, which can be viewed as an explicit example of the general scheme presented in Fig. 5.1.

Assuming that for every component x_i in the input vector $\mathbf{x}$ we have $x_{i,\min}\leq x_i\leq x_{i,\max}$, we map them linearly to acceleration values in a fixed range between a_0 and $a_0+\Delta a$, namely

$$x_i\mapsto a_i=a_0+\Delta a\times\frac{x_i-x_{i,\min}}{x_{i,\max}-x_{i,\min}}. \tag{5.23}$$

We then impose a piecewise-constant proper acceleration [272] $a(\tau)$ to the harmonic detector. The pieces have proper acceleration values $(a_1, -a_1, -a_1, a_1, \cdots, a_N, -a_N, -a_N, a_N)$ and each piece has a duration of $T/2$ in the proper frame of the detector, and we repeat this encoding sequence m times. Assuming the detector to be initially at rest at $x^\mu(\tau = 0) = (t = 0, x = 0)$, this acceleration profile guarantees that at each instant $\tau = nT$, $n \in \mathbb{N}$, the detector is at rest, and that at $\tau = 2nT$ it comes back to its original spatial position at $x = 0$. Note that for a circuit QED implementation the modulation of the driving fields can directly control the analog of the proper acceleration with respect to the proper time τ (see Sec. IV.1). The detector world line for a general proper acceleration $a(\tau)$ is (see Appendix C for a derivation)

$$x(\tau) = \int_0^\tau \mathrm{d}\tau' \sinh[\xi(\tau')]\,,\ t(\tau) = \int_0^\tau \mathrm{d}\tau' \cosh[\xi(\tau')], \tag{5.24}$$

where $\xi(\tau) = \int_0^\tau \mathrm{d}\tau' a(\tau')$ is the rapidity [273]. Instead, in the Newtonian case, the (unphysical) world line is simply

$$x_{\mathrm{Newt}}(\tau) = \int_0^\tau \mathrm{d}\tau' \xi(\tau')\,,\ t_{\mathrm{Newt}}(\tau) = \tau. \tag{5.25}$$

Each input data point $\mathbf{x}$ determines a single time evolution of the system $\hat{\rho}(\tau)$. We can then measure the detector at times $\tau_n = n \times \Delta T$ to obtain the expectation values of the quadrature operators $\hat{q} = (\hat{b} + \hat{b}^\dagger)/\sqrt{2}$, $\hat{p} = \mathrm{i}(\hat{b}^\dagger - \hat{b})/\sqrt{2}$ and of the number operator $\hat{n} = \hat{b}^\dagger \hat{b}$. The measurements are then collected into a feature vector $\boldsymbol{X}(\mathbf{x})$ [46] [see Fig. 5.2(e)]. Finally, our trial function reads

$$\hat{f}(\mathbf{x}) = \boldsymbol{w}^T \boldsymbol{X}(\mathbf{x}) + b, \tag{5.26}$$

where the weight $\boldsymbol{w}$ and bias b are parameters to be optimized in order for $\hat{f}$ to approximate the target function f. To simplify the notation, in the following we will absorb b into the vector $\boldsymbol{w}$ by appending a constant component 1 to the vector $\boldsymbol{X}(\mathbf{x})$. This gives back our trial function the form $\hat{f}(\mathbf{x}) = \boldsymbol{w}^T \boldsymbol{X}(\mathbf{x})$ as considered previously in the general framework introduced in Sec. II.

IV Results and discussion

As an illustrative example, we consider a nontrivial task: the two-spiral classification problem [274]. The goal is to distinguish two interlocking spiral planar patterns. This task serves as a well-known benchmark for binary pattern classification that is considered hard for multi-layer perceptron models due to its complicated decision boundary [275]. The input data are the two coordinates of each point in the two-spiral pattern $\mathbf{x} = (\mathrm{x}_1, \mathrm{x}_2)$. The task function f to be learned is such that $f(\mathbf{x}) = 1$ if the point belongs to the first spiral branch, and $f(\mathbf{x}) = -1$ for the other branch [see Fig. 5.2(a)]. To train the model, we draw a training dataset of $N_{\mathrm{train}} = 4000$ sample points $\{\mathbf{x}^{(1)}, \mathbf{x}^{(2)}, \cdots, \mathbf{x}^{(N_{\mathrm{train}})}\}$ with labels $y^{(i)} = f(\mathbf{x}^{(i)})$ and minimize the L_2-regularized least-square cost function (5.5), and the optimal weights are given by (5.7). The performance of the model is then evaluated

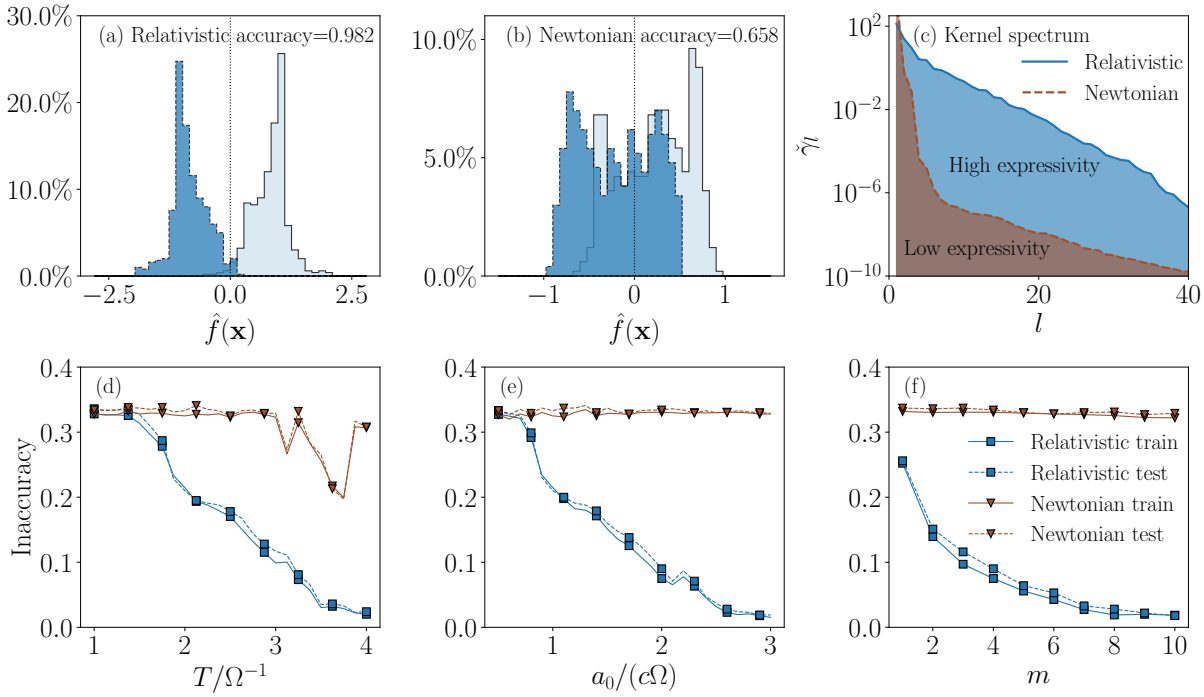

Figure 5.3: Figures of merit of the relativistic reservoir-computing protocol evaluated on the two-spiral classification problem. (a) The distribution of the testing samples in the feature space represented by $\hat{f}(\mathbf{x})$. Light and dark histograms correspond to samples belonging to different branches of the spiral pattern. Parameters: $a_0 = 3$, $T = 2$ and $m = 4$. (b) Same quantity plotted for the Newtonian model with the same parameters. (c) The empirical kernel spectrum computed for the relativistic (solid line) and Newtonian (dashed line) models with same parameters. The first 40 nonzero empirical eigenvalues $\check{\gamma}_l$ are plotted in descending order. (d) Inaccuracy of the relativistic (triangles) and Newtonian (squares) models evaluated on both the training (solid lines) and testing (dashed lines) set, as a function of the acceleration time T. Parameters: $a_0 = 1$ and $m = 4$. (e) Same quantities plotted as a function of the base acceleration a_0, for $T = 2$ and $m = 4$. (f) Same quantities plotted as a function of the number of repetitions m, for $a_0 = 2$ and $T = 2$. Quantities are expressed in natural units, where the scale is fixed by the proper frequency of the atom Ω.

on a testing set with $N_{\text{test}} = 1000$ points. We evaluate the classification accuracy $\mathcal{A}_{\text{test}}$ on the testing samples as the fraction of correctly classified points among N_{test}. The training accuracy $\mathcal{A}_{\text{train}}$, which indicates how well the reservoir-computing model fits the training set, is defined analogously.

Throughout our simulations, we fixed the coupling constant to $\lambda = 0.1\Omega$, the interval of measurement to $\Delta T = T/2$ and $\Delta a/a_0 = 0.1$. The detector's proper frequency is set to be resonant with the third cavity mode[7] $\Omega = \omega_3$, the latter being initially in a coherent state $|\alpha\rangle$ with $\alpha = 10\mathrm{i}$. We express all quantities in natural units with the scale fixed by Ω. The

[7]This is to ensure that the cavity is long enough for the atom to remain inside. For the circuit QED implementation this is not an important detail.

regularization is set to $l = 10^{-6}$; this is equivalent to having a Gaussian measurement noise of variance l in the observables [50]. Fig. 5.3(a) shows the distribution of testing samples in feature space, represented by $\hat{f}(\mathbf{x})$. The same quantities are plotted in Fig. 5.3(b) in a non-relativistic setting, that is, considering Newtonian world lines [Eq. (5.25)]. As appears from Fig. 5.3(a) and (b), the relativistic model correctly separates the two classes with high accuracy. By contrast, the system undergoing unphysical Newtonian dynamics exhibits a poor performance. The empirical kernel spectra of the two models are plotted in Fig. 5.3(c), where we show the first 40 nonzero eigenvalues in descending order. The flatter distribution of the relativistic kernel spectrum implies that for a fixed cutoff threshold on the eigenvalues (or a fixed regularization [258]), it has more eigenfunctions with nonzero eigenvalues that can contribute to the expressivity of the trial function $\hat{f}$ in comparison with the Newtonian model. Importantly, this relativistically enhanced kernel expressivity associated to the dynamics is *task-independent* and explains the much higher accuracy achieved by the relativistic model for the specific two-spiral classification task.

In Fig. 5.3(d), we examine the impact of the acceleration time T on the performance of the model. As T increases, the inaccuracy $(1 - \mathcal{A})$ of the relativistic model decreases to around 0, whereas the performance of the Newtonian model remains poor. This is consistent with the results of Fig. 5.3(e), where we vary the base acceleration a_0 for fixed T. Therein, we also found the inaccuracy of the relativistic model to be decreasing as a function of a_0 as the motion enters the relativistic regime, and a poor performance of the Newtonian model, which remains insensitive to a_0.

In Fig. 5.3(f) we study the effect of the number of repetitions m of the encoding sequence on the performance. As we are taking measurements at a constant interval ΔT, a larger value of m allows for more features to be collected in the feature vector $\boldsymbol{X}(\mathbf{x})$, improving the efficiency. By contrast, in the Newtonian setting, the supplementary features are close-to-linearly related to the previous ones, thus yielding a negligible improvement. The induced nonlinearity of the feature map associated to the dynamics of the relativistic reservoir ensures that the generated features remain nontrivial after many repetitions. The advantage of the relativistic model can be understood from Eq. (5.20). Indeed, as discussed in Ref. [224], the phases $\mathrm{e}^{-\mathrm{i}[\Omega\tau \pm \omega_n t(\tau)]}$ depend nontrivially on τ due to the relativistic (time-dilation) effects, which yields an input-dependent modulation of the cavity-detector resonance condition, absent in the Newtonian model, where one always has $t_{\mathrm{Newt}}(\tau) = \tau$.

IV.1 Implementation with circuit QED

The accelerations considered in the presented scheme are on the order of $c\Omega$, which is proportional to the detector's proper frequency. As discussed in [224], for a detector gap on the order of GHz, this corresponds to an acceleration of $10^{16}g$ (where g is the Earth's surface gravitational acceleration) and is far beyond experimental reach, which is common for almost all existing proposals for relativistic quantum information. However, as shown in the literature [226], the Hamiltonian (5.20) can be synthesized on circuit QED platforms.

We hereby present a potential analog implementation of the proposed relativistic model with circuit QED inspired by [226], which consists of a Josephson artificial atom with

bosonic mode operator $\hat{b}$ (simulating the harmonic oscillator detector) coupled to a transmission line microwave cavity in the strong-coupling regime [see Fig. 5.2(d)]. Denoting the microwave cavity mode operator by $\hat{a}$, the noninteracting Hamiltonian of the system is

$$\hat{H}_0(\tau) = \omega_0 \hat{a}^\dagger \hat{a} + \epsilon \hat{b}^\dagger \hat{b} + \eta \zeta(\tau) \hat{b}^\dagger \hat{b}\,, \tag{5.27}$$

where ω_0 is the cavity bare frequency, ϵ is the energy of the artificial atom, and we assumed that the Josephson junction has negligible nonlinearity. This can be achieved for example by replacing a single Josephson junction with a sufficiently long chain of junctions[8]. The opposite extreme case, where the Josephson atom is a two-level system (qubit), yields similar results, as revealed by corresponding simulations reported in Section IV.2. $\zeta(\tau)$ is a driving function that takes the following form[9]:

$$\begin{aligned} \zeta(\tau) &= \frac{\mathrm{d}}{\mathrm{d}\tau} F(\tau)\,, \\ F(\tau) &= F_+(\tau) + F_-(\tau)\,, \end{aligned} \tag{5.28}$$

where

$$F_\pm = \cos[\omega_\pm \tau \mp \theta_\mp(\tau)] - \cos[\omega_\pm \tau \mp \theta_\pm(\tau)]\,. \tag{5.29}$$

Assuming that the phases $\theta_\pm(\tau)$ are modulated slowly compared to the driving frequencies $\omega_\pm$, as will indeed be the case in what follows, the driving function $\zeta(\tau)$ can be well approximated by

$$\begin{aligned} \zeta(\tau) \simeq &- \omega_+ \sin[\omega_+ \tau - \theta_-(\tau)] \\ &+ \omega_+ \sin[\omega_+ \tau - \theta_+(\tau)] \\ &- \omega_- \sin[\omega_- \tau + \theta_+(\tau)] \\ &+ \omega_- \sin[\omega_- \tau + \theta_-(\tau)]. \end{aligned} \tag{5.30}$$

The interaction Hamiltonian in the Schrödinger picture is $\hat{H}_I = g(\hat{b}^\dagger + \hat{b})(\hat{a} + \hat{a}^\dagger)$. Passing to the interaction picture with respect to $\hat{H}_0(\tau)$ and assuming $\eta \ll 1$ in the driving term, we get

$$\begin{aligned} \hat{H}_I(\tau) =& g[\hat{b}^\dagger \mathrm{e}^{\mathrm{i}\epsilon\tau} \mathcal{G}(\tau) + \text{H.c.}](\hat{a}\mathrm{e}^{-\mathrm{i}\omega_0\tau} + \text{H.c.})\,, \\ \mathcal{G}(\tau) =& \mathrm{e}^{\mathrm{i}\eta F(\tau)} \simeq 1 + \mathrm{i}\eta F(\tau)\,. \end{aligned} \tag{5.31}$$

To simulate a harmonic oscillator with proper frequency Ω and world line $x^\mu(\tau) = (t(\tau), x(\tau))$ coupled to the n-th mode of a massless scalar field of frequency $\omega_n = k_n$ as considered in our protocol, we now choose $\omega_\pm = \epsilon \pm \omega_0 - \Omega$ as the driving frequencies and $\theta_\pm(\tau) = \omega_n t(\tau) \pm k_n x(\tau)$ as the phase modulations. In the regime where ϵ, ω_0, $|\epsilon \pm \omega_0| \gg g$, the interaction Hamiltonian becomes (keeping only slowly rotating terms)

$$\begin{aligned} \hat{H}_I(\tau) \simeq& g\eta \sin[k_n x(\tau)] \times \\ & \hat{b}(\hat{a}\mathrm{e}^{-\mathrm{i}[\Omega\tau + \omega_n t(\tau)]} + \hat{a}^\dagger \mathrm{e}^{-\mathrm{i}[\Omega\tau - \omega_n t(\tau)]}) + \text{H.c.}\,, \end{aligned} \tag{5.32}$$

[8]The anharmonicity of a Josephson atom can be made arbitrarily small by replacing a junction by a chain of junctions, as the anharmonicity scales as $1/N_J^2$ where N_J is the number of junctions

[9]Note that our driving term is different from that in [226], as they considered simulating a quantum field in free space, while in the present work, the simulated quantum field is confined within a cavity with Dirichlet boundary conditions, resulting in different mode functions.

which takes the form of the interaction Hamiltonian (5.20) for a single mode of the quantum field. Note that since we always consider a single-mode coherent state as the field initial state in our model, the main contribution to the dynamics of the harmonic oscillator comes uniquely from this mode, as one can verify using perturbation theory [224]. We also checked numerically that a single-mode approximation for the quantum field is enough for obtaining accurate results for the simulations presented in this chapter. Nonetheless, it is possible to simulate the full many-mode Hamiltonian by using multiple modes in the circuit QED microwave cavity.

As considered in [226], the energy scales ϵ and ω_0 for circuit QED are in the GHz regime, while g, Ω and ω_n can be on much slower time scales, such as in the MHz regime. The modulation rate of the phases $\dot{\theta}_\pm(\tau)$ can be expressed in terms of the simulated time-dependent acceleration $a(\tau)$ as [using the world line in Eq. (C.5)]

$$\begin{aligned}\dot{\theta}_\pm(\tau) &= \frac{\mathrm{d}}{\mathrm{d}\tau}[\omega_n t(\tau) \pm k_n x(\tau)] \\ &= \omega_n \cosh[\xi(\tau)] \pm k_n \sinh[\xi(\tau)] \\ &= \omega_n \cosh\left[\int_0^\tau \mathrm{d}\tau' a(\tau')\right] \pm k_n \sinh\left[\int_0^\tau \mathrm{d}\tau' a(\tau')\right].\end{aligned} \tag{5.33}$$

Let us consider a typical world line studied in our simulations, for example with $a_0 = 2$, $\Delta a/a_0 = 0.1$, $T = 2$ and $\omega_n = \Omega$ [the values used in Fig. 5.3(f)] in the units fixed by Ω. Then, we have $\dot{\theta}_\pm(\tau) \lesssim 10\Omega$, meaning that the phases in the driving (5.29) need to be modulated at roughly the same timescale as Ω, in the MHz band, which is much slower than the circuit QED timescales and should be experimentally feasible.

Finally, let us consider a concrete example of typical parameter values of the analog circuit QED system. Let the parameters of the system be $\omega_0 = 1\,\mathrm{GHz}$, $\epsilon = 1.1\,\mathrm{GHz}$, $\Omega = 1\,\mathrm{MHz}$, $g = 10/\sqrt{3\pi}\,\mathrm{MHz} \simeq 3.3\,\mathrm{MHz}$, $\eta = 0.01$. The driving frequencies are then $\omega_+ = 2.099\,\mathrm{GHz}$ and $\omega_- = 0.099\,\mathrm{GHz}$. This simulates the harmonic detector coupled to the $n = 3$ mode of the quantum field (with $\Omega = \omega_n = k_n$ and $\lambda = 0.1\Omega$) as considered in our simulations. To simulate the acceleration sequence in our protocol for the case of $a_0 = 2$, $\Delta a/a_0 = 0.1$ and $T = 2$, the required phase modulations $\theta_\pm(\tau)$ as well as their rates $\dot{\theta}(\tau)$, given by Eq. (5.33), are plotted in Fig. 5.4.

IV.2 Results with a qubit instead of a harmonic oscillator

We report here the simulation results when we replace the harmonic detector with a qubit (two-level atom initially in its ground state) for the same parameters considered in the simulations with a harmonic detector. To model the configuration with the qubit, we have to replace the bosonic mode operator $\hat{b}$ with the Pauli operator $\hat{\sigma}^-$ in the Hamiltonian. Since the Gaussian formalism can no longer be applied, we assumed a single-mode approximation for the quantum field (considering only the mode that is initially in the coherent state and in resonance with the proper frequency of the qubit), which matches the exact form of the single-mode circuit-QED Hamiltonian in Eq. (5.32). The feature vector now contains the expectation values of the operators that are respectively analogous to the bosonic occupation number and the quadratures, namely $\hat{\sigma}^+\hat{\sigma}^-$, $(\hat{\sigma}^- + \hat{\sigma}^+)/\sqrt{2}$ and $\mathrm{i}(\hat{\sigma}^+ - \hat{\sigma}^-)/\sqrt{2}$. This is equivalent to measuring the Pauli operators $\hat{\sigma}^z$, $\hat{\sigma}^x$ and $\hat{\sigma}^y$

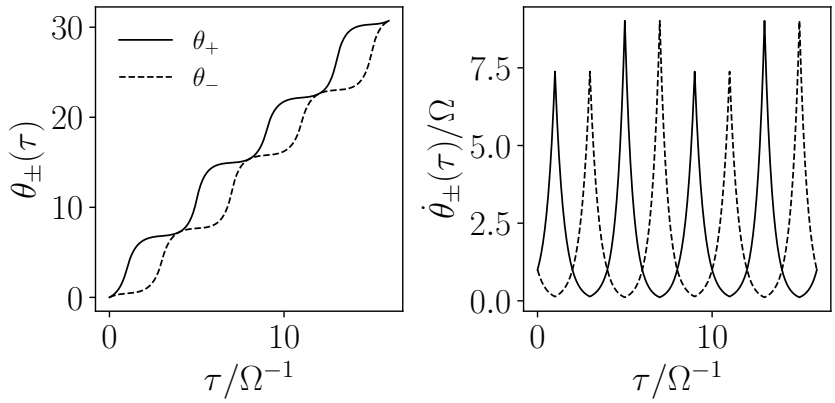

Figure 5.4: The phase modulations $\theta_\pm(\tau)$ (left panel) and the corresponding rates $\dot{\theta}_\pm(\tau)$ that provide the desired simulation of the accelerated motion, where $\Omega = 1\,\mathrm{MHz}$. Note that modulation rates are in the regime of $\dot{\theta}_\pm(\tau) \lesssim 10\Omega = 10\,\mathrm{MHz}$.

respectively. The counterparts of Fig. 5.3(d) and (e) are presented in Fig. 5.5(a) and (b) for the qubit model. We recover results similar to the case of the harmonic detector. Note that the Newtonian model has a slightly improved yet still very poor performance, which can be ascribed to the additional nonlinearity provided by the qubit. These results clearly show that the details of the spectrum of the detector are not crucial for the expressive power of the relativistic quantum dynamics.

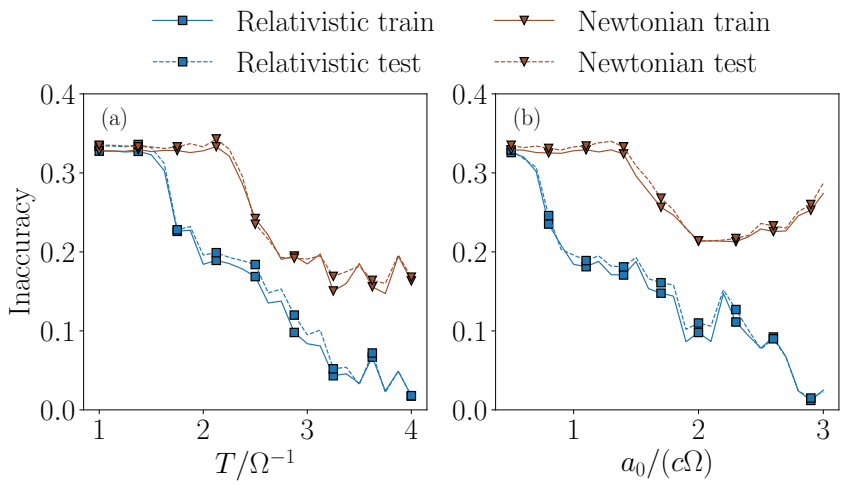

Figure 5.5: Performances of the reservoir-computing model with a qubit replacing the harmonic oscillator. Same parameters as Fig. 5.3(d) and (e) respectively, showing very similar results.

V Conclusions

We have shown how relativistic quantum dynamics can provide a dramatic enhancement of the expressive power for reservoir computing. Given that analogs of the considered relativistic quantum model can be implemented in state-of-the-art quantum platforms, such as superconducting circuits and trapped ions, our theoretical findings pave the way to relativity-inspired machine-learning protocols with enhanced capabilities.

The original results presented in this chapter are published in [ϵ].

General conclusion

In this manuscript, we have explored reservoir-induced dynamics and reservoir computing in the context of quantum optics. In the current Noisy Intermediate-Scale Quantum (NISQ) era, *reservoir* is an inevitable subject in the study of quantum technologies, since it can, for example, represent the omnipresent environment that couples to the quantum devices of interest. In this context, our results can be arranged into three major directions of research:

1. dissipative dynamics of a quantum system due to coupling to the environment (an uncontrolled reservoir);

2. harnessing dissipation as a resource by appropriate design of the reservoir to achieve desired effective control over a quantum system (reservoir engineering);

3. exploiting the rich dynamics of a reservoir itself for information-processing applications (reservoir computing).

1.— Along the first path, we studied a dissipative phase transition in a photonic system. We proposed a technique for probing the role of spatial dimensionality in determining criticality, and implemented it in a planar semiconductor microcavity subjected to a coherent optical drive. In our scheme, the spatial geometry of the system is controlled by designing the intensity profile of the drive, and can therefore be tuned *in situ* and in an all-optical way. Our theoretical findings suggest that a first-order dissipative phase transition emerges for the 2D geometry, and is absent in 1D. This prediction has been experimentally observed and represents the first experimental demonstration of a dimension-dependent phase transition in photonic systems. Our results also suggest that the optical response of the cavity can be tuned as a function of the driving intensity profile, which could be useful for designing polaritonic devices such as all-optical polariton transistors, which rely on the switching between the low and high output intensities as a function of the input (drive) intensity. On the other hand, the flexibility of the proposed scheme provides the possibility of studying more complicated geometries on the same underlying cavity substrate, such as fractal patterns or fractional dimensions, which could be exploited to address the problem of lower critical dimension. Furthermore, it could be worth exploring phase transitions with spontaneous symmetry breaking with the proposed setup by considering, for example, an incoherent drive [which preserves the $U(1)$ symmetry in the phase of the photonic field] or N-photon drive (with $\mathbb{Z}_n$ symmetry). Our finding hopefully paves the way to a novel approach to exploring the many-body physics of photons and critical phenomena in the out-of-equilibrium regime.

2.— We then addressed the theory of reservoir engineering, where the setup consists of a bipartite system-reservoir ensemble, with the reservoir having a much faster time scale allowing it to be adiabatically eliminated. We explicitly derived the general effective dynamics induced by a single-mode reservoir (a strongly dissipative cavity mode) and found that it is capable of creating both coherent and dissipative couplings between the system's degrees of freedom that the reservoir couples to. This was then illustrated with an application in quantum simulation of antiferromagnetism. We proposed a setup where spins are simulated by quadratically driven photonic cavities, and their interaction is mediated via the engineered reservoir consisting of single-mode dissipative cavities. The theoretical result previously derived allowed us to obtain an effective description, where coherent and dissipative couplings induced by the reservoir are identified, both capable of mimicking antiferromagnetism. In particular, we demonstrated via numerical simulations that the effective dissipative coupling alone is inducing frustration in the steady state of the system. As our setup can be easily generalized to larger geometries such as lattices, this could be a promising experimental platform for simulating frustrated spin systems such as spin glasses and spin liquids, where the couplings can be easily tuned.

3.— Finally, we introduced the paradigm of relativistic quantum reservoir computing, where the framework of reservoir computing is explored in the context of relativistic quantum information. We designed an information-processing protocol based on the Unruh-DeWitt model for relativistic light-matter interactions, where a quantum detector undergoes relativistic motion inside a cavity. We proposed to embed the input information in the motion of the detector, and exploited its quantum dynamics to perform a feature-space embedding, which nonlinearly transforms the input into a high-dimension space, providing useful representations of the input. This was demonstrated with the illustrative example of the two-spiral supervised classification problem, a well-known benchmark for binary classifiers. We then showed using kernel theory that the proposed reservoir-computing model exhibits enhanced performance when the motion of the detector enters relativistic regime. The enhancement can be understood as the relativistic effects (such as time dilation) providing nontrivial modulations in the resonance condition of the detector-cavity interaction, and can therefore be regarded as computing power harnessed from the fundamental laws of physics. We further discussed a possible analog implementation in circuit QED platforms, endowing the proposed scheme with practical interest. Our theoretical findings could pave the way to relativity-inspired machine-learning devices or algorithms with enhanced capabilities.

A Change of frame and interaction picture

The change of frame for the internal degrees of freedom of a quantum operator $\hat{O}(t)$ can be described by a unitary transformation, that we denote by

$$\tilde{O}(t) = \hat{U}^\dagger(t)\hat{O}(t)\hat{U}(t), \tag{A.1}$$

where $\hat{U}^\dagger(t)\hat{U}(t) = \hat{\mathbb{1}}$ and we assume that the transformation can be time-dependent. Note that the unitary condition immediately implies that

$$\frac{\mathrm{d}\hat{U}^\dagger}{\mathrm{d}t}\hat{U} + \hat{U}^\dagger\frac{\mathrm{d}\hat{U}}{\mathrm{d}t} = 0, \tag{A.2}$$

which means that $\mathrm{i}\hat{U}^\dagger\frac{\mathrm{d}\hat{U}}{\mathrm{d}t}$ is hermitian. Consider now a density matrix $\hat{\rho}(t)$ that follows a completely positive trace preserving (CPTP) time-evolution, that can be in general cast in the Lindblad form

$$\frac{\mathrm{d}\hat{\rho}}{\mathrm{d}t} = -\frac{\mathrm{i}}{\hbar}\left[\hat{H}, \hat{\rho}\right] + \sum_j \gamma_j \mathcal{D}[\hat{L}_j]\hat{\rho}\,, \tag{A.3}$$

and we allow the Hamiltonian $\hat{H}$ and the jump operators $\hat{L}_j$ to have time dependence. The time-evolution of the density matrix $\tilde{\rho} = \hat{U}^\dagger\hat{\rho}\hat{U}$ in the transformed frame is therefore

$$\begin{aligned}
\frac{\mathrm{d}\tilde{\rho}}{\mathrm{d}t} &= \left(\frac{\mathrm{d}\hat{U}^\dagger}{\mathrm{d}t}\right)\hat{\rho}\hat{U} + \hat{U}^\dagger\left(\frac{\mathrm{d}\hat{\rho}}{\mathrm{d}t}\right)\hat{U} + \hat{U}^\dagger\hat{\rho}\left(\frac{\mathrm{d}\hat{U}}{\mathrm{d}t}\right) \\
&= \left(\frac{\mathrm{d}\hat{U}^\dagger}{\mathrm{d}t}\hat{U}\right)\tilde{\rho} + \hat{U}^\dagger\left(\frac{\mathrm{d}\hat{\rho}}{\mathrm{d}t}\right)\hat{U} + \tilde{\rho}\left(\hat{U}^\dagger\frac{\mathrm{d}\hat{U}}{\mathrm{d}t}\right) \\
&= \hat{U}^\dagger\left(\frac{\mathrm{d}\hat{\rho}}{\mathrm{d}t}\right)\hat{U} - \frac{\mathrm{i}}{\hbar}\left[-\mathrm{i}\hbar\hat{U}^\dagger\frac{\mathrm{d}\hat{U}}{\mathrm{d}t}, \tilde{\rho}\right] \\
&= -\frac{\mathrm{i}}{\hbar}\left[\tilde{H} - \mathrm{i}\hbar\hat{U}^\dagger\frac{\mathrm{d}\hat{U}}{\mathrm{d}t}, \tilde{\rho}\right] + \sum_j \gamma_j \mathcal{D}[\tilde{L}]\tilde{\rho}\,.
\end{aligned} \tag{A.4}$$

We can identify the effective Hamiltonian $\hat{H}' = \tilde{H} - \mathrm{i}\hbar\hat{U}^\dagger\frac{\mathrm{d}\hat{U}}{\mathrm{d}t}$ for the transformed frame, which has a term reminiscent of a fictitious force in addition to the naive transformation if $\hat{U}$ is time-dependent.

I Interaction picture

A particularly useful frame in situations involving interactions between different parts of a system is the so-called *interaction picture*, which is given by the time-evolution operator generated by the free (non-interacting) Hamiltonian $\hat{H}_0$ of the system. While it is assumed in many texts that $\hat{H}_0$ be time-independent, this condition is in fact not necessary for defining the transformation, as we will clarify in the following.

Consider a generic Hamiltonian of the form

$$\hat{H}(t) = \hat{H}_0(t) + \hat{H}_I(t)\,, \tag{A.5}$$

where we assume time dependence for both the free and the interaction Hamiltonians. The time evolution operator $\hat{U}_0(t)$ generated by $\hat{H}_0$ is given by the Schrödinger equation

$$\mathrm{i}\hbar\frac{\mathrm{d}}{\mathrm{d}t}\hat{U}_0(t) = \hat{H}_0(t)\hat{U}_0(t)\,. \tag{A.6}$$

Using the generic expression for the effective Hamiltonian derived above, we have, in the frame defined by $\hat{U}_0(t)$,

$$\begin{aligned}\hat{H}'(t) &= \hat{U}_0^\dagger(t)\Big(\hat{H}_0(t) + \hat{H}_I(t)\Big)\hat{U}_0(t) - \mathrm{i}\hbar\hat{U}_0^\dagger(t)\frac{\mathrm{d}}{\mathrm{d}t}\hat{U}_0(t)\\ &= \tilde{H}_0(t) + \tilde{H}_I(t) - \mathrm{i}\hbar\hat{U}_0^\dagger(t)\Big(\frac{1}{\mathrm{i}\hbar}\hat{H}_0(t)\hat{U}_0(t)\Big)\\ &= \tilde{H}_0(t) + \tilde{H}_I(t) - \tilde{H}_0(t)\\ &= \tilde{H}_I(t)\,.\end{aligned} \tag{A.7}$$

As the free Hamiltonian has been eliminated, this interaction picture is useful for studying the dynamics stemming only from the interaction $\hat{H}_I$. In order to obtain practical expressions for $\tilde{H}_I(t)$, $\hat{H}_0(t)$ is usually chosen such that it commutes with itself at different times, i.e. $[\hat{H}_0(t), \hat{H}_0(t')] = 0\,, \forall t, t'$, which is a typical case that arises when performing a reparametrization of the time. In this case, the transformation is simply

$$\hat{U}_0(t) = \mathrm{e}^{-\frac{\mathrm{i}}{\hbar}\int_0^t \hat{H}_0(t)\mathrm{d}t}\,, \tag{A.8}$$

which does not involve time-ordering and the transformed Hamiltonian can be efficiently evaluated.

B Scalar quantum field theory

We present here (by following [121]) the quantization of a real scalar field in the $(d+1)$-dimensional Minkowski spacetime (i.e. one time dimension and d spatial dimensions) with the metric $\eta_{\mu\nu} = \mathrm{diag}(+1, -1, \cdots, -1)$. The Lagrangian density for the classical real scalar field $\phi(x^\mu)$ is given by:

$$\mathcal{L} = \frac{1}{2}\eta^{\mu\nu}(\partial_\mu\phi)(\partial_\nu\phi) - \frac{1}{2}m^2\phi^2\,, \tag{B.1}$$

where m is the mass parameter. This determines the conjugate momentum

$$\Pi = \frac{\partial\mathcal{L}}{\partial(\partial_0\phi)} = \dot{\phi}\,, \tag{B.2}$$

and the Hamiltonian density

$$\mathcal{H} = \Pi\dot{\phi} - \mathcal{L} = \frac{1}{2}\Pi^2 + \frac{1}{2}(\nabla\phi)^2 + \frac{1}{2}m^2\phi^2\,, \tag{B.3}$$

where $(\nabla\phi)^2 \equiv \delta^{ij}(\partial_i)(\partial_j)$ with the indices i, j running through only the spatial coordinates. The equation of motion of the field can be obtained by the variational principle:

$$\delta\Big(\int \mathrm{d}^{d+1}x\ \mathcal{L}\Big) = 0 \quad\Longrightarrow\quad \Box\phi + m^2\phi = 0\,, \tag{B.4}$$

which is the Klein-Gordon equation [276, 277]. Note that for the massless scalar field $m = 0$, this equation reduces to $\Box\phi = 0$, which resembles the Maxwell equations in the Lorenz gauge (1.7) for a single field component. The canonical quantization of the field proceeds by promoting the conjugate variables to operators $(\phi, \Pi) \mapsto (\hat{\phi}, \hat{\Pi})$ and by imposing the equal-time commutation relations:

$$\Big[\hat{\phi}(t, \boldsymbol{x}), \hat{\Pi}(t, \boldsymbol{x}')\Big] = \mathrm{i}\delta^{(d)}(\boldsymbol{x} - \boldsymbol{x}')\,, \tag{B.5}$$

and all the other equal-time commutators vanish.

I Quantization in a cavity

Let us first consider the field in a cavity with Dirichlet boundary conditions (corresponding to perfectly reflecting mirrors in the case of an optical field). Let the cavity be represented

by the Hyperrectangular region $\mathbb{V} \equiv \{0 \leq x^j \leq L_j \mid j = 1, \cdots, d\}$, and the boundary condition can be written as $\phi(t, \boldsymbol{x} \in \partial\mathbb{V}) = 0$. One can find a family of standing-wave solutions $\{u_{\boldsymbol{n}}(x^\mu)\}_{\boldsymbol{n}\in\mathbb{Z}^d}$ that satisfy the equation of motion (B.4) and the Dirichlet boundary condition:

$$u_{\boldsymbol{n}}(t, \boldsymbol{x}) = \sqrt{\frac{2^{d-1}}{\omega_{\boldsymbol{n}} V}} \mathrm{e}^{-\mathrm{i}\omega_{\boldsymbol{n}} t} \prod_{j=1}^{d} \sin\left(\frac{n_j \pi}{L_j} x_j\right), \quad \omega_{\boldsymbol{n}} = \sqrt{\sum_{j=1}^{d} \left(\frac{n_j \pi}{L_j}\right)^2 + m^2}, \tag{B.6}$$

with $V \equiv \Pi_{j=1}^{d} L_j$ the volume of the cavity. Note that the spectrum is discrete due to the boundary conditions. It is straightforward to verify that they form an orthonormal basis

$$\langle u_{\boldsymbol{n}}, u_{\boldsymbol{n}'} \rangle_{\mathrm{KG}} = \delta_{\boldsymbol{n},\boldsymbol{n}'}, \quad \langle u^*_{\boldsymbol{n}}, u^*_{\boldsymbol{n}'} \rangle_{\mathrm{KG}} = -\delta_{\boldsymbol{n},\boldsymbol{n}'}, \quad \langle u_{\boldsymbol{n}}, u^*_{\boldsymbol{n}'} \rangle_{\mathrm{KG}} = 0, \tag{B.7}$$

where the Klein-Gordon inner product is defined as

$$\langle f, g \rangle_{\mathrm{KG}} \equiv \mathrm{i} \int_{\Sigma_t} \mathrm{d}^d x \left(f^* \dot{g} - \dot{f}^* g \right), \tag{B.8}$$

and the integral is performed on a constant-time hypersurface Σ_t. The quantized field $\hat{\phi}$ can then be written as a mode expansion in terms of these basis functions

$$\hat{\phi}(x^\mu) = \sum_{\boldsymbol{n}} \left[u_{\boldsymbol{n}}(x^\mu) \hat{a}_{\boldsymbol{n}} + u^*_{\boldsymbol{n}}(x^\mu) \hat{a}^\dagger_{\boldsymbol{n}} \right], \tag{B.9}$$

where the operators $\hat{a}^\dagger_{\boldsymbol{n}}$ and $\hat{a}_{\boldsymbol{n}}$ satisfy the Bosonic commutation relations

$$\left[\hat{a}_{\boldsymbol{n}}, \hat{a}^\dagger_{\boldsymbol{n}'} \right] = \delta_{\boldsymbol{n},\boldsymbol{n}'}, \tag{B.10}$$

as one can verify using $\hat{a}_n = \langle u_{\boldsymbol{n}}, \hat{\phi} \rangle_{\mathrm{KG}}$ and the commutation relations (B.5). This mode expansion also allows us to write the Hamiltonian as

$$\hat{H} = \int \mathrm{d}^d x \, \mathcal{H} = \sum_{\boldsymbol{n}} \left(\omega_{\boldsymbol{n}} \hat{a}^\dagger_{\boldsymbol{n}} \hat{a}_{\boldsymbol{n}} + \frac{1}{2} \right). \tag{B.11}$$

For the (1+1)-dimensional ($d = 1$) cavity of length L considered in Chapter 5, the mode expansion of the massless ($m = 0$) scalar field is therefore

$$\hat{\phi}(t, x) = \sum_{n=1}^{\infty} \frac{1}{\sqrt{\omega_n L}} \left(\mathrm{e}^{-\mathrm{i}\omega_n t} \hat{a}_n + \mathrm{e}^{\mathrm{i}\omega_n t} \hat{a}^\dagger_n \right) \sin(k_n x), \quad \omega_n = k_n = \frac{n\pi}{L}, \tag{B.12}$$

which is Eq. (5.19) used in Chapter 5.

II Quantization in free space

Another scenario we considered in the main text is the scalar field in free space, when we derived the Unruh effect in Sec. IV.3 of Chapter 1. The quantization in this case is done in a very similar way as above, where we wish to write down the mode expansion in terms

of an orthonormal basis and the corresponding creation and annihilation operators. Such a basis can be the family of plane-wave solutions $\{v_{\boldsymbol{k}}(x^\mu)\}_{\boldsymbol{k}\in\mathbb{R}^d}$, where

$$v_{\boldsymbol{k}}(t,\boldsymbol{x}) = \frac{1}{\sqrt{(2\pi)^d 2\omega_{\boldsymbol{k}}}}\mathrm{e}^{-\mathrm{i}(\omega_{\boldsymbol{k}}t-\boldsymbol{k}\cdot\boldsymbol{x})}\,, \quad \omega_{\boldsymbol{k}} = \sqrt{\|\boldsymbol{k}\|^2+m^2}\,, \tag{B.13}$$

which satisfies the orthonormality condition:

$$\langle v_{\boldsymbol{k}}, v_{\boldsymbol{k}'}\rangle_{\mathrm{KG}} = \delta^{(d)}(\boldsymbol{k}-\boldsymbol{k}')\,, \quad \langle v^*_{\boldsymbol{k}}, v^*_{\boldsymbol{k}'}\rangle_{\mathrm{KG}} = -\delta^{(d)}(\boldsymbol{k}-\boldsymbol{k}')\,, \quad \langle v_{\boldsymbol{k}}, v^*_{\boldsymbol{k}'}\rangle_{\mathrm{KG}} = 0\,. \tag{B.14}$$

Note that we have the Dirac deltas instead of the Kronecker deltas as the modes form a continuum in free space. The mode expansion of the field operator is then

$$\hat{\phi}(x^\mu) = \int \mathrm{d}^d\boldsymbol{k}\,\left[v_{\boldsymbol{k}}(x^\mu)\hat{a}_{\boldsymbol{k}} + v^*_{\boldsymbol{k}}(x^\mu)\hat{a}^\dagger_{\boldsymbol{k}}\right], \tag{B.15}$$

with the Bosonic commutation relations for the creation and annihilation operators:

$$\left[\hat{a}_{\boldsymbol{k}}, \hat{a}^\dagger_{\boldsymbol{k}'}\right] = \delta^{(d)}(\boldsymbol{k}-\boldsymbol{k}')\,. \tag{B.16}$$

The Hamiltonian is, accordingly,

$$\hat{H} = \int \mathrm{d}^d\boldsymbol{k}\,\omega_{\boldsymbol{k}}\left[\hat{a}^\dagger_{\boldsymbol{k}}\hat{a}_{\boldsymbol{k}} + \frac{1}{2}\delta^{(d)}(\boldsymbol{0})\right], \tag{B.17}$$

where the divergent integral over $\frac{1}{2}\delta^{(d)}(\boldsymbol{0})$ [bearing the same origin as the infinite sum over the constant $\frac{1}{2}$ in the cavity Hamiltonian (B.11)] is known as the *zero-point energy*, which can lead to physical consequences such as the Casimir effect [278, 279]. The zero-point energy is also related to open challenges in physics such as the cosmological constant problem [280]. However, in the scope of the present manuscript, it is safe to ignore this term in all our calculations.

Finally, for the (3+1)-dimensional ($d=3$) free space, the mode expansion (B.15) for the massless scalar field is

$$\hat{\phi}(t,\boldsymbol{x}) = \int \frac{\mathrm{d}^3\boldsymbol{k}}{(2\pi)^{\frac{3}{2}}}\sqrt{\frac{1}{2\omega_{\boldsymbol{k}}}}\left(\hat{a}_{\boldsymbol{k}}\mathrm{e}^{-\mathrm{i}(\omega_{\boldsymbol{k}}t-\boldsymbol{k}\cdot\boldsymbol{x})} + \hat{a}^\dagger_{\boldsymbol{k}}\mathrm{e}^{\mathrm{i}(\omega_{\boldsymbol{k}}t-\boldsymbol{k}\cdot\boldsymbol{x})}\right), \quad \omega_{\boldsymbol{k}} = \|\boldsymbol{k}\|\,, \tag{B.18}$$

which is Eq. (1.82) considered in Sec. IV.3 of Chapter 1.

C World line of an accelerated observer

We derive here the world line for an observer with time-dependent proper acceleration $a(\tau)$ in 1+1D Minkowski spacetime with metric $\eta_{\mu\nu} = \mathrm{diag}(+1, -1)$ and natural units $c = 1$. We parametrize the world line by the proper time $x^\mu(\tau) = (t(\tau), x(\tau))$ and denote

$$\begin{aligned} u^\mu(\tau) =& \frac{\mathrm{d}}{\mathrm{d}\tau} x^\mu(\tau) = (u^t(\tau), u^x(\tau)), \\ a^\mu(\tau) =& \frac{\mathrm{d}}{\mathrm{d}\tau} u^\mu(\tau) = (a^t(\tau), a^x(\tau)). \end{aligned} \tag{C.1}$$

From the definition of these quantities, we get

$$\begin{aligned} u^\mu u_\mu =& 1 = (u^t)^2 - (u^x)^2, \\ a^\mu u_\mu =& 0 = a^t u^t - a^x u^x, \\ a^\mu a_\mu =& -a(\tau)^2 = (a^t)^2 - (a^x)^2. \end{aligned} \tag{C.2}$$

It follows that

$$a^x = \frac{\mathrm{d}u^x}{\mathrm{d}\tau} = a(\tau)\sqrt{1 + (u^x)^2}. \tag{C.3}$$

Integrating from $\tau' = 0$ to $\tau' = \tau$ gives

$$\begin{aligned} u^x(\tau) =& \sinh[\xi(\tau)], \\ \xi(\tau) =& \sinh^{-1}[u^x(\tau = 0)] + \int_0^\tau \mathrm{d}\tau' a(\tau'). \end{aligned} \tag{C.4}$$

Integrating again gives the position. For the time, a similar treatment applies. We finally obtain:

$$\begin{aligned} x(\tau) =& x_0 + \int_0^\tau \mathrm{d}\tau' \sinh[\xi(\tau')], \\ t(\tau) =& t_0 + \int_0^\tau \mathrm{d}\tau' \cosh[\xi(\tau')], \end{aligned} \tag{C.5}$$

Note that for a constant acceleration, this gives the well-known Rindler observer's world line:

$$t(\tau) = \frac{1}{a}\sinh(a\tau)\,,\ x(\tau) = \frac{1}{a}\cosh(a\tau)\,. \tag{C.6}$$

D Gaussian formalism

we briefly summarize the Gaussian formalism for calculating the time-evolution of a Bosonic quantum system with a quadratic Hamiltonian and a Gaussian initial state. We denote the vector of bosonic mode operators by

$$\hat{\mathbf{\Psi}} = (\hat{a}_0, \hat{a}_1, \hat{a}_2, \cdots, \hat{a}_N, \hat{a}_0^\dagger, \hat{a}_1^\dagger, \hat{a}_2^\dagger, \cdots, \hat{a}_N^\dagger)^T, \tag{D.1}$$

that satisfies the commutation relation

$$\left[\hat{\Psi}_i, \hat{\Psi}_j\right] = \mathbf{\Omega}_{ij}, \tag{D.2}$$

where

$$\mathbf{\Omega} = \begin{bmatrix} \mathbf{0} & \mathbb{1} \\ -\mathbb{1} & \mathbf{0} \end{bmatrix} = -\mathbf{\Omega}^T \tag{D.3}$$

is the symplectic form. If the Hamiltonian can be written in the form of

$$\hat{H} = \hat{\mathbf{\Psi}}^T \mathbf{F}(t) \hat{\mathbf{\Psi}}, \tag{D.4}$$

it then preserves the Gaussianity of states [269]. The Heisenberg equations of motion can be written as

$$\frac{\mathrm{d}}{\mathrm{d}t} \hat{\mathbf{\Psi}} = -\mathrm{i}\mathbf{\Omega}\mathbf{F}^{\mathrm{sym}}(t) \hat{\mathbf{\Psi}}, \tag{D.5}$$

where $\mathbf{F}^{\mathrm{sym}} = \mathbf{F} + \mathbf{F}^T$. We now define the propagator $\mathbf{S}(t)$ via the relation

$$\hat{\mathbf{\Psi}}(t) = \mathbf{S}(t) \hat{\mathbf{\Psi}}(0), \tag{D.6}$$

which can be efficiently constructed by solving the first order linear differential equation

$$\frac{\mathrm{d}}{\mathrm{d}t} \mathbf{S}(t) = -\mathrm{i}\mathbf{\Omega}\mathbf{F}^{\mathrm{sym}}(t) \mathbf{S}(t) \tag{D.7}$$

with the initial condition $\mathbf{S}(0) = \mathbb{1}$. The evolution of the covariance matrix

$$\sigma_{ij} = \langle \hat{\Psi}_i \hat{\Psi}_j \rangle - \langle \hat{\Psi}_i \rangle \langle \hat{\Psi}_j \rangle \tag{D.8}$$

is given by

$$\boldsymbol{\sigma}(t) = \mathbf{S}(t) \boldsymbol{\sigma}(0) \mathbf{S}^T. \tag{D.9}$$

$\boldsymbol{\sigma}$ together with $\langle \hat{\mathbf{\Psi}} \rangle$ will completely specify a Gaussian state[1].

[1] This property can also be regarded as the definition of a Gaussian state

E Résumé substantiel

Cette thèse explore la dynamique induite par réservoir et le traitement de l'information par réservoir dans des systèmes d'optique quantique. Elle est structurée autour de trois directions de recherche principales :

(i) la dynamique dissipative d'un système quantique en contact avec son environnement (chapitres 1 et 2) ;

(ii) le contrôle d'un système quantique par ingénierie de réservoir (chapitres 3 et 4) ;

(iii) l'apprentissage automatique au moyen de réservoirs (chapitre 5).

Dans un premier temps, la dynamique effective d'un système quantique faiblement couplé à son environnement est décrite par le formalisme des *systèmes quantiques ouverts*, où l'environnement est modélisé par un réservoir thermique non contrôlé à la dynamique de relaxation rapide. L'évolution temporelle de l'état du système, représenté par sa matrice densité $\hat{\rho}$, s'écrit sous la forme d'une équation maîtresse de Lindblad (on adopte le système d'unités naturelles où $\hbar = c = 1$) :

$$\frac{\mathrm{d}}{\mathrm{d}t}\hat{\rho} = \mathcal{L}(\hat{\rho}) \equiv -\mathrm{i}\Big[\hat{H}, \hat{\rho}\Big] + \sum_j \mathcal{D}[\hat{L}_j]\hat{\rho}\,, \tag{E.1}$$

où le *liouvillien* $\mathcal{L}$ désigne le superopérateur générateur de cette dynamique. Ci-dessus, le hamiltonien $\hat{H}$ détermine l'évolution unitaire du système. Les effets dissipatifs issus du réservoir sont décrits par les dissipateurs, ayant pour action

$$\mathcal{D}[\hat{L}]\hat{\rho} = \hat{L}\hat{\rho}\hat{L}^\dagger - \frac{1}{2}\Big(\hat{L}^\dagger\hat{L}\hat{\rho} + \hat{\rho}\hat{L}^\dagger\hat{L}\Big)\,, \tag{E.2}$$

définie ici pour un opérateur de saut quelconque $\hat{L}$.

Dans ce contexte, nous étudions la dynamique dissipative d'un système photonique soumis à un pompage optique cohérent quasirésonant. Nous proposons une technique permettant de contrôler la géométrie spatiale du système *in situ* de manière purement optique et l'implémentons sur une plateforme consistant en une microcavité planaire en matériau semiconducteur. Les excitations élémentaires de ce système, rendu non-linéaire grâce au couplage fort entre la matière et la lumière, sont des quasiparticules hybrides issues de ce couplage, appelées des *polaritons*. Dans l'approximation du champ moyen,

la dynamique effective du champ polaritonique ψ est donnée par l'équation de Gross-Pitaevskii :

$$\mathrm{i}\frac{\partial}{\partial t}\psi(\boldsymbol{r},t) = \left(-\Delta - \frac{\hbar}{2m}\nabla^2\right)\psi(\boldsymbol{r},t) + g|\psi(\boldsymbol{r},t)|^2\psi(\boldsymbol{r},t) - \mathrm{i}\frac{\gamma}{2}\psi(\boldsymbol{r},t) + \mathcal{F}(\boldsymbol{r})\,, \tag{E.3}$$

où Δ désigne le désaccord entre la fréquence du pompage et celle du mode fondamental de la cavité, m est la masse effective du polariton, g décrit la nonlinéarité et γ est le taux de dissipation. La dimension du système est ajustée en modulant le profil de l'intensité du pompage $\mathcal{F}(\boldsymbol{r})$ et nous étudions l'émergence de la criticalité en augmentant l'étendue spatiale du pompage (voir la figure 2.2). En mesurant l'intensité de sortie en fonction de celle du pompage sur l'état stationnaire du système, nous mettons en évidence avec nos résultats théoriques l'émergence d'une transition de phase du premier ordre dans la configuration à deux dimensions et son absence en une dimension (voir la figure 5.3). Nous présentons également la confirmation expérimentale de nos prédictions par nos collaborateurs au laboratoire Kastler Brossel, ce qui constitue la première démonstration expérimentale du rôle de la dimensionnalité spatiale dans la l'existence des transitions de phase dans des systèmes photoniques.

Les chapitres 3 et 4 sont consacrés à l'étude théorique de l'ingénierie de réservoir, qui consiste à agir sur l'environnement d'un système quantique afin de contrôler sa dynamique effective induite. Nous déduisons d'abord la dynamique effective générale d'un système couplé à un réservoir fortement dissipatif à un seul mode bosonique. L'évolution de l'état de l'ensemble bipartite $\hat{\rho}_{SR}$ est décrite par l'équation maîtresse suivante :

$$\frac{\mathrm{d}}{\mathrm{d}t}\hat{\rho}_{SR} = \mathcal{L}_S\hat{\rho}_{SR} + \mathcal{L}_R\hat{\rho}_{SR} - \mathrm{i}[\hat{H}_I, \hat{\rho}_{SR}]\,. \tag{E.4}$$

Nous supposons le liouvillien libre du réservoir sous la forme $\mathcal{L}_R(\bullet) = -\mathrm{i}[-\tilde{\Delta}\hat{b}^\dagger\hat{b}, \bullet] + \gamma_b\mathcal{D}[\hat{b}](\bullet)$ et un hamiltonien de couplage donné par $\hat{H}_I = \lambda\gamma_b(\hat{A}^\dagger\hat{b} + \hat{A}\hat{b}^\dagger)$, où $\hat{b}$ est l'opérateur d'annihilation du réservoir, γ_b désigne le taux de relaxation de ce dernier et l'opérateur $\hat{A}$ n'agit que sur le système (dont le liouvillien libre est $\mathcal{L}_S$). Enfin, $\lambda \ll 1$ est une constante sans dimension pour marquer la faiblesse relative du couplage par rapport à γ_b. Dans l'approximation adiabatique $\|\mathcal{L}_S\hat{\rho}_{SR}\|/\gamma_b \lesssim \lambda^2$, la dynamique effective du système est donnée par l'équation maîtresse suivante :

$$\frac{\mathrm{d}}{\mathrm{d}t}\hat{\rho}_S = \mathcal{L}_S\hat{\rho}_S - \mathrm{i}[\lambda^2\Lambda\hat{A}^\dagger\hat{A}, \hat{\rho}_S] + \lambda^2\Gamma\mathcal{D}[\hat{A}]\hat{\rho}_S\,, \tag{E.5}$$

où les quantités Λ et Γ ne dépendent que des paramètres $\tilde{\Delta}$ et γ_b du réservoir (voir la discussion dans la section I du chapitre 3). Cette dynamique effective intègre les contributions cohérente et dissipative du réservoir, permettant de coupler effectivement différents degrés de liberté du système via le réservoir.

Ce formalisme est ensuite appliqué à l'étude d'un réseau de cavités photoniques (le *système*), qui sont couplées de façon indirecte via des cavités auxiliaires fortement dissipatives (le *réservoir*). Grâce à un tel dispositif physique, où chaque cavité du système est soumise à un pompage à deux photons, nous proposons un simulateur photonique pour des spins antiférromagnétiques. Ce pompage quadratique a pour effet de placer l'état de

chaque cavité du système dans un mélange statistique d'états cohérents aux phases opposées (voir la discussion dans la section III du chapitre 3), ce qui simule des spins. Pour une chaîne unidimensionnelle périodique (voir la figure 4.1), le hamiltonien total de l'ensemble système-réservoir s'écrit comme

$$\begin{aligned}\hat{H}(t) &= \sum_j \hat{H}_j(t)\,,\\ \hat{H}_j(t) &= \omega_0 \hat{a}_j^\dagger \hat{a}_j + (\omega_0 - \tilde{\Delta})\hat{b}_j^\dagger \hat{b}_j - J\Big[(\hat{a}_j + \hat{a}_{j+1})\hat{b}_j^\dagger + (\hat{a}_j^\dagger + \hat{a}_{j+1}^\dagger)\hat{b}_j\Big]\\ &\quad + \frac{U}{2}\hat{a}_j^{\dagger 2}\hat{a}_j^2 + \frac{G}{2}\hat{a}_j^{\dagger 2}\mathrm{e}^{-\mathrm{i}\omega_d t} + \frac{G^*}{2}\hat{a}_j^2 \mathrm{e}^{\mathrm{i}\omega_d t}\,,\end{aligned} \tag{E.6}$$

où J désigne l'amplitude du couplage, $\tilde{\Delta}$ est le désaccord entre la fréquence d'une cavité du système et celle d'une cavité du réservoir, U représente la nonlinéarité Kerr et G est l'amplitude du pompage à deux photons (de fréquence ω_d). L'équation maîtresse totale de l'ensemble est ainsi donnée par

$$\frac{\mathrm{d}\hat{\rho}}{\mathrm{d}t} = -\,\mathrm{i}[\hat{H}, \hat{\rho}] + \sum_j \Big(\gamma \mathcal{D}[\hat{a}_j] + \gamma_b \mathcal{D}[\hat{b}_j] + \eta \mathcal{D}[\hat{a}_j^2]\Big)\hat{\rho}\,. \tag{E.7}$$

Dans le régime $\gamma_b \gg \gamma$, le formalisme exposé plus haut nous permet d'éliminer de façon adiabatique le réservoir (voir la discussion de la section II.2 du chapitre 4), ce qui donne le liouvillien effectif du système

$$\mathcal{L}_{\text{eff}}(\bullet) = -\,\mathrm{i}[\hat{H}_{\text{eff}}, \bullet] + \sum_j (\gamma \mathcal{D}[\hat{a}_j] + \eta \mathcal{D}[\hat{a}_j^2] + \kappa \mathcal{D}[\hat{a}_j + \hat{a}_{j+1}])(\bullet)\,, \tag{E.8}$$

avec le hamiltonien effectif

$$\hat{H}_{\text{eff}} = \sum_j \Big(-\Delta_{\text{eff}} \hat{a}_j^\dagger \hat{a}_j + \frac{U}{2}\hat{a}_j^{\dagger 2}\hat{a}_j^2 + \frac{G}{2}\hat{a}_j^{\dagger 2} + \frac{G^*}{2}\hat{a}_j^2\Big) - J_{\text{eff}} \sum_{\langle j,j'\rangle} (\hat{a}_j^\dagger \hat{a}_{j'} + \hat{a}_j \hat{a}_{j'}^\dagger)\,, \tag{E.9}$$

ici exprimé dans un référentiel tournant à la fréquence $\omega_d/2$. Les paramètres effectifs Δ_{eff}, J_{eff} et κ sont des fonctions des paramètres originaux du liouvillien total et représentent les contributions cohérente et dissipative du réservoir à la dynamique effective du système. En particulier, le signe du couplage cohérent effectif J_{eff} est réglable selon le choix des paramètres et donnera une interaction antiférromagnétique dans le cas $J_{\text{eff}} < 0$. D'autre part, le dissipateur effectif $\kappa\mathcal{D}[\hat{a}_j + \hat{a}_{j+1}]$ est nonlocal et a pour effet d'annihiler l'alignement des phases dans des cavités voisines, ce qui privilégie ainsi un ordre antiférromagnétique des phases.

Ces observations sont confirmées par des simulations numériques. Dans un premier temps, nous étudions un système à $N = 2$ cavités, en traçant la fonction de corrélation $g_{1,2}^{(1)} = \mathrm{Tr}[\hat{\rho}_{\text{SS}}\hat{a}_1^\dagger \hat{a}_2]/\mathrm{Tr}[\hat{\rho}_{\text{SS}}\hat{a}_1^\dagger \hat{a}_1]$ et l'entropie de von Neuman $S = -\mathrm{Tr}[\hat{\rho}_{\text{SS}} \ln \hat{\rho}_{\text{SS}}]$ en fonction de l'amplitude du pompage G (voir la figure 4.4). Dans la limite du fort pompage, $g_{1,2}^{(1)}$ et S convergent vers -1 et $\ln(2)$ respectivement, signe d'un anti-alignement des phase entre les deux cavité. Le système à $N = 3$ cavités est ensuite traité de la même façon et nous constatons les signatures d'une frustration géométrique mise en évidence par $g_{1,2}^{(1)} \to -1/3$ et $S \to \ln(6)$. Notons que le couplage dissipatif effectif seul en absence du

couplage cohérent effectif est capable d'induire cette frustration (voir les figures 4.5 et 4.6). Nous vérifions également l'exactitude du modèle effectif par rapport à l'équation maîtresse complète et constatons une correspondance très fidèle (voir les figures 4.7 et 2.3). Le dispositif proposé peut jouer le rôle d'un élément constitutif d'un simulateur de lattices de spins antiférromagnétiques, facilement implémentable sur des plateformes photoniques.

Enfin, nous introduisons le paradigme de l'apprentissage automatique par réservoir quantique relativiste dans le chapitre 5. Nous exploitons la dynamique d'un système quantique relativiste (le *réservoir* dans le contexte actuel) pour traiter de l'information d'entrée $\mathbf{x}$. Dans cette tâche d'apprentissage automatique supervisé, l'on cherche à approximer une fonction $f(\mathbf{x})$ inconnue par un ansatz $\hat{f}(\mathbf{x})$ d'après un échantillon limité de paires de valeurs $\mathcal{S} = \{(\mathbf{x}^{(j)}, f(\mathbf{x}^{(j)}))\}_j$. Le système étudié comprend un détecteur quantique en mouvement relativiste dans une cavité optique initialisée dans un état cohérent (voir la figure 5.2). Il est décrit par le hamiltonien dit d'Unruh-DeWitt :

$$\hat{H}(\tau) = \lambda \hat{m}(\tau)\hat{\phi}[x^\mu(\tau)]\,, \tag{E.10}$$

où λ est la constante de couplage, l'opérateur $\hat{m}$ désigne le monopole du détecteur, $\hat{\phi}$ est celui du champ quantique dans la cavité et $x^\mu(\tau) \equiv (t(\tau), x(\tau))$ décrit la ligne d'univers (trajectoire dans l'espace-temps) du détecteur paramétrisée, par son temps propre τ. Nous proposons d'encoder l'entrée $\mathbf{x}$ dans le mouvement relativiste du détecteur avec une séquence d'accélérations propres paramétrisées par $\mathbf{x}$ et de mesurer certaines observables du détecteur au cours de son évolution temporelle pour construire un vecteur de caractéristiques (*feature*) de l'entrée $\boldsymbol{X}(\mathbf{x})$. La fonction ansatz prend la forme d'une transformation linéaire du vecteur de caractéristiques :

$$\hat{f}(\mathbf{x}) = \boldsymbol{w}^T \boldsymbol{X}(\mathbf{x})\,, \tag{E.11}$$

avec le vecteur de poids $\boldsymbol{w}$ que nous optimisons analytiquement à l'aide de l'échantillon $\mathcal{S}$ (voir la discussion de la section III du chapitre 5). Nous évaluons le protocole proposé sur une tâche de classification binaire en simulant numériquement le système et mettons en évidence une augmentation de la performance dans le régime relativiste du mouvement. Nous analysons les représentations de l'entrée apprises par le système à l'aide de la théorie des machines à noyau et constatons que la fonction ansatz est considérablement plus expressive dans le régime relativiste (voir la figure 5.3). Aussi Proposons-nous une implémentation analogique du protocole dans des plateformes à base de circuits supraconducteurs, rendant possible la construction de dispositifs d'apprentissage automatique inspirés de la relativité.

Bibliography

[α] Z. Li, A. Soret and C. Ciuti, "Dissipation-induced antiferromagneticlike frustration in coupled photonic resonators", Physical Review A **103**, 022616 (2021).

[β] V. Vinel, Z. Li, A. Borne, A. Bensemhoun, I. Favero, C. Ciuti and G. Leo, "Non-Hermitian bath model for arrays of coupled nanoresonators", Optics Express **29**, 34015 (2021).

[γ] Z. Li, F. Claude, T. Boulier, E. Giacobino, Q. Glorieux, A. Bramati and C. Ciuti, "Dissipative Phase Transition with Driving-Controlled Spatial Dimension and Diffusive Boundary Conditions", Physical Review Letters **128**, 093601 (2022).

[δ] V. Heyraud, Z. Li, Z. Denis, A. Le Boité and C. Ciuti, "Noisy quantum kernel machines", Physical Review A **106**, 052421 (2022).

[ϵ] Z. Li, V. Heyraud, K. Donatella, Z. Denis and C. Ciuti, "Machine learning via relativity-inspired quantum dynamics", Physical Review A **106**, 032413 (2022).

[1] M. K. E. L. Planck, "Zur Theorie des Gesetzes der Energieverteilung im Normalspectrum", Verhandl. Dtsc. Phys. Ges. **2**, 237 (1900).

[2] A. Einstein, "Die Grundlage der allgemeinen Relativitätstheorie", Annalen der Physik **354**, 769–822 (1916).

[3] D. Kleppner and R. Jackiw, "One Hundred Years of Quantum Physics", Science **289**, 893–898 (2000).

[4] M. K. Gaillard, P. D. Grannis and F. J. Sciulli, "The standard model of particle physics", Reviews of Modern Physics **71**, S96–S111 (1999).

[5] N. Bohr, "I. on the constitution of atoms and molecules", The London, Edinburgh, and Dublin Philosophical Magazine and Journal of Science **26**, 1–25 (1913).

[6] W. Heisenberg, *Physics and Beyond: Encounters and Conversations* (G. Allen & Unwin, 1971).

[7] C. Davisson and L. H. Germer, "Diffraction of Electrons by a Crystal of Nickel", Physical Review **30**, 705–740 (1927).

[8] W. Gerlach and O. Stern, "Der experimentelle Nachweis der Richtungsquantelung im Magnetfeld", Zeitschrift für Physik **9**, 349–352 (1922).

[9] E. Schrödinger, "Die gegenwärtige Situation in der Quantenmechanik", Naturwissenschaften **23**, 807–812 (1935).

[10] C. J. Myatt, B. E. King, Q. A. Turchette, C. A. Sackett, D. Kielpinski, W. M. Itano, C. Monroe and D. J. Wineland, "Decoherence of quantum superpositions through coupling to engineered reservoirs", Nature **403**, 269–273 (2000).

[11] A. G. J. MacFarlane, J. P. Dowling and G. J. Milburn, "Quantum technology: the second quantum revolution", Philosophical Transactions of the Royal Society of London. Series A: Mathematical, Physical and Engineering Sciences **361**, 1655–1674 (2003).

[12] A. Steane, "Quantum computing", Reports on Progress in Physics **61**, 117–173 (1998).

[13] R. P. Feynman, "Simulating physics with computers", International Journal of Theoretical Physics **21**, 467–488 (1982).

[14] M. A. Nielsen and I. L. Chuang, *Quantum Computation and Quantum Information: 10th Anniversary Edition* (Cambridge University Press, 2010).

[15] P. Ball, "How decoherence killed Schrödinger's cat", Nature, `10.1038/news000120-10` (2000).

[16] J. I. Cirac and P. Zoller, "Quantum Computations with Cold Trapped Ions", Physical Review Letters **74**, 4091–4094 (1995).

[17] H. Häffner, C. F. Roos and R. Blatt, "Quantum computing with trapped ions", Physics Reports **469**, 155–203 (2008).

[18] R. Blatt and C. F. Roos, "Quantum simulations with trapped ions", Nature Physics **8**, 277–284 (2012).

[19] W. S. Warren, "The Usefulness of NMR Quantum Computing", Science, `10.1126/science.277.5332.1688` (1997).

[20] J. A. Jones and M. Mosca, "Implementation of a quantum algorithm on a nuclear magnetic resonance quantum computer", The Journal of Chemical Physics **109**, 1648–1653 (1998).

[21] D. Loss and D. P. DiVincenzo, "Quantum computation with quantum dots", Physical Review A **57**, 120–126 (1998).

[22] C. Kloeffel and D. Loss, "Prospects for Spin-Based Quantum Computing in Quantum Dots", Annual Review of Condensed Matter Physics **4**, 51–81 (2013).

[23] P. Kok, W. J. Munro, K. Nemoto, T. C. Ralph, J. P. Dowling and G. J. Milburn, "Linear optical quantum computing with photonic qubits", Reviews of Modern Physics **79**, 135–174 (2007).

[24] J. L. O'Brien, "Optical Quantum Computing", Science **318**, 1567–1570 (2007).

[25] N. C. Menicucci, S. T. Flammia and O. Pfister, "One-Way Quantum Computing in the Optical Frequency Comb", Physical Review Letters **101**, 130501 (2008).

[26] J. Q. You and F. Nori, "Superconducting Circuits and Quantum Information", Physics Today **58**, 42–47 (2005).

[27] G. Wendin, "Quantum information processing with superconducting circuits: a review", Reports on Progress in Physics **80**, 106001 (2017).

[28] F. Arute et al., "Quantum supremacy using a programmable superconducting processor", Nature **574**, 505–510 (2019).

[29] H.-S. Zhong, H. Wang, Y.-H. Deng, M.-C. Chen, L.-C. Peng, Y.-H. Luo, J. Qin, D. Wu, X. Ding, Y. Hu, P. Hu, X.-Y. Yang, W.-J. Zhang, H. Li, Y. Li, X. Jiang, L. Gan, G. Yang, L. You, Z. Wang, L. Li, N.-L. Liu, C.-Y. Lu and J.-W. Pan, "Quantum computational advantage using photons", Science **370**, 1460–1463 (2020).

[30] W. G. Unruh, "Maintaining coherence in quantum computers", Physical Review A **51**, 992–997 (1995).

[31] T. Pellizzari, S. A. Gardiner, J. I. Cirac and P. Zoller, "Decoherence, Continuous Observation, and Quantum Computing: A Cavity QED Model", Physical Review Letters **75**, 3788–3791 (1995).

[32] W. H. Zurek, "Decoherence, einselection, and the quantum origins of the classical", Reviews of Modern Physics **75**, 715–775 (2003).

[33] J. Preskill, "Quantum Computing in the NISQ era and beyond", Quantum **2**, 79 (2018).

[34] D. Marković and J. Grollier, "Quantum neuromorphic computing", Applied Physics Letters **117**, 150501 (2020).

[35] H.-P. Breuer and F. Petruccione, *The Theory of Open Quantum Systems* (Oxford University Press, Oxford, 2007).

[36] P. Comaron, G. Dagvadorj, A. Zamora, I. Carusotto, N. P. Proukakis and M. H. Szymańska, "Dynamical Critical Exponents in Driven-Dissipative Quantum Systems", Physical Review Letters **121**, 095302 (2018).

[37] B. Zhu, J. Marino, N. Y. Yao, M. D. Lukin and E. A. Demler, "Dicke time crystals in driven-dissipative quantum many-body systems", New Journal of Physics **21**, 073028 (2019).

[38] H. Landa, M. Schiró and G. Misguich, "Multistability of Driven-Dissipative Quantum Spins", Physical Review Letters **124**, 043601 (2020).

[39] I. Carusotto and C. Ciuti, "Quantum fluids of light", Reviews of Modern Physics **85**, 299–366 (2013).

[40] M. Brambilla, L. A. Lugiato, V. Penna, F. Prati, C. Tamm and C. O. Weiss, "Transverse laser patterns. II. Variational principle for pattern selection, spatial multistability, and laser hydrodynamics", Physical Review A **43**, 5114–5120 (1991).

[41] K. Staliunas, "Laser Ginzburg-Landau equation and laser hydrodynamics", Physical Review A **48**, 1573–1581 (1993).

[42] E. M. Kessler, G. Giedke, A. Imamoglu, S. F. Yelin, M. D. Lukin and J. I. Cirac, "Dissipative phase transition in a central spin system", Physical Review A **86**, 012116 (2012).

[43] Z. Leghtas, S. Touzard, I. M. Pop, A. Kou, B. Vlastakis, A. Petrenko, K. M. Sliwa, A. Narla, S. Shankar, M. J. Hatridge et al., "Confining the state of light to a quantum manifold by engineered two-photon loss", Science (New York, N.Y.) **347**, 853–857 (2015).

[44] F. Minganti, N. Bartolo, J. Lolli, W. Casteels and C. Ciuti, "Exact results for Schrödinger cats in driven-dissipative systems and their feedback control", Scientific reports **6**, 1–8 (2016).

[45] S. Touzard, A. Grimm, Z. Leghtas, S. O. Mundhada, P. Reinhold, C. Axline, M. Reagor, K. Chou, J. Blumoff, K. M. Sliwa, S. Shankar, L. Frunzio, R. J. Schoelkopf, M. Mirrahimi and M. H. Devoret, "Coherent Oscillations inside a Quantum Manifold Stabilized by Dissipation", Physical Review X **8**, 021005 (2018).

[46] D. Grimmer, I. Melgarejo-Lermas and E. Martin-Martinez, "Machine learning quantum field theory with local probes", arXiv:1910.03637 (2019).

[47] Z. Denis, A. Biella, I. Favero and C. Ciuti, "Permanent Directional Heat Currents in Lattices of Optomechanical Resonators", Physical Review Letters **124**, 083601 (2020).

[48] Z. Denis, "Reservoir-induced control and learning in quantum and classical systems", PhD thesis (Université de Paris, 2021).

[49] Y. LeCun, Y. Bengio and G. Hinton, "Deep learning", Nature **521**, 436–444 (2015).

[50] I. Goodfellow, Y. Bengio and A. Courville, *Deep Learning*, edited by F. Bach, Adaptive Computation and Machine Learning Series (MIT Press, Cambridge, MA, USA, 2016).

[51] G. Carleo, Y. Nomura and M. Imada, "Constructing exact representations of quantum many-body systems with deep neural networks", Nature Communications **9**, 5322 (2018).

[52] K. Choo, A. Mezzacapo and G. Carleo, "Fermionic neural-network states for ab-initio electronic structure", Nature Communications **11**, 2368 (2020).

[53] K. Choo, G. Carleo, N. Regnault and T. Neupert, "Symmetries and Many-Body Excitations with Neural-Network Quantum States", Physical Review Letters **121**, 167204 (2018).

[54] M. J. Hartmann and G. Carleo, "Neural-Network Approach to Dissipative Quantum Many-Body Dynamics", Physical Review Letters **122**, 250502 (2019).

[55] R. G. Melko, G. Carleo, J. Carrasquilla and J. I. Cirac, "Restricted Boltzmann machines in quantum physics", Nature Physics **15**, 887–892 (2019).

[56] A. Nagy and V. Savona, "Variational Quantum Monte Carlo Method with a Neural-Network Ansatz for Open Quantum Systems", Physical Review Letters **122**, 250501 (2019).

[57] O. Sharir, Y. Levine, N. Wies, G. Carleo and A. Shashua, "Deep Autoregressive Models for the Efficient Variational Simulation of Many-Body Quantum Systems", Physical Review Letters **124**, 020503 (2020).

[58] F. Vicentini, A. Biella, N. Regnault and C. Ciuti, "Variational Neural-Network Ansatz for Steady States in Open Quantum Systems", Physical Review Letters **122**, 250503 (2019).

[59] N. Yoshioka and R. Hamazaki, "Constructing neural stationary states for open quantum many-body systems", Physical Review B **99**, 214306 (2019).

[60] T. Fösel, P. Tighineanu, T. Weiss and F. Marquardt, "Reinforcement Learning with Neural Networks for Quantum Feedback", Physical Review X **8**, 031084 (2018).

[61] H. P. Nautrup, N. Delfosse, V. Dunjko, H. J. Briegel and N. Friis, "Optimizing Quantum Error Correction Codes with Reinforcement Learning", Quantum **3**, 215 (2019).

[62] L. Pilozzi, F. A. Farrelly, G. Marcucci and C. Conti, "Machine learning inverse problem for topological photonics", Communications Physics **1**, 1–7 (2018).

[63] G. Torlai, G. Mazzola, J. Carrasquilla, M. Troyer, R. Melko and G. Carleo, "Neural-network quantum state tomography", Nature Physics **14**, 447–450 (2018).

[64] G. Carleo, I. Cirac, K. Cranmer, L. Daudet, M. Schuld, N. Tishby, L. Vogt-Maranto and L. Zdeborová, "Machine learning and the physical sciences", Reviews of Modern Physics **91**, 045002 (2019).

[65] A. Fratalocchi, A. Fleming, C. Conti and A. D. Falco, "NIST-certified secure key generation via deep learning of physical unclonable functions in silica aerogels", Nanophotonics **10**, 457–464 (2021).

[66] M. Schuld, I. Sinayskiy and F. Petruccione, "An introduction to quantum machine learning", Contemporary Physics **56**, 172–185 (2015).

[67] J. Biamonte, P. Wittek, N. Pancotti, P. Rebentrost, N. Wiebe and S. Lloyd, "Quantum machine learning", Nature **549**, 195–202 (2017).

[68] P. Mujal, R. Martínez-Peña, J. Nokkala, J. García-Beni, G. L. Giorgi, M. C. Soriano and R. Zambrini, "Opportunities in Quantum Reservoir Computing and Extreme Learning Machines", Advanced Quantum Technologies **4**, 2100027 (2021).

[69] A. Peres and D. R. Terno, "Quantum information and relativity theory", Reviews of Modern Physics **76**, 93–123 (2004).

[70] R. B. Mann and T. C. Ralph, "Relativistic quantum information", Classical and Quantum Gravity **29**, 220301 (2012).

[71] I. Newton, *Opticks or a Treatise of the Reflexions, Refractions, Inflexions and Colours of Light : also two Treatises of the Species and Magnitude of Curvilinear Figures* (1704).

[72] A. Einstein, "Über einen die Erzeugung und Verwandlung des Lichtes betreffenden heuristischen Gesichtspunkt", Annalen der Physik **322**, 132–148 (1905).

[73] T. H. Maiman, "Stimulated Optical Radiation in Ruby", Nature **187**, 493–494 (1960).

[74] V. Giovannetti, S. Lloyd and L. Maccone, "Advances in quantum metrology", Nature Photonics **5**, 222–229 (2011).

[75] LIGO Scientific Collaboration and Virgo Collaboration et al., "Observation of Gravitational Waves from a Binary Black Hole Merger", Physical Review Letters **116**, 061102 (2016).

[76] C. H. Bennett and D. P. DiVincenzo, "Quantum information and computation", Nature **404**, 247–255 (2000).

[77] S. Haroche and D. Kleppner, "Cavity Quantum Electrodynamics", Physics Today **42**, 24–30 (1989).

[78] P. R. Berman, "Cavity quantum electrodynamics", (1994).

[79] H. Walther, B. T. H. Varcoe, B.-G. Englert and T. Becker, "Cavity quantum electrodynamics", Reports on Progress in Physics **69**, 1325–1382 (2006).

[80] J. C. Maxwell, "VIII. A dynamical theory of the electromagnetic field", Philosophical Transactions of the Royal Society of London **155**, 459–512 (1865).

[81] H. Minkowski, "Die grundgleichungen für die elektromagnetischen vorgänge in bewegten körpern", Nachrichten von der Gesellschaft der Wissenschaften zu Göttingen, Mathematisch-Physikalische Klasse **1908**, 53–111 (1908).

[82] M. E. Peskin and D. V. Schroeder, *An Introduction to quantum field theory* (Addison-Wesley, Reading, USA, 1995).

[83] S. Weinberg, *The quantum theory of fields*, Vol. 1 (Cambridge University Press, Cambridge, 1995).

[84] S. Weinberg, *The quantum theory of fields*, Vol. 2 (Cambridge University Press, Cambridge, 1996).

[85] A. Amo and J. Bloch, "Cavity Polaritons: Crossroad Between Non-Linear Optics and Atomic Condensates", in *Strong Light-Matter Coupling* (WORLD SCIENTIFIC, 2013), pp. 207–239.

[86] O. El Daïf, A. Baas, T. Guillet, J.-P. Brantut, R. I. Kaitouni, J. L. Staehli, F. Morier-Genoud and B. Deveaud, "Polariton quantum boxes in semiconductor microcavities", Applied Physics Letters **88**, 061105 (2006).

[87] K. Kakazu and Y. S. Kim, "Quantization of electromagnetic fields in cavities and spontaneous emission", Physical Review A **50**, 1830–1839 (1994).

[88] S. A. Fulling, "Nonuniqueness of Canonical Field Quantization in Riemannian Space-Time", Physical Review D **7**, 2850–2862 (1973).

[89] P. C. W. Davies, "Scalar production in Schwarzschild and Rindler metrics", Journal of Physics A: Mathematical and General **8**, 609–616 (1975).

[90] W. G. Unruh, "Notes on black-hole evaporation", Physical Review D **14**, 870–892 (1976).

[91] S. W. Hawking, "Particle creation by black holes", Communications in Mathematical Physics **43**, 199–220 (1975).

[92] W. Heisenberg and H. Euler, "Folgerungen aus der diracschen theorie des positrons", Zeitschrift für Physik **98**, 714–732 (1936).

[93] M. Aaboud et al., "Evidence for light-by-light scattering in heavy-ion collisions with the ATLAS detector at the LHC", Nature Physics **13**, 852–858 (2017).

[94] A. Tomadin and R. Fazio, "Many-body phenomena in QED-cavity arrays [Invited]", JOSA B **27**, A130–A136 (2010).

[95] C. Monroe, "Quantum information processing with atoms and photons", Nature **416**, 238–246 (2002).

[96] A. A. Houck, H. E. Türeci and J. Koch, "On-chip quantum simulation with superconducting circuits", Nature Physics **8**, 292–299 (2012).

[97] C. Noh and D. G. Angelakis, "Quantum simulations and many-body physics with light", Reports on Progress in Physics **80**, 016401 (2016).

[98] E. Jaynes and F. Cummings, "Comparison of quantum and semiclassical radiation theories with application to the beam maser", Proceedings of the IEEE **51**, 89–109 (1963).

[99] M. O. Scully and M. S. Zubairy, *Quantum Optics* (Cambridge University Press, Cambridge, 1997).

[100] W. G. Unruh and R. M. Wald, "What happens when an accelerating observer detects a Rindler particle", Physical Review D **29**, 1047–1056 (1984).

[101] S. W. Hawking and W. Israel, *General Relativity: An Einstein Centenary Survey* (Univ. Pr., Cambridge, UK, 1979).

[102] E. Martín-Martínez, M. Montero and M. del Rey, "Wavepacket detection with the Unruh-DeWitt model", Physical Review D **87**, 064038 (2013).

[103] E. G. Brown, E. Martín-Martínez, N. C. Menicucci and R. B. Mann, "Detectors for probing relativistic quantum physics beyond perturbation theory", Physical Review D **87**, 084062 (2013).

[104] R. S. Knox, "Theory of excitons.", Solid State Physics, Vol. 58 **5** (1963).

[105] H. A. Gersch and G. C. Knollman, "Quantum Cell Model for Bosons", Physical Review **129**, 959–967 (1963).

[106] A. Blais, A. L. Grimsmo, S. M. Girvin and A. Wallraff, "Circuit quantum electrodynamics", Reviews of Modern Physics **93**, 025005 (2021).

[107] N. Bartolo, F. Minganti, W. Casteels and C. Ciuti, "Exact steady state of a Kerr resonator with one- and two-photon driving and dissipation: Controllable Wigner-function multimodality and dissipative phase transitions", Physical Review A **94**, 033841 (2016).

[108] S. R. K. Rodriguez, W. Casteels, F. Storme, N. Carlon Zambon, I. Sagnes, L. Le Gratiet, E. Galopin, A. Lemaître, A. Amo, C. Ciuti and J. Bloch, "Probing a Dissipative Phase Transition via Dynamical Optical Hysteresis", Physical Review Letters **118**, 247402 (2017).

[109] A. Baas, J.-P. Karr, M. Romanelli, A. Bramati and E. Giacobino, "Optical bistability in semiconductor microcavities in the nondegenerate parametric oscillation regime: Analogy with the optical parametric oscillator", Physical Review B **70**, 161307 (2004).

[110] C. M. Wilson, G. Johansson, A. Pourkabirian, M. Simoen, J. R. Johansson, T. Duty, F. Nori and P. Delsing, "Observation of the dynamical Casimir effect in a superconducting circuit", Nature **479**, 376–379 (2011).

[111] S. A. Fulling, P. C. W. Davies and R. Penrose, "Radiation from a moving mirror in two dimensional space-time: Conformal anomaly", Proceedings of the Royal Society of London. A. Mathematical and Physical Sciences **348**, 393–414 (1976).

[112] E. Martín-Martínez and P. Rodriguez-Lopez, "Relativistic quantum optics: The relativistic invariance of the light-matter interaction models", Physical Review D **97**, 105026 (2018).

[113] C. W. Misner, K. S. Thorne and J. A. Wheeler, *Gravitation* (W. H. Freeman, 1973).

[114] F. Giacomini and A. Kempf, "Second-quantized Unruh-DeWitt detectors and their quantum reference frame transformations", Physical Review D **105**, 125001 (2022).

[115] J. Foo, S. Onoe and M. Zych, "Unruh-deWitt detectors in quantum superpositions of trajectories", Physical Review D **102**, 085013 (2020).

[116] J. Foo, S. Onoe, R. B. Mann and M. Zych, "Thermality, causality, and the quantum-controlled Unruh–deWitt detector", Physical Review Research **3**, 043056 (2021).

[117] L. C. Barbado, E. Castro-Ruiz, L. Apadula and Č. Brukner, "Unruh effect for detectors in superposition of accelerations", Physical Review D **102**, 045002 (2020).

[118] K. Becker, M. Becker and J. H. Schwarz, *String theory and m-theory: a modern introduction* (Cambridge university press, 2006).

[119] C. Rovelli, "Loop Quantum Gravity", Living Reviews in Relativity **11**, 5 (2008).

[120] N. D. Birrell and P. C. W. Davies, *Quantum Fields in Curved Space*, Cambridge Monographs on Mathematical Physics (Cambridge University Press, Cambridge, 1982).

[121] S. M. Carroll, *Spacetime and geometry: An introduction to general relativity* (Cambridge University Press, Cambridge, 2019).

[122] E. Martín-Martínez, I. Fuentes and R. B. Mann, "Using Berry's Phase to Detect the Unruh Effect at Lower Accelerations", Physical Review Letters **107**, 131301 (2011).

[123] G. Cozzella, A. G. S. Landulfo, G. E. A. Matsas and D. A. T. Vanzella, "Proposal for Observing the Unruh Effect using Classical Electrodynamics", Physical Review Letters **118**, 161102 (2017).

[124] W. Rindler, "Kruskal Space and the Uniformly Accelerated Frame", American Journal of Physics **34**, 1174–1178 (1966).

[125] K. Schwarzschild, "Über das gravitationsfeld einer kugel aus inkompressibler flüssigkeit nach der einsteinschen theorie", Sitzungsberichte der königlich preußischen Akademie der Wissenschaften zu Berlin, 424–434 (1916).

[126] S. Dimopoulos and G. Landsberg, "Black Holes at the Large Hadron Collider", Physical Review Letters **87**, 161602 (2001).

[127] W. B. Atwood et al., "THE LARGE AREA TELESCOPE ON THE FERMI GAMMA-RAY SPACE TELESCOPE MISSION", The Astrophysical Journal **697**, 1071–1102 (2009).

[128] H. S. Nguyen, D. Gerace, I. Carusotto, D. Sanvitto, E. Galopin, A. Lemaître, I. Sagnes, J. Bloch and A. Amo, "Acoustic Black Hole in a Stationary Hydrodynamic Flow of Microcavity Polaritons", Physical Review Letters **114**, 036402 (2015).

[129] J. Steinhauer, "Observation of quantum Hawking radiation and its entanglement in an analogue black hole", Nature Physics **12**, 959–965 (2016).

[130] J. R. Muñoz de Nova, K. Golubkov, V. I. Kolobov and J. Steinhauer, "Observation of thermal Hawking radiation and its temperature in an analogue black hole", Nature **569**, 688–691 (2019).

[131] V. I. Kolobov, K. Golubkov, J. R. Muñoz de Nova and J. Steinhauer, "Observation of stationary spontaneous Hawking radiation and the time evolution of an analogue black hole", Nature Physics **17**, 362–367 (2021).

[132] H. Stanley, *Introduction to phase transitions and critical phenomena*, International Series of Monographs on Physics (Oxford University Press, 1987).

[133] T. C. Hansen, "The everlasting hunt for new ice phases", Nature Communications **12**, 3161 (2021).

[134] J. Buck, "Synchronous rhythmic flashing of fireflies. ii.", The Quarterly review of biology **63**, 265–289 (1988).

[135] É. Durkheim, *Les formes élémentaires de la vie religieuse : le système totémique en Australie* (1912).

[136] C. Castellano, S. Fortunato and V. Loreto, "Statistical physics of social dynamics", Reviews of Modern Physics **81**, 591–646 (2009).

[137] P. W. Anderson, "More Is Different", Science **177**, 393–396 (1972).

[138] S. Sachdev, *Quantum phase transitions* (Cambridge University Press, 2009).

[139] V. F. Gantmakher and V. T. Dolgopolov, "Superconductor–insulator quantum phase transition", Physics-Uspekhi **53**, 1 (2010).

[140] H. J. Carmichael, "Breakdown of Photon Blockade: A Dissipative Quantum Phase Transition in Zero Dimensions", Physical Review X **5**, 031028 (2015).

[141] H. Weimer, "Variational Principle for Steady States of Dissipative Quantum Many-Body Systems", Physical Review Letters **114**, 040402 (2015).

[142] M. Benito, C. Sánchez Muñoz and C. Navarrete-Benlloch, "Degenerate parametric oscillation in quantum membrane optomechanics", Physical Review A **93**, 023846 (2016).

[143] J. J. Mendoza-Arenas, S. R. Clark, S. Felicetti, G. Romero, E. Solano, D. G. Angelakis and D. Jaksch, "Beyond mean-field bistability in driven-dissipative lattices: Bunching-antibunching transition and quantum simulation", Physical Review A **93**, 023821 (2016).

[144] W. Casteels, F. Storme, A. Le Boité and C. Ciuti, "Power laws in the dynamic hysteresis of quantum nonlinear photonic resonators", Physical Review A **93**, 033824 (2016).

[145] W. Casteels, R. Fazio and C. Ciuti, "Critical dynamical properties of a first-order dissipative phase transition", Physical Review A **95**, 012128 (2017).

[146] W. Casteels and C. Ciuti, "Quantum entanglement in the spatial-symmetry-breaking phase transition of a driven-dissipative Bose-Hubbard dimer", Physical Review A **95**, 013812 (2017).

[147] M. Foss-Feig, P. Niroula, J. T. Young, M. Hafezi, A. V. Gorshkov, R. M. Wilson and M. F. Maghrebi, "Emergent equilibrium in many-body optical bistability", Physical Review A **95**, 043826 (2017).

[148] M. Biondi, G. Blatter, H. E. Türeci and S. Schmidt, "Nonequilibrium gas-liquid transition in the driven-dissipative photonic lattice", Physical Review A **96**, 043809 (2017).

[149] A. Biella, F. Storme, J. Lebreuilly, D. Rossini, R. Fazio, I. Carusotto and C. Ciuti, "Phase diagram of incoherently driven strongly correlated photonic lattices", Physical Review A **96**, 023839 (2017).

[150] V. Savona, "Spontaneous symmetry breaking in a quadratically driven nonlinear photonic lattice", Physical Review A **96**, 033826 (2017).

[151] W. Verstraelen, R. Rota, V. Savona and M. Wouters, "Gaussian trajectory approach to dissipative phase transitions: The case of quadratically driven photonic lattices", Physical Review Research **2**, 022037 (2020).

[152] F. Vicentini, F. Minganti, R. Rota, G. Orso and C. Ciuti, "Critical slowing down in driven-dissipative Bose-Hubbard lattices", Physical Review A **97**, 013853 (2018).

[153] L. M. Sieberer, S. D. Huber, E. Altman and S. Diehl, "Dynamical Critical Phenomena in Driven-Dissipative Systems", Physical Review Letters **110**, 195301 (2013).

[154] L. M. Sieberer, S. D. Huber, E. Altman and S. Diehl, "Nonequilibrium functional renormalization for driven-dissipative Bose-Einstein condensation", Physical Review B **89**, 134310 (2014).

[155] E. Altman, L. M. Sieberer, L. Chen, S. Diehl and J. Toner, "Two-Dimensional Superfluidity of Exciton Polaritons Requires Strong Anisotropy", Physical Review X **5**, 011017 (2015).

[156] G. Dagvadorj, M. Kulczykowski, M. H. Szymańska and M. Matuszewski, "First-order dissipative phase transition in an exciton-polariton condensate", Physical Review B **104**, 165301 (2021).

[157] T. E. Lee, S. Gopalakrishnan and M. D. Lukin, "Unconventional Magnetism via Optical Pumping of Interacting Spin Systems", Physical Review Letters **110**, 257204 (2013).

[158] J. Jin, A. Biella, O. Viyuela, L. Mazza, J. Keeling, R. Fazio and D. Rossini, "Cluster Mean-Field Approach to the Steady-State Phase Diagram of Dissipative Spin Systems", Physical Review X **6**, 031011 (2016).

[159] T. E. Lee, H. Häffner and M. C. Cross, "Antiferromagnetic phase transition in a nonequilibrium lattice of Rydberg atoms", Physical Review A **84**, 031402 (2011).

[160] C.-K. Chan, T. E. Lee and S. Gopalakrishnan, "Limit-cycle phase in driven-dissipative spin systems", Physical Review A **91**, 051601 (2015).

[161] R. Rota, F. Storme, N. Bartolo, R. Fazio and C. Ciuti, "Critical behavior of dissipative two-dimensional spin lattices", Physical Review B **95**, 134431 (2017).

[162] V. R. Overbeck, M. F. Maghrebi, A. V. Gorshkov and H. Weimer, "Multicritical behavior in dissipative Ising models", Physical Review A **95**, 042133 (2017).

[163] D. Roscher, S. Diehl and M. Buchhold, "Phenomenology of first-order dark-state phase transitions", Physical Review A **98**, 062117 (2018).

[164] T. Fink, A. Schade, S. Höfling, C. Schneider and A. Imamoglu, "Signatures of a dissipative phase transition in photon correlation measurements", Nature Physics **14**, 365–369 (2018).

[165] M. Fitzpatrick, N. M. Sundaresan, A. C. Y. Li, J. Koch and A. A. Houck, "Observation of a Dissipative Phase Transition in a One-Dimensional Circuit QED Lattice", Physical Review X **7**, 011016 (2017).

[166] A. Le Boité, M.-J. Hwang and M. B. Plenio, "Metastability in the driven-dissipative Rabi model", Physical Review A **95**, 023829 (2017).

[167] A. Le Boité, "Theoretical Methods for Ultrastrong Light–Matter Interactions", Advanced Quantum Technologies **3**, 1900140 (2020).

[168] F. Minganti, A. Biella, N. Bartolo and C. Ciuti, "Spectral theory of Liouvillians for dissipative phase transitions", Physical Review A **98**, 042118 (2018).

[169] T. Kato, *Perturbation theory for linear operators* (Springer Science & Business Media, 2013).

[170] K. Vogel and H. Risken, "Quasiprobability distributions in dispersive optical bistability", Physical Review A **39**, 4675–4683 (1989).

[171] H. J. Carmichael, *Statistical methods in quantum optics 1* (Springer Berlin Heidelberg, 1999).

[172] R. Chartrand, "Numerical Differentiation of Noisy, Nonsmooth Data", ISRN Applied Mathematics **2011**, e164564 (2011).

[173] D. Ballarini, M. De Giorgi, E. Cancellieri, R. Houdré, E. Giacobino, R. Cingolani, A. Bramati, G. Gigli and D. Sanvitto, "All-optical polariton transistor", Nature Communications **4**, 1778 (2013).

[174] H. J. Carmichael, *Statistical Methods in Quantum Optics 2: Non-Classical Fields* (Springer Science & Business Media, 2009).

[175] M. H. Devoret and R. J. Schoelkopf, "Superconducting circuits for quantum information: an outlook", Science (New York, N.Y.) **339**, 1169–1174 (2013).

[176] A. Blais, J. Gambetta, A. Wallraff, D. I. Schuster, S. M. Girvin, M. H. Devoret and R. J. Schoelkopf, "Quantum-information processing with circuit quantum electrodynamics", Physical Review A **75**, 032329 (2007).

[177] R. Rota, F. Minganti, C. Ciuti and V. Savona, "Quantum critical regime in a quadratically driven nonlinear photonic lattice", Physical Review Letters **122**, 110405 (2019).

[178] N. Bartolo, F. Minganti, J. Lolli and C. Ciuti, "Homodyne versus photon-counting quantum trajectories for dissipative Kerr resonators with two-photon driving", The European Physical Journal Special Topics **226**, 2705–2713 (2017).

[179] M. Mirrahimi, Z. Leghtas, V. V. Albert, S. Touzard, R. J. Schoelkopf, L. Jiang and M. H. Devoret, "Dynamically protected cat-qubits: a new paradigm for universal quantum computation", New Journal of Physics **16**, 045014 (2014).

[180] R. W. Heeres, P. Reinhold, N. Ofek, L. Frunzio, L. Jiang, M. H. Devoret and R. J. Schoelkopf, "Implementing a universal gate set on a logical qubit encoded in an oscillator", Nature Communications **8**, 94 (2017).

[181] R. Lescanne, M. Villiers, T. Peronnin, A. Sarlette, M. Delbecq, B. Huard, T. Kontos, M. Mirrahimi and Z. Leghtas, "Exponential suppression of bit-flips in a qubit encoded in an oscillator", Nature Physics **16**, 509–513 (2020).

[182] R. Schoelkopf and S. Girvin, "Wiring up quantum systems", Nature **451**, 664–669 (2008).

[183] S. Schmidt and J. Koch, "Circuit QED lattices: towards quantum simulation with superconducting circuits", Annalen der Physik **525**, 395–412 (2013).

[184] D. I. Tsomokos, S. Ashhab and F. Nori, "Using superconducting qubit circuits to engineer exotic lattice systems", Physical Review A **82**, 052311 (2010).

[185] A. Ramirez, "Strongly geometrically frustrated magnets", Annual Review of Materials Science **24**, 453–480 (1994).

[186] R. Moessner and A. P. Ramirez, "Geometrical frustration", Physics Today **59**, 24 (2006).

[187] J. T. Chalker, P. C. Holdsworth and E. Shender, "Hidden order in a frustrated system: Properties of the Heisenberg Kagomé antiferromagnet", Physical review letters **68**, 855 (1992).

[188] Q. Si and E. Abrahams, "Strong correlations and magnetic frustration in the high T c iron pnictides", Physical Review Letters **101**, 076401 (2008).

[189] K. Le Hur and M. Rice, "Superconductivity close to the Mott state: From condensed-matter systems to superfluidity in optical lattices", Annals of Physics **324**, 1452–1515 (2009).

[190] A. Ramires, "Frustration can be critical", Nature Physics **15**, 1212–1214 (2019).

[191] W. Giauque and J. Stout, "The entropy of water and the third law of thermodynamics. The heat capacity of ice from 15 to 273° K.", Journal of the American Chemical Society **58**, 1144–1150 (1936).

[192] G. Wannier, "Antiferromagnetism. the triangular ising net", Physical Review **79**, 357 (1950).

[193] M. Mézard, G. Parisi and M. Virasoro, *Spin glass theory and beyond: An introduction to the replica method and its applications*, Vol. 9 (World Scientific Publishing Company, 1987).

[194] L. Balents, "Spin liquids in frustrated magnets", Nature **464**, 199–208 (2010).

[195] Y. Zhou, K. Kanoda and T.-K. Ng, "Quantum spin liquid states", Reviews of Modern Physics **89**, 025003 (2017).

[196] S. Yan, D. A. Huse and S. R. White, "Spin-liquid ground state of the S= 1/2 kagome Heisenberg antiferromagnet", Science (New York, N.Y.) **332**, 1173–1176 (2011).

[197] Y. Shimizu, K. Miyagawa, K. Kanoda, M. Maesato and G. Saito, "Spin liquid state in an organic Mott insulator with a triangular lattice", Physical review letters **91**, 107001 (2003).

[198] R. Coldea, D. Tennant, A. Tsvelik and Z. Tylczynski, "Experimental realization of a 2D fractional quantum spin liquid", Physical review letters **86**, 1335 (2001).

[199] L. Savary and L. Balents, "Quantum spin liquids: a review", Reports on Progress in Physics **80**, 016502 (2016).

[200] H. Weimer, M. Müller, I. Lesanovsky, P. Zoller and H. P. Büchler, "A rydberg quantum simulator", Nature Physics **6**, 382–388 (2010).

[201] T. Cantat-Moltrecht, R. Cortiñas, B. Ravon, P. Méhaignerie, S. Haroche, J. M. Raimond, M. Favier, M. Brune and C. Sayrin, "Long-lived circular Rydberg states of laser-cooled rubidium atoms in a cryostat", Physical Review Research **2**, 022032 (2020).

[202] S. Kuhr, "Quantum-gas microscopes: a new tool for cold-atom quantum simulators", National Science Review **3**, 170–172 (2016).

[203] D. Pierangeli, G. Marcucci and C. Conti, "Large-Scale Photonic Ising Machine by Spatial Light Modulation", Physical Review Letters **122**, 213902 (2019).

[204] D. Pierangeli, D. Pierangeli, G. Marcucci, G. Marcucci, C. Conti and C. Conti, "Adiabatic evolution on a spatial-photonic Ising machine", Optica **7**, 1535–1543 (2020).

[205] D. Pierangeli, M. Rafayelyan, C. Conti and S. Gigan, "Scalable Spin-Glass Optical Simulator", Physical Review Applied **15**, 034087 (2021).

[206] A. Aspuru-Guzik and P. Walther, "Photonic quantum simulators", Nature physics **8**, 285–291 (2012).

[207] M. J. Hartmann, "Quantum simulation with interacting photons", Journal of Optics **18**, 104005 (2016).

[208] D. G. Angelakis, *Quantum simulations with photons and polaritons* (Springer, 2017).

[209] A. Amo and J. Bloch, "Exciton-polaritons in lattices: A non-linear photonic simulator", Comptes Rendus Physique **17**, 934–945 (2016).

[210] T. Boulier, M. J. Jacquet, A. Maître, G. Lerario, F. Claude, S. Pigeon, Q. Glorieux, A. Amo, J. Bloch, A. Bramati et al., "Microcavity polaritons for quantum simulation", Advanced Quantum Technologies, 2000052 (2020).

[211] N. G. Berloff, M. Silva, K. Kalinin, A. Askitopoulos, J. D. Töpfer, P. Cilibrizzi, W. Langbein and P. G. Lagoudakis, "Realizing the classical XY Hamiltonian in polariton simulators", Nature materials **16**, 1120–1126 (2017).

[212] V. Goblot, B. Rauer, F. Vicentini, A. Le Boité, E. Galopin, A. Lemaître, L. Le Gratiet, A. Harouri, I. Sagnes, S. Ravets, C. Ciuti, A. Amo and J. Bloch, "Nonlinear Polariton Fluids in a Flatband Reveal Discrete Gap Solitons", Physical Review Letters **123**, 113901 (2019).

[213] S. Haroche, M. Brune and J. Raimond, "From cavity to circuit quantum electrodynamicst", Nature Physics **16**, 243–246 (2020).

[214] Editorial, "The ABC of cQED", Nature Physics **16**, 233–233 (2020).

[215] R. Rota and V. Savona, "Simulating frustrated antiferromagnets with quadratically driven QED cavities", Physical Review A **100**, 013838 (2019).

[216] M. Kounalakis, C. Dickel, A. Bruno, N. K. Langford and G. A. Steele, "Tuneable hopping and nonlinear cross-Kerr interactions in a high-coherence superconducting circuit", npj Quantum Information **4**, 1–7 (2018).

[217] S. Haddadi, P. Hamel, G. Beaudoin, I. Sagnes, C. Sauvan, P. Lalanne, J. A. Levenson and A. Yacomotti, "Photonic molecules: tailoring the coupling strength and sign", Optics Express **22**, 12359–12368 (2014).

[218] J. Stephenson, "Ising-model spin correlations on the triangular lattice", Journal of Mathematical Physics **5**, 1009–1024 (1964).

[219] D. E. Bruschi, C. Sabín, P. Kok, G. Johansson, P. Delsing and I. Fuentes, "Towards universal quantum computation through relativistic motion", Scientific Reports **6**, 18349 (2016).

[220] D. E. Bruschi, A. Dragan, A. R. Lee, I. Fuentes and J. Louko, "Relativistic Motion Generates Quantum Gates and Entanglement Resonances", Physical Review Letters **111**, 090504 (2013).

[221] D. E. Bruschi, J. Louko, D. Faccio and I. Fuentes, "Mode-mixing quantum gates and entanglement without particle creation in periodically accelerated cavities", New Journal of Physics **15**, 073052 (2013).

[222] N. Friis, M. Huber, I. Fuentes and D. E. Bruschi, "Quantum gates and multipartite entanglement resonances realized by nonuniform cavity motion", Physical Review D **86**, 105003 (2012).

[223] S. L. Braunstein and P. van Loock, "Quantum information with continuous variables", Reviews of Modern Physics **77**, 513–577 (2005).

[224] E. Martín-Martínez, D. Aasen and A. Kempf, "Processing Quantum Information with Relativistic Motion of Atoms", Physical Review Letters **110**, 160501 (2013).

[225] J. R. Johansson, G. Johansson, C. M. Wilson and F. Nori, "Dynamical Casimir Effect in a Superconducting Coplanar Waveguide", Physical Review Letters **103**, 147003 (2009).

[226] M. del Rey, D. Porras and E. Martín-Martínez, "Simulating accelerated atoms coupled to a quantum field", Physical Review A **85**, 022511 (2012).

[227] S. Felicetti, C. Sabín, I. Fuentes, L. Lamata, G. Romero and E. Solano, "Relativistic motion with superconducting qubits", Physical Review B **92**, 064501 (2015).

[228] L.-M. Duan and C. Monroe, "Colloquium: Quantum networks with trapped ions", Reviews of Modern Physics **82**, 1209–1224 (2010).

[229] G. Tanaka, T. Yamane, J. B. Héroux, R. Nakane, N. Kanazawa, S. Takeda, H. Numata, D. Nakano and A. Hirose, "Recent advances in physical reservoir computing: A review", Neural Networks **115**, 100–123 (2019).

[230] G. V. der Sande, D. Brunner and M. C. Soriano, "Advances in photonic reservoir computing", Nanophotonics **6**, 561–576 (2017).

[231] S. Sunada, K. Kanno and A. Uchida, "Using multidimensional speckle dynamics for high-speed, large-scale, parallel photonic computing", Optics Express **28**, 30349–30361 (2020).

[232] D. Pierangeli, G. Marcucci and C. Conti, "Photonic extreme learning machine by free-space optical propagation", Photon. Res. **9**, 1446–1454 (2021).

[233] K. Vandoorne, P. Mechet, T. Van Vaerenbergh, M. Fiers, G. Morthier, D. Verstraeten, B. Schrauwen, J. Dambre and P. Bienstman, "Experimental demonstration of reservoir computing on a silicon photonics chip", Nature Communications **5**, 3541 (2014).

[234] F. D.-L. Coarer, M. Sciamanna, A. Katumba, M. Freiberger, J. Dambre, P. Bienstman and D. Rontani, "All-Optical Reservoir Computing on a Photonic Chip Using Silicon-Based Ring Resonators", IEEE Journal of Selected Topics in Quantum Electronics **24**, 1–8 (2018).

[235] A. Opala, S. Ghosh, T. C. Liew and M. Matuszewski, "Neuromorphic Computing in Ginzburg-Landau Polariton-Lattice Systems", Physical Review Applied **11**, 064029 (2019).

[236] D. Ballarini, A. Gianfrate, R. Panico, A. Opala, S. Ghosh, L. Dominici, V. Ardizzone, M. De Giorgi, G. Lerario, G. Gigli, T. C. H. Liew, M. Matuszewski and D. Sanvitto, "Polaritonic Neuromorphic Computing Outperforms Linear Classifiers", Nano Letters **20**, 3506–3512 (2020).

[237] R. Mirek, A. Opala, P. Comaron, M. Furman, M. Król, K. Tyszka, B. Seredyński, D. Ballarini, D. Sanvitto, T. C. H. Liew, W. Pacuski, J. Suffczyński, J. Szczytko, M. Matuszewski and B. Piętka, "Neuromorphic Binarized Polariton Networks", Nano Letters **21**, 3715–3720 (2021).

[238] M. S. Kulkarni and C. Teuscher, "Memristor-based reservoir computing", in Proceedings of the 2012 IEEE/ACM International Symposium on Nanoscale Architectures, NANOARCH '12 (2012), pp. 226–232.

[239] C. Du, F. Cai, M. A. Zidan, W. Ma, S. H. Lee and W. D. Lu, "Reservoir computing using dynamic memristors for temporal information processing", Nature Communications **8**, 2204 (2017).

[240] S. Boyn, J. Grollier, G. Lecerf, B. Xu, N. Locatelli, S. Fusil, S. Girod, C. Carrétéro, K. Garcia, S. Xavier, J. Tomas, L. Bellaiche, M. Bibes, A. Barthélémy, S. Saïghi and V. Garcia, "Learning through ferroelectric domain dynamics in solid-state synapses", Nature Communications **8**, 14736 (2017).

[241] R. Nakane, G. Tanaka and A. Hirose, "Reservoir Computing With Spin Waves Excited in a Garnet Film", IEEE Access **6**, 4462–4469 (2018).

[242] D. Marković, N. Leroux, M. Riou, F. Abreu Araujo, J. Torrejon, D. Querlioz, A. Fukushima, S. Yuasa, J. Trastoy, P. Bortolotti and J. Grollier, "Reservoir computing with the frequency, phase, and amplitude of spin-torque nano-oscillators", Applied Physics Letters **114**, 012409 (2019).

[243] G. Marcucci, D. Pierangeli and C. Conti, "Theory of Neuromorphic Computing by Waves: Machine Learning by Rogue Waves, Dispersive Shocks, and Solitons", Physical Review Letters **125**, 093901 (2020).

[244] R. A. Bravo, K. Najafi, X. Gao and S. F. Yelin, "Quantum Reservoir Computing Using Arrays of Rydberg Atoms", PRX Quantum **3**, 030325 (2022).

[245] S. Ghosh, A. Opala, M. Matuszewski, T. Paterek and T. C. H. Liew, "Quantum reservoir processing", npj Quantum Information **5**, 1–6 (2019).

[246] S. Ghosh, A. Opala, M. Matuszewski, T. Paterek and T. C. H. Liew, "Reconstructing Quantum States With Quantum Reservoir Networks", IEEE Transactions on Neural Networks and Learning Systems **32**, 3148–3155 (2021).

[247] S. Ghosh, T. Paterek and T. C. H. Liew, "Quantum Neuromorphic Platform for Quantum State Preparation", Physical Review Letters **123**, 260404 (2019).

[248] S. Ghosh, T. Krisnanda, T. Paterek and T. C. H. Liew, "Realising and compressing quantum circuits with quantum reservoir computing", Communications Physics **4**, 1–7 (2021).

[249] T. Krisnanda, S. Ghosh, T. Paterek and T. C. H. Liew, "Creating and concentrating quantum resource states in noisy environments using a quantum neural network", Neural Networks **136**, 141–151 (2021).

[250] H. Xu, T. Krisnanda, W. Verstraelen, T. C. H. Liew and S. Ghosh, "Superpolynomial quantum enhancement in polaritonic neuromorphic computing", Physical Review B **103**, 195302 (2021).

[251] C. Fernando and S. Sojakka, "Pattern Recognition in a Bucket", in Advances in Artificial Life, edited by W. Banzhaf, J. Ziegler, T. Christaller, P. Dittrich and J. T. Kim, Lecture Notes in Computer Science (2003), pp. 588–597.

[252] D. Nikolić, S. Haeusler, W. Singer and W. Maass, "Temporal dynamics of information content carried by neurons in the primary visual cortex", in Advances in Neural Information Processing Systems, Vol. 19 (2006).

[253] B. Jones, D. Stekel, J. Rowe and C. Fernando, "Is there a Liquid State Machine in the Bacterium Escherichia Coli?", in 2007 IEEE Symposium on Artificial Life (2007), pp. 187–191.

[254] J. Dong, M. Rafayelyan, F. Krzakala and S. Gigan, "Optical Reservoir Computing Using Multiple Light Scattering for Chaotic Systems Prediction", IEEE Journal of Selected Topics in Quantum Electronics **26**, 1–12 (2020).

[255] M. Rafayelyan, J. Dong, Y. Tan, F. Krzakala and S. Gigan, "Large-Scale Optical Reservoir Computing for Spatiotemporal Chaotic Systems Prediction", Physical Review X **10**, 041037 (2020).

[256] A. Saade, F. Caltagirone, I. Carron, L. Daudet, A. Drémeau, S. Gigan and F. Krzakala, "Random projections through multiple optical scattering: Approximating Kernels at the speed of light", in 2016 IEEE International Conference on Acoustics, Speech and Signal Processing (ICASSP) (2016), pp. 6215–6219.

[257] R. Ohana, J. Wacker, J. Dong, S. Marmin, F. Krzakala, M. Filippone and L. Daudet, "Kernel Computations from Large-Scale Random Features Obtained by Optical Processing Units", in ICASSP 2020 - 2020 IEEE International Conference on Acoustics, Speech and Signal Processing (ICASSP) (2020), pp. 9294–9298.

[258] Z. Denis, I. Favero and C. Ciuti, "Photonic Kernel Machine Learning for Ultrafast Spectral Analysis", Physical Review Applied **17**, 034077 (2022).

[259] T. Hastie, R. Tibshirani and J. Friedman, *The Elements of Statistical Learning: Data Mining, Inference, and Prediction* (Springer Science & Business Media, 2013).

[260] M. H. Hassoun and A. P. o. C. E. M. H. Hassoun, *Fundamentals of Artificial Neural Networks* (MIT Press, 1995).

[261] J. von Neumann, "First draft of a report on the EDVAC", IEEE Annals of the History of Computing **15**, 27–75 (1993 [1945]).

[262] G.-B. Huang, Q.-Y. Zhu and C.-K. Siew, "Extreme learning machine: Theory and applications", Neurocomputing, Neural Networks **70**, 489–501 (2006).

[263] J. Suykens and J. Vandewalle, "Least Squares Support Vector Machine Classifiers", Neural Processing Letters **9**, 293–300 (1999).

[264] J. Mercer and A. R. Forsyth, "XVI. Functions of positive and negative type, and their connection the theory of integral equations", Philosophical Transactions of the Royal Society of London. Series A, Containing Papers of a Mathematical or Physical Character **209**, 415–446 (1909).

[265] V. I. Paulsen and M. Raghupathi, *An Introduction to the Theory of Reproducing Kernel Hilbert Spaces*, Cambridge Studies in Advanced Mathematics (Cambridge University Press, Cambridge, 2016).

[266] C. Williams and M. Seeger, "Using the nyström method to speed up kernel machines", in Advances in neural information processing systems 13 (2001), pp. 682–688.

[267] A. Ahmadzadegan, R. B. Mann and E. Martín-Martínez, "Measuring motion through relativistic quantum effects", Physical Review A **90**, 062107 (2014).

[268] B. Šoda, V. Sudhir and A. Kempf, "Acceleration-Induced Effects in Stimulated Light-Matter Interactions", Physical Review Letters **128**, 163603 (2022).

[269] R. Simon, E. C. G. Sudarshan and N. Mukunda, "Gaussian pure states in quantum mechanics and the symplectic group", Physical Review A **37**, 3028–3038 (1988).

[270] C. Weedbrook, S. Pirandola, R. García-Patrón, N. J. Cerf, T. C. Ralph, J. H. Shapiro and S. Lloyd, "Gaussian quantum information", Reviews of Modern Physics **84**, 621–669 (2012).

[271] G. Adesso, S. Ragy and A. R. Lee, "Continuous Variable Quantum Information: Gaussian States and Beyond", Open Systems & Information Dynamics **21**, 1440001 (2014).

[272] S. Vriend, D. Grimmer and E. Martín-Martínez, "The Unruh Effect in Slow Motion", Symmetry **13**, 1977 (2021).

[273] W. Rindler, *Introduction to Special Relativity* (Clarendon Press, 1982).

[274] K. Lang, "Learning to tell two spiral apart", in Proceedings of the 1988 connectionist models summer school (1989), pp. 52–59.

[275] C.-C. Yu and B.-D. Liu, "A backpropagation algorithm with adaptive learning rate and momentum coefficient", in Proceedings of the 2002 International Joint Conference on Neural Networks. IJCNN'02 (Cat. No.02CH37290), Vol. 2 (2002), 1218–1223 vol.2.

[276] O. Klein, "Quantentheorie und fünfdimensionale Relativitätstheorie", Zeitschrift für Physik **37**, 895–906 (1926).

[277] W. Gordon, "Der Comptoneffekt nach der Schrödingerschen Theorie", Zeitschrift für Physik **40**, 117–133 (1926).

[278] H. B. Casimir, "On the attraction between two perfectly conducting plates", in Proc. kon. ned. akad. wet. Vol. 51 (1948), p. 793.

[279] G. Bressi, G. Carugno, R. Onofrio and G. Ruoso, "Measurement of the Casimir Force between Parallel Metallic Surfaces", Physical Review Letters **88**, 041804 (2002).

[280] S. Weinberg, "The cosmological constant problem", Reviews of Modern Physics **61**, 1–23 (1989).